



**HAL**  
open science

## Fuel cells active layers realisation by printing processes

Chloé Bois

► **To cite this version:**

Chloé Bois. Fuel cells active layers realisation by printing processes. Other. Université de Grenoble, 2012. English. NNT: 2012GRENI076 . tel-00844403

**HAL Id: tel-00844403**

**<https://theses.hal.science/tel-00844403>**

Submitted on 15 Jul 2013

**HAL** is a multi-disciplinary open access archive for the deposit and dissemination of scientific research documents, whether they are published or not. The documents may come from teaching and research institutions in France or abroad, or from public or private research centers.

L'archive ouverte pluridisciplinaire **HAL**, est destinée au dépôt et à la diffusion de documents scientifiques de niveau recherche, publiés ou non, émanant des établissements d'enseignement et de recherche français ou étrangers, des laboratoires publics ou privés.

## THÈSE

Pour obtenir le grade de

## DOCTEUR DE L'UNIVERSITÉ DE GRENOBLE

Spécialité : Matériaux, Mécanique, Génie civil, Electrochimie

Arrêté ministériel : 7 août 2006

Présentée par

**Chloé Bois**

Thèse dirigée par **Anne Blayo** et  
codirigée par **Didier Chaussy**

préparée au sein du **Laboratoire de Génie des Procédés Papetiers**  
dans l'**École Doctorale I-MEP2**

# Fabrication d'Assemblages Membrane-Electrodes de Piles à Combustible par Procédés d'Impression

Thèse soutenue publiquement le **26 octobre 2012**

devant le jury composé de :

**Pr. Yann BULTEL** Président

**Pr. Dr. rer. nat. Reinhard BAUMANN** Rapporteur

**Dr. François LAPICQUE** Rapporteur

**Dr. Patrick ACHARD** Examineur

**Dr. Anne BLAYO** Membre

**Pr. Didier CHAUSSY** Membre





<b>Table of contents</b> .....	<b>1</b>
<b>Abbreviations and symbols</b> .....	<b>3</b>
<b>General introduction</b> .....	<b>7</b>
<b>Chapter 1 Literature review</b> .....	<b>13</b>
Introduction .....	17
1. Fuel Cells .....	19
2. Proton Exchange Membrane Fuel Cell .....	30
3. Proton Exchange Membrane Fuel Cell Manufacturing by Printing Processes.....	48
Conclusion .....	63
<b>Chapter 2 Materials and methods</b> .....	<b>65</b>
Introduction .....	69
1. Materials and Processes .....	70
2. Devices and methods for characterising printed substrates and substrate before printing .....	73
Conclusion .....	86
<b>Chapter 3 Catalyst Coated Membrane</b> .....	<b>87</b>
Introduction .....	91
1. Proton exchange membrane characterisation .....	93
2. Improvement of the membrane printability .....	107
Conclusion .....	124
<b>Chapter 4 Catalyst Coated Backing</b> .....	<b>125</b>
Introduction .....	129
1. Gas diffusion layers printability.....	131
2. Gas diffusion electrodes made by flexography .....	148
Conclusion .....	164
<b>Chapter 5 Multilayer</b> .....	<b>165</b>
Introduction .....	169
1. Multilayer characterisation .....	170
2. Designing catalyst layers .....	183
Conclusion .....	200
<b>General conclusion</b> .....	<b>201</b>
<b>Appendices</b> .....	<b>205</b>
<b>Scientific publications</b> .....	<b>225</b>
<b>References</b> .....	<b>229</b>
<b>Résumé en français</b> .....	<b>247</b>



# Abbreviations and Symbols



**Main abbreviations used in the manuscript**

AFC	Alkaline Fuel Cell
CCB	Catalyst Coated Backing
CCM	Catalyst Coated Membrane
CD	Cross Direction
CL	Catalyst Layer
DOE	(US) Department Of Energy
ESA	Electrochemical Surface Area
FC	Fuel Cell
FCV	Fuel Cell Vehicle
GDE	Gas Diffusion Electrode
GDL	Gas Diffusion Layer
MCFC	Molten Carbonate Fuel Cell
MD	Machine Direction
PAFC	Phosphoric Acid Fuel Cell
PEM Proton	Exchange Membrane
PEMFC	Proton Exchange Membrane Fuel Cell
PFSA	PerFluoroSulfonic Acid
Pt	Platinum
PTFE	PolyTetraFluoroEthylene
RH%	Relative Humidity (given in percentage)
SOFC	Solid Oxide Fuel Cell

**Symbols**

$\Delta\varepsilon$ (%)	Strain amplitude
$\Delta L$ (mm)	Sample length variations or expansion
$\Delta P$ (Pa)	Pressure
$\varepsilon$ (%)	Sample macroscopically strain
$\varepsilon_{ave}$ (%)	Average strain
$\varepsilon_{irr}$ (%)	Irreversible strain
$EW$ (g mol <sup>-1</sup> )	Equivalent Weight
$\dot{\gamma}$ (s <sup>-1</sup> )	Shear rate
$\gamma$ (mN m <sup>-1</sup> )	Surface Energy or surface tension
$\gamma^D$ (mN m <sup>-1</sup> )	Dispersive contribution of the surface energy
$\gamma_L$ (mN m <sup>-1</sup> )	Surface tension (in case of a liquid)
$\gamma^P$ (mN m <sup>-1</sup> )	Polar contribution of the surface energy
$\gamma_S$ (mN m <sup>-1</sup> )	Surface energy (in case of a solid)
$h$ (μm)	average depth of relief (PPS)
$I$ (cd)	Light intensity
$K$ (m <sup>2</sup> s <sup>-1</sup> Pa <sup>-1</sup> )	intrinsic permeability of 1 m <sup>3</sup> of sample crossed by an air flow at a constant relative applied pressure
$k$	PPS coefficient for $h$ calculation
$\lambda$	number of water molecules by sulfonic acid group of Nafion <sup>®</sup> polymer
$\lambda$ (nm)	or light wavelength
$L_0$ (mm)	Sample initial length
$\mu$ (Pa s)	Viscosity
$m$ (mg)	Mass of a sample
$M_w$ (g mol <sup>-1</sup> )	Molecular mass of the water
OD	Optical Density
$P_w$ (Pa)	Water vapour pressure of the in the air
$P_{ws}(T)$ (Pa)	Water vapour pressure in a saturated air at the temperature equal to $T$
$Q$ (cm <sup>3</sup> s <sup>-1</sup> )	Air flow
$R$ (m <sup>-1</sup> s Pa)	Air flow resistance
R (%)	Reflectance
$S$ (m <sup>2</sup> )	Surface
$\tau$ (Pa)	Shear stress
$T$ (m)	Thickness
X% (%)	Ink coverage

# General introduction



## General introduction

### 1 Context of the Project

The project CATIMINHY had been named from the abbreviation of French terms “Couches Actives développées par des Technologies d’IMpressioN Hybrides”, which means catalyst layers developed by combined printing technologies. This project was funded by the French National Research Agency (ANR) from January 2009 to June 2012 through the National Plan of Action for Hydrogen 2008 (PAN-H 2008).

This project was based on the triptych described in Figure 1. It is composed of scientific, environmental and economical issues.

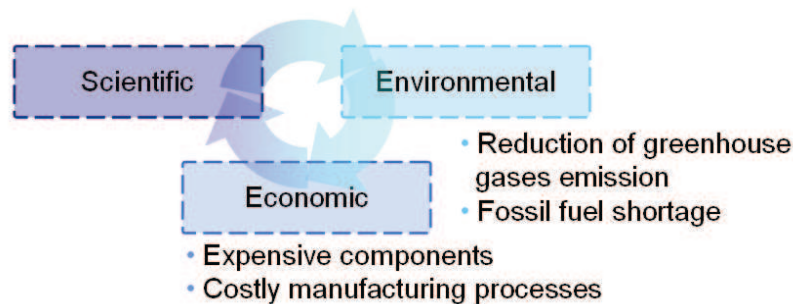


Figure 1 CATIMINHY triptych

Fossil fuel shortage and the necessity in greenhouse gases reduction require investigation on new sources of primary energy. One of the suggested concepts is based on the Equ.1 that links water and energy to oxygen and hydrogen.



The system that converts the chemical energy into electrical energy is a fuel cell. The present project was dedicated to one type of fuel cell, the Proton Exchange Membrane Fuel Cell (PEMFC), which is adapted to portable, automotive and small power supply applications. The core of a PEMFC is composed of five main layers. An electrolyte, the proton exchange membrane, is placed at the centre of the multilayer system for controlling the charge transport. At both sides of the membrane, oxygen and hydrogen (the fuel) react in Catalyst Layers (CLs). Finally, at each side of the catalyst layers, a Gas Diffusion Layer (GDL) insures the gases homogenisation. One major concern is that these highly specialised components are very expensive. Moreover, the conventional manufacturing processes have a high cost and only small capacity of production, while the fuel cell market is constantly growing.

In this context, the CATIMINHY project proposed to fabricate fuel cell components with innovative and economically relevant processes, from printing industry, that should lower the cost of production and enlarge the production capacity.

## 2 CATIMINHY Project

The project focused on the printing processes as breakthrough techniques of deposition for manufacturing PEMFC components using membrane and GDL as printing substrates. Printing processes are mask-less deposition techniques, able to accurately deposit inks on a substrate, with a good reproducibility. They control the thickness of the deposit and optimise the deposit/substrate interface. Depending on the type of printing process, these techniques are adequate for productions that vary from laboratory to mass-commercialisation scale.

Developing these processes for manufacturing catalyst layers was a substantial challenge. Consequently, it was divided into three main tasks, as detailed in Figure 2.

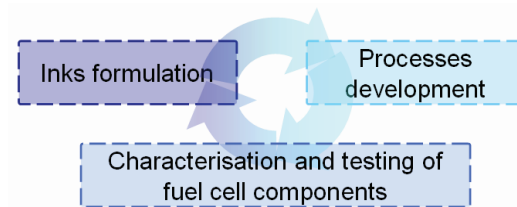


Figure 2 Tasks division

These tasks were distributed among three laboratories:

- CEA, French Nuclear Energy Agency: modeling, characterisation and testing of the fuel cell components, developing the inks and the screen printing process, providing a technico-economical study;
- LEGI, Laboratory of Geophysical and Industrial Flows: investigation on the masterless processes;
- LGP2, Laboratory of Pulp and Paper sciences: investigation on printing processes with contact;

and three industrial partners:

- Siliflow: specialist of liquids handling,
- Paxitech: fuel cell manufacturer,
- and Rhodia: specialty chemicals suppliers, in charge of the ink components development.

### 3 LGP2

Among other expertises, the laboratory of Pulp and Paper Sciences has developed substantial knowledge and skills dedicated to the printing processes. These processes are conventionally focused on office printing, packaging, magazines, books... manufacturing. Since one decade, in addition to pigments and dyes, functional elements are incorporated into the inks formulation. Consequently, the printing processes are also able to give additional functionalities to the substrates.

In the CATIMINHY project, the task of the LGP2 focused on the development of a printing process called the flexography. This process is known to be flexible, especially regarding the substrates requirements and the possibility of roll-to-roll manufacturing.

### 4 Thesis orientations

The goal of the thesis was the demonstration of the relevance of printing processes applied to fuel cell components manufacturing. For this purpose, the guidelines of the thesis are summarised in Figure 3.

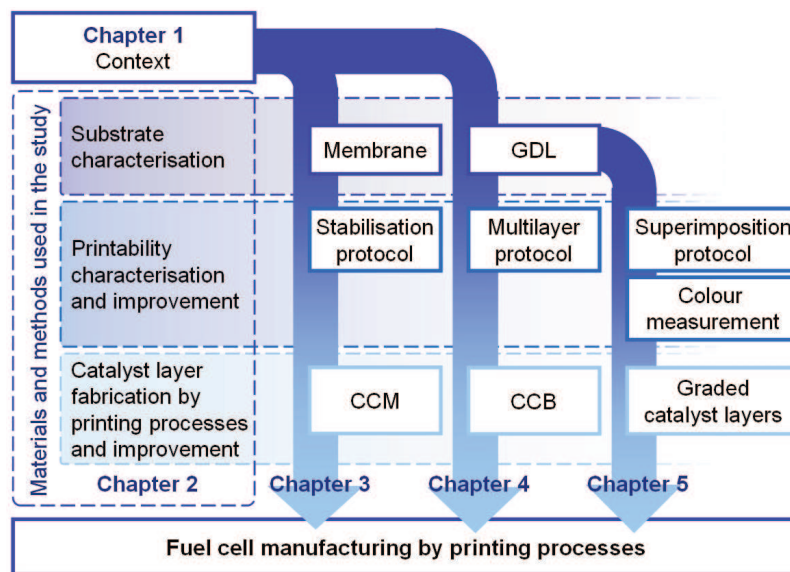


Figure 3 Guidelines of the thesis

The work was performed according to three steps:

- the substrate characterisation,
- the printability characterisation and improvement,
- the catalyst layer fabrication and improvement.

Chapter 1 presents a literature review focusing first on the principles and manufacturing of fuel cells. Secondly, the printing processes are described and their capability for fuel

cells manufacturing is discussed. Chapter 2 is dedicated to the materials and the methods developed during the thesis. Then, the results are detailed in the chapters 3 to 5.

Chapter 3 focuses on the manufacturing of efficient Catalyst Coated Membrane (CCM), where membrane was used as a printing substrate. The substrate characterisation showed that the membrane had a poor printability: a hydrophobic surface combined with a low stability in presence of water and inks. Consequently, the main challenge was to overpass the membrane dimensional variations occurring during printing. A solution to improve the electrolyte printability was proposed and tested.

Chapter 4 details the investigations on the flexography relevance for manufacturing Catalyst Coated Backing (CCB). Similarly to the membrane, the Gas Diffusion Layer (GDL) has a poor printability: its surface has a very hydrophobic behaviour. Nonetheless, it was used as a printing substrate for comparing the ability of conventional and printing deposition techniques for manufacturing catalyst layers.

Chapter 5 demonstrates the advantages of the printing techniques in fuel cell manufacturing. A spectrophotometry measurement, typical from the printing industry, was tested for fuel cell characterisation. It is a fast in-line process control which is able to reduce ex-situ testing. A second study details the promising potential of printing processes to design multilayers in the context of fuel cell.

Finally, conclusions on this study on the fuel cell development are given and future works are proposed.

# Chapter 1

## Literature review



<b>INTRODUCTION .....</b>	<b>17</b>
<b>1 FUEL CELLS.....</b>	<b>19</b>
1.1 THE HYDROGEN ECONOMY .....	19
1.2 MAIN CONCERNS IN THE HYDROGEN ECONOMY.....	20
1.2.1 <i>Hydrogen production</i> .....	21
1.2.2 <i>Hydrogen storage and transportation</i> .....	21
1.3 FUEL CELL HISTORICAL DEVELOPMENT .....	23
1.4 FUEL CELL PRINCIPLE .....	25
1.5 FUEL CELL TECHNOLOGIES.....	26
1.6 MAIN CHALLENGES IN THE FUEL CELL DOMAIN .....	27
<b>2 PROTON EXCHANGE MEMBRANE FUEL CELL .....</b>	<b>30</b>
2.1 MEMBRANE ELECTRODE ASSEMBLY .....	30
2.2 BIPOLAR PLATES.....	32
2.3 GAS DIFFUSION LAYER .....	33
2.3.1 <i>Structure and composition</i> .....	33
2.3.2 <i>Efforts for reducing the GDL manufacturing cost</i> .....	34
2.4 PROTON EXCHANGE MEMBRANE .....	35
2.4.1 <i>Nafion<sup>®</sup> structure</i> .....	36
2.4.1.1 <i>Nafion<sup>®</sup> core structure</i> .....	36
2.4.1.2 <i>Nafion<sup>®</sup> surface structure</i> .....	37
2.4.2 <i>Trends in membrane improvements</i> .....	38
2.5 CATALYST LAYER.....	38
2.5.1 <i>Structure</i> .....	39
2.5.2 <i>Composition</i> .....	39
2.5.3 <i>Catalyst efficiency and cost improvements</i> .....	41
2.6 PEMFC CATALYST LAYERS MANUFACTURING BY DISPERSION DEPOSITION .....	42
<b>3 PRINTING PROCESSES USED FOR PROTON EXCHANGE MEMBRANE FUEL CELL MANUFACTURING .....</b>	<b>48</b>
3.1 PRINTING PROCESSES USED FOR CATALYST LAYER MANUFACTURING .....	49
3.1.1 <i>Screen printing used for fuel cell manufacturing</i> .....	50
3.1.2 <i>Ink jet used for PEM fuel cell manufacturing</i> .....	51
3.1.3 <i>Limits of the ink-jet and screen-printing for manufacturing direct catalyst layers for PEMFC</i> 53	
3.2 THE FLEXOGRAPHY .....	56
3.2.1 <i>Printing groups</i> .....	57

3.2.2	<i>Flexographic inks</i> .....	58
3.2.3	<i>Anilox</i> .....	59
3.2.4	<i>Doctor blade</i> .....	60
3.2.5	<i>Printing plate or cliché</i> .....	60
3.3	FLEXOGRAPHY POTENTIAL FOR MANUFACTURING FUEL CELL COMPONENTS.....	61
	<b>CONCLUSION OF CHAPTER 1 .....</b>	<b>63</b>

## Introduction

In the energy field, the leading objectives are the reduction of the use of hydrocarbon resources and the reduction of pollutants emissions. One potential solution is called “Hydrogen Economy”. It is based on fuel cells technology, which converts chemical energy into electrical energy without any hydrocarbon utilisation and carbon dioxide production. However, nowadays, the cost of this energy remains higher than the energy produced by converting hydrocarbon resources.

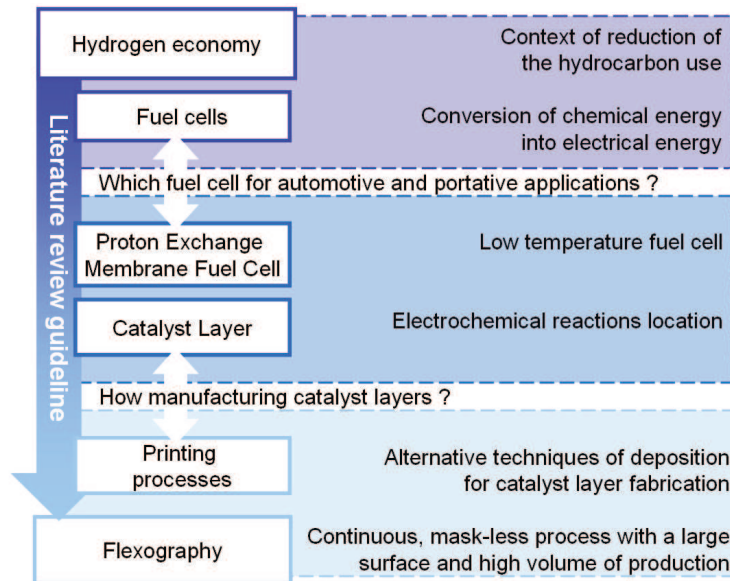


Figure 4 Guideline of the literature review presented in this chapter

This context is developed in the first part of this chapter. Then, following the guideline presented in Figure 4, the literature review summarises the advantages and the main challenges that limit the development of the hydrogen economy, and the different fuel cells types with their characteristics and dedicated applications. The present work focused on Proton Exchange Membrane Fuel Cells (PEMFC), detailed in the second part of the chapter that details the PEMFC’s components and main characteristics. The PEMFC is dedicated to automotive and portative applications, since the electrochemical reactions occur at low temperature in a part of the fuel cell called catalyst layer. More particularly, the manufacturing processes that commonly enter in the PEMFC components fabrication are described. Indeed, this work contributes to the development of the PEMFC by proposing alternative processes for manufacturing the catalyst layers. The proposed process is described in the last part of this chapter. It is a continuous printing process called flexography which allows for producing large surfaces and high volumes of production in conventional printing. Such characteristics represent an interesting potential on the flexography for fuel cell manufacturing compared to the conventional processes.

The literature review details the context of the study which orientated the research and the main goals of the experimental studies presented in the further chapters.

## 1 Fuel cells

The hydrocarbon economy is based on the petroleum utilisation as primary power source. However, in a context of fossil fuel shortage and in pollutant reduction, this type of economy tends to be overtaken by technologies that combine new energy sources and sustainable behaviour.

One of the potential alternatives as world primary energy source is based on:

- fuel cells, which convert chemical energy into electrical energy,
- and hydrogen, which is an energy carrier, and provide the chemical energy to the fuel cell.

Fuel cells and hydrogen are the visible part of a concept called “hydrogen economy”. The paternity of the concept of hydrogen economy is attributed to John O’M. Bockris, Professor of Chemistry at Texas A&M University and to Edward Justi a Physics Professor at the University of Hanover in the 1970s.

The hydrogen economy was described as an economy based on the use of hydrogen to transport energy from renewable sources [Bockris, 2002]. Hydrogen would have been used in fuel cell to produce electricity and as a replacement to natural gas with no pollutant production [Veziroglu, 2000] especially no carbon dioxide formation [Bockris, 2008]. Since, the concern into hydrogen economy has grown up, the concept has been accepted, research was made, development and commercialisation are progressing [Muradova and Veziroglu, 2005; Lattina and Utgikar, 2007]. One indicator of this interest is the evolution of the Fuel cell market, which grew from \$ 353 million in 2005 to \$ 498 million in 2009. The future trend is estimated to reach 1.2 billion by 2014. For example, in 2010, the U.S. Department Of Energy projected that the Japanese production of vehicles equipped with fuel cells will reach 2 million in 2025.

The following parts describe the hydrogen economy (1.1) and its related issues (1.2). But also, fuel cells: their history (1.3), the principle (1.4) and the different types of technologies (1.5).

### 1.1 The hydrogen economy

The concept of hydrogen economy is described by the recycling loop of water on our planet, through the Equ. 1 of water production.



The hydrogen cycle is based on three main components: water, dioxygen and hydrogen, and is composed of seven steps [Goltsova and Verizoglu, 2001] described in Figure 5:

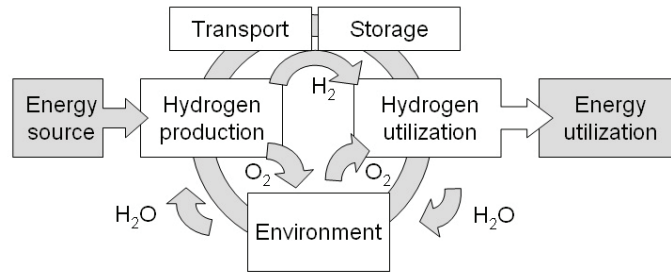


Figure 5 Hydrogen cycle

- an energy source, which is required for water decomposition into oxygen and hydrogen,
- a hydrogen production, which converts the energy into chemical energy,
- a hydrogen transportation,
- a way for storing hydrogen,
- an hydrogen utilization, which converts the chemical energy into electrical energy and/or thermal energy thanks to fuel cell,
- an energy utilization, such as transportation, residential, commercial and industry needs,
- and the environment, from which the water and oxygen are taken and given back.

## 1.2 Main concerns in the hydrogen economy

The hydrogen economy concept does not reach the total agreement of the scientific community. Some authors highlight limitations about the real potential of this solution [Bossel, 2006]:

- the production, storage and transportation of hydrogen induce significant energy loss,
- and the use of clean water as a primary source of hydrogen production will increase the water needs. Unfortunately, obtaining clean water is already a main concern for populations worldwide.

The scientific community faces numerous issues supported by the U.S. government through the Department Of Energy (DOE). This department manages the energy transition from fossil fuel to hydrogen fuel through the Hydrogen and Fuel Cell Program, which details the barriers facing the development of hydrogen economy and fuel cells. The DOE is often used as a reference for fuel cell development, scheduling goals for improving all the aspects of this technology such as hydrogen production (developed in

section 1.2.1), storage and transportation (section 1.2.2), but also fuel cell technologies challenges (section 1.6) [Satyapal *et al.*, 2007; Williams *et al.*, 2004; Marcinkoski *et al.*, 2008; Spendelow and Papageorgopoulos, 2011].

### 1.2.1 Hydrogen production

Hydrogen does not exist in a pure form on Earth. Consequently it has to be industrially produced, and many ways are used [Ortiz-Rivera *et al.*, 2007]:

- steam reforming that is economically beneficial but that is based on hydrocarbon resources and that produces pollutants,
- bio-production that uses organic components and produces hydrocarbon pollutants,

These two methods come against the main principle of the hydrogen economy that rejects hydrocarbon use and production. On a contrary of the two following methods:

- water splitting requiring so much electrical energy that it annuls the interest of using hydrogen as energy carrier,
- sulphur-iodine cycle, a promising method that require several years of improvements,

In Table 1, the four main methods of hydrogen production are compared.

Table 1 Synthesis of hydrogen production methods and issues

Hydrogen production method	Use of organic compounds	Organics by-products	Other drawbacks
Steam reforming of methane or natural gas	$C_nH_m$	$CO_2$ , $CO$ and $C$	
Water splitting	No	No	Low energy efficiency
Sulphur-iodine cycle	No	No	In development
Bio-production	$C_nH_mO_p$	$CO_2$	

Moreover, the production methods should be supplied by clean sources of energy to achieve the no-hydrocarbon goal of the hydrogen economy.

### 1.2.2 Hydrogen storage and transportation

The current industrial production of hydrogen, generally performed by hydrocarbon reforming, mainly uses pipeline (with compressed hydrogen gas) or tanks (with liquid hydrogen or compressed hydrogen) as it is made for natural gas transportation [van der Zwaan *et al.*, 2011; Yang and Ogden, 2007].

However, the ability of this gas to damage the container is a main concern; therefore improvements of the material resistance to embrittlement and corrosion are focused [Chatzidouros *et al.*, 2011].

Moreover, the implementation of hydrogen as a widely use energy carrier will induce a drastic increase of its production and demand.

For these reasons, it will lead to completely change or adapt of the current transportation and storage methods to connect production and utilisation sites. Pipelines networks should be enlarged, as much in number of pipelines as in pipes dimension.

From the hydrogen production sites to the refuelling stations or to high-consumption sites, pipelines and tanks remain suitable for hydrogen delivery as a function of the demand and would insure the hydrogen accessibility for personal use [Chatzidouros *et al.*, 2011].

After being transported, the hydrogen is stored before being used. For that purpose, solutions that gather zero-carbon dioxide production targets and sufficient efficiency are currently under development. For Fuel Cell Vehicles (FCVs), in 2003, the U.S. Department of Energy (DOE) gave objectives through the National Hydrogen Storage Project [Satyapal *et al.*, 2007]. In 2015, the solution of storing have to provide more than 500 km of driving, with a storage density of  $1.8 \text{ kWh kg}^{-1}$  (5.5 w/w% hydrogen) and  $1.3 \text{ kWh L}^{-1}$  ( $40 \text{ g L}^{-1}$ ) [Satyapal *et al.*, 2007].

The solutions and their limitations for individual hydrogen storage are summarised in the Table 2.

Table 2 Synthesis of hydrogen storage methods and issues

Storage solutions	Fulfil the DOE requirements?	Delivery to hydrogen vehicle users?	Other drawback
Compressed hydrogen	No	Direct delivery by refilling the tank or tank replacement	
Cryo-compressed hydrogen	Yes	Direct delivery by refilling the tank or tank replacement	About 1wt% per day of hydrogen loss in cryostats
Adsorbed hydrogen	No	Tank replacement	
Carbon nanotubes	Low hydrogen storing capacity		
Materials with micro and nano-porous structures	Research state		
Absorbed hydrogen	No	Tank replacement	
Metal hydrides	High energy to release $H_2$		
Carbohydrates	Produce $CO_2$ and require a reformer		
Synthesized hydrocarbons	Produce $CO_2$ and require a reformer (except for SOFC)		
Ammonia and derivatives	Require a reformer		
Formic acid	Produce $CO_2$		
Carbonite	Research state		

One other concern with the transport and storage of the fuel is possible fuel contamination during these steps. Indeed, some fuel cells, and especially PEMFC, are highly sensitive to fuel impurities ( $CO$ ,  $CO_2$ ,  $H_2S$  and  $NH_3$ ), which drastically limit the fuel cell efficiency.

### 1.3 Fuel cell historical development

The interest in this energy conversion technology is recent, only about 30 years. However, the discover and the development of the fuel cell began one and a half century ago, contemporary to the voltaic pile of Alessandro Volta.

In 1800, Sir Anthony Carlisle and William Nicholson decomposed water into hydrogen and oxygen using electricity as detailed in Equ. 2 [Faraday, Schönbein, published in 1899].



The technology appears in the late 1830s when, in 1838, Schönbein noticed that after stopping the water electrolysis an opposite current occurred [Stone and Morrison, 2002; Ortiz-Rivera *et al.*, 2007]. This observations was the first describing the fuel cell principle [Schönbein, 1843]. Contemporary, Sir W. Grove successfully tested and described the “gas voltaic battery” in 1839 [Grove, 1839 a and b; Grimes, 2000; Andujar and Segura, 2009]. Grove experimented a hydrogen/oxygen cell in sulphuric acid/water electrolyte with

platinum electrodes that is considered as the first fuel cell. When electricity was first applied to the system, the electrolyte was electrolyzed into hydrogen and oxygen (Equ. 2). The gases produced by electrolysis were stored in appropriate electrodes and reused when the power source was disconnected to produce water at the platinum electrodes (Equ. 3) [Grimes, 2000].



The paternity of the fuel cell discovery remains controversial between these both leading inventors Grove [1839 a and b] and Schönbein [1843] who were, at their times, in a scientific rivalry [Andujar and Segura, 2009].

The term fuel cell appears in 1889 where Mond and Langer described their experiments known as the Mond process [Mond *et al.*, 1890], that produces nickel with a gas-powered battery and thin perforated platinum electrodes [Mond and Langer, 1889; Andujar and Segura, 2009].

The theoretical approach of the previous experiments on fuel cells was given by Ostwald in 1893. Developing Grove's empirical explanations, the roles of each fuel cell component were thus detailed and developed: the electrolyte, electrodes, oxidant and reducer agents, anions and cations [Ortiz-Rivera *et al.*, 2007]. In 1896, Jacques developed the first operating fuel cell.

In 1930, Baur and Preis developed a high temperature fuel cell with solid oxide electrolytes. In the late 1930s, Bacon began his research on alkali electrolyte fuel cell. He developed the first fuel cell that converted air and fuel directly into electricity through electrochemical process. In 1939, a fuel cell was used by the Royal Navy for powering submarines. In 1958, a demonstrator for Britain's National Research Corporation attracted the attention of Pratt & Whitney that licensed his work for Apollo spacecraft missions.

In 1950, a new material, the polytetrafluoroethylene (PTFE or Teflon<sup>®</sup>) was available. It helped to develop aqueous fuel cells as it is currently known now [Andujar and Segura, 2009]. The first fuel cells using this polymer were either with platinum electrodes and an acid electrolyte or with carbon electrodes and alkaline electrolyte. In 1955, a General Electric Company chemist, Thomas Grubb, modified the fuel cell and introduced an ion exchange polystyrene sulphated electrolyte in the fuel cell. Later, Niedrach, who also worked in General Electric Company as a chemist, deposited platinum onto such a membrane. It acted as a catalyst for the hydrogen and oxygen reactions at the anode and the cathode. General Electric Company developed technology for NASA and McDonnell Aircraft. Proton Exchange Membranes Fuel Cells (PEMFCs) were part of the NASA

Gemini project for piloted space program (PEMFC are developed in part 2 of this chapter). This program tested the relevance of new materials, equipments and procedures for lunar flights of the Apollo project that required power sources with longer life time. PEM fuel cells of General Electric Company were selected but encountered several problems. Consequently, batteries that were used to provide power to the previous Mercury missions continued to be used instead of fuel cells.

The new fuels and electrolytes diversified the types of fuel cells and develop new applications. For example, in 1959, the team of Harry Ihrig built the Allis Chalmers fuel cell tractor. The 20 horses tractor was powered by 1008 cells of 1 V each, with potassium hydroxide electrolyte and fed by a mixture of methan and hydrogen gases, and oxygen as the oxidizing agent.

In the late 1950s, Broers and Ketelaar proposed molten salts as electrolyte for high temperature fuel cell as an answer to the electrical conductivity problems and undesired chemical reactions that occurred in solid oxide fuel cell.

In 1961, Elmore and Tanner made a Phosphoric Acid Fuel Cell that works directly fed with air. In 1965, the US Army tested Molten Carbonated Fuel Cells made by Texas Instruments.

#### 1.4 Fuel cell principle

The hydrogen/oxygen fuel cell principles are based on the Equ. 3. The chemical energy (or Gibbs free energy  $\Delta G$  (J.mol<sup>-1</sup>)) of this reaction is directly converted into electrical energy (Equ. 4).

$$\Delta G + nFE_{eq} = 0 \quad \text{Equ. 4}$$

with:  $E_{eq}$ (V), the electromotive force of the cell at equilibrium

$n$  (mol), the number of electrons exchanged between the two sides of the cell

$F$  (C), the Faraday number representing the electricity quantity of one mole of electrons

The Equ. 3 represents what happens in the fuel cell core. The reactions occurring in both side of the fuel cell are:

- in an acid environment :



- in a basic (alkaline) environment :





The reactions of oxidation (Equ. 5 and Equ. 7) are located at the anode part of the fuel cell, fed by hydrogen, while the reduction reactions (Equ. 6 and Equ. 8) occur at the cathode, fed by oxygen. The anode produces electrons and the cathode requires electrons. The potential difference between the electrodes induces an electron migration from one part of the fuel cell to the other. However, both electrodes are separated by an electrolyte that blocks the electrons move. Consequently, the electrical current occurs only when the electrodes are connected by a conductive circuit.

Additionally to its ability to block electrons, the electrolyte makes also possible the migrations of ions:

- the protons  $H^+$  coming from the anode to the cathode in the acid fuel cells,
- the  $OH^-$  going from the cathode to the anode in the alkaline fuel cells.

Finally, the electrolyte also avoids the reactive gases crossing from one side to another.

### 1.5 Fuel Cell technologies

The selection of a fuel cell technology principally depends on its application. Different fields can be targeted:

- stationary applications [Williams *et al.*, 2004]
  - decentralized electric generators that produce hundred of megawatts (MW),
  - industrial cogeneration systems that produce up to 50 MW,
  - personal cogeneration systems that produce from 1 to 10 MW,
  - power supply of isolated places that requires from 10 to 20 MW.
- transport applications:
  - electrical vehicles with a power around 80 MW,
  - buses with a power around 200 MW,
  - ships and submarines with power supply units of 200 to 500 MW,
  - spacecrafts and spatial vehicles that require from 10 to 50 MW,
- and portative applications with power ranging from 1 to 10 MW.

The environmental quality of the fuel allows them to produce electricity closed to consumer sites. The heat produced by the operating fuel cell can be used as a co-generation system either directly or by steam production. The steam and heat produce more electricity with combined cycles of gas or steam turbines with fuel cells:

- high temperature fuel cells are pressurised and used as a combustion chamber for the gas turbine.

- the heat produced by the fuel cell is used in a boiler for steam production. The steam is used in a steam turbine.
- gas and steam turbines can be coupled.

Five major types of fuel cells exist. Their name generally describes the electrolyte they incorporate:

- Solid Oxide Fuel Cell (SOFC),
- Molten Carbonate Fuel Cell (MCFC),
- Phosphoric Acid Fuel Cell (PAFC),
- Alkaline Fuel Cell (AFC),
- Proton Exchange Membrane Fuel Cell (PEMFC).

Their electrochemical reactions, components, operating and economical characteristics are presented in Appendix 1. Only the PEMFC are developed in the part 2 of this chapter.

### 1.6 Main challenges in the fuel cell domain

The fuel cells challenges are graded by the DOE depending on their targeted applications. Concerning the fuel cell for stationary application, the main challenges described by the 2011 Department of Energy Hydrogen and Fuel Cells Program Plan are:

- the system cost: it has to range from 1,000 to 1,500 \$ kW<sup>-1</sup> depending on the size and application,
- and the durability and reliability: the life time of the fuel cell system has to range from 50,000 and 60,000 h.

For automotive applications, such as Fuel Cell Vehicles (FCVs), four main issues are highlighted:

- the system cost (\$ kW<sup>-1</sup>),
- durability and reliability (h),
- system size,
- and the air, thermal, and water management.

The first limiting parameter is the cost of the power produced by a fuel cell. For automotive application, the cost of the power of an internal-combustion engine, used for conventional automotive, is estimated to vary from 25 to 35 \$ kW<sup>-1</sup>. To be competitive, the DOE set the target of the cost of the fuel cell systems dedicated to Fuel Cell Vehicles (FCVs) equal to 30 \$ kW<sup>-1</sup>. Such a value is targeted for a 80 kW<sub>net</sub> fuel cell system based on a manufacturing volume of 500,000 units per year. In Figure 6, the target of 30 \$ kW<sup>-1</sup>, and the projected system costs given by different literature sources are detailed.

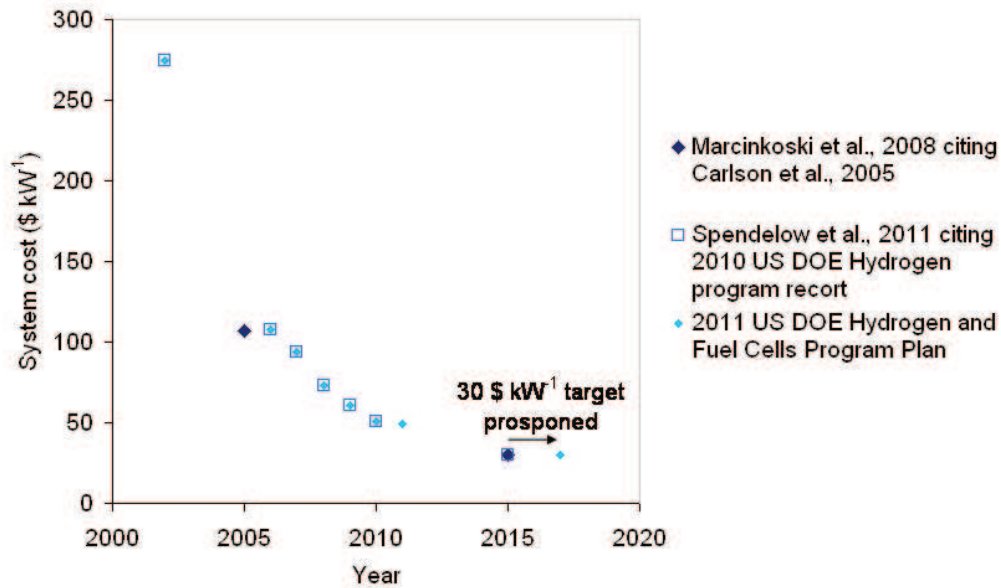


Figure 6 Projected system cost as a function of the time, cited by different authors depending of the year of publication of US reports on hydrogen development [Marcinkoski *et al.*, 2008; 2011 DOE Hydrogen and Fuel Cells Program Plan; Spendelow and Papageorgopoulos, 2011]

The data presented in Figure 6 are extracted from three references, based on 2005, 2010 and 2011 DOE reports on hydrogen development [Marcinkoski *et al.*, 2008; 2011 DOE Hydrogen and Fuel Cells Program Plan; Spendelow *et al.*, 2011].

In 2002, the system cost was around 275 \$ kW<sup>-1</sup>. In 2005, the cost analysis showed that the cost of the fuel cell system is separated between the fuel cell stack (63 %) and the balance of plant (34 %), the last 3 % accounts for the assembly. In such a fuel cell stack, the electrodes represent 77 % of the cost [Marcinkoski *et al.*, 2008]. In 2010, despite of the 2010 DOE target of 45 \$ kW<sup>-1</sup>, the system cost reaches 51 \$ kW<sup>-1</sup>, where the balance of plant and the stack accounted to 51 and 49 % respectively [Spendelow and Papageorgopoulos *et al.*, 2011]. The cost of the system decreases to reach 49 \$ kW<sup>-1</sup> in 2011.

In 2005 and 2010, the target of 30 \$ kW<sup>-1</sup> was set in 2015. However, in 2011, the DOE's Hydrogen and Fuel Cells Program Plan postponed this target to 2017.

In 2011, the Department of Energy Hydrogen and Fuel Cells Program Plan demonstrated that the influence of the manufacturing volume on the system cost varying from 219 to 49 \$ kW<sup>-1</sup> for manufacturing volume from 1,000 to 500,000 systems per year.

The cost reduction of the system is closely related to the enhancement of the whole fuel cell system (fuel cell stack and balance of plant). Indeed, the technical limitation of the complex fuel cell system of FCV is also pointed by the DOE. First of all, the size and weight of the stack of fuel cell and of the balance of plant have both to be reduced before their implementation in a vehicle. The hydrogen storage, as described before is a main

concern since the hydrogen has a very low energy by volume of the hydrogen gas is very low compared to the hydrocarbon one.

The prevailing fuel cell technology for FCVs is a low temperature (around 80°C) fuel cell call PEM fuel cell. However, if a low temperature is an advantage for consumer security, it induces thermal management limitations. Indeed, the low temperature gap between the ambient air and the operating temperature limits the heat removing by the cooling system [Pischinger *et al.*, 2006]. The increase of the temperature in the stack leads to water loss. However the water is essential for properly insuring the proton conduction and maintaining high performances.

Moreover, the DOE indicates that a low operating temperature limits the heat recovery by heat and power cogeneration systems (The Department of Energy Hydrogen and Fuel Cells Program Plan). The good combination of air, water and thermal managements is key technical specifications in fuel cell vehicle development.

More details concerning the efforts proposed by the DOE for reducing the cost of the power of the PEM fuel cell stack are described in the following part of this literature chapter.

## 2 Proton Exchange Membrane Fuel Cell

Proton Exchange Membrane Fuel Cells (PEMFCs) operate at low temperature (60 to 80 °C depending on the authors). They are mainly dedicated to automotive applications. The main challenges of PEMFC described by the DOE are related to the cost of the system: the durability, the reliability, the size and the weight of the system and the system's air-thermal-water management.

### 2.1 Membrane Electrode Assembly

The core of a fuel cell is Membrane Electrode Assembly (MEA). MEAs (Figure 7) are composed of two electrodes separated by an electrolyte. Each electrode is composed of a Gas Diffusion Layer (GDL, described in section 2.3) and of a Catalyst Layer (CL, developed in part 2.5). These components are hot pressed at 2 to 200 MPa and at 120 to 195 °C during 50 to 300 s [Lin *et al.*, 2009]. These parameters depend on the authors [Therdthianwong *et al.*, 2012]. Creating intimate interfaces between the different layers by melting the polymers of each layer is crucial for insuring a continuous polymeric matrix. In order to validate the efficiency of the MEA, ranges of electrochemical characterisations are applied. They are described in Appendix 2.

In a fuel cell system, several MEAs are placed in parallel and separated by bipolar plates. Such structure forms a stack of fuel cell. For example, hundreds of cells composed the 20 kW Genepac fuel cell stack [Glipa *et al.*, 2012].

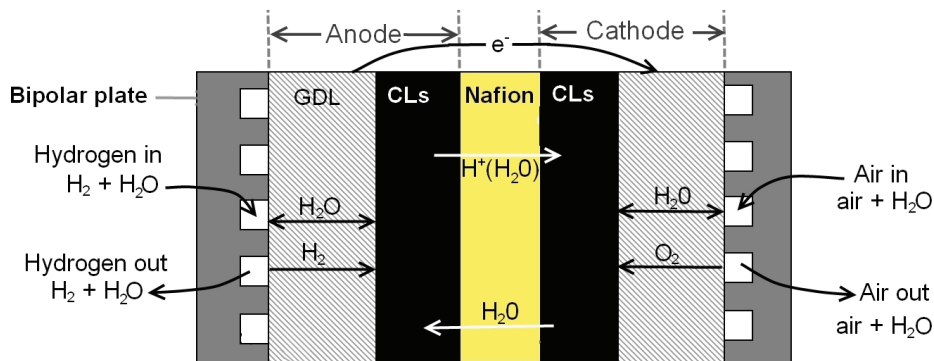


Figure 7 MEA cross view, schematic description

In operating conditions, each cell is the place of different flows of mass and charges. The major of them are drawn in Figure 7 and can be separated into [Ji *et al.*, 2009]:

- mass transport:
  - water, in liquid and gas states, and sometimes in solid state,
  - and reactive gases, hydrogen and oxygen (or air).
- and charges diffusion, electrons and protons.

Humidified gases bring water in vapour state from the bipolar plate's channels to the core of the fuel cell. Inside the operating cell, the protons generated in the anode side of the cell are surrounded by water molecules. Consequently, when the electro-osmotic drag induces the protons migration from the anode to the cathode, it also induces the migration of water molecules. Moreover, the water is also produced by oxygen reduction in the cathode part. These two phenomena induce a water gradient from the cathode to the anode. In the extreme case, it can lead to a cathode flooding and anode drying. That is why the reactive gases are humidified in order to limit the catalyst layer drying. Moreover the gradient leads to a second and reverse flow, coming from the cathode to the anode, which reduces the difference of water amounts between anode and cathode sides. Finally, the excess of water is ejected from the MEA through the bipolar plates' channels. The multiple and bi-directional flows of water occur simultaneously to gases flows that come from the bipolar plates to the catalyst layers. In operating conditions, the water, in liquid and gas states, and the reactive gases share the place available in the MEA structure as detailed in Figure 8.

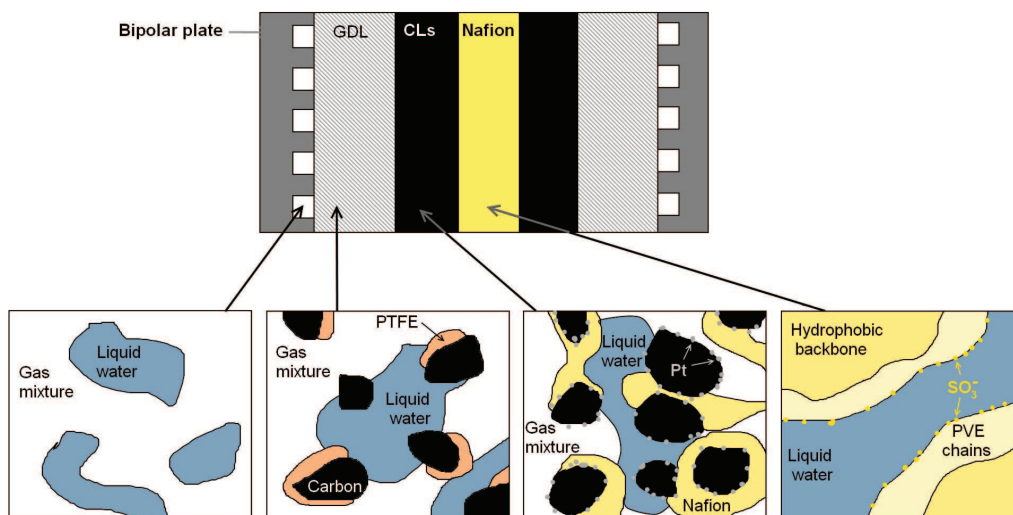


Figure 8 Cross view of a MEA, focus on the structure and components in each layer during normal operating conditions [Jiao and Li, 2011]

The electron flows follow the network of conductive elements (carbon and metal), which composes the catalyst layers, the GDLs and the bipolar plates. The simultaneous management of water, gas and charges in each stack component is a main concern in fuel cell study and influences the chemistry and physical structure of each element of the stack, as developed thereafter.

Stacks have been indicated by the DOE as containing a lot of expensive components. The estimation of the system cost shows that the stack represents 49 % of the system cost or 25 \$ kW<sup>-1</sup> (for a 80 kW PEM fuel cell stack manufacturing volume of 500,000 systems

per years) [Spendelow and Papageorgopoulos, 2011]. The distribution of the cost between the stack components is highlighted in Figure 9.

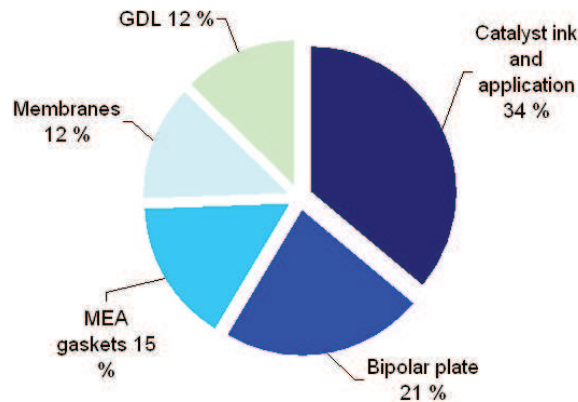


Figure 9 Cost distribution in 2011 between the stack components (for a production of 500,000 systems of 80 kW PEM fuel cells per year)

The reduction of the cost of each component, the enhancement of performances and the durability are the main objectives of the DOE. For each component, proposed solutions are detailed thereafter. At the end of this part, the issues concerning the manufacturing of the MEA components are developed in order to extract the limits of the conventional processes currently used (2.6).

## 2.2 Bipolar plates

The bipolar plates provide:

- an in-series electrical connection between the cells,
- a physical separation between the fuel cells's MEAs, limiting the reactive gas mixing.
- a structural support for the entire fuel cell

and insure:

- the conduction of the heat from the active cell to a coolant
- the transport of the gas toward the whole surface of cell [Yu H. N. *et al.*, 2011].

The active zone of a bipolar plate has striated shape at the interface with the GDL with several channels for gas transportation. Depending on the bipolar plate types, the channels have various designs in the three dimensions such as parallel design, serpentine design and interdigitated design (each dimension of the channel is about millimetre) [Jiao and Li, 2011]. There is generally only one input and output for the required reactive gas by side of a bipolar plate.

In 2007, the targeted cost of the alloy used for the bipolar plate was estimated above 14 \$ kg<sup>-1</sup>. Moreover, the material has to present several properties that have been measured by the U.S. DOE such as [Taherian *et al.*, 2011]:

- in plane electrical and thermal conductivity ( $> 100 \text{ S cm}^{-1}$  and  $> 20 \text{ W m}^{-1} \text{ K}^{-1}$ ),
- low gas permeability ( $> 2 \cdot 10^{-8} \text{ m}^3 \text{ m}^{-2} \text{ s}^{-1}$ ),
- high mechanical properties (flexural strength  $> 59 \text{ MPa}$ , tensile strength  $> 41 \text{ MPa}$  and Impact strength  $> 40.5 \text{ J.m}^{-1}$ ),
- and corrosion resistance ( $< 16 \cdot 10^{-4} \mu\text{A m}^{-2}$  at pH 4).

Three main materials are suitable for bipolar plate manufacturing:

- graphite, but it has poor mechanical properties [Sharma *et al.*, 2011, Yu H. N. *et al.*, 2011],
- metals, however it requires expensive surface treatment against corrosion, [Ender *et al.*, 2011; Mevlut *et al.*, 2011],
- and composites, but they have lower electrical conductivity than the targets of the DOE [Taherian *et al.*, 2011; Wang *et al.*, 2011].

For example, in the Genepac fuel cell, each bipolar plate is composed of two pressed sheets of metal that are placed perpendicularly. The space remaining between the two sheets forms the cooling system. Each sheet is in contact with either a cathode or an anode, and consequently transports either oxygen or hydrogen. The channel geometry parameters ranged from 0.1 to 3 mm [Glipa *et al.*, 2012].

### 2.3 Gas Diffusion Layer

Gas Diffusion layers (GDLs) are located at the interface between the bipolar plate and the Catalyst Layer (CL). This material insures [Wilde *et al.*, 2004]:

- The gas homogenisation from the bipolar plate channels to the catalyst layer,
- The transport of the reactive gases, water, electrons and heat from one side to another as described before,

However, the GDLs also mechanically support the MEA components, bridge MEA and the bipolar plates, and insure corrosion stability.

#### 2.3.1 Structure and composition

GDL properties are crucial for fuel cell characteristics in operating conditions. These characteristics have often interconnected and opposite effects on the GDL functions. The main challenge is to reach a compromise between the multiple physical and chemical properties of the GDL [Cindrella *et al.*, 2009]: electrical conductivity, thermal conductivity,

pore size, pore distribution, air permeability, hydrophobicity, hydrophilicity, surface homogeneity, free of cracks, oxidation stability, bending stiffness, and compressibility.

The transport functions of the GDL are mainly directed by the pore characteristics and hydrophobicity/hydrophilicity behaviour of the material [Jiao and Li, 2011]. Porosity influences the electrical conductivity and the mass transport in inverse ways. For example, a small porosity, with high percolation of the conductive components, induces a good electrical conductivity [Lee *et al.*, 2004]. However, it limits the mass transport of water and gas [Jiao and Li, 2011]. The pore size diminishes from the macroporous layer to the microporous layers. It creates an increasing capillarity gradient from the catalyst layer to the bipolar plate that ejected the excess of water produced in the catalyst layer. The pore size of common macroporous substrate ranges from 1 to 100  $\mu\text{m}$ .

The GDL structure and chemistry have to reach the best compromise between hydrophobicity and hydrophilicity, which respectively influence the water expelling and water retaining. Indeed, potential water flooding or drying have critical consequences on the operating fuel cell [Cindrella *et al.*, 2009].

The carbon corrosion due to oxidation leads to degrade the uniformity of the GDL thickness and mass. This phenomenon affects the mechanical support given by the GDL to the MEA and the fuel cell performances.

For fulfilling the optimum properties, GDLs are separated in two main layers:

- a macroporous layer that insures the main mechanical functions of the GDL. It is placed at the interface with the bipolar plate. It is composed of graphitised carbon fibers nonwoven material forming a web. The web is then dip coated in an aqueous dispersion of PTFE (or Teflon<sup>®</sup>). The PTFE gives a hydrophobic behaviour to the layer.
- one or several microporous layers, which complete the macroporous actions on the porosity. It is made by coating a dispersion at the surface of the macroporous layer. The dispersion is mainly composed of carbon black powder and PTFE, which is used here as a binder [Park *et al.*, 2008]. The coating step is followed by a sintering step at 350 °C for 10 min [Wilde *et al.*, 2004].

### 2.3.2 Efforts for reducing the GDL manufacturing cost

The efforts of the DOE for reducing the cost of the fuel cell focus also on the GDL. The raw materials used for GDL are cheaper compared to Nafion<sup>®</sup> or platinum. Therefore, the efforts concentrate on reducing the global manufacturing cost of this element. In order to

match with the 2011 targeted cost, which was set to 14 \$ kW<sup>-1</sup> [De Castro, 2011], the proposed solutions focus on:

- understanding the relation between process parameters and fuel cell performances.
- reducing the number of process steps,
- continuous technologies with a high volume of production,
- and creating and utilising in-line processes control and measurement tools to reduce ex-situ testing,

## 2.4 Proton Exchange Membrane

In PEMFC, the electrolyte transports protons from the anode to the cathode, known as Proton Exchange Membrane. It also avoids electrons and reactants pathways from one side of the cell to the other.

Perfluorosulfonated membranes (Figure 10) are mainly used as electrolyte for PEMFC. Their molar mass is estimated around 10<sup>5</sup> and 10<sup>6</sup> g mol<sup>-1</sup>. This type of polymer was the first material to be called ionomer. It is composed of a PTFE backbone on which polyvinyl alkyl ether pendant chains are grafted. The pendant chains are ended by sulfonated acid groups. The mass of polymer per mole of sulfonic groups defines the Equivalent Weight (EW g mol<sup>-1</sup>) of the membrane. The acid groups ( $SO_3^- + H^+$ ), that are highly hydrophilic, attract the protons  $H^+$  (or the hydronium ions  $H_3O^+$ ) into the membrane core, and transports them in a water environment from one sulfonated group to another by the bending of one pendant chain toward an other one [Jiao and Li, 2011]. At the other side, the PTFE backbone has a highly hydrophobic character that is repelled by water. It leads to really specific structures and mechanisms occurring in the Nafion<sup>®</sup>, depending on the water content.

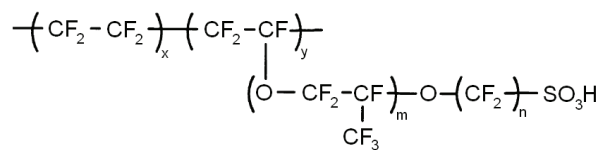


Figure 10 Monomer of perfluorosulfonic acid membranes

In Figure 10, x, y, m and n depend on the supplier [Rikukawa and Samui, 2000]:

- Dow<sup>®</sup> (Dow Chemical, New York, USA), m = 0, n = 2, x = 3.6 - 10, y = 1,
- Aciplex<sup>®</sup> (Asahi Chemicals, Tokyo, Japan), m = 0, n = 2 - 5, x = 1.5 - 14, y = 1,
- Flemion<sup>®</sup> (Asahi Glass, Tokyo, Japan), m = 0, n = 1 - 5, x = 5 - 13.5, y = 1,
- Nafion<sup>®</sup> (DuPont, Wilmington, USA), m = 1, n = 2, x = 5 - 13.5, y = 1.

This study only used Nafion<sup>®</sup> membranes. For that reason, this type of membrane is focused in the sections thereafter.

#### 2.4.1 Nafion<sup>®</sup> structure

The Nafion<sup>®</sup> structure is the topic of a high number of studies, which proposed different models of core (2.4.1.1) and surface (2.4.1.2) structures.

##### 2.4.1.1 Nafion<sup>®</sup> core structure

The different models explain structural variations of the membrane core, which are induced by the scale and/or the variations of hygrothermal conditions:

- the **scale** changes,
  - at small scales (10 to 100 Å), the polymer backbones form crystalline aggregates that have cylindrical or ribbonlike shape [Rubatat *et al.*, 2002]. The ribbons are surrounded by a first layer composed by the PVE pendant chains that are oriented toward the membrane outer. A second layer is composed of the sulfonic groups. Water molecules can move into the layers around the ribbon.
  - at medium scale (~500 Å), ribbons are statistically aligned and form organised bundles [van der Heijden *et al.*, 2004].
  - at a higher scale (>1 µm), bundles are parted by amorphous regions. Their main orientation depends on the manufacturing process and impact on the membrane isotropy/anisotropy at higher scales.
- or the variations of the **hygrothermal conditions**, as the membranes sorb and desorb water. It leads to a swelling phenomenon in the three dimensions of the membrane [Gebel, 2000]. From dry membrane to polymeric dispersion, the proposed structures as regards to the water volume fraction are:
  - in dry membrane, ionic clusters gather the sulfonic groups in a hydrophobic matrix. This configuration is close to the structural model of Macknight detailed in the 1970s [Macknight *et al.*, 1974],
  - up to 25 % of water volume fraction, the membrane swells. Water molecules fill the ionic clusters,
  - at 25 % of water volume fraction, bigger clusters percolated and channels join the clusters to each other. In the 1980s, such structure was firstly described by Hsu *et al.* [1983],

- up to 50 % of water volume fraction, a structure inversion occurs. Polymeric chains form hydrophobic clusters and hydrophobic channels covered by hydrophilic skin composed of the acid groups,
- above a water volume fraction of 75 %, Nafion<sup>®</sup> chains form connected rods,
- finally, the polymer forms a colloidal dispersion of rod like particles.

#### 2.4.1.2 Nafion<sup>®</sup> surface structure

The structure of the Nafion<sup>®</sup> surface depends on the type of the interface with water. This phenomenon was characterised in very narrow subsurface layers using X-ray scattering [Bass *et al.*, 2010] or at the membrane surface using atomic force microscopy [Affoune *et al.*, 2005; Ma *et al.*, 2006; Hiesgen *et al.* 2009]:

- in the case of a solid/vapour interface, the hydrophobic backbones tend to cover the surface. The crystalline bundles are oriented in parallel with the surface direction [Bass *et al.*, 2010]. The surface is smooth and covered by a PTFE-like skin [Affoune *et al.*, 2005; Bass *et al.*, 2010].
- in solid/liquid interface conditions, the hydrophilic parts, *i.e.* the sulfonic acid groups, tend to migrate at the interface formed with the liquid. The bundles are oriented almost perpendicularly to the surface. As a consequence, the Nafion<sup>®</sup> surface is covered by three distinct elements: (i) a hydrophobic PTFE skin, (ii) hydrophilic sulfonic groups that surround (iii) water clusters having a size of few nanometers [Affoune *et al.*, 2005; Ma *et al.*, 2006; Kim *et al.*, 2003; Hiesgen *et al.* 2009]. This structural change is combined to a roughening of the Nafion<sup>®</sup> membrane surface.

The structural variations due to hygrothermal changes impact the Nafion<sup>®</sup> mechanical properties. This behaviour is demonstrated in liquid water [Kusoglu *et al.*, 2009] or in vapour phase, where the membranes are more deformable when the air relative humidity increases [Kusoglu *et al.*, 2009; Barclay *et al.*, 2009]. In contact with water at liquid or vapour state, an increase in the temperature leads to decrease the membrane stiffness [Kusoglu *et al.*, 2009 and 2010; Barclay *et al.*, 2009].

Moreover, the manufacturing process affects the mechanical properties of the membrane [Kusoglu *et al.*, 2009]. For example, Nafion<sup>®</sup> 212 and 112 are two different types of membrane commercialised by Dupont<sup>®</sup>. They are respectively made by evaporation casting and extrusion. They have the same equivalent weight; however, due to its process which induces directional strain, Nafion<sup>®</sup> 112 has anisotropic structure and consequently shows different properties in the machine direction and in the cross direction.

### 2.4.2 Trends in membrane improvements

DOE 2011 report described that the main issues in membrane development deal with:

- the cost, the 2015 target is lower than 20 \$ m<sup>-2</sup>,
- the durability, decreasing the membrane degradation in order to reach at least 20,000 cycles (under RH% cycles) [Meyer *et al.*, 2006 ; Fernandes and Ticianelli, 2009; Tang *et al.*, 2007b],
- the performances, with an area specific resistance to proton diffusion lower than 0.02 Ω cm<sup>2</sup> at 80 °C and water partial pressures varying from 25 – 45 kPa, and a membrane conductivity equal to 0.10 S cm<sup>-1</sup> in operating temperatures.

For that purpose, among others, the proposed solutions are:

- decreasing the membrane thickness under 25 μm, for reducing the cost of the membrane [Mittelsteadt, 2011],
- corrugating the membrane in order to increase the catalyst layer efficiency [Grot, 2011],
- patterning the membrane surface, for diminishing the membrane instability in presence of water or polar solvents[Mittelsteadt, 2011],
- creating new polymers and composites [Meyer *et al.*, 2006; Pintauro, 2011; Herring, 2011; Hamrock, 2011] in order to diminishing the membrane instability in presence of water or polar solvents [Kusoglu *et al.*, 2009] and operating at higher temperatures (120 °C) and lower RH% (25 RH%).
- increasing the production volume and the membrane consistency [Mittelsteadt, 2011].

### 2.5 Catalyst layer

The electrochemical reactions at the anode (Equ. 5) and the cathode (Equ. 6) take place in the catalyst layers. For both catalyst layers, the reactions require the presence of:

- the reactants gases ( $H_2$  at the anode, electron and protons and  $O_2$  at cathode),
- a catalyst, based on Platinum Group Metals (PGMs) with a size of few nanometers,
- an electron conductor, based on carbon powder (ranging from few micrometers to 20 micrometers [Li; 2006]),
- and a proton conductor made of Nafion<sup>®</sup>.

The site where all these elements are in contact is the triple contact point [Therdthianwong *et al.*, 2012].

### 2.5.1 Structure

In catalyst layers, a specific and complex structure manages the gas accessibility and water transport [Yu X. *et al.*, 2011]. In Figure 11, a simplified schema highlights the main mass transports and charges diffusion occurring in the cathode catalyst layer.

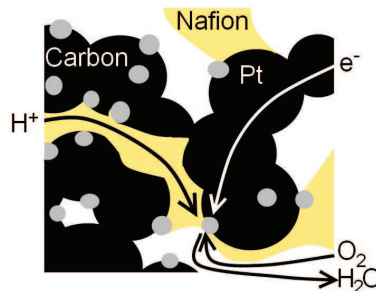


Figure 11 Simplified flows of gas, water, electrons and protons closed to a triple point in a cathode catalyst layer

The structure is mainly composed of:

- ionomer (Nafion<sup>®</sup>) channels that allow the protons and water to diffuse from the membrane to the catalysts,
- the percolated carbon particles form an electronically conductive network that conducts the electrons toward the catalysts,
- gas and water transported through the pores.

As the surface of contact between platinum and the reactants directly impacts the reaction efficiency, an optimal catalyst layer structure has to maximize the surface area of platinum exposed to the reactants. Moreover, the structure must have a uniform film thickness and film density in order to insure a uniform mass transport and conductivity properties [Engle, 2012].

### 2.5.2 Composition

In order to obtain the specific structure described before, and high electrochemical properties, the composition of catalyst layer is a delicate optimum between the carbon nanoparticles, which supports the catalysts and the ionomer.

The optimum ionomer content in the catalyst layer has already been investigated in numerous works [Uchida *et al.*, 1995; Paganin *et al.*, 1996; Antolini *et al.*, 1999; Chaparro *et al.*, 2009; Caillard *et al.*, 2009; Sasikumar *et al.*, 2004; Kim *et al.*, 2010; Xie *et al.*, 2010; Jeon *et al.*, 2010; Suzuki *et al.*, 2011]. The ionomer content is given in weight percentage (w/w %) as regards to the entire catalyst layer. In Figure 12, this parameter is compared to the

platinum loading of the catalyst layer ( $\text{mg}_{\text{Pt}} \text{cm}^{-2}$ ), which is a parameter that gives the mass of platinum nanoparticles (in mg) per unit of surface (in  $\text{cm}^{-2}$ ).

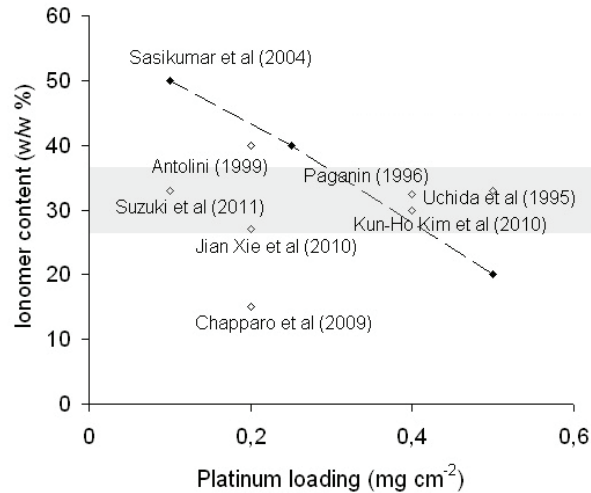


Figure 12 Ionomer content as a function of the platinum loading of the catalyst layer

The average ionomer content considered as a reference in the literature is around 30 w/w %. In Figure 13, the ionomer content as a function of the Electrochemical Surface Area (ESA here in  $\text{m}^2 \text{g}^{-1}$ ) of platinum provides another way to choose the optimum ionomer content.

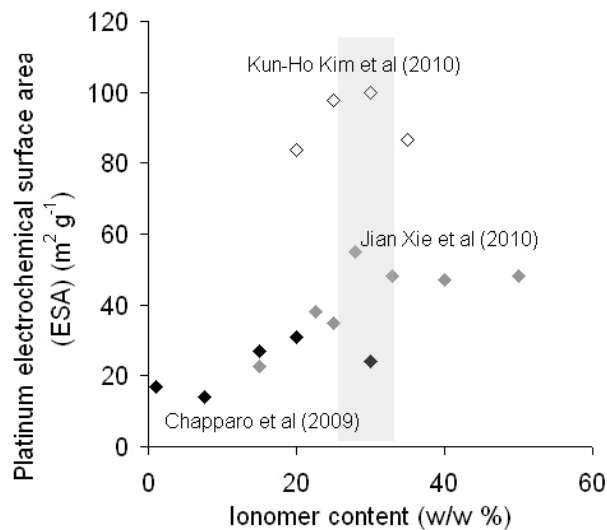


Figure 13 Electrochemical Surface Area (ESA) of platinum as a function of the ionomer content in the catalyst

The ESA indicates the surface of catalyst that is available to catalyse the electrochemical reactions in the catalyst layer (this physical quantity is detailed in Appendix 1). Once again, the best ESA values are obtained with an ionomer content around 30 w/w %.

### 2.5.3 Catalyst efficiency and cost improvements

The Platinum Group Metals (PGMs) are strategic metals for development of new technologies thanks to their unusual properties. They are chemically inert and resist to corrosion and oxidation. They have a high fusion point and are very efficient catalyst for numerous reactions such as hydrogenations [Krupk *et al.*, 2007], hydrosilylations [Troegel *et al.*, 2011], oxidations [Geletii *et al.*, 2007], dehydrogenations [Gudgila and Leclerc, 2011]... Some example of PGMs, with their atomic number  $Z$  and their molecular weight  $M$  (mol g<sup>-1</sup>) are [Kettler, 2003]: Rutherfordium (Ru),  $Z = 44$ ,  $M = 101.1$ , Rhodium (Rh),  $Z = 45$ ,  $M = 102.9$ , Palladium (Pa),  $Z = 46$ ,  $M = 106.4$ , Osmium (Os),  $Z = 76$ ,  $M = 190.2$ , Iridium (Ir),  $Z = 77$ ,  $M = 192.2$ , And platinum (Pt),  $Z = 78$ ,  $M = 195.1$ .

Their crucial properties and their scarcity made them very expensive [Sun *et al.*, 2011]. Some of them, such as platinum, cost twice as much as gold. Consequently, the reduction of the catalyst cost in PEMFC, is a main challenge on fuel cell development. The DOE set targeted at 3 \$ kW<sup>-1</sup> at 51.55 \$ g<sup>-1</sup> for PGM. For that purpose, the DOE targets focus on:

- the limitation of the quantity of PGM to 0.2 g kW<sup>-1</sup> in 2015 [Murthi, 2011],
- the increasing in the performances by increasing the catalyst activity for the Oxygen Reduction Reaction (ORR) [Escudero *et al.*, 2002; Zhang *et al.*, 2004; Markovic, 2011] with a minimum specific activity of 720  $\mu\text{A cm}^{-2}$ ,
- the increased catalyst durability, reaching at least 5,000 h at temperatures higher than 80°C in automotive cycling conditions, and 40,000 under stationary applications conditions, by reducing the catalyst degradation and migration into the cell [Bi *et al.*, 2008] due to both electro-oxidation of the platinum in high voltage conditions [Hu *et al.*, 2006] and carbon corrosion [Arico *et al.*, 2008] occurring during fuel starvation or start-up/shut-down [Hu *et al.*, 2006].

In order to reach these goals, the possible solutions are based on:

- the development of new catalyst structure, such as core-shell catalysts which are made of platinum nanometric skin deposited by nanosegregation [Markovic, 2011] or electrodeposition [Wei *et al.*, 2008]. It forms nanostructured thin film (NSTF) of electrocatalyst on alloys nanoparticles, nanowires or carbon nanotubes [Debe, 2011; Pivovar, 2011]. It improves the ORR rates and gives a higher stability to the platinum located in the catalyst surface.
- the development of new materials based on PGM alloys. This could increase the cathode catalyst durability [Murthi, 2011], or limit the damage caused by

overpotential [Atanasoski, 2011; Markovic, 2011]. This solution also diminishes the PGM use [Serov *et al.*, 2009; Gojkovic *et al.*, 2010; Garzon, 2011]. Another solution for reducing PGM use is the development of non-PGM complex, such as iron, with oxygen and nitrogen and carbon that facilitate the transfer of electron toward oxygen [Mukerjee, 2011]. However, the used of non noble materials, alloyed with PGM or as catalyst, may lead to fuel cell degradation as they are not stable in the corrosive environment of the operating fuel cell [Spendelow and Papageorgopoulos, 2011].

- Increasing the volume manufacturability [Debe, 2011],
- And finally, the development of the reuse of the platinum of fuel cells [Zhao *et al.*, 2007].

## 2.6 PEMFC catalyst layers Manufacturing by dispersion deposition

Depending on the manufacturing protocol, different denominations exist for qualifying the catalyst layer.

- in **direct** protocol, the catalyst layer is deposited:
  - either onto the membrane, called a Catalyst Coated Membrane (**CCM**),
  - or onto the GDL, called a Catalyst Coated Backing (**CCB**), as the GDL is often named either backing or substrate.
- in **indirect** protocol, the catalyst layer is made on a substrate, which is not a fuel cell component. The dispersion, composed of dispersed ionomers, and carbon supported platinum catalysts in a solvent, is deposited onto a smooth and hydrophobic surface. PTFE cloth [Suzuki *et al.*, 2011] or aluminium foil [Song *et al.*, 2010] are often used as substrates. The catalyst layer is transferred at the both side of a PEM from the substrate by hot pressing. Then the substrates are removed [Rajalakshmi and Dhathathreyan, 2007; Yoon *et al.*, 2011].

This protocol is called the **decal** method.

The comparison of the three deposition protocols, CCM, CCB and Decal, is made in Table 3.

Table 3 Comparison of the deposition protocol for catalyst layer manufacturing

Protocol	Advantages	Limitations	Proposed solutions
Decal + CCM	- No membrane deformation during processing [Thanasilp and Hunsom, 2010]	- Poor interface between CL and PEM [Yoon <i>et al.</i> , 2011].	- Deposition of a dispersion of Nafion® on the CL before pressing for forming an interface [Song <i>et al.</i> , 2010].
CCM	- Better interfacial properties [Thanasilp and Hunsom, 2010] - Higher electrochemical performances [Prasanna <i>et al.</i> , 2004; Tang <i>et al.</i> , 2007a], - Power density, low ohmic resistance, low charge transfer resistance [Tang <i>et al.</i> , 2007a]	- Membrane swelling [Song <i>et al.</i> , 2010 ; Thanasilp and Hunsom, 2010; Park <i>et al.</i> , 2010] - Membrane wrinkling [Thanasilp and Hunsom, 2010]	- Adaptation of the dispersion vehicle [Sun <i>et al.</i> , 2010] - Membrane stabilisation by soaking in ethylen glycol during fabrication [Sun <i>et al.</i> , 2010] - High temperature spray deposition for rapid drops drying and membrane immobilisation via Van der Walz force [Sun <i>et al.</i> , 2010]
CCB	- Large scale and mass production [Thanasilp and Hunsom, 2010]	- Lower performances in high current density (DMFC) [Reshetenko <i>et al.</i> , 2006]	

The properties that differentiate the three protocols are related to the achieved interfacial qualities of the system composed of CL/PEM or CL/GDL:

- direct CCM protocol seems to give better interfaces, which induces lower ohmic and charge transfer resistances. However, the creation of good CL/PEM interfaces by CCM protocol is limited by the swelling behaviour of the membrane.
- the decal method gets around this difficulty by drying the dispersion before putting in contact the CL with the membrane. However, it creates poor interfaces properties.
- the CCB protocol limits the contact between the liquid dispersion and the membrane, by depositing the liquid dispersion and drying it directly on the GDL. Such catalyst layers made that way reach lower performances.

The deposition of the dispersion by CCM, CCB or decal + CCM can be made by different processes (Table 4):

- **Hand painting** [Bender *et al.*, 2003], also called brushing [Mazur *et al.*, 2011], where the dispersion is painted using a brush [Hwang *et al.*, 2011].
- **Blade coating** [Park *et al.*, 2010]. This process consists in scraping the dispersion onto the substrate with a squeegee (or a doctor blade). The

deposited quantity depends of the distance between the squeegee and the substrate.

- **Screen printing.** As for blade coating, the screen printing consists in scraping a dispersion using a squeegee. During screen printing, a pasty dispersion is scraped on the substrate through a meshed screen, which properties impact the deposited quantity of dispersion [Krucinska *et al.*, 2011].
- **Electro-spray** deposition, where the dispersion is ejected in a conical fine aerosol spray.

Table 4 Comparison of dispersion deposition techniques for catalyst layer manufacturing

Deposition process	Advantages	Limitations	Proposed solutions
+ Hand painting (brushing)  + Blade coating	- Have large numbers of test samples of MEA	- High variation coefficient of platinum loading (about 12 %) [Bender <i>et al.</i> , 2003] - Time consuming (at least 6h to several days) [Bender <i>et al.</i> , 2003]	- Developing other methods [Bender <i>et al.</i> , 2003]
	- Continuous process [Yoon <i>et al.</i> , 2011]	- Hot temperatures that damage the PEM during pressing [Yoon <i>et al.</i> , 2011]. - Difficult CL separation from the substrate [Yoon <i>et al.</i> , 2011].	- Development of new Low temperature decal [Krishnan <i>et al.</i> , 2010; Yoon <i>et al.</i> , 2011] - Decal layer between the substrate and CL [Krishnan <i>et al.</i> , 2010].
+ Screen printing	- Simple and scalable to large area [Rajalakshmi and Dhathathreya, 2007]		
Hand painting or brushing	- Multilayer process for platinum loading control [Mazur <i>et al.</i> , 2011]	- Not suitable for large scale production [Hwang <i>et al.</i> , 2011]	
Blade coating	- Simpler and more efficient than blade coating by decal [Park <i>et al.</i> , 2010]		
Screen printing	- Good reproducibility, - Easy procedures, - Economic catalyst usage [Hwang <i>et al.</i> , 2011], - due to pattern deposition [Bonifácio <i>et al.</i> , 2011] - Suitable for mass production, - Uniform pore size [Hwang <i>et al.</i> , 2011]	- Cracks formation during drying [Hwang <i>et al.</i> , 2011]	
	- Large scale MAE [Thanasip and Hunsom, 2010; Song <i>et al.</i> , 2010] - Suitable for mass commercialisation [Thanasip and Hunsom, 2010] - Simple deposition methods for laboratory scale [Hwang <i>et al.</i> , 2011] - Better performances compared to decal + electro spray [Thanasip and Hunsom, 2010] - Low cracks formation [Hwang <i>et al.</i> , 2011]	- Large catalyst waste [Thanasip and Hunsom, 2010] - Not suitable for large scale production [Hwang <i>et al.</i> , 2011] - Poor catalyst dispersion in the ink [Millington <i>et al.</i> , 2011]	- Development of ultrasonic spray technique [Millington <i>et al.</i> , 2011]
Electrospray deposition			

According to these authors, the parameters that differentiate the processes for catalyst layer manufacturing often are the surface of production (small, large or scalable), the catalyst loading precision and repeatability and the catalyst waste.

The hand brushing technique, both in direct and decal method appears adapted to rapid fabrication at a laboratory scale. However, the precision and repeatability are questioned. Decal is seen as a continuous process adapted to large production. However, the high temperatures for hot pressing induce PEM degradation and the poor separability of the CL from the substrate leads to catalyst waste.

The decal and the hand brushing technique fabricate catalyst layers that lead to MEAs with lower efficiency, as a comparison, the blade coating, screen printing and spray technique.

The spray technique is subject to controversy. Indeed, it is sometimes described as adapted to laboratory scale production, and sometimes suitable for mass commercialisation. Besides, blade coating and screen printing perform large surface and reach large scale of production.

The spray and the blade coating require a mask for delimiting the deposition pattern. Consequently, for manufacturing a catalyst layer, several steps are required, as depicted by the Figure 14.

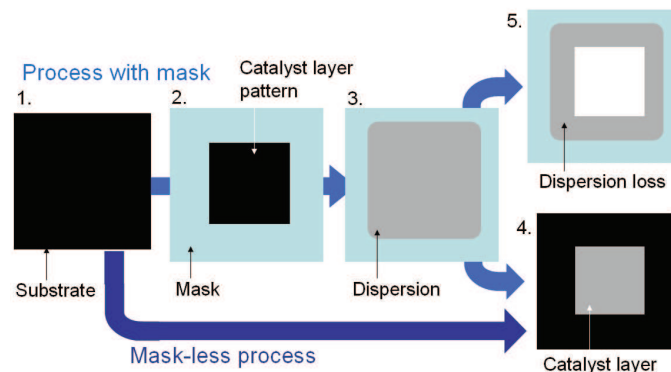


Figure 14 Schematic description of the steps of a process using mask and of a mask-less process

The mask is placed onto the substrate (Figure 14.2) and the dispersion is sprayed or coated on the mask/substrate system (Figure 14.3). However, a part of the mask is covered by the dispersion. The catalyst layer is obtained by removing the mask (Figure 14.4). Consequently, it leads to catalyst loss (Figure 14.5).

On the contrary, the screen printing is a maskless process that directly deposits the dispersion on the substrate at the shape of the desired catalyst layer. The loss of catalyst is therefore limited, and matches with the reduction of the cost of production of fuel cell.

Using mask-less processes limits the loss of expensive materials. Other printing processes than screen printing fulfil this requirement, with good precision, repeatability and suitable for different scales of production. The use of this type of processes is developed in the following part of this chapter.

### 3 Printing processes used for Proton Exchange Membrane Fuel cell manufacturing

A printing press is composed of several printing units, drying steps and substrates feeder and collector. Each printing unit deposits one type of ink, such as colour inks or varnishes, onto the substrate, and is composed of:

- an inking mechanism, that contains, transports and homogenises the ink from the ink stock to the printing form,
- and sometimes, a printing form, or printing plate, that detailed the pattern to be printed with the ink of the printing group.

Diverse methods exist for transferring the ink onto the substrate:

- non-impact processes, called masterless processes, where the ink is ejected onto the substrate and where there is no physical contact between the printing unit and the substrate. The ink jet process most famous non contact printing process.
- processes with contact, or with a printing form, which require a counter pressure system in the printing group. It physically anchored the ink onto the substrate.

The main processes used in the printing industry are summarised in Figure 15.

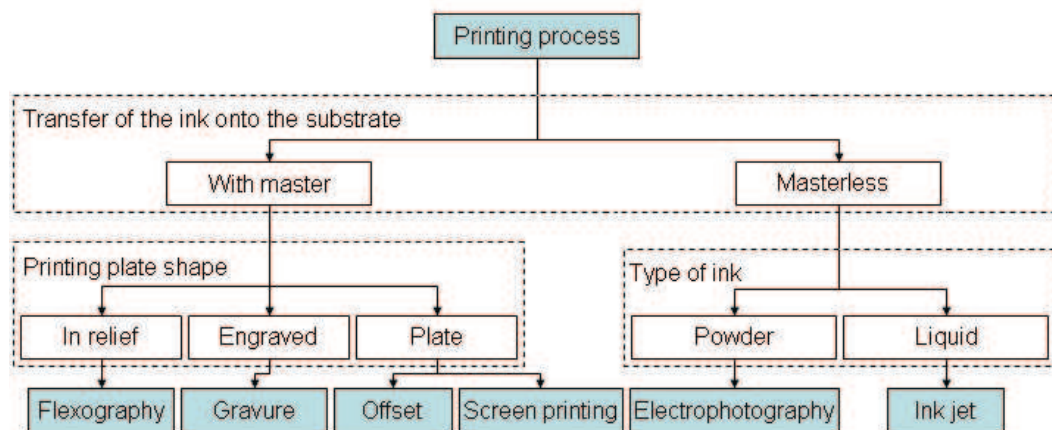


Figure 15 Printing processes categories

Conventional printing is dedicated to the manufacturing of packaging, paperboards, polymers or papers with coloured patterns. Moreover, their ability to transfer a coloured ink is also suitable for depositing functional dispersions such as catalyst layers, as it is made by screen printing process.

### 3.1 Printing processes used for catalyst layer manufacturing

Besides the screen printing, two other printing processes are cited in the literature for fuel cell applications.

The first is the **ink jet**. The ink jet is a technology where small ink droplets (with a volume about  $10^{-12}$  L) are ejected from a small ink chamber through a nozzle onto a substrate without any physical contact between the inking system and the substrate. Two main techniques exist:

- continuous Ink Jet (CIJ), where the ink droplets are frequently ejected [Chiarot *et al.*, 2009]. Some droplets are directed toward the substrate by electrostatic deviation when the non-required drops are re-used.
- or Drop On Demand ink jet (DOD). The ink droplets are generated when required [Khalate *et al.*, 2011]. The two main drop generation systems are:
  - piezoelectric system, which controls the volume of the ink chamber. A small contraction of volume leads to eject an ink droplet through the nozzle.
  - and thermal system, which forms a vapour bubble by locally heating the ink in the ink chamber. The bubble pushes the ink through the nozzle until a droplet of ink is formed. When the vapour bubble bursts, the ink droplet detaches from the nozzle.

The second printing process is the **gravure** process. In this process, the ink is directly transferred from its stock to a printing form, consisting in an engraved cylinder. Then, the excess of ink is removed by a blade and the cylinder cells filled by the ink are then put in contact with the substrate to transfer the ink. Among the printing processes, this technique has the fastest speed, longest run, high productivity and smallest waste amount [Kopola *et al.*, 2011]. However, it requires an expensive and time-consuming cylinder preparation. The substrates must be very smooth and compressive. It is used for PEMFC catalyst layer manufacturing by decal protocol [Siegel *et al.*, 2011]. For reaching the required layer thickness, Siegel adapts the screening of the engraved cylinder and show the relevance of this process for catalyst layer manufacturing.

Finally, only three printing processes have already been tested as process for fuel cell components fabrication: screen printing, ink jet and gravure. Their characteristics are described in Table 5.

Table 5 Main characteristics of printing processes for conventional applications [Blayo *et al.*, 2005; Denneulin, 2010]

Processes	Screen printing	Ink jet	Gravure
Type of process	Contact process	Non contact process	Contact process
Printing form	Meshed screen	No printing form	Engraved cylinder
Resolution (dpi)	120	> 600	200
(mm)	0.2	< 0.04	0.1
Wet ink film thickness	20 to 100 $\mu\text{m}$	1 to 2 $\mu\text{m}$	8 to 12 $\mu\text{m}$
Speed or run	Slow process 800 sheets h <sup>-1</sup>	Slow process > 150 m min <sup>-1</sup> > 1600 sheets h <sup>-1</sup>	Long run > 1 000 000 sheets
Dedicated substrate	Various substrates	All substrates	Dedicated substrates
Type of ink	Oil-based	Liquid	Liquid
Ink vehicle	Solvents	Solvents Water UV	Solvents Some with water
Ink viscosity (Pas)	0.1 to 10	About 0.01	0.01 to 0.05
Main applications	Commercial posters Advertising Packaging	Office printer Customizing Textiles	Publishing Packaging Decors
Catalyst layer manufacturing	Direct method detailed in part 3.1.1	Direct method detailed in part 3.1.2	Decal

### 3.1.1 Screen printing used for fuel cell manufacturing

As detailed before, the screen printing process is generally used for manufacturing ceramic based components for SOFC, such as electrolyte [Zhang *et al.*, 2006; Hansch *et al.*, 2009], interconnect protective layer [Tsai *et al.*, 2010], and electrodes [Piao *et al.*, 2008]. The screen printing is widely used because it is considered as a low cost and simple deposition technique. The current studies on SOFC are more turned toward the development of new ceramic composites and metallic alloys, than toward the development of the screen printing methods and protocols.

This process is also already used for manufacturing catalyst layers for PEM fuel cell by direct deposition [Hwang *et al.*, 2011; Bonifácio *et al.*, 2011]. These studies are compared in Table 6.

Table 6 Advantages and limitations of the use of screen-printing in fuel cell components manufacturing

Reference	Main goal of the study	Advantages	Limitations
Hwang <i>et al.</i> , 2011	Relation between the catalyst layer morphology and its electrochemical performances	<ul style="list-style-type: none"> <li>- Reproducibility,</li> <li>- Easy procedures</li> <li>- Low catalyst waste</li> <li>- Mass production</li> <li>- Uniform pore size</li> </ul>	<ul style="list-style-type: none"> <li>- Visible cracks formation compared to spray technique</li> </ul>
Bonifácio <i>et al.</i> , 2011	Reduction of the MEA cost of production	<ul style="list-style-type: none"> <li>- Adaptation of the ink quantity deposited by printing speed and screen ruling line value</li> <li>- One layer deposition for saving cost and time</li> </ul>	<ul style="list-style-type: none"> <li>- Solvent evaporation limits the accuracy of deposition of the ink</li> </ul>

In these studies, the screen printing appears relevant for manufacture catalyst layers. It is able to deposit one layer of ink with a control quantity of functional elements, without catalyst waste. However, the good properties of the catalyst layers also result from adequate ink formulation.

### 3.1.2 Ink jet used for PEM fuel cell manufacturing

The ink jet enters in the methods of fabrication for PEMFC [Taylor *et al.*, 2007] and SOFC [El-Toni *et al.*, 2008; Young *et al.*, 2008; Sukeshini *et al.*, 2009]. Among these four authors, two of them used a DIMATIX DMP 2831 (FujiFilm, Santa Clara, CA) [Young *et al.*, 2008; Sukeshini *et al.*, 2009], which is a drop on demand ink jet printer, with piezoelectric cartridges forming droplets of 10 pL for Young [2008]. El-Toni [2008] used a drop on demand printer KEGON-M3 with piezoelectric cartridges of 42 pL droplets [El-Toni *et al.*, 2008]. Taylor [2007] used a thermal cartridge Lexmark 17G0050 that forms 28 pL droplets with a Lexmark Z32 printer. From the conclusion drawn by the authors, the goals, advantages and limitations of using ink jet are summed up in the Table 7.

Table 7 Advantages and limitations of the use of ink-jet in fuel cell components manufacturing

Type of fuel cell	Reference	Main goal of the study	Advantage of the ink jet	Limitations
PEMFC	Taylor <i>et al.</i> , 2007	Catalyst layer manufacturing (anode only, cathode made by hand painting)	<ul style="list-style-type: none"> <li>- Suitable for ultra low (&lt;0.5 mg Pt cm<sup>-2</sup>) loadings (compared to screen printing and spray)</li> <li>- In thickness graded distribution of Pt/C catalyst structure</li> <li>- Versatile</li> <li>- Fast (10 min vs. 45 min for hand painting method)</li> </ul>	<p>Ink properties</p> <ul style="list-style-type: none"> <li>- Low ink viscosity</li> <li>- Small particle size</li> <li>- Good dispersion</li> </ul> <p>for preventing from nozzles clogging</p> <ul style="list-style-type: none"> <li>- High surface tension</li> </ul> <p>for preventing from leaking from the nozzles</p>
SOFC	Young <i>et al.</i> , 2008;	Electrolyte and anode-interlayer manufacturing for planar SOFC	<ul style="list-style-type: none"> <li>- Scalable methods from lab scale to mass commercialisation</li> <li>- Able to fabricate ceramic layers</li> <li>- Able to manufacture 3D structures</li> <li>- Fine resolution control compared to powder pressing, tape casting, screen-printing, or conventional spray methods</li> </ul>	
	Sukeshini <i>et al.</i> , 2009	All SOFC components manufacturing : Anode interlayer, electrolyte layer, cathode interlayer and cathode current collector for planar SOFC	<ul style="list-style-type: none"> <li>- Maskless deposition of materials</li> <li>- Optimal methods combining:               <ul style="list-style-type: none"> <li>- Good layer uniformity</li> <li>- Scalability</li> <li>- Low cost</li> <li>- Simplicity,</li> <li>- Accurate control of features</li> <li>- High reproducibility</li> </ul> </li> <li>- compared to chemical vapor deposition, electrochemical vapor deposition, sol-gel based, and spray, magnetron sputtering, thermal spray, and pulsed laser deposition screen-printing, tape casting, slurry coating, slip casting, tape calendaring, and electrophoretic deposition</li> </ul>	<ul style="list-style-type: none"> <li>- Problem microstructure due to ink design/formulation and printing parameters</li> </ul>
	El-Toni <i>et al.</i> , 2008	Electrolyte and electrodes of honeycomb type SOFC	<ul style="list-style-type: none"> <li>- Fully automated and computer controlled</li> <li>- Simple device,</li> <li>- Low cost,</li> <li>- Facile fabrication process,</li> <li>- Ease of mass fabrication</li> <li>- Fabrication of complex 3D structure</li> </ul>	<ul style="list-style-type: none"> <li>- Require multi-passing for achieving sufficient ink thickness</li> </ul>

For the PEMFC or SOFC applications, the ink jet is described as a versatile, low cost, scalable and simple method for manufacturing fuel cell components. However, the importance of the ink properties on the ink transferability and final deposit characteristics is often undervalued by the authors and limits the technology. The formulation of the ink has to reach appropriate viscosity, surface tension and particles size for optimising the use of this technology. Moreover, the low viscosity of the inks leads to the deposition of low solid content. Such behaviour either limits the platinum loading or requires several passes for reaching higher platinum loading which takes more time.

### **3.1.3 Limits of the ink-jet and screen-printing for manufacturing direct catalyst layers for PEMFC**

In the literature, direct manufacturing of catalyst layers was performed by ink jet and screen-printing. Table 8 summarises the protocols used for achieving catalyst layers with these two processes.

Table 8 Comparison of the protocol for manufacturing catalyst layer for PEMFC by printing processes

Printing processes	Reference	Ink preparation	Printing protocol	Drying step	MEA				
Ink jet	Taylor <i>et al.</i> , 2007	<table border="1"> <thead> <tr> <th>Anode</th> <th>Cathode</th> </tr> </thead> <tbody> <tr> <td>Water based ink for ink jet. - 75 w/w% Pt/C (20 w/w% of Pt) - 25 w/w% Nafion® (5 w/w% of ionomer in aliphatic alcohols mixture) dispersed in a solvent mixture (mainly methanol) + sonificated 30 min + micro stirred 30 min</td> <td>For hand painting - 63 w/w% of Pt/C - 2.5 w/w% of Nafion® dispersion - 1.2 w/w% of Teflon® dispersed in a isopropanol/water mixture at 50/50 ratio</td> </tr> </tbody> </table>	Anode	Cathode	Water based ink for ink jet. - 75 w/w% Pt/C (20 w/w% of Pt) - 25 w/w% Nafion® (5 w/w% of ionomer in aliphatic alcohols mixture) dispersed in a solvent mixture (mainly methanol) + sonificated 30 min + micro stirred 30 min	For hand painting - 63 w/w% of Pt/C - 2.5 w/w% of Nafion® dispersion - 1.2 w/w% of Teflon® dispersed in a isopropanol/water mixture at 50/50 ratio	CCB - Thermal ink jet printer Lexmark Z32 (for their bigger nozzles compared to piezo technology) + Lexmark 17G0050 cartridge droplet volume 28 pL - Platinum loading calculated from droplet volume, resolution and ink density	Oven 180 °C for 1 h	Nafion 117 hot pressed at 130 °C for 5 min at 10 MPa.
Anode	Cathode								
Water based ink for ink jet. - 75 w/w% Pt/C (20 w/w% of Pt) - 25 w/w% Nafion® (5 w/w% of ionomer in aliphatic alcohols mixture) dispersed in a solvent mixture (mainly methanol) + sonificated 30 min + micro stirred 30 min	For hand painting - 63 w/w% of Pt/C - 2.5 w/w% of Nafion® dispersion - 1.2 w/w% of Teflon® dispersed in a isopropanol/water mixture at 50/50 ratio								
Screen printing	Hwang <i>et al.</i> , 2011	Water based ink - 21 w/w% Pt/C (20 w/w% of Pt) - 35 w/w% Nafion® dispersion at 20 w/w% - 44 w/w% isopropanol/water at 14.3/60.71 w/w% + stirring + sonification 30 min	CCB - Control of the Screen mesh from 80 to 150 - Platinum loading calculated by difference of mass weight before and after printing - If the Pt loading is not adequate, another layer is coated onto the catalyst layer	Oven 60°C for 8 h	Nafion 112 hot pressed at 130 °C, under 40 kgf cm <sup>-2</sup> for 7 min				
	Bonifácio <i>et al.</i> , 2011	Alcohol based ink - 15 w/w% of Pt/C (20 w/w% of Pt) - 85 w/w% of Nafion® dispersion (at 10 w/w% of ionomer) in a Ethylen glycol/1-heptanol vehicle at 100/0 or 95/5 w/w%	CCB Cathode at 0.6 mgPt.cm <sup>-2</sup> and anode at 0.4 mgPt.cm <sup>-2</sup> - Estimation of the platinum loading based on the ink properties and transfer quality - Control of the ink quantity deposited by ink surface tension and printing speed - Platinum loading calculated by difference of mass weight before and after printing	Drying complete solvent evaporation	No MEA				

According to these authors, the use of printing processes appears to be dedicated to CCB manufacturing. One of the major concerns deals with the control of the platinum loading transferred by ink deposition. The authors developed two main methods. One is based on the estimation of the platinum loading on the substrate using formulation specification, the ink density and the estimated volume of droplets [Taylor *et al.*, 2007; Bonifácio *et al.*, 2011]. The second is based on the determination of the mass of dry ink deposited by mass measurement before and after ink deposition and drying. Then, the catalyst quantity is calculated as regards to the ink formulation [Bonifácio *et al.*, 2011; Hwang *et al.*, 2011]. The error occurring with using the first technique has been estimated by Bonifácio around 2 w/w % compared to the use of the second method. The first method is more adapted to low platinum loading, when the dry ink mass is difficult to measure by mass differential. The ink formulation is mainly driven by fuel cell requirements [Taylor *et al.*, 2007 and Hwang *et al.*, 2011]. However, Bonifácio and Siegel [Siegel *et al.*, 2011] did a complete work on the ink formulation. The ink/substrate deposition issues were deeply studied and took into consideration the surface tension of the ink and the surface energy of the substrate. The process requirements entered also into the ink formulation choice, through the study of the ink viscosity and the relation between ink viscosity, printing speed and the quantity of ink deposited onto the substrate.

The ink/substrate affinity is the core of the ink formulation in conventional printing industry and is more developed in the Appendix 2.

The comparison of the screen printing and ink jet process for catalyst layers manufacturing is described in Table 9.

Table 9 Comparison of the advantages and limitations of the screen printing and ink jet for fuel cell applications [Taylor *et al.*, 2007; Young *et al.*, 2008; El-Toni *et al.*, 2008; Sukeshini *et al.*, 2009; Bonifácio *et al.*, 2011; Hwang *et al.*, 2011 and Kipphan 2001]

Processes	Screen printing	Ink jet
Advantages	Large surface Low pressure applied for ink transfer Various substrates Versatile process Single printing step	Easy implantable, handling and versatile No printing form No pressure applied on the substrate Various substrate Cheap technology
Limitations	One pass by colour Dedicated for depositing high quantity of ink Dryers required for thick ink film drying High thickness and drying induce catalyst layer cracks Limited particles size for ink to get through the screen	Small surface Low speed Limited particles size Anilox clogging Fine specifications for ink formulation Low ink quantity deposited Require multilayer for reaching targeted platinum loading
Typical printing defect	Deposition of irregular quantity of ink due to the meshed screen	Dotted pattern Coffee ring effect during drying Satellite droplets during transfer of the main ink drop Placement error of the drop

The use of ink jet and screen printing for manufacturing PEMFC components remains rare. However they are described as good candidate for up scaling the catalyst layers production. Several improvements, particularly of the inks, but also of the platinum loading measure, are necessary before using all the advantages described for these two processes. Each of them has also limitations for catalyst layer manufacturing:

- for screen printing, the main limitation is the mono-layer deposition type,
- for ink-jet, the printed surfaces are small, and the low viscosity induces a low solid content.

In addition, both are discontinuous printing processes with low speed compare to the continuous printing processes. Among them, the flexography, that is a continuous process, has suitable properties for manufacturing catalyst layers. Moreover, this process had never been investigated for catalyst layer manufacturing. That is why this process is the core of the following part.

### 3.2 The Flexography

The first name given to the flexography was “aniline” printing, because of the use of the aniline dyes in the first flexography inks. However, the aniline was classified as unsuitable for food by the U.S. Food and drug Administration in the 1940s. Widely used

in the food packaging industry, the aniline printing declined. It leads to a change of both the inks formulation and of the process named into flexography in 1951. One of the main features of the flexography is the use of flexible printing plates and low viscosity inks. This process is mainly used for packaging and labels printing thanks to its versatility of substrates.

The official definition of flexography is [FFTA, 1999]: “Flexography is a method of direct rotary printing that uses resilient relief image plates of rubber or photopolymer material. The plates are affixable to plate cylinders of various repeat lengths, inked by a cell-structured ink metering roll, with or without a reverse-angle doctor blade, and carrying a fast drying fluid ink to plates that print onto virtually any substrate, absorbent or non-absorbent. Flexography is a rotary printing method, which means for every revolution of the printing plate cylinder, an image is produced.”

### 3.2.1 Printing groups

Ink is put in contact by a doctor blade (Figure 16.1) with a micro-engraved cylinder (anilox) (Figure 16.2) whose cells are filled with a constant ink volume. Anilox are defined by their theoretical volume in  $\text{cm}^3$  of ink contained for  $1\text{m}^2$  of cells ( $\text{cm}^3 \text{m}^{-2}$ ). Then, the ink is transferred onto a printing form (Figure 16.3) defining the pattern information. Thus, the inked pattern is pressed against the substrate (Figure 16.4) in the nip zone (Figure 16.5) between the printing form and a printing cylinder (Figure 16.6). The ink transfer onto the substrate is performed with the lowest possible pressure. This particularity has given the nickname “kiss printing” to the flexography [Kipphan, 2001].

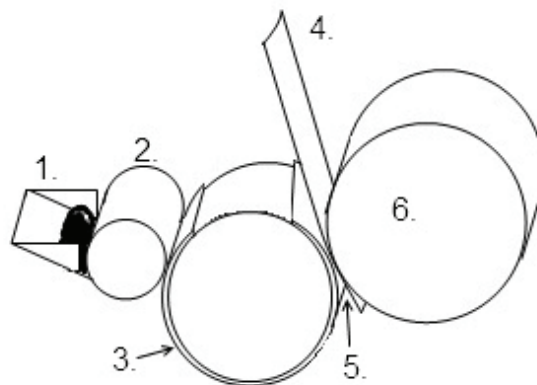


Figure 16 Flexography printing unit

Thanks to the low pressure applied in the nip, the flexography is able to transfer ink:

- on fragile substrates: corrugated boards, that could be flattened during printing and then lost their thickness, and self-adhesive labels, that are composed of a layer made of adhesive;

- smooth substrates can also be printed by flexography: plastics, foils or glass.

Flexography web presses reach speeds higher than  $600 \text{ m min}^{-1}$ . For multicolour printing (four colours, specific colours and varnishes) are usually composed of:

- a substrate unwinder at the head of the web press,
- a registering system,
- a transportation system,
- a web tension controller,
- several printing groups,
- several ink dryers,
- and a substrate rewinder at the tail of the press.

The design of the printing groups can be made following three main configurations:

- In-line unit design, commonly dedicated to production with narrow width (tens of centimetres), as for label printing.
- Central impression cylinder press, where the printing cylinder is shared with all printing units placed around it. The printing cylinder have a higher diameter (more than 2 meter) and a large width (up to 100 cm),
- Stack-type design, where printing groups are vertically stacked. Due to their low registering, these presses are used for simple routine operations.

### 3.2.2 Flexographic inks

The inks used in flexography are water-based, solvents based or UV curing inks. The formulation of an ink is a complex process. Indeed, for flexography as well as for other processes, it highly impacts the deposits characteristics (as it is demonstrated by Bonifácio *et al.* [2011] for screen printing process).

Generally speaking, an ink is a suspension of solid particles in a liquid composed of solvents and polymers. The solid particles have functionalities depending on their application. The liquid part of the ink is called the ink vehicle. It stabilises the solid particles and gives to the ink its rheological behaviour in order to suits to the process. The ink vehicle is either evaporated (for oily and water based inks), or reticulated (in UV-curing inks).

The vehicle formulation must take into consideration:

- the process requirements: rheological properties such as viscosity, physico-chemistry such as surface tension, particles sizes and solvents compatibility. The ink viscosity for flexography has to be adjusted around 10 to 100 mPa s.

Moreover, the ratio between the anilox cells specific dimensions and the particle maximal size have to be higher than ten.

- the drying properties with solvents that induce different drying mechanisms depending on the drying techniques: air or IR drying.
- the substrate characteristics influence the affinity with the ink: surface state (roughness) and surface energy (developed in Appendix 2).

For catalyst layers application, one concern is the complete elimination of the vehicle after ink deposition [Taylor *et al.*, 2007; Hwang *et al.*, 2011; Bonifácio *et al.*, 2011]. Consequently, UV-curing inks are not suitable for this application because the polymer remains in the dried ink film. In flexography, the ink film thickness generally ranges between 6 to 8  $\mu\text{m}$ . The typical components of water and solvent-based ink formulations are presented in Table 10.

Table 10 Typical formulation of flexography water and solvents based inks

Ink components	Main purposes	Formulation (w/w %)	
		Water-based inks	Solvents-based inks
Pigments, dyes or functional particles	Colour properties	15 – 20	10
Resin	Control of the viscosity and binder	55 – 65	15 – 25
Solvents	Resin solubilisation Viscosity control	3 – 5	55 – 70
Additives (softener, dispersion agents, wetting agents, anti foam, fungicide, adhesion promoter)	Ink stability and durability Drying properties Dried film resistance and appearance	3 – 5	5 – 10
Water	Control of the viscosity	10 – 15	

### 3.2.3 Anilox

The anilox is a metering roll used in the flexography process to deposit a controlled amount of ink onto the printing plate described in part 3.2.5 [FFTA, 1999]. The anilox is a cylinder with a metal core (stainless steel or aluminium) and covered by specific layers (copper, chrome and/or ceramics). The upper layer is engraved with micro-cells. The cells have preferential shape that is defined by their gravure angle, for example hexagonal shape induced by gravure angles equal to  $30^\circ$  or  $60^\circ$  or quadrangular shape induces by  $45^\circ$  gravure angle. The screen running of the cells and the cell width vary depending on the required cell volume from 80 to 600 cells  $\text{cm}^{-1}$  and from 10 to 30  $\mu\text{m}$  respectively.

Empirically, for gravure angle equal to  $60^\circ$ , the ratio between the anilox screen and the printing plate screen is equal to 5 or up in order to optimise the ink transfer. During the

ink transfer from the anilox to the printing plate, the ink contained in the cells split and a part of the ink remains into the cell (typically about 25 % in volume).

### 3.2.4 Doctor blade

The doctor blade is multi tasking constituent of the flexography inking unit [Jewell *et al.*, 2000]:

- ink container,
- ink distributor,
- and finally, ink scraping on the anilox roller.

Two technologies exist:

- opened doctor blade composed by an ink container and one blade (Figure 17),
- and enclosed chambered doctor blades, with two blades under and above the ink container (Figure 18).

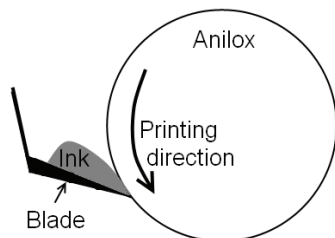


Figure 17 Doctor blade

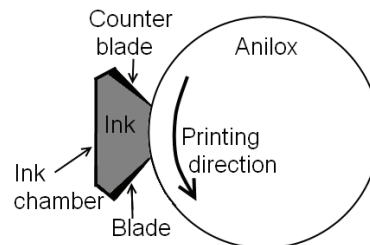


Figure 18 Chambered doctor blade

The chambered doctor blade equips the majority of the presses because this technology insures a better control of the ink volume transfer onto the plate. It limits the dead volume of ink in the inking system and the solvent evaporation, which are crucial parameters for catalyst layers fabrication.

### 3.2.5 Printing plate or cliché

The flexography printing form, the cliché, is a plate or a sleeve made of flexible and compressive polymer. The material is shaped for forming patterns, whom relief received the ink from the anilox cells. It is characterised by its hardness and thickness in order to fit the substrate and the printing pattern. Different cliché materials and patterning technologies exist: molding or laser engraving of rubber plates, or the use of photopolymeric plates or sleeves. When the cliché is pressed against the substrate, it deforms. It forms a typical defect of the flexography: a halo that surrounds the deposit.

### 3.3 Flexography potential for manufacturing fuel cell components

The main advantages and limitations of this process for conventional printing are reported in Table 11.

Table 11 Advantages and limitations of flexography process [Kipphan, 2001; FFTA, 1999]

	Advantages	Limitations
Flexography press	<ul style="list-style-type: none"> <li>- Continuous process</li> <li>- Web or sheet-fed process</li> <li>- Low pressure applied to the substrate</li> <li>- High speed 600 m min<sup>-1</sup></li> </ul>	<ul style="list-style-type: none"> <li>- Profitable for long print run (from 10,000 to 100,000 sheets for conventional production)</li> <li>- Typical printing defects of halo surrounding the edges of the printing patterns</li> </ul>
Inking system	<ul style="list-style-type: none"> <li>- Control of the ink volume transfer on the anilox cells by doctor blade</li> </ul>	<ul style="list-style-type: none"> <li>- Dead volume in the inking system</li> </ul>
Anilox	<ul style="list-style-type: none"> <li>- Accept bigger particles compared to ink jet</li> <li>- Control the uniformity of the ink film transfer on the printing plate</li> <li>- The volume of the anilox can be adapted to the desired deposited ink thickness</li> </ul>	<ul style="list-style-type: none"> <li>- Anilox clogging</li> <li>- The anilox volume limit the platinum loading deposited by pass</li> <li>- Expensive</li> </ul>

Considering the advantages and drawbacks of ink jet and screen printing for catalyst layer manufacturing, it was possible to presume on the future qualities and limits of the flexography for this application.

As a continuous and fast process, flexography appears as a good candidate for reduction of the production cost of catalyst layer. In conventional printing, long printing runs are favoured for compensating the higher cost of the consumable elements. But for high added value production, such as catalyst layers production, which use expensive raw material, this parameter is less crucial. Consequently, this process is suitable for up scaling catalyst layer production from small to high production, as an additional technique of ink jet for lab-scale production and screen printing.

The halo printing defect that surrounds the printing pattern induces an important dot gain. This is a problem for fine pattern reproduction. However, for catalyst layer manufacturing, the printing patterns are large solid areas. Therefore, this printing pattern is not a major limitation for this application.

The ink film thickness is conventionally about 6 to 8  $\mu\text{m}$ , which is higher than the ink jet printed layer (around 1 to 2  $\mu\text{m}$ ) or lower than the screen printed layer (from 20 to 100  $\mu\text{m}$ ). It limits the platinum loading, and requires the superimposition of several ink layers for reaching a high platinum loading. It also increases the printing versatility, with

graded structure for example [Taylor *et al.*, 2007] or a finer control of the platinum loading [Hwang *et al.*, 2011].

This is a main advantage because the control of the ink film thickness provides a higher repeatability, which is a crucial parameter for catalyst layer manufacturing [Bender *et al.*, 2003].

One major problem is the anilox clogging, which induces the loss of the repeatability of the ink film thickness transferred onto the cliché. Moreover, because of the price of the ink components, the necessity of a dead volume in the inking system is the substantial drawback of the flexography. The use of multi-groups press leads to multiply the dead volumes of ink and consequently, the fixed cost for launching a print.

## Conclusion of chapter 1

The challenge of the PEMFC is the reduction of the system cost in order to get a lower price of the produced power. For that purpose, saving up is targeted by the DOE on all components of the fuel cell system, from their manufacturing to their materials and passing by their efficiency and durability.

The present study proposed to investigate the use of a continuous process, the flexography, which is able to produce large surfaces of catalyst layers with a high speed and with low waste compared to conventional processes. Table 12 gives additional advantages and limitations of this process for the catalyst layer manufacturing application.

Table 12 Potential advantages and limitations of the flexography for manufacturing catalyst layer for PEMFC

Advantages	Limitations
<ul style="list-style-type: none"> <li>- High speed (<math>600 \text{ m min}^{-1}</math>) and continuous process, web or sheet-fed process</li> <li>- Large surface</li> <li>- Various and delicate substrates</li> <li>- Ink film thickness 6 to <math>8 \mu\text{m}</math> with bigger particles compared to ink jet</li> <li>- Control the uniformity of the ink film transfer on the printing plate by using a metering roll called anilox, which can be adapted to the desired deposited ink thickness</li> </ul>	<ul style="list-style-type: none"> <li>- Profitable for long print run (from 10 000 to 100 000 sheets for conventional production)</li> <li>- Typical printing defects of halo surrounding the edges of the printing patterns</li> <li>- The anilox are expensive, their cell may clog, and the anilox volume limits the platinum loading deposited by pass</li> <li>- <b>Dead volume in the inking system</b></li> </ul>

Consequently, the flexography has an important potential to contribute to the reduction of the cost of the power produced by a PEMFC. This objective guides the works presented among the following chapters.



# Chapter 2

## Materials and Methods



<b>INTRODUCTION .....</b>	<b>69</b>
<b>1 MATERIALS AND PROCESSES.....</b>	<b>70</b>
1.1 SUBSTRATES .....	70
1.2 INKS .....	70
1.3 PRINTING PROCESS.....	71
<b>2 DEVICES AND METHODS FOR CHARACTERISING PRINTED SUBSTRATES AND SUBSTRATE BEFORE PRINTING.....</b>	<b>73</b>
2.1 ROOM CONDITIONS OF TESTS .....	73
2.2 INFLUENCE OF THE ENVIRONMENTAL CONDITIONS .....	73
2.2.1 <i>Membrane water uptake as a function of the RH%.....</i>	<i>73</i>
2.2.2 <i>Measurement of membrane dimensions under air humidity variations .....</i>	<i>74</i>
2.2.2.1 Influence of the RH% on the membrane thickness .....	75
2.2.2.2 Influence of the RH% on the membrane dimensional variations in the plane direction.	75
2.2.3 <i>Production of air with a controlled RH%.....</i>	<i>76</i>
2.2.4 <i>Humidity cycles.....</i>	<i>77</i>
2.2.5 <i>Measure of the mass of a the dried membrane sample .....</i>	<i>78</i>
2.3 SURFACE CHARACTERISATION .....	78
2.3.1 <i>Scattering Electron Microscopy (SEM) observations .....</i>	<i>78</i>
2.3.1.1 Environmental Scattering Electron Microscopy (ESEM) .....	78
2.3.1.2 BackScattered Electrons detection (BSE) .....	79
2.3.2 <i>Surface Roughness.....</i>	<i>79</i>
2.3.3 <i>Surface wettability .....</i>	<i>79</i>
2.4 BULK CHARACTERISATION.....	81
2.4.1 <i>Substrate thickness.....</i>	<i>81</i>
2.4.2 <i>Gas Diffusion Layer permeability.....</i>	<i>81</i>
2.4.3 <i>Catalyst layer permeability.....</i>	<i>82</i>
2.5 EVALUATION OF THE PRINTING QUALITY .....	82
2.5.1 <i>Platinum loading quantification .....</i>	<i>82</i>
2.5.2 <i>Surface covered by the ink.....</i>	<i>82</i>
2.5.3 <i>Optical density values.....</i>	<i>83</i>
2.5.4 <i>Spectroscopy.....</i>	<i>83</i>
2.5.5 <i>Ink intrinsic reflectance and optical density .....</i>	<i>84</i>
2.6 ELECTROCHEMICAL CHARACTERISATION.....	84
2.7 CATALYST LAYERS ELECTROCHEMICAL PROPERTIES .....	84
2.7.1 <i>Cyclic voltammetry (CV).....</i>	<i>84</i>
2.7.2 <i>Electrochemical Surface Area (ESA).....</i>	<i>85</i>

2.7.3 <i>Electrochemical Impedance Spectroscopy (EIS)</i> .....	85
<b>CONCLUSION OF CHAPTER 2</b> .....	<b>86</b>

## Introduction

For the present study, the manufacturing of MEAs depends upon:

- substrates, Gas Diffusion Layers or Proton Exchange Membrane samples (GDLs or a PEM),
- inks, with the necessary functional elements,
- and the selected printing process, which transfers the ink onto the substrate.

They are detailed in the first part of this chapter.

The second part of this chapter is depicted in Figure 19.

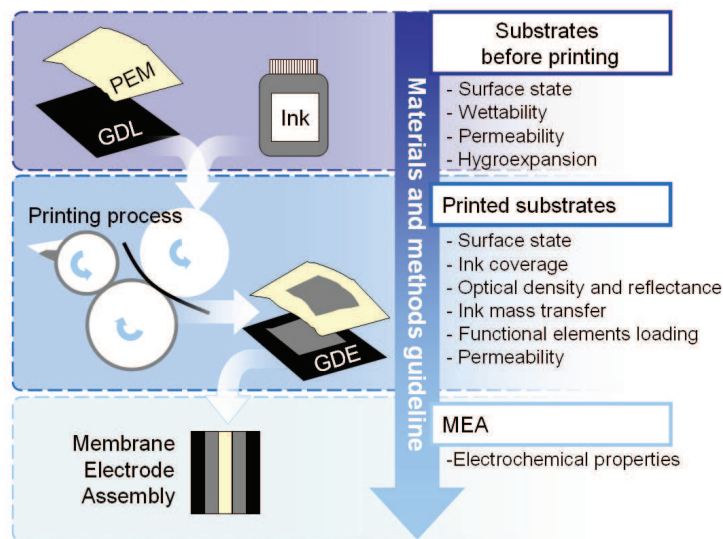


Figure 19 Outline of the materials and methods chapter

Complementary methods and devices were applied for performing characterisations onto the non-printed substrates, the printed substrates and consequently on the catalyst layers, and finally on the MEAs prepared with the printed catalyst layers.

## 1 Materials and processes

### 1.1 Substrates

The CCB and CCM protocols consisted in depositing catalyst layers respectively on:

- a GDL, the GDL 24 BC (Sigracet, SGL Group, Meitingen, Germany),
- a PEM, Nafion<sup>®</sup> NRE 212 (DuPont, Wilmington, Delaware, USA).

In this chapter, the GDL and PEM samples are not only considered as printing substrates and but also as fuel cell components. Consequently, they are also characterised with techniques dedicated for this application.

### 1.2 Inks

Two water-based inks were formulated to fulfil the requirements of the flexography process and the fuel cell. Water, already used in running MEA, was chosen as the solvent vehicle of the catalyst ink. It limits the potential pollutants that could damage electrochemical properties of the MEA. Furthermore, it is compatible with flexography process and reduces the use of volatile organic components. Some functional elements were added to the ink formulation:

- Nafion<sup>®</sup> polymer dispersion (22 w/w % Nafion) in aliphatic alcohols and deionised water (DE2020, DuPont TM, Wilmington, USA),
- carbon powders at various ratio of the platinum nanoparticles:
  - either carbon-supported platinum catalysts (Tanaka Kikinzo, Tokyo, Japan) with 45.4 w/w % platinum as regards to the carbon-supported platinum. This component entered into the formulation of an ink specifically made for this study named I<sub>33</sub> which is used for manufacturing catalyst layers.
  - or carbon powder (Cabot Corporation, Alpharetta, USA) was used as a replacement for the carbon supported platinum, in order to control the amount of platinum in the dry content when required. This carbon powder entered into the formulation of the ink I<sub>0</sub>.

The ink I<sub>0</sub> had two main purposes. Firstly, as the catalyst is very expensive, it reduces the use of platinum nanoparticles, for manufacturing catalyst layers that did not require electrochemical properties. Secondly, if required, inks I<sub>0</sub> and I<sub>33</sub> were mixed for making inks with a controlled amount of platinum in the dry content.

There is a risk to set fire when platinum is in contact with alcohol elements. That is why the components were incorporated in a specific order: carbon supported catalyst, then the water, and the Nafion<sup>®</sup>. 30 min of sonification and 15 minutes of stirring insure a complete inks mixing.

The rheological properties of the inks were measured by a Physica MCR 301 (Anton Paar, Graz, Austria), using a cone-plate CP 50-1 measuring geometry with a diameter of 25 mm. The gap of measure was set at 0.5 mm. The shear stress (Pa) was measured as a function of a shear rate ( $s^{-1}$ ) values that logarithmically varied from 10 to 2500  $s^{-1}$ . For each type of ink, three measures were performed. For each measure, as the inks were quasi-Newtonian fluids in this range of shear rates, the viscosity (Pa.s) was extracted from the curves of shear stress as a function of the shear rate, using a linear regression.

The surface tension of the inks was evaluated by a tensiometer K10ST (Krüss, Hamburg, Germany) using the ring methods (du Nouy Method). Ten measurements were performed for each type of ink.

### 1.3 Printing process

The flexography printing tests were performed on a sheet-fed laboratory proofing device: the Flexiproof (Testing Machines Inc. TMI, New Castle, USA) (Figure 20).

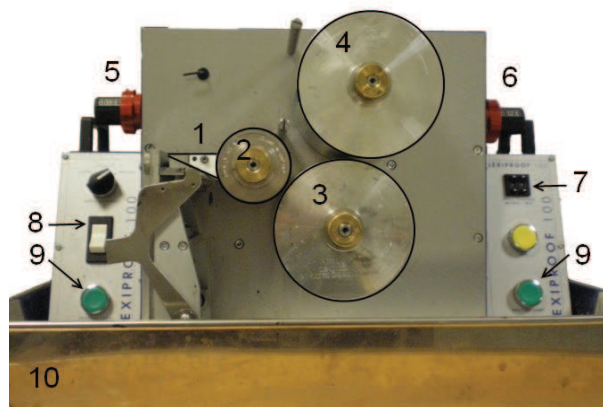


Figure 20 front view of the flexiproof device

Similarly to the flexography printing unit, the system is composed of a flexography printing group, that transfers the ink from the doctor blade (Figure 20.1), to the cells of anilox cylinder (Figure 20.2). The ink is deposited onto the plate's relief, which transfers the ink onto the substrate in the nip zone formed by the plate cylinder (Figure 20.3) and the printing cylinder (Figure 20.4).

In the Flexiproof device, micrometric settings control the gap between:

- the anilox and the plate (Figure 20.5),
- the plate and the printing cylinder (Figure 20.6).

It modifies the ink transfer by adjusting the pressure in the nip zone. The printing speed ranges from 1 to 99 m min<sup>-1</sup> (Figure 20.7). A button switch launches the anilox rotation and the ink transfer onto the cell (Figure 20.8). The substrate is taped onto the printing cylinder and the printing trial is initiated by pressing the two buttons (Figure 20.9). For safety reason, the whole device is placed in a container (Figure 20.10) in order to limit the spreading of ink containing nanoparticles.

For fuel cell printing tests, the printed samples were square solid patterns, with dimensions depended on the type of tests performed on the deposits thereafter. Generally, the edges of a sample were not printed on at least 1 cm due to technological requirements related to the assembly of the fuel cell. The maximal printing size was 75 × 240 mm. The manufacturing of a printing deposit was performed at 25 m min<sup>-1</sup> by successively superimposing up to six ink layers at the centre of this substrate.

In this study, two different anilox volumes were used 13 cm<sup>3</sup> m<sup>-2</sup> and 4 cm<sup>3</sup> m<sup>-2</sup>.

## 2 Devices and methods for characterising printed substrates and substrate before printing

### 2.1 Room conditions of tests

The tests and the storage were performed in a room with controlled conditions 50 *RH%* and 23 °C. Each sample was placed 24 h in these conditions before any testing.

### 2.2 Influence of the environmental conditions

Hygroexpansion is the phenomenon of dimensional variations that occur during changes of the water content in a material. The related phenomena are:

- water uptake (2.2.1),
- and dimensional variations (2.2.2), in the thickness or in the plane direction of the sample.

For measuring such properties which are commonly characterised in the printing and paper fields, two specific devices were designed: the Varimass (2.2.1) and the Varidim (2.2.2.2). The devices were fed by an air generator (2.2.3) that applied different relative humidity (*RH%*) settings (2.2.4) into the closed chambers of the devices where the samples were placed.

#### 2.2.1 Membrane water uptake as a function of the *RH%*

The Varimass device evaluated the water uptake of membrane as a function of the air relative humidity content. This device measures the weight of a sample as a function of the time (every 15 s) for several air relative humidity contents. A sample, about 1 to 2 g, was hung on a sample carrier as it is described by Figure 21. At each measurement, a scale weights the mass ( $m_{tot}$ ) of a system composed of the sample ( $m_s$ ) and the sample carrier ( $m_c$ ).

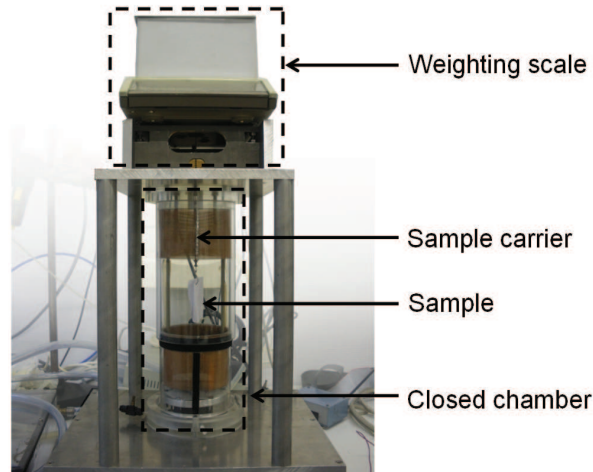


Figure 21 Sample in Varimass device (here, paper sample)

The mass of the water uptake ( $m_w$ ) was obtained by subtracting the sample mass ( $m_s$ ) from the sample mass reference ( $m_{ref}$ ) as shown in Equ. 9.

$$m_w = m_s - m_{ref} \quad \text{Equ. 9}$$

$\lambda$  is defined as the number of water molecules by sulfonic acid group of the membrane (Equ. 10).

$$\lambda = \frac{m_s - m_{ref}}{m_{ref}} \cdot \frac{EW}{M_w} \quad \text{Equ. 10}$$

Where,

$EW$  ( $\text{g mol}^{-1}$ ) is the Equivalent Weight of the membrane representing the mass of membrane by mole of sulfonic acid, it is equal to  $1100 \text{ g mol}^{-1}$  for Nafion<sup>®</sup> 212,  
 $M_w$  ( $\text{g mol}^{-1}$ ) is the molecular mass of the water, equal to  $18 \text{ g mol}^{-1}$  at  $20^\circ\text{C}$ ,  
 $m_s$  and  $m_{ref}$  are the mass of the sample and the mass of the same sample in the reference condition ( $50 \text{ RH}\%$   $23^\circ\text{C}$ ) respectively.

$\lambda$  indicates the number of water molecules gained or lost per sulfonic acid group during the experiment, compared to the reference sample.

During the tests, the  $\text{RH}\%$  accuracy is about 2%. The sample mass uncertainty when changing the  $\text{RH}\%$  of 2% was lower than  $\pm 0.3 \text{ w/w}\%$

### 2.2.2 Measurement of membrane dimensions under air humidity variations

The tests described thereafter were performed on ten samples. The results presented in the experimental chapter are the average of the results acquired on the ten samples.

### 2.2.2.1 Influence of the RH% on the membrane thickness

For the tests in air with a relative humidity differing from 50 RH%, the micrometer described in the sections 2.4.1 was entirely covered by a hermetic cloth, forming a bell jar, in which the thickness measurements and membrane conditioning were realised.

### 2.2.2.2 Influence of the RH% on the membrane dimensional variations in the plane direction

The Varidim device characterised the membrane strain as a function of the RH%. In Varidim device, the length variations or expansion,  $\Delta L_{measured}$ , of ten samples having an initial length,  $L_0$ , of 100 mm and a width of 15 mm were simultaneously measured each 40 s. The accuracy of the sample length in Varidim device was  $\pm 3 \mu\text{m}$ . As detailed in Figure 22, two pairs of magnetic pliers vertically maintained the samples strips. The underneath bottom pliers were 20 g and were freely related by magnetic attachment to a Linear Variable Differential Transformer (LVDT) motion sensor. Thus the test was performed with a constant stress of 0.26 MPa applied on each sample.

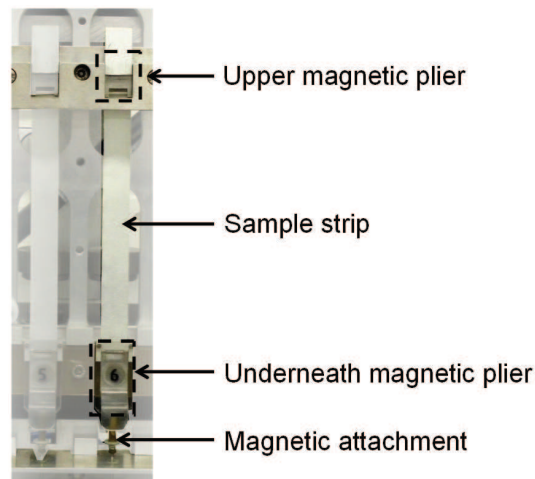


Figure 22 Focus on a sample hung in Varidim device (here, paper sample)

Several parameters were calculated from the raw data  $\Delta L_{measured}$ .

A reference of measurements,  $\Delta L_{measured, 50RH\%}$ , was set during the first 50 RH% step of the first cycle when the humidity content regulation is stable. Consequently, in order to define the sample expansion, the value  $\Delta L_{measured, 50RH\%}$  of the first cycle was subtracted to each  $\Delta L_{measured}$  in Equ. 11.

$$\Delta L = \Delta L_{measured} - \Delta L_{measured, 50RH\%} \quad \text{Equ. 11}$$

The macroscopically strain ( $\epsilon$ ) in the vertical plan was calculated thanks to Equ.12.

$$\varepsilon = \frac{\Delta L}{L_0} \quad \text{Equ. 12}$$

The strain amplitude  $\Delta\varepsilon$  was calculated in Equ. 13 using the strain values obtained at the maximal and minimal  $RH\%$  values which were 85 and 10  $RH\%$  respectively.

$$\Delta\varepsilon = \varepsilon_{85RH\%} - \varepsilon_{10RH\%} \quad \text{Equ. 13}$$

The average strain ( $\varepsilon_{ave}$ ) was half of the strain amplitude (Equ. 14).

$$\varepsilon_{ave} = \frac{\Delta\varepsilon}{2} = \frac{\varepsilon_{85RH\%} - \varepsilon_{10RH\%}}{2} \quad \text{Equ. 14}$$

### 2.2.3 Production of air with a controlled $RH\%$

For creating different conditions for hygroexpansion tests in the Varidim and Varimass devices, an air generator controlled the value of  $RH\%$ . The humidity was fixed at the selected value within 2 %, the temperature was set to  $23\text{ }^\circ\text{C} \pm 0.5\text{ }^\circ\text{C}$ . The air generator had 10 s inertia, a standard flow of 4 to 5  $\text{m}^3\text{ h}^{-1}$  and an output pressure of 0.1 to 0.2 bar.

Figure 23 shows the generator connected to a computer which controlled the humidity system and acquired data. The air fed a closed chamber containing the samples.

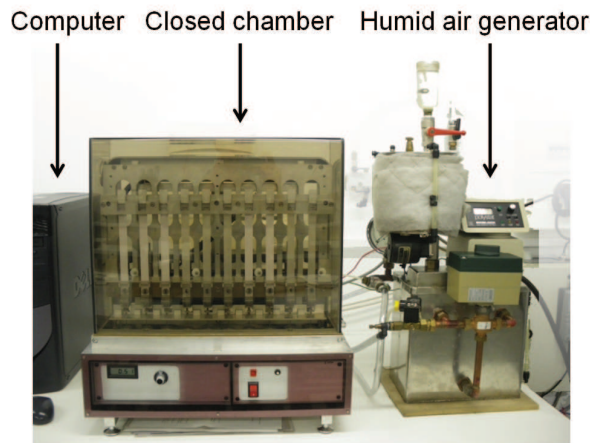


Figure 23 Home made air generator feeding the closed chamber of a Varidim device (detailed in part 2.2.2) and connected to a computer

The production of an air with more than 85  $RH\%$  may induce water condensation in the closed chamber. In order to avoid such a phenomena, that could significantly impact the measurements efficiency and the samples properties, the 85  $RH\%$  was the maximal tested value in this work.

The limits of precision of the generator for Nafion<sup>®</sup> samples test were investigated. The study is detailed in the appendix 5.

### 2.2.4 Humidity cycles

The different RH% values applied on the samples for hygroexpansion tests were sequenced as following:

- the RH% values can be modified as a function of time. Each setting can be hold for 1 to 200 000 s. Each combination of air humidity content and duration is referred as a step.
- different steps can be sequenced to form a cycle.
- finally, a cycle can be repeated.

The values of air relative humidity are reported as a function of the time, and describe the conditions in which the measures were performed. For example in Figure 24, two cycles were performed; each cycle was composed of eight 2 hours-steps.

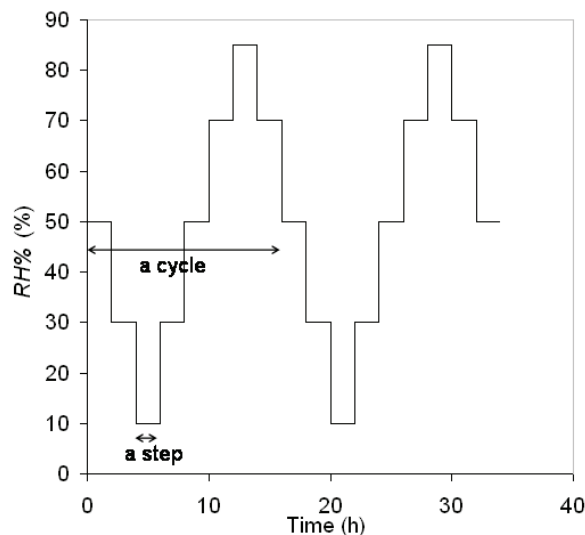


Figure 24 Air relative humidity content along time during the experiment

In this work, mainly two types of cycles, namely characterisation and ageing cycles, were performed:

- The characterisation cycle was composed of eight steps set at 50, 30, 10, 30, 50, 70, 85, 70 and 50 RH%, for 90 minutes each. Figure 24 gives an example of two following characterisation steps.
- The ageing cycle consisted in repeating ten steps of 20 and 80 RH% of 30 minutes.

The RH% values applied in the closed chamber were measured and controlled simultaneously with the mass or length measurements.

A full test of membrane ageing was composed of the five times repetition of an ageing cycle that follows a characterisation cycle as described in Figure 25.

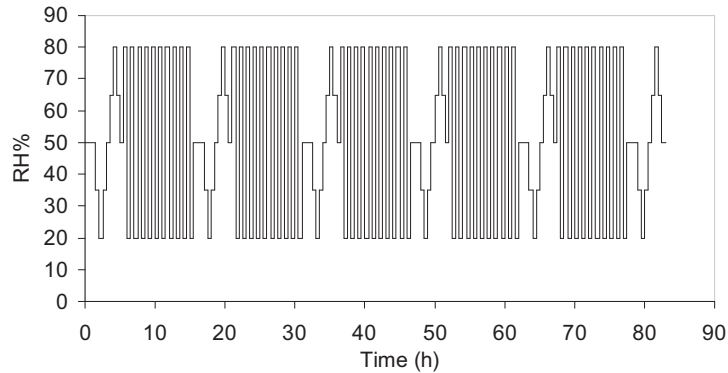


Figure 25  $RH\%$  values as a function of the time, for a full ageing test.

### 2.2.5 Measure of the mass of a the dried membrane sample

The mass of dry perfluorosulfonic acid membrane samples ( $m_d$ ) was measured after drying 30, 60 and 120 minutes in a oven at 105 °C. The sample was supposed to be dried when the mass value is stable within 10 w/w%. However, at this temperature in dry air, the sample became yellow then brown. This is caused by a partial degradation of this material, which induces mass change. This phenomenon limits the accuracy and relevance of the test. For this reason, the reference mass of a sample ( $m_{ref}$ ) was measured when it is in stabilised storage conditions, after 24 h at 50 RH% and 23 °C, rather than in dry conditions.

## 2.3 Surface characterisation

### 2.3.1 Scanning Electron Microscopy (SEM) observations

Surface and cross views of specimens were characterized by optical and Environmental Scanning Electron Microscopy (ESEM) (Quanta 200 FEI, Hillsboro, Oregon, USA) device equipped with an Everhart-Thornley Detector.

#### 2.3.1.1 Environmental Scanning Electron Microscopy (ESEM)

The microscope used in this work was an Environmental Scanning Electron Microscope, which performs observation of samples in environmental condition by controlling the temperature and pressure (and consequently the  $RH$  value). The samples did not require any preparation and can be observed conserving their water content.

This particularity was also used for modifying the  $RH$  value of the chamber during an observation. For that purpose the temperature was changed from -5 °C to 60 °C using a Peltier plate as well as the applied pressure (from 133 Pa to 1070 Pa) at the thermoelectric stage. Some examples of couples of pressure and temperature used in this work, and the corresponding  $RH\%$  value are given in Table 13.

Table 13 Pressures and temperatures applied in the ESEM and the corresponding *RH%*

Pressure (Pa)	Temperature (°C)	<i>RH%</i>
533	0.9	100
1070	24.8	40
667	24.8	20
133	24.8	< 5

### 2.3.1.2 BackScattered Electrons detection (BSE)

The ESEM was equipped with a BackScattered Electrons detection (BSE). This device generates a high energy electron beam that reflects out of the sample detection volume. The peculiarity is that the heavy elements backscatter the incident electrons more strongly than the light elements. Consequently, elements with a high atomic number ( $Z$ ) appear brighter on the image [Hirano *et al.*, 1997]. In this study, this technique created contrast in the picture between the platinum ( $Z = 78$ ) and the other elements existing in the fuel cell core, namely: carbon ( $Z = 6$ ), oxygen ( $Z = 8$ ), fluorine ( $Z = 9$ ) and sulphur ( $Z = 16$ ).

### 2.3.2 Surface Roughness

The roughness is also estimated using the Alicona InfiniteFocus (Alicona, Alicona Imaging GmbH, Raaba, Austria). It is an optical system used for dimensional measurements, surface analysis and characterisation. It builds a three-dimensional view of the surface of a sample from a stack of images. It is typically used for paper and printing topography measurements [Vernhes *et al.*, 2009], semiconductor characterisation [Rosle *et al.*, 2010], or in anthropology and archaeology fields [Bello *et al.*, 2009]. It allows measurement of textures and profiles, according to ISO 25178.

### 2.3.3 Surface wettability

The surface wettability is the ability of a surface to be covered by a liquid. In this work, this characteristic is evaluated by contact angle measurement.

Measurement of drops contact angle on substrates has several purposes. Firstly, the affinity between a liquid and a substrate was quantified by the contact angle made by the liquid on the substrate. Indeed, a contact angle under  $90^\circ$  shows the wetting or spreading of the liquid on the substrate, and the affinity is qualified as good, whereas above  $90^\circ$ , the liquid tends to forms droplets on the surface and the affinity is poor. Secondly, it makes possible the calculation of the polar and dispersive contributions of surface energy of the tested substrate. For that matter, the Owens-Wendt theory was used. It relates the Young's contact angle of drop liquid to the polar and dispersive contributions of the

surface tension of the liquid and of the surface energy of the substrate (Equ. 15). Introduction to this topic based on literature is regards in appendix 3.

$$\gamma_L (\cos \theta + 1) = 2 \left( \sqrt{\gamma_L^p \cdot \gamma_S^p} + \sqrt{\gamma_L^d \cdot \gamma_S^d} \right) \quad \text{Equ. 15}$$

Where  $\gamma_L$  is the surface tension of the tested liquid,

$\theta$  is the apparent contact angle of the liquid droplet,

$\gamma_L^p$  is the polar contribution of the surface tension of the tested liquid,

$\gamma_S^p$  is the polar contribution of the surface energy of the substrate surface,

$\gamma_L^d$  is the dispersive contribution of the surface tension of the tested liquid,

$\gamma_S^d$  is the polar dispersive of the surface energy of the substrate surface.

Seven liquids were tested on the substrate, their contact angles were measured and their polar and dispersive contributions were known. Consequently, it was possible to estimate the polar and dispersive contributions of the surface energy of the substrate.

For testing Nafion<sup>®</sup> samples, which is very sensitive to contact with liquid, a specific device had been designed (Figure 26). It maintains small strips of 15 mm wide during the tests. The strip was hold by two jaws, with a length available for testing about 40 mm. Before locking the second jaws, a 20 g mass was hung at one extremity of the specimen to apply the same axial load on each tested sample. Thanks to that device, the samples were hung but can freely deform or swell if necessary. The GDL is composed of very stable materials. Consequently, the samples were fixed using a double sided tape onto a flat and smooth surface before their surface were tested.

The surface of test was placed under the needle tip of a syringe which deposited 2  $\mu$ L liquid droplets at the centre of the sample. A goniometer gave the measure of the initial contact angle of the 2  $\mu$ l drop of probe solvents. The advancing contact angle of the droplets was measured with the optical contact measuring system (OCA 5, Dataphysics Instruments GmbH, Filderstadt, Germany) [Kwok *et al.*, 1997]. The device provides a  $\pm 0.2^\circ$  reading accuracy and acquired data at a rate of eight pictures per second. Then, side views of the drops were extracted from the movie to estimate the chosen parameters.

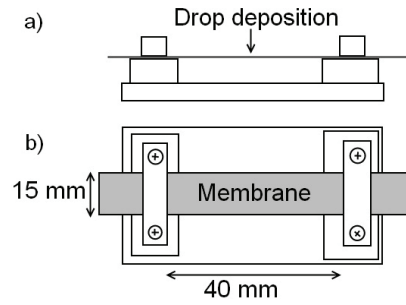


Figure 26 a) side and b) top views of the device that holds the membrane specimens during wetting tests

## 2.4 Bulk characterisation

### 2.4.1 Substrate thickness

The thickness of the samples was measured with a micrometer Lhomargy MI20 by applying a 100 kPa pressure on a 1 cm disk surface, with a  $\pm 0.5\%$  accuracy, according to the paper standard method ISO 534:2005. The thickness is given in micrometer ( $\mu\text{m}$ )

### 2.4.2 Gas Diffusion Layer permeability

As detailed in Figure 27, the Bendtsen device evaluates the permeability of the sample by measuring the air flow passing through a  $10\text{ cm}^2$  surface of substrate under a constant air pressure of 1.47 kPa (ISO 5636-3:1992). The testing ring applied a 98.1 kPa pressure on the sample.

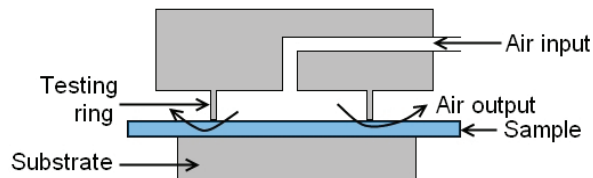


Figure 27 Cross view of the Bendtsen device measurement head

Thanks to the Darcy Law (Equ. 16), the permeability parameter  $K$  ( $\text{m}^2\text{ s}^{-1}\text{ Pa}^{-1}$ ) was calculated using the substrate thickness.

$$Q = K \cdot S \cdot \frac{\Delta P}{T} \quad \text{Equ. 16}$$

The  $K$  parameter ( $\text{m}^2\text{ s}^{-1}\text{ Pa}^{-1}$ ) indicates the intrinsic permeability of  $1\text{ m}^3$  of sample crossed by an air flow at a constant relative applied pressure. Thus,  $Q$  is the volumetric air flow ( $\text{m}^3\text{ s}^{-1}$ ) that crosses surface  $S$  ( $\text{m}^2$ ) of a sample having a thickness  $T$  (m), under applied pressure  $\Delta P$  (Pa).

### 2.4.3 Catalyst layer permeability

The intrinsic permeabilities  $K$  of the GDL and GDE ( $K_{GDL}$  and  $K_{GDE}$ ) were deduced from the volumetric flows  $Q$  obtained by Bendtsen apparatus and thickness  $T$  measurement by micrometer. Using the Darcy law (Equ. 16), the air flow resistance  $R$  was defined as the ratio of the sample thickness  $T$  by the sample surface that was crossed by the air flow and the  $K$  parameter. The calculation of the  $R_{GDE}$  or  $R_{GDL}$  is given in Equ. 17 (where letter  $a$  corresponds to either GDL or CL)

$$R_a = \frac{T_a}{K_a} \quad \text{Equ. 17}$$

Considering a multilayer as a stack of two components: the GDL and the catalyst layer, the sum of the air flow resistances of each component ( $R_{GDL}$  and  $R_{CL}$ ) was equal to the global air flow resistance  $R_{GDE}$  (Equ. 18).

$$R_{GDE} = R_{GDL} + R_{CL} \quad \text{Equ. 18}$$

The intrinsic permeability of the catalyst layer  $K_{CL}$  was obtained combining Equ. 17 and Equ. 18 in Equ. 19.

$$\frac{T_{CL}}{K_{CL}} = \frac{T_{GDE}}{K_{GDE}} - \frac{T_{GDL}}{K_{GDL}} \quad \text{Equ. 19}$$

The  $K_{CL}$  values were obtained thanks to the volumetric air flow values through the GDE ( $Q_{GDE}$ ) and the GDL ( $Q_{GDL}$ ) using Equ. 20 that combines Equ. 16 and Equ. 19.

$$K_{CL} = \left( \frac{Q_{GDE} \cdot Q_{GDL}}{Q_{GDE} - Q_{GDL}} \right) \cdot \frac{T_{CL}}{\Delta P \cdot S} \quad \text{Equ. 20}$$

This parameter makes it possible to compare different catalyst layer structures independently of the thickness of the deposit. The uncertainties in  $K_{CL}$  determination are given in Appendix 4.

## 2.5 Evaluation of the printing quality

### 2.5.1 Platinum loading quantification

The platinum loading of catalyst layers was determined by the measure of the mass of the substrate sample before and after printing, when the catalyst layer was completely dried. The minimum time between the printing stage and the second weighing was 24 h.

### 2.5.2 Surface covered by the ink

SEM observations using the BSE device measure the ink coverage onto the substrate. The ink deposition on Nafion<sup>®</sup> membranes was also quantified by the measurements of the ink coverage  $X\%$ . It is performed using an image treatment procedure which consisted of:

- scanning (Ricoh, Tokyo, Japan) an image of the specimens' surface in 8-bit coded grey levels,
- binarising this image using a threshold (IsoData threshold filter),
- and calculating the ratio of printed and non-printed zones.

This procedure was carried out using the software ImageJ<sup>®</sup> (U.S. National Institute of Health, Bethesda, USA).

A second parameter is the number of defects per unit of surface appearing onto a printed sample. This value was estimated by counting the number of defects exhibited by ten samples. Then the total of defects was divided by the total printed surface of all the samples.

### 2.5.3 Optical density values

The optical density (*OD*) was measured using a GretagMac Beth, C 19 densitometer (X-rite, Grand Rapids, USA). The *OD* is the logarithm of the ratio between  $I_R$  retrodiffused part and  $I_0$  incident part of the light, which depends on the wavelength  $\lambda$  (Equ. 21).

$$OD(\lambda) = -\log\left(\frac{I_R(\lambda)}{I_0(\lambda)}\right). \quad \text{Equ. 21}$$

The lower the retrodiffused part of the incident light intensity, the higher the optical density and the darker the surface is visually experienced.

Geometric conditions of the C 19 densitometer are described in ISO 5-4:2009 (45/0 or 0/45) and the spectral conditions in ISO 5-3:2009. For reflexion density, incandescent tungsten illumination (standard illuminant A) and status E were used respectively to illuminate the material and select the spectral response. In this study, as deposited inks contain carbon powder particles that were opaque, an increase in optical density indicated higher in thickness of the deposited ink layer. The device was calibrated using the GDL as blank.

### 2.5.4 Spectroscopy

The reflectance spectra of catalyst layers were measured with an i1 Pro spectrophotometer (X-Rite, Grand Rapids, USA). The reflectance values were measured from 380 to 730 nm, with a 10 nm step, with 45°/0° ring illumination optics.

The measurements were performed with an illuminant D50 and a 10° observer, on a surface of a 6.0 mm disk. Before each test, this device was calibrated with a ceramic tile based on barium sulphate according to DIN 5033 and then each catalyst layer was characterised ten times. For each transfer number, five samples were printed. The results

presented are the average of five measurements performed on each of the five samples with constant printing parameters.

### 2.5.5 Ink intrinsic reflectance and optical density

The intrinsic reflectance ( $R_{\infty}$ ) and the intrinsic optical density values of the inks ( $OD_{\infty}$ ) were evaluated on a sample made by depositing a substantial quantity of ink on a substrate. In this study, the inks were coated on a GDL by scraping the ink at 0.5, 1, 1.5 and 2 mm from the substrate. The reflectance spectrum, the optical density and the thickness were then measured on the dried deposit that was transferred on GDL. The measurements were performed until there was no significant variation of the reflectance and optical density with regard to the deposit thickness.

## 2.6 Electrochemical characterisation

### 2.6.1 Catalyst layers electrochemical properties

The catalyst layer performances were characterised with a 25 cm<sup>2</sup> fuel cell. The tested catalyst layer was placed as a cathode, then:

- when a CCB had to be tested, a standard catalyst layer made by CCB using blade coating was placed as anode and a membrane (Nafion<sup>®</sup> 212 or 112) separate both electrodes,
- when a CCM had to be tested, it was placed between a SGL 24 BC and a standard catalyst layer made by CCB using blade coating was placed as anode.

The multilayer was hotpressed at 135°C with a pressure of 30 kg for 3 min, then at 980 kg for 3 other min. The MEA was placed between two gaskets and inserted between two bipolar plates. Humidified hydrogen and air are fed into the cell at 50 RH%. The test was carried out at a cell temperature of 80 °C and at pressure of 1.5 Bar.

Electrochemical characterisation was carried out by Cyclic Voltammetry (CV) and Electrochemical Impedance Spectroscopy (EIS) using a BioLogic VMP2B apparatus.

### 2.6.2 Cyclic voltammetry (CV)

In Cyclic voltammetry, the inert gas Nitrogen fed the tested electrode; hydrogen fed the other electrode. Increasing and decreasing ramps of potential were linearly applied as a function of time on the system and the faradic current in response was measured.

### 2.6.3 Electrochemical Surface Area (ECSA)

The voltammograms are used for calculating Electrochemical Surface Area (ECSA) [Hu *et al.*, 2006]. ESA was determined by integration of the adsorption peak of the hydrogen using  $210 \mu\text{C cm}^{-2}_{\text{Pt}}$  as a conversion factor. A Fuel Con - Evaluator-C test station was used. The scanning speed is equal to  $50 \text{ mV s}^{-1}$  from 50 to 800 mV.

### 2.6.4 Electrochemical Impedance Spectroscopy (EIS)

EIS characterises the different phenomena that take place on the running cathode catalyst layer [Bultel *et al.*, 2002; Pozio *et al.*, 2002; Franco *et al.*, 2007]. Impedance was measured and diagrams were plotted. Redox reactions are commonly modelled by resistor / capacitor in parallel equivalent circuits. The impedance diagram of such a circuit without mass-transfer limitation is a Nyquist diagram representing the opposite of the imaginary part of the impedance as a function of the impedance modulus. It forms a semicircular curve with a diameter equal to the equivalent resistance of the system. At higher frequencies, the interfacial charge-transfer resistance and the catalyst layer properties are highlighted. At lower frequencies, the gas transport limitations in the gas diffusion layer are determined. The test conditions were  $80^{\circ}\text{C}$ , 50 RH%, at 1.5 Bar, fed by hydrogen and air at a stoichiometry of 1.2/2. The applied current amplitude was equal to 100 mA for applied currents of 1 and 2 A, then 200 mA for higher currents.

### Conclusion of chapter 2

The different materials and methods described in this chapter were used in the following experimental chapters. Table 14 detailed the chapter(s) in which the materials and methods previously described were used.

Table 14 Summary of the main material and methods

Material and or methods/measured parameter	Experimental chapter(s)
Micrometer/thickness measurement	3, 4 and 5
Bendtsen/air flow and permeability measurement	4
Varidim and Varimass/Hydroexpansion	3
SEM, ESEM, BSE/visual observations	5
Alicona/surface topography	4
Goniometer/advancing contact angle	3 and 4
Immersion in water/sample preparation	3
Flexography/catalyst layer deposition	3, 4 and 5
Mass measurement/ink, Nafion <sup>®</sup> and Platinum loading	4 and 5
ImageJ/surface area of ink	3 and 4
Densitometer/optical density	3 and 5
Spectrometer/reflectance	5
Polarisation curves/performances	3, 4 and 5
Cyclic voltammetry/Electrode surface area	4 and 5
Electrochemical impedance spectroscopy/mass and transfer limitations	4 and 5

# Chapter 3

## Catalyst Coated Membrane



<b>INTRODUCTION .....</b>	<b>91</b>
<b>1 PROTON EXCHANGE MEMBRANE CHARACTERISATION .....</b>	<b>93</b>
1.1 WATER UPTAKE .....	93
1.2 HYGROEXPANSION OF THE MEMBRANE .....	94
1.2.1 <i>Hygroexpansion in the thickness direction</i> .....	94
1.2.2 <i>In the plane directions</i> .....	96
1.2.2.1 Membrane hygroexpansion evaluation when applying a step of RH% .....	96
1.2.2.2 Membrane hygroexpansion when applying a complete characterisation cycle .....	97
1.2.2.3 Membrane anisotropy .....	99
1.2.2.4 Influence of the number of cycles applied on the membrane on its dimensional variations 101	
1.2.2.5 Membrane ageing.....	103
1.3 CONCLUSION.....	105
<b>2 IMPROVEMENT OF THE MEMBRANE PRINTABILITY .....</b>	<b>107</b>
2.1 MEMBRANE BEHAVIOUR WHEN DEPOSITING WATER DROPS .....	108
2.1.1 <i>Apparent contact angle of water drops</i> .....	110
2.1.2 <i>Membrane elevation under water drops</i> .....	111
2.2 NAFION <sup>®</sup> DIMENSIONAL RESPONSE TO MODEL INK DROPS DEPOSITION.....	112
2.2.1 <i>Apparent contact angle of ink drops</i> .....	112
2.2.2 <i>Membrane elevation under ink drops</i> .....	113
2.3 MEMBRANE BEHAVIOUR IN CONTACT WITH WATER AND INK .....	113
2.3.1 <i>Evolution of the apparent contact angle of water drops with the immersion duration and time</i> .....	113
2.3.2 <i>Blistering phenomenon in the case of the deposition of water drops</i> .....	116
2.4 INTERACTIONS BETWEEN NAFION <sup>®</sup> MEMBRANE AND THE WATER-BASED INK .....	117
2.5 AGEING OF THE PRE-TREATED MEMBRANES .....	117
2.6 MEMBRANE PRINTING .....	119
2.6.1 <i>Evaluation of the membrane printability</i> .....	119
2.6.2 <i>Electrochemical characterisation of printed catalyst layers</i> .....	121
2.7 CONCLUSION.....	122
<b>CONCLUSION OF CHAPTER 3 .....</b>	<b>124</b>



## Introduction

As detailed in Chapter 1, the Catalyst Coated Membranes (CCMs) are generally made using the decal process: the catalyst layer is firstly deposited onto an aluminium foil or a PTFE cloth, and then transferred by hot pressing onto the proton exchange membrane. However, limitations were described, such as the lower performances and the poor interfacial properties compared to direct CCM [Prasanna *et al.*, 2004; Tang *et al.*, 2007a; Thanasilp *et al.*, 2010]. Despite of these limitations, the decal process is still used because it has the major advantages to overpass a significant problem occurring when using the membrane for direct catalyst layer deposition: the membrane instability in contact with liquids.

In the present study, the goal was to produce catalyst layers by a direct CCM protocol using the flexography process. The membrane used in the present study was Nafion<sup>®</sup> 212. It is a perfluorosulfonic acid/PTFE copolymer membrane which is obtained by dispersion-casting (DuPont<sup>™</sup>, Wilmington, USA). It has a thickness of 51  $\mu\text{m}$ , an equivalent weight of 1100 g of polymer per mol of sulfonic acid groups and a basis weight of 100  $\text{g}/\text{m}^2$  [Sahu *et al.*, 2009].

The methods for achieving proper catalyst layers by direct CCM is described in Figure 28.

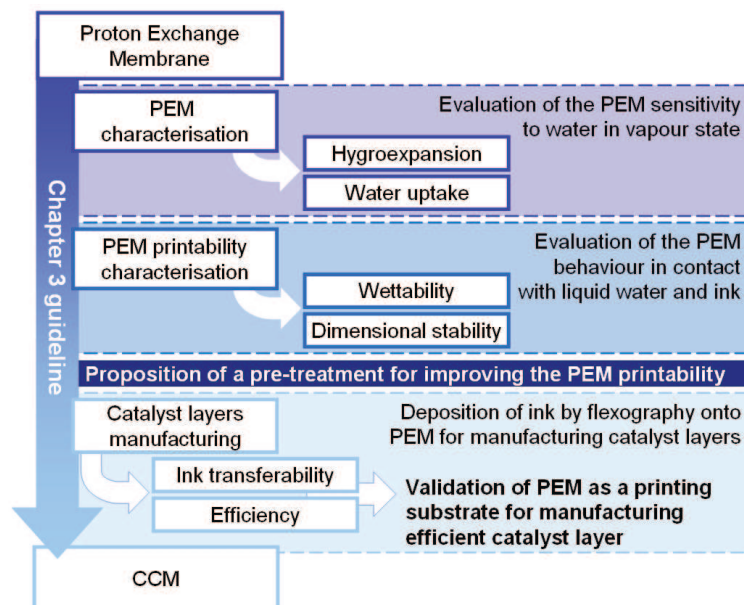


Figure 28 Guideline of chapter 3

The first step for achieving CCM was to characterise the printability of the membrane. The printability describes the interrelationships between a substrate (the membrane) and a

liquid (namely the printing ink). The factors affecting the printability of the substrate include surface properties (surface energy, roughness...) as well as structural properties (thickness, porosity, permeability to gas and liquids, mechanical properties, dimensional stability...). Printability is often associated to runnability, or how a substrate behaves during the printing process.

In the first part, the influence of vapour onto the membrane properties is focused. Then, the ability of the Nafion<sup>®</sup> to swell, curl and deform in contact with water and its hydrophobicity was quantified. The dimensional stability and the wettability of water and water-based inks onto the membrane surface were characterised.

A solution was proposed for improving the membrane printability. The impact of the treatment on the printability was measured. Finally, electrochemical tests were performed on the catalyst layers manufactured by direct CCM by flexography using this new protocol.

## 1 Proton exchange membrane characterisation

The Nafion<sup>®</sup> is very sensitive to atmospheric changes (especially humidity). To limit contacts with its environment, the membrane is supplied in roll packaging, positioned between a coversheet and the backing film on which it was produced. However, the protective films have to be removed before printing and testing. That is why the temperature and *RH%* conditions were controlled when using Nafion<sup>®</sup> samples.

In this part, the sensitivity of the membrane to the room conditions was studied. The temperature was set to 23°C. The experimental approach focused on the impact of the *RH%* conditions on the membrane properties: the water uptake (1.1) and the hygroexpansion (1.2). Thereafter, some tests were performed on the ageing of the membrane (1.2.2.5).

### 1.1 Water uptake

Mass variations of a Nafion 212 sample as a function of *RH%* is shown on Figure 29. The experiment imposed sorption from 10 to 85 %*RH* and desorption from 85 to 0 %*RH*.

The water uptake as well as the  $\lambda$  factor (number of water molecules by sulfonic acid group that have been gain or loss compared to the sample reference – defined in chapter 2, sections 2.1.5) were calculated.

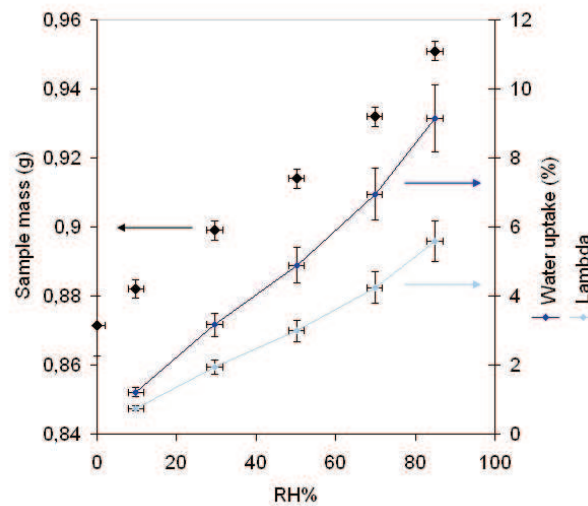


Figure 29 Mass, water uptake and lambda ( $\lambda$ ) of a sample from 0 (dried in oven) to 85 *RH%* (measured from 10 to 85 *RH%* in Varimass)

The mass of the sample varied from  $0.871 \pm 0.009$  mg (dried weigh), to  $0.882 \pm 0.003$  mg at 10 *RH%* and to  $0.951 \pm 0.003$  g at 85 *RH%*. The water mass gain was about  $8.0 \pm 0.8$  mg from dried to 85 *RH%*. The water uptake and the factor  $\lambda$  reached  $9 \pm 1$  w/w % and

$5.6 \pm 0.6$  at 85 *RH%*. As water uptake (w/w %) and the factor  $\lambda$  do not depend on the initial sample mass, they are comparable with literature results.

Such curves that represent the water uptake and the factor  $\lambda$  as a function of the *RH%* value was already described in the literature [Colette *et al.*, 2009]. This author also detailed that the initial part, from 0 to 30 *RH%*, was related to the absorption of water molecules on the polar ionic groups of the polymers (especially the sulfonic acid groups). Then, the intermediate zone, from 30 to 70 *RH%*, was governed by diffusion mechanisms. In the final part, from 70 *RH%*, the water molecules formed water clusters into the polymer.

Several authors described mechanisms occurring in the Nafion<sup>®</sup> membrane that induces structural modifications [Macknight *et al.*, 1974; Hsu *et al.*, 1983 and Gebel, 2000]. The relation between the factor  $\lambda$  and the Nafion<sup>®</sup> structure was modelled by Hofmann *et al.* [2009]. In the case of a Nafion<sup>®</sup> membrane with an Equivalent Weight (EW) equal to 1087  $\text{gmol}^{-1}$ , a  $\lambda$  inferior to 6 is considered as typical to a structure with isolated water domains (or clusters).

The variations of the *RH%* from 0 to 85 % induces an absorption of water molecules until  $9 \pm 1$  w/w %, which indicated the presence of isolated water clusters from 70 *RH%*. It shows that the chosen conditions of *RH%* have a measurable impact on the mass of the Nafion<sup>®</sup> 212 samples. Consequently, this method is suitable for evaluating the hygroexpansion of the Nafion<sup>®</sup> 212, the related results are given thereafter.

## 1.2 Hygroexpansion of the membrane

The modifications of the water content of the membrane samples could induce inducing structural changes of the membrane and dimensional variations both in the thickness (1.2.1) and in the plane directions (1.2.2) of the tested samples.

### 1.2.1 Hygroexpansion in the thickness direction

The Nafion<sup>®</sup> 212 thickness given by Dupont data is equal to 50.8  $\mu\text{m}$ . However, environmental conditions may influence this value. That is why the hygroexpansion of Nafion<sup>®</sup> 212 in the thickness dimension was evaluated under *RH%* varying from 10 to 85 *RH%* in the Varidim device. A micrometer was placed under controlled conditions, and was used for measuring the thickness of membrane samples as a function of the *RH%* value (Figure 30).

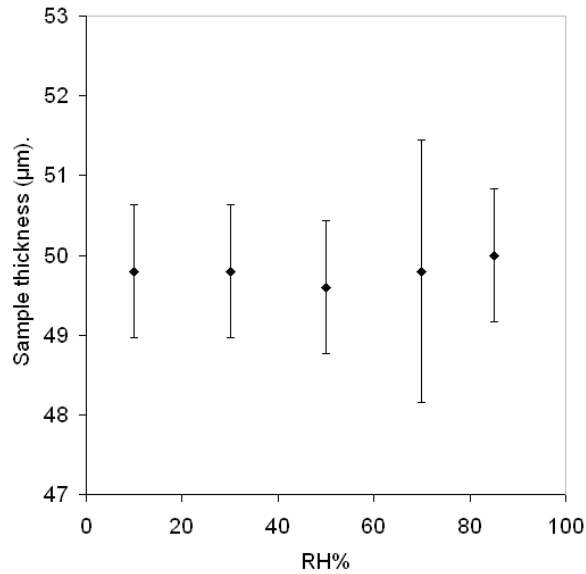


Figure 30 Thickness as regards to the  $RH\%$

Whatever the  $RH\%$ , no significant variation of thickness was measurable when taking into account the uncertainty of the method. At 10  $RH\%$  the thickness was equal to  $49.8 \pm 0.8 \mu\text{m}$  and at 85  $RH\%$  it reached  $50.0 \pm 0.8 \mu\text{m}$ . This method had a limitation: the 100 kPa stress applied on the sample could have compressed the membrane, which could have hidden the thickness variations.

As a complement, ESEM was used for applying four  $RH\%$  values, 100, 40, 20 and 5 to a Nafion<sup>®</sup> sample by a method described in chapter 2. The cross view of the sample was recorded as a function of the time and of the ESEM conditions. Selected observations are presented in Figure 31.

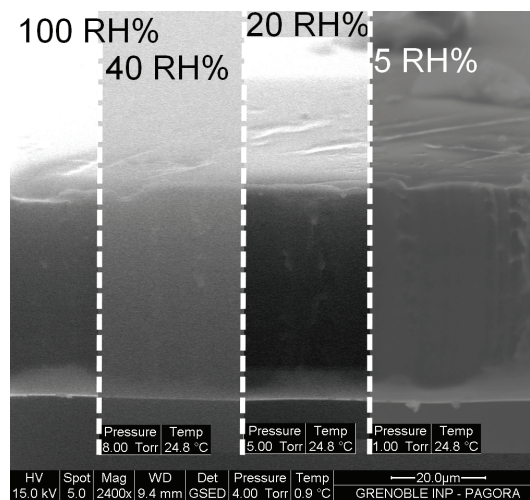


Figure 31 Cross views of a Nafion<sup>®</sup> 212 sample after at least 1 min at 100, 40, 20 and 5  $RH\%$

The thickness of the sample presented in Figure 31 was estimated equal to  $45.3 \pm 0.6 \mu\text{m}$  at 100  $RH\%$  and reaches  $45.1 \pm 0.7 \mu\text{m}$  at 5  $RH\%$ . No measurable thickness value

variations were obtained during this test. However, the value measured is about 5  $\mu\text{m}$  lower than expected; it is possible that the sample is not strictly perpendicular to the electron beam. This could have limited the thickness variation measurement.

Finally, considering the application, the measurement accuracy was sufficient and the Nafion<sup>®</sup> 212 thickness was supposed to be stable from 10 to 85 *RH%* and equal to  $49.8 \pm 0.8 \mu\text{m}$ .

### 1.2.2 In the plane directions

In the plane directions, the hygroexpansion was evaluated by applying:

- a step (1.2.2.1),
- a characterisation cycle (1.2.2.2),
- five characterisation cycles (1.2.2.4),
- and an ageing cycle (1.2.2.5).

The experiments were performed on a batch of ten 100 mm long ( $L_0$ ) 15 mm wide samples, which were tested together into the Varidim chamber. The values presented in the following parts are obtained by averaging the values of the ten samples.

#### 1.2.2.1 Membrane hygroexpansion evaluation when applying a step of *RH%*

Figure 32 shows the time variation of the length expansion ( $\Delta L$  ( $\mu\text{m}$ )) of the samples when applying a *RH%* variation. Here, *RH%* varied from 50 to 70 *RH%* as a function of the time.

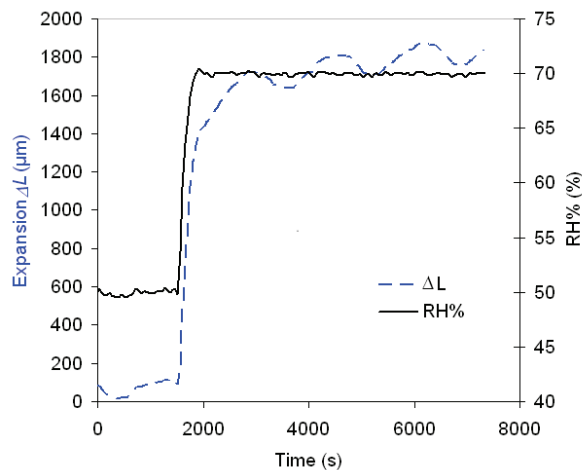


Figure 32 Example of  $\Delta L$  ( $\mu\text{m}$ ) of a Nafion<sup>®</sup> 212 sample as a function of the time (s) when the conditions varies from 50 to 70 *RH%*

The average expansion of ten samples was about  $1700 \pm 100 \mu\text{m}$  when the *RH%* varied from 50 to 70 %.

This result showed that the proposed experimental method based on  $RH\%$  variations was relevant for measuring the hygroexpansion of the Nafion® 212 membrane.

### 1.2.2.2 Membrane hygroexpansion when applying a complete characterisation cycle

Deeper studies were performed on the Nafion® 212 hygroexpansion by applying a complete cycle of characterisation on ten samples. As detailed in Chapter 2, in section 2.1.4, a characterisation cycle was composed of nine steps: 50, 30, 10, 30, 50, 70, 86, 70 and 50  $RH\%$ , lasting 90 min each. The average strain (%) values of the membrane samples and the  $RH\%$  values as a function of the time (h) are described in Figure 33.

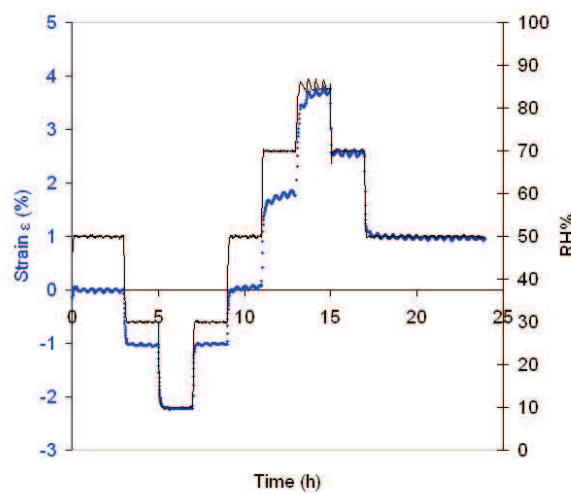


Figure 33 Strain (%) and  $RH\%$  as a function of time (h) during a characterisation cycle

As in Figure 32, at each setting change, the strain variations followed the  $RH\%$  variations. However, slight differences appeared:

- from 0 to 7 h, from 50 to 10  $RH\%$ , then from 10 to 30  $RH\%$ , the strain variations were very similar to the  $RH\%$  variations, and both rapidly reached a plateau, like a decreasing and increasing step-function,
- from 7 to 15 h, from 30 to 85  $RH\%$ , the  $RH\%$  variations are still as fast as before. The stabilisation of the strain values seems to be slower. Noticed that, at 85  $RH\%$  the regulation seems unstable.
- from 15 to 20 h, from 85 to 50  $RH\%$ , the  $RH\%$  variations followed the same trend as before. The strain stabilisation looks faster, similarly to those occurring from 0 to 7 h.

These observations show that the membrane samples were less able to sorb than to desorb water.

In order to avoid the device influences on the membrane dimensional variations, the stabilised values of strain were considered as shown in Figure 34.

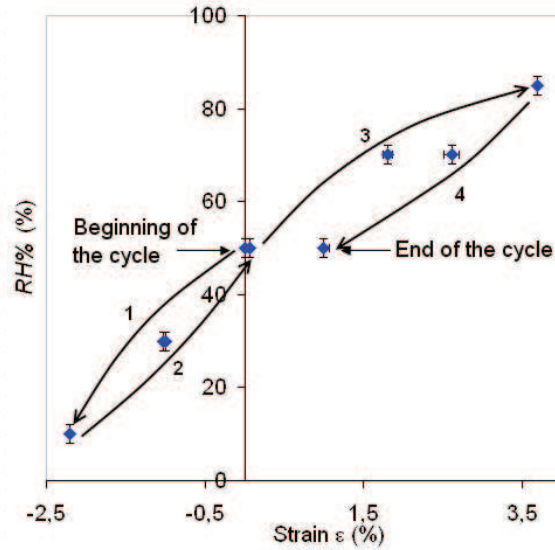


Figure 34 Strain (%) as a function of the  $RH\%$  varying from 10 to 85% (the lines are plotted between the dots for a better understanding of the figure, but they have not physical meaning)

This graph is typical of the hygroexpansion of materials like paper or paperboard, with the  $RH\%$  as a function of strain in % of stabilised samples. As detailed in Chapter 2, the samples reference dimensions were measured when the samples were stabilised at the end of the first step (at 50  $RH\%$ ). In this figure, the dot referred as the beginning of the cycle represents a strain equal to zero.

The hygroexpansion curve in Figure 34 is split into four main parts:

1. when the  $RH\%$  varied from 50 to 10  $RH\%$ , the samples length showed an average decrease of  $-2.20 \pm 0.01 \%$ .
2. when the  $RH\%$  rose 50 % again, the strain, equal to zero at the beginning of the cycle, reached  $0.07 \pm 0.03 \%$ . Consequently, the decrease in the  $RH\%$  value until 10 % led to an irreversible deformation of  $0.07 \pm 0.03 \%$ .
3. the  $RH\%$  rose to 85 %, and the samples strain raised to  $3.69 \pm 0.03 \%$ . Higher  $RH\%$  values impacted more the dimensional variations than the lower  $RH\%$ .
4. finally, when the  $RH\%$  setting came back to 50 %, the samples strain was equal to  $0.99 \pm 0.07 \%$ . The increase in the  $RH\%$  from 50 to 85% led to an irreversible strain of  $0.95 \pm 0.07 \%$ .

As a conclusion, the  $RH\%$  cycle applied onto Nafion<sup>®</sup> samples induced an irreversible strain equal to  $1.00 \pm 0.07 \%$ . The low  $RH\%$  values had a slight impact on the dimensional variations ( $-2.20 \pm 0.01 \%$ ) and on the irreversible strain ( $0.07 \pm 0.03 \%$ ) of

the samples, while the higher  $RH\%$  led to higher strain ( $3.69 \pm 0.03 \%$ ) and caused major irreversible strain ( $0.95 \pm 0.07 \%$ ).

### 1.2.2.3 Membrane anisotropy

The tests presented in the previous section 1.2.2 were performed on membrane strips, bars  $15 \times 100$  mm in dimension, that were sampled with their length parallel to the membrane cylinder unreeling. Considering the membrane manufacturing, the unreeling direction of the cylinder corresponds to the direction of production of the membrane, also called Machine Direction (MD). Three other directions were chosen for testing the impact of sample directions on the sample behaviour under  $RH\%$  variations as described in Figure 35.

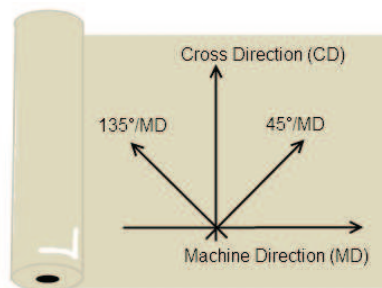


Figure 35 Machine Direction (MD), Cross Direction (CD) and intermediate directions ( $45^\circ$  and  $135^\circ$  compared to the MD) of sampling into the membrane roll

Indeed, when materials are manufactured by web process, such as paper or extruded polymer, the components may have a preferential orientation that leads to anisotropic properties. For example, Nafion<sup>®</sup> 112, 115 and 117, made by extrusion casting, showed preferential direction of conductivity [Soboleva *et al.*, 2008] or swelling [Blumenthal *et al.*, 1996].

Dupont<sup>™</sup> data on the Nafion 212 gave physical properties (tensile strength, elongation to break...) that had low variations as regards to the direction (DuPont<sup>™</sup> Nafion<sup>®</sup> PFSA Membranes description). Thereafter the anisotropy of the Nafion<sup>®</sup> 212 was deeply investigated by  $RH\%$  cycling. For that purpose, sampling was performed in the four main directions: MD,  $45^\circ/MD$ , CD and  $135^\circ/MD$  as described in Figure 35. In Figure 36, the  $RH\%$  values are plotted as a function of the strains reached by the four types of samples.

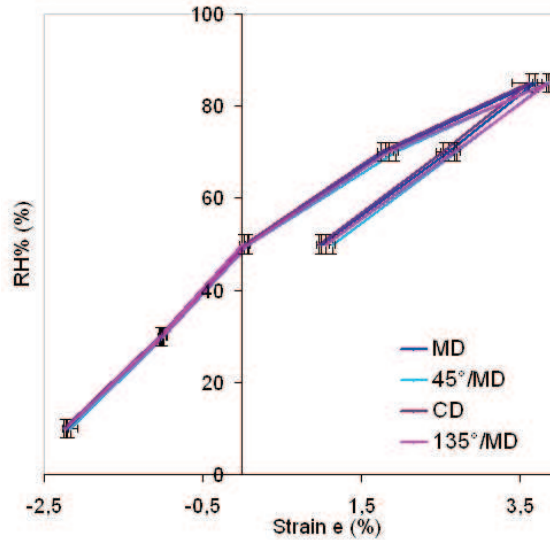


Figure 36 *RH%* cycling of membrane samples as a function of the strain for different sampling directions (the lines are plotted between the symbols for a better understanding of the figure, but they have not physical meaning)

The samples with the 45°/MD, CD and 135°/MD directions had similar behaviour than those of the samples cut in the machine direction (MD) detailed in the previous section. Some differences appear at high *RH%* value, especially at 85 *RH%*. The strains values are detailed in Table 15 for different sampling directions and *RH%* values.

Table 15 Strain values of samples as a function of their sampling directions at different *RH%*

<i>RH%</i>	MD strain (%)	45°/MD strain (%)	CD strain (%)	135°/MD strain (%)
50 % (reference)	0	0	0	0
30 %	-1.024 ± 0.006	-0.99 ± 0.03	-1.056 ± 0.004	-1.03 ± 0.01
10 %	-2.203 ± 0.004	-2.164 ± 0.08	-2.257 ± 0.004	-2.23 ± 0.03
30 %	-0.999 ± 0.001	-0.99 ± 0.05	-1.032 ± 0.002	-0.99 ± 0.02
50 %	0.07 ± 0.03	0.08 ± 0.01	0.018 ± 0.05	0.07 ± 0.01
70 %	1.807 ± 0.06	1.94 ± 0.02	1.75 ± 0.05	1.85 ± 0.04
<b>85 %</b>	<b>3.69 ± 0.03</b>	<b>3.84 ± 0.06</b>	<b>3.6 ± 0.2</b>	<b>3.86 ± 0.01</b>
70 %	2.6 ± 0.1	2.71 ± 0.04	2.53 ± 0.08	2.67 ± 0.03
<b>50 %</b>	<b>0.99 ± 0.07</b>	<b>1.14 ± 0.03</b>	<b>1.14 ± 0.03</b>	<b>1.05 ± 0.02</b>

At 85 *RH%*, the membranes samples with their main direction in MD, 45°/MD, CD and 135°/ND respectively reached  $3.69 \pm 0.03$ ,  $3.84 \pm 0.06$ ,  $3.6 \pm 0.2$  and  $3.86 \pm 0.01$  %. The strain values were slightly lower in MD and CD as compared to 45°/MD and 135°/MD.

At the end of the cycle, at 50*RH%*, the total irreversible strain for each type of samples is equal to  $0.99 \pm 0.07$ ,  $1.14 \pm 0.03$ ,  $1.14 \pm 0.03$  and  $1.05 \pm 0.02$ . The irreversible strains of 45°/MD and CD samples were scarcely higher than the strains of MD and 135°/MD samples.

Some behaviour differences appeared depending on the sampling. However, the trend described at 85 RH% was different than the trend at 50 RH%. Consequently, it cannot really be expressed that the Nafion<sup>®</sup> 212 dimensional variations occur in a preferential direction.

In sheet fed device or press, like Flexiproof, it is preferable to use the same direction at each printing test in order to maximise the runnability of the Nafion<sup>®</sup> and the reproducibility. In web-press, the anisotropy of the substrate could be neglected because the web is always used in the machine direction of production.

#### 1.2.2.4 Influence of the number of cycles applied on the membrane on its dimensional variations

The previous studies were performed on one cycle of RH% variations. Here, samples were submitted to five RH% cycles. Figure 37 depicts the RH% values as a function of the average strain reached by ten samples cycled five times in the Varidim device.

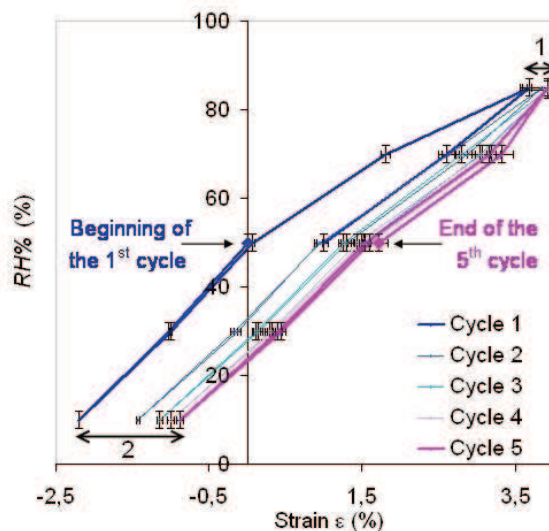


Figure 37 RH% as a function of the strain of samples cycled five times (the lines are plotted between the dots for a better understanding of the figure, but they have not physical meaning)

At a given RH% value, hysteresis phenomenon occurred. Indeed, the more the samples were submitted to cycling, the more the strain value increased. From the beginning of the first cycle to the end of the fifth cycle, an irreversible strain occurred, equal to  $1.75 \pm 0.09$  %. The irreversible strain measured at the end of the first cycle reached  $1.05 \pm 0.07$  % (a comparable value to the one described in section 1.2.2 that reached  $0.99 \pm 0.07$  %). Consequently, the impact on the four following cycles on the irreversible strain was estimated about  $0.7 \pm 0.1$  %.

The impact of the four last cycles on the samples irreversible dimensional variations was lower than the effect of the first cycle. The hysteresis phenomenon progressively diminishes with the number of cycles.

Other noticeable results are the value of the strains at 85 RH%. Indeed, from the first to the fifth cycle, the strains values showed a poorly significant variation (Figure 37.1), equal to  $-0.6 \pm 0.2 \%$ , compared to their variations that occurred at 10 RH% (Figure 37.2), equal to  $1.4 \pm 0.1 \%$ .

For highlighting this observation, the strain values as the function of the total time of the test was plotted in Figure 38. Besides, the values of the average strains reached at 10, 50 and 85 RH% are given in Table 16.

Figure 38 emphasizes the impact of the cycling on the strain values, especially at 10, 50 and 85 RH%. The strains values reached stabilised ones if more cycles were performed on these samples.

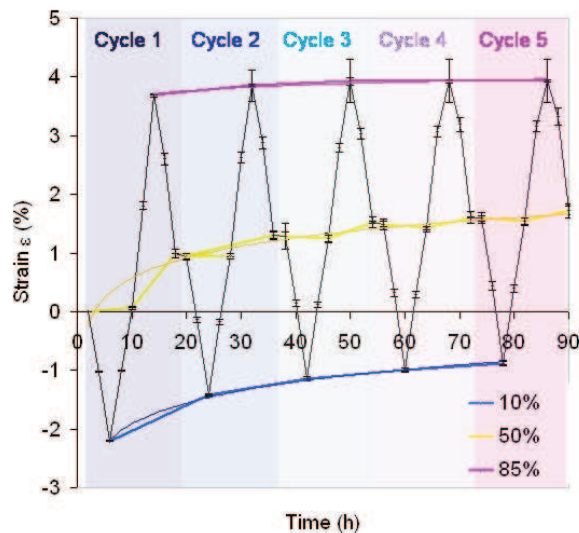


Figure 38 Strain of samples cycled five times as a function of the total time of test (the lines are plotted between the dots for a better understanding of the figure, but they have not physical meaning)

The calculation of the average strain ( $\epsilon_{ave}$ ), the strain amplitude ( $\Delta\epsilon$ ) and the irreversible strain ( $\epsilon_{irr}$ ) for each cycle is given in Table 16.

Table 16 Strain values as regards to the number of applied cycles and related parameters

Cycle	Strain $\epsilon$ (%)			$\epsilon_{ave}$ (%)	$\Delta\epsilon$ (%)	$\epsilon_{irr}$ (%)
	at 10 RH%	at 50 RH%	at 85 RH%			
1	$-2.21 \pm 0.06$	$0.06 \pm 0.03$	$3.8 \pm 0.1$	$0.8 \pm 0.3$	$6.0 \pm 0.2$	$1.05 \pm 0.07$
2	$-1.38 \pm 0.12$	$0.89 \pm 0.33$	$4.0 \pm 0.2$	$1.3 \pm 0.5$	$5.4 \pm 0.4$	$0.4 \pm 0.1$
3	$-1.1 \pm 0.1$	$1.29 \pm 0.09$	$3.09 \pm 0.07$	$1.5 \pm 0.5$	$5.1 \pm 0.4$	$0.2 \pm 0.2$
4	$-1.0 \pm 0.1$	$1.46 \pm 0.09$	$3.24 \pm 0.09$	$1.5 \pm 0.5$	$5.0 \pm 0.4$	$0.1 \pm 0.2$
5	$-0.8 \pm 0.1$	$1.57 \pm 0.09$	$3.4 \pm 0.1$	$1.6 \pm 0.5$	$4.9 \pm 0.4$	$0.1 \pm 0.2$

From the first to the fifth cycle, the average strain varied from  $0.8 \pm 0,3 \%$  to  $1.6 \pm 0.5 \%$ . That demonstrated that the samples were more and more elongated (about  $1.2 \pm 0.5 \%$ ). This value is slightly lower than the irreversible strain equal to  $1.75 \pm 0.09 \%$ . The difference was caused by the difference of calculation of the two parameters: the irreversible strain was the difference between the beginning and the end of a cycle (as shown in Figure 34), while the average strain is the average of the strain at 10 *RH%* and the strain reached at 85 *RH%*. This observation is consistent with the fact that the total average strain was lower than the total irreversible strain.

The strain amplitude decreased about  $1.1 \pm 0.4 \%$ , from  $6.0 \pm 0.2 \%$  to  $4.9 \pm 0.4 \%$ . The sample dimensions were less and less able to vary as cycles went along. Moreover, the strain amplitude reduce from the first to the fifth cycle was comparable to the average strain variation. The hysteresis phenomenon becomes less visible when applying more and more cycles. It could indicate that the material showed similar behaviour when applying *RH%* variations, which suggested that the samples were stabilised after 60 h of cycling.

Further study was performed on the membrane Nafion 212<sup>®</sup> in order to deeply understand the material behaviour when a lot of cycles were applied. It also evaluated the relevance of the “plateau” hypothesis. These tests were consisted in ageing the material and are detailed in the section below.

#### **1.2.2.5 Membrane ageing**

The samples were placed under ageing conditions as detailed in chapter 2. The maximal *RH%* value was fixed at 80 % and the minimal value was equal to 20 %. The average strains of ten stabilised samples, reached at 20 and 80 *RH%* during 80 h, are presented in Figure 39.

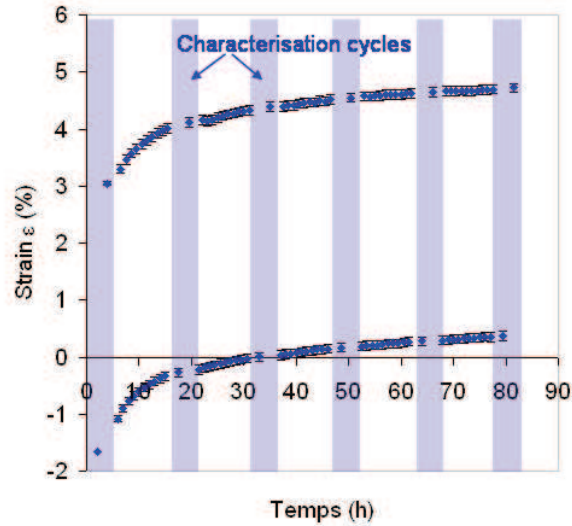


Figure 39 80 h membrane ageing

Similarly to the previous study, at 20 *RH%* and 80 *RH%* the strain increased as a function of time. The ageing test were composed of five characterisation steps, numbered from C1 to C5, each was followed by ten 20 and 80 *RH%* variations. Finally a last characterisation cycle C6 was applied. It led to submit 56 times 20 and 80 *RH%* values to the samples. The strain values at 20, 50 and 80 *RH%* that were reached during the characterisation cycles are given in Table 17.

Table 17 Strain values as regards to the number of applied cycles and related parameters

Characterisation cycle	Strain $\varepsilon$ (%)			$\varepsilon_{ave}$ (%)	$\Delta\varepsilon$ (%)	$\varepsilon_{irr}$ (%)
	at 20 <i>RH%</i>	at 50 <i>RH%</i>	at 80 <i>RH%</i>			
C1	$-1.66 \pm 0.03$	$0.0310 \pm 0.008$	$3.05 \pm 0.05$	$0.7 \pm 0.1$	$4.71 \pm 0.09$	$0.73 \pm 0.09$
C2	$-0.27 \pm 0.09$	$1.55 \pm 0.08$	$4.11 \pm 0.08$	$1.9 \pm 0.2$	$4.4 \pm 0.2$	$0.0 \pm 0.2$
C3	$0.01 \pm 0.08$	$1.84 \pm 0.08$	$4.39 \pm 0.08$	$2.2 \pm 0.2$	$4.4 \pm 0.2$	$0.0 \pm 0.2$
C4	$0.16 \pm 0.08$	$2.00 \pm 0.08$	$4.55 \pm 0.08$	$2.3 \pm 0.2$	$4.4 \pm 0.2$	$0.0 \pm 0.2$
C5	$0.28 \pm 0.08$	$2.11 \pm 0.08$	$4.64 \pm 0.08$	$2.5 \pm 0.2$	$4.4 \pm 0.2$	$0.0 \pm 0.2$
C6	$0.37 \pm 0.08$	$2.20 \pm 0.08$	$4.7 \pm 0.1$	$2.5 \pm 0.3$	$4.4 \pm 0.2$	$0.0 \pm 0.2$
Values difference between of C1 and C6	$2.0 \pm 0.1$	$2.2 \pm 0.1$	$1.7 \pm 0.1$	$1.8 \pm 0.4$	$-0.36 \pm 0.3$	$0.7 \pm 0.3$

At 20 *RH%*, the strain varied from  $-1.66 \pm 0.03$  % to  $0.37 \pm 0.08$  %, corresponding to an irreversible strain equal to  $2.0 \pm 0.1$ . At 50 and at 80 *RH%*, the irreversible strains were respectively equal to  $2.2 \pm 0.1$  % and  $1.7 \pm 0.1$  %. These values were lower than those obtained in the previous study (1.2.2.4). It was explained by the use of different cycles of *RH%* values, that varied here from 20 to 80 %, whereas it previously varied from 10 to 85 %.

The average strain ( $\varepsilon_{ave}$ ), the strain amplitude ( $\Delta\varepsilon$ ) and the irreversible strain depending of the characterisation cycle had stabilised values from C3. Moreover, at 50 RH%, from C3, the strain variations from a characterisation cycle to another were respectively equal to 0.06, 0.11 and  $0.09 \pm 0.08$ . Consequently, from C3 or 30 h of cycling, the material presented a similar behaviour, with no more hysteresis phenomenon, when applying similar RH% values, meaning that the material was stabilised.

At the last characterisation cycle of the ageing tests, the strains values still showed variations. As 20g jaws were hang on the samples strips, the samples might have creped during the tests and been favoured by the water acting as a plasticizer. Considering the DuPont™ data, the Nafion 212 has an elongation to break reaching 350 %. The samples stabilisation may require more cycling, inducing higher strain, before showing a stabilising or breaking due to the mass of water. Further investigations could provide a deeper understanding of the phenomena.

### 1.3 Conclusion

In this first part, membrane samples were placed under different air relative humidity (RH%) conditions. The chosen method and variations of RH% had a measurable impact on the water content of Nafion® 212 samples. Their relevance led to perform hydroexpansion tests under variations of RH% value from 10 to 85 RH%.

The hydroexpansion of the membrane was first tested in the thickness, by ESEM methods and by micrometer measurement. Consequently, the Nafion® 212 thickness was considered equal to  $49.8 \pm 0.8 \mu\text{m}$ .

The in plane hydroexpansion of the membrane was evaluated by testing ten samples on Varidim device. First of all, a change of the RH% setting, varying from 50 to 70 RH%, was applied on the samples. Sample dimensional variations ranged similarly to the air generator regulation.

Then, samples were submitted to a complete cycle of RH%. The membrane appeared very sensitive to the RH% variations and presented higher deformation at high RH%, than at low RH%. Cycling of Nafion® 212 membranes showed hysteresis, which induced an irreversible strain equal to  $0.99 \pm 0.07 \%$ .

The membrane was sampled in different directions for the investigation of its anisotropy. No preferential directions of strain could be evidenced, but small differences were observed. It led to advise keeping the same sampling direction when performing tests on Nafion® membrane. Sampling parallel to the machine direction was preferred in the present study.

Five cycles were applied on the membrane samples. The hysteresis behaviour diminished when applying more and more cycles on the samples. After 60 h of cycling, the material showed similar behaviour when applying *RH%* variations, which suggested that the samples were stabilised. Similar observation was made when Ageing cycled were applied on the membrane.

Even if the time before their use is short, a change of the *RH%* value could lead to membrane deformations and to change the membrane behaviour afterwards. The storing conditions before printing have to be precisely controlled, at 50 *RH%* for example, in order to print a material with similar properties.

Moreover, the temperature has also to be fixed. Indeed, this parameter was not studied but it is known to have coupled impact with *RH%* on the membrane mechanical behaviour [Kusoglu *et al.*, 2009]. Same problems way occur during the printing test. A relevant solution is to stabilise the membrane before its use, although it requires some hours.

## 2 Improvement of the membrane printability

The goal of this study is to perform catalyst layer by direct Catalyst Coated Membrane (CCM). However, during the first printing tests, some problems occurred in the printing procedure of the membrane. The printing protocol consisted in superimposing ink layers onto the membrane without drying between the layer transfers, whose protocol will be investigated in chapter 4. The first ink layer was easily transferred onto the membrane sample. However, during the printing of the second ink layer, the membrane curled and swelled. It led to printing defects: lack of ink, heterogeneous ink film... as expected given the lack of stability of the membrane.

For possible CCM, instead of limiting the dimensional variations that occurred during the printing step, the samples were deformed before printing by immersion in the vehicle of the ink. We postulated that, in such case, the impact of the printing step on the sample dimensions could have been limited and the printing defects reduced.

In order to evaluate the relevance of the proposed pre-treatment on the CCM fabrication different durations of immersion were tested: membrane samples were pre-treated during 30, 60, 90 and 120 s as described in Figure 40.1. The immersion was followed by a 10 s wiping step between blotting-papers which aimed at reducing water drops remaining on the Nafion<sup>®</sup> surface (Figure 40.2). During this operation, a 0.7 kPa compressive stress was applied. In the following sections, such specimens are referred to as immersed, treated or pre-treated samples. In order to limit potential modifications of the immersed membranes by contact with air, the samples were printed (Figure 40.3) or characterised within one minute after removal of the immersion bath and wiping stage.

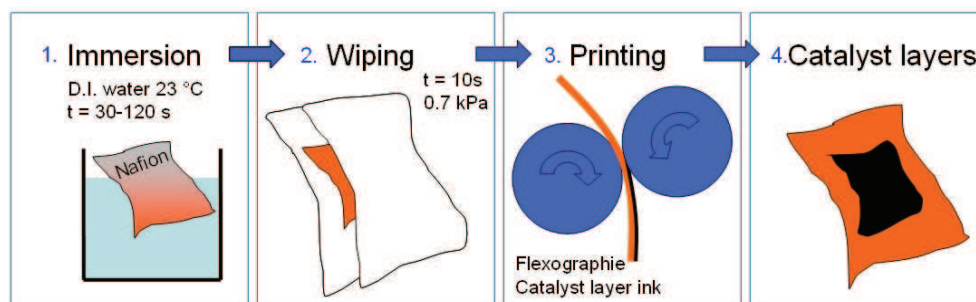


Figure 40 Steps of CCM fabrication: 1. immersion protocol, 2. membrane wiping, 3. flexography printing and 4. CCM

The study of these samples started by focusing on the membrane printability. Water drops (2.1), and ink drops (2.2) were deposited onto immersed samples and non-treated ones. The impacts of the duration of the treatment onto the membrane behaviour were observed

and discussed (2.3). Finally, printing tests were performed (2.6) using a model ink  $I_0$  (2.6.1) and using the ink  $I_{33}$  for catalyst layer manufacturing (2.6.2). The catalyst layers made by direct deposition of the ink  $I_{33}$  onto immersed samples were tested as cathode in fuel cells.

## 2.1 Membrane behaviour when depositing water drops

Water drops were deposited onto Nafion<sup>®</sup> membrane samples placed between the jaws of the device described in Chapter 2 section 2.2.3.

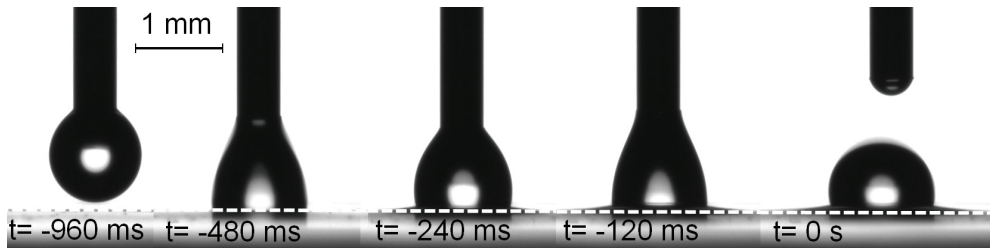


Figure 41 Side views of the deposition of water drops onto the Nafion<sup>®</sup> membrane, and definition of the initial time  $t = 0$  s used as reference time for experiments in this study

Figure 41 demonstrated that less than one second was required to complete the drop deposition. It consisted of putting in contact a water drop held by the needle of a syringe with the sample surface. Right after the contact, the needle was lifted back until the water drop detaches from the needle tip. The time when the drop was freely deposited onto the membrane surface has been chosen as the initial time ( $t = 0$  s). Figure 42 illustrates the phenomena appearing from  $t = 0$  s to 120 s for various immersion durations (here 0, 60 and 120 s).

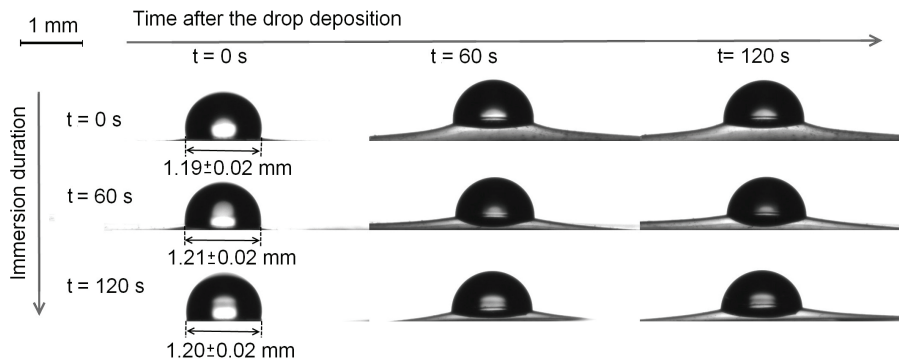


Figure 42 Side views of typical evolution of the geometry of water drops with respect to time onto the Nafion<sup>®</sup> membrane immersed for 0, 60 and 120 s

The 2  $\mu$ L drops have a contact diameter with the membrane ranging from 1.19 to 1.21  $\pm$  0.02 mm.

Figure 42 reveals the occurrence of two main phenomena:

- the membrane was deformed under and in the vicinity of the drop: it blistered. The amplitude of the blistering deformation was time-dependent. This phenomenon also appeared to be dependent upon the membrane pre-treatment.
- the shape of the drop evolved with time too.

Figure 43 details the two parameters that were selected to describe the drop geometry when deposited onto the Nafion<sup>®</sup> membrane.

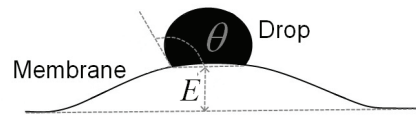


Figure 43 Parameters used to describe the geometry of a drop deposited onto the tested membranes

The parameter  $E$  quantifies the elevation between the initial level of the membrane (before the drop deposition) and the current level of the membrane. This parameter had already been described in similar experiments of drop deposition [Goswami *et al.*, 2008]. The parameter  $\theta$  was the apparent contact angle formed by the drop on the substrate at the liquid/solid/gaseous interface. This parameter is commonly used in wettability tests. Above  $90^\circ$ , the wettability of the surface is considered as poor. Below  $90^\circ$ , the liquid spreads onto the surface. In this last case, the wettability is qualified as good.

In Figure 42, at  $t = 0$  s, blistering of the Nafion<sup>®</sup> membrane was observable on all the samples. These blistering were equal to  $70 \pm 20 \mu\text{m}$ ,  $50 \pm 20 \mu\text{m}$  and  $30 \pm 20 \mu\text{m}$  at times of immersion equal to 0, 60 and 120 s respectively. Indeed, as described in Figure 41, the water drops were in contact with the membrane 500 ms before the initial time  $t = 0$  s was taken. This short period was certainly sufficient to induce blistering phenomena of the membrane.

Various factors may impact the values of  $\theta$  and  $E$ . Firstly, evaporation and/or absorption phenomena may occur during these experiments and may influence the evolution of  $\theta$  and  $E$ . However, Goswami *et al.*[2008] demonstrated that the mass of a Nafion<sup>®</sup> 115 sample on which a drop of  $10 \mu\text{L}$  was deposited in a dry gas chamber decreased significantly due to evaporation after several minutes (typically  $\sim 4$  min). Furthermore this evaporation seemed to have an observable effect on their drop-membrane-air tested system only after a period of 250 s. Here, the experiment duration was about 2 min long and the drop volume of  $2 \mu\text{L}$ . Thus, it was roughly estimated from the observations of Goswami *et al.* [2008] that the evaporation should not have affected the present experimental results at least up to a drop deposition time equal to 60 s. If the evaporation phenomenon was neglected during this period, absorption phenomena of water by the Nafion<sup>®</sup> membrane might have been present. Secondly, the effect of possible drop volume decrease due to

evaporation and/or absorption on apparent contact angle was neglected since previous experiments showed no effect of a volume variation of  $\pm 0.5 \mu\text{l}$  ( $\pm 25\%$  of the drop volume) on the two measured parameters.

In the two following sections, the influence of the immersion duration and deposition times on the parameters  $\theta$  (2.1.1) and  $E$  (2.1.2) were investigated with respect to the time after drop deposition, for the five immersion durations previously detailed.

### 2.1.1 Apparent contact angle of water drops

Figure 44 shows the variation of the contact angle of water droplet with time after being deposited onto membrane samples. These samples were previously immersed during different times (30, 60, 90 and 120 s) and compared with non treated-samples.

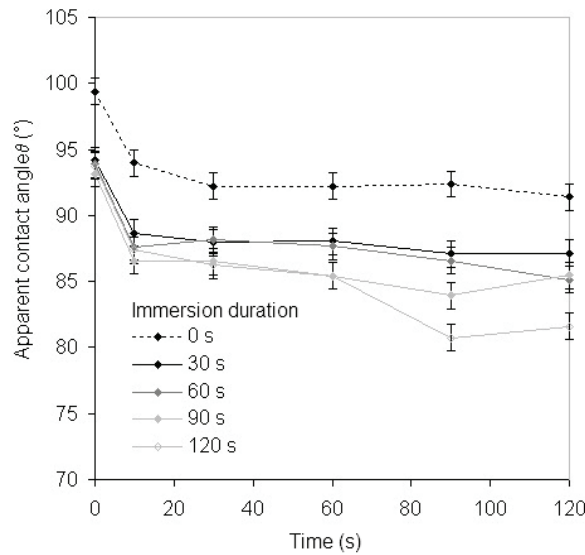


Figure 44 Apparent contact angle  $\theta$  of water drops deposited on Nafion<sup>®</sup> membranes immersed for 0, 30, 60, 90 and 120 s as a function of the time

Whatever the immersion duration, the apparent contact angle  $\theta$  sharply decreased between times of 0 and 10 s. Then it progressively stabilised between 10 s and 60 s for membranes having an immersion duration of 0, 30 and 60 s, whereas it exhibited a slight decrease for membranes immersed during 90 and 120 s. Over 60 s, the apparent contact angle started again to vary in a wide range depending on the immersion duration. This phenomenon was observed for drops deposited onto membranes immersed for 90 and 120 s.

At time  $t = 0$  s, the apparent contact angle of the non immersed Nafion<sup>®</sup> membranes (0 s) was equal to  $99^\circ \pm 2^\circ$ , whereas those of the membranes immersed for 30, 60, 90 and 120 s were very close to each other and equal to  $94^\circ \pm 2^\circ$ . At time  $t = 10$  s, the non immersed membranes had an apparent contact angle equal to  $94 \pm 2^\circ$ . This value was

similar to the contact angles measured at  $t = 0$  s for the immersed membranes. At  $t = 10$  s, the other immersed membranes had apparent contact angles equal to  $89^\circ$ ,  $88^\circ$ ,  $87^\circ$  and  $88^\circ \pm 2^\circ$ . Between  $t = 0$  and 10 s, the apparent contact angle variation rate was roughly estimated to  $-0.54$ ,  $-0.55$ ,  $-0.62$ ,  $-0.66$  and  $-0.64 \pm 0.4$  deg/s for immersion times respectively equal to 0, 30, 60, 90 and 120 s. For times longer than 60 s, the difference between the apparent contact angles of the water drop onto the non immersed and immersed membranes even reached  $15^\circ$ .

Therefore, the longer the Nafion<sup>®</sup> was immersed, the faster the apparent contact angle decreased. The apparent contact angle remained above  $90^\circ$  for the non immersed samples whatever the time after the drop deposition. For the other samples, the apparent contact angles remained under the value of  $90^\circ$  after 10 s. These observations demonstrated the efficiency of the immersion procedure to improve the wettability of the Nafion<sup>®</sup> membrane by water.

### 2.1.2 Membrane elevation under water drops

In Figure 45, the elevation values of membrane samples immersed during different times are plotted as a function of time.

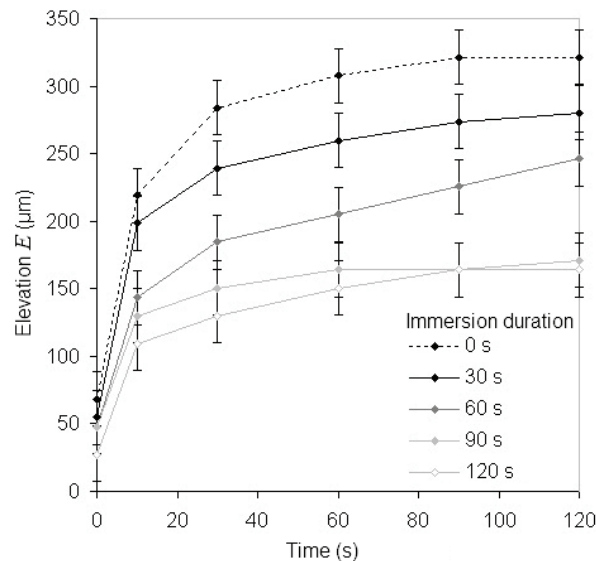


Figure 45 Elevation  $f$  of Nafion<sup>®</sup> membranes immersed for 0, 30, 60, 90 and 120 s as a function of the time

At  $t = 0$  s, the elevation of the membranes immersed for 0, 30, 60, 90 and 120 s were equal to  $68$ ,  $55$ ,  $48$ ,  $48$  and  $27 \pm 20$   $\mu\text{m}$ , respectively. The longest time the drop was in contact with the membrane, the more the sample elevation increased. The elevation of the non immersed membranes was always larger than those of the immersed ones (at  $t = 60$  s,  $E = 310 \pm 20$   $\mu\text{m}$  for the non immersed membranes, whereas  $E = 260 \pm 20$   $\mu\text{m}$  for a

membrane immersed during 30 s, for instance). The immersion duration had a large influence on the membrane elevation: the longer the membrane immersion, the lower their elevations were. The membranes immersed during 90 s were an exception; they exhibited a similar behaviour to that of the membranes immersed for 120 s after 60 s. The membrane elevation was to six times higher than the membrane thickness and reached about 30 % of the initial drop diameter in contact with the membrane.

## 2.2 Nafion<sup>®</sup> dimensional response to model ink drops deposition

In the case of the flexography printing process, the ink transfer takes place in the nip area. The ink transfer occurs within one millisecond [Aspler *et al.*, 1993]. The ability of the Nafion<sup>®</sup> membranes to be used as printing substrates was evaluated at the initial drop deposition time. It was also observed in the previous sections (2.1.1 and 2.1.2) that the behaviour of the immersed Nafion<sup>®</sup> membranes was not largely influenced by the duration at  $t = 0$  s. Therefore, in the following, the phenomena related to the deposition of the model ink were studied for non immersed membranes and membranes immersed for only 30 s. The next sections develop the evolution of the apparent contact angle (2.2.1) and the membrane elevation (2.2.2) with respect to the ink drop deposition time.

### 2.2.1 Apparent contact angle of ink drops

Figure 46 depicts the values of apparent contact angles as a function of time after ink drops were deposited on non treated and 30 s immersed membrane samples.

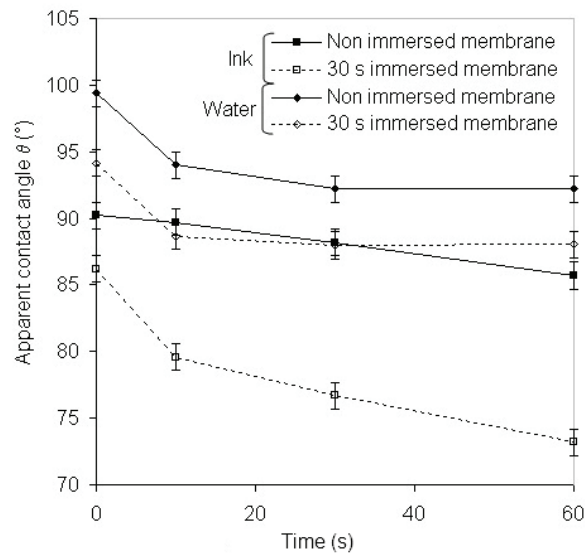


Figure 46 Apparent contact angle at 0, 10, 30 and 60 s after the deposition of drops of water or model ink on non-immersed and 30 s immersed membranes

The apparent contact angle of ink drops ranged between  $90^\circ \pm 2^\circ$  and  $86^\circ \pm 2^\circ$  between 0 and 60 s when using the non immersed Nafion<sup>®</sup> membrane. These values were lower when using immersed membranes as they were equal to  $86^\circ \pm 2^\circ$  and  $73^\circ \pm 2^\circ$  for the same period. Similarly to the previous observations performed using water, the wettability of the Nafion<sup>®</sup> membranes was enhanced by the immersion.

### 2.2.2 Membrane elevation under ink drops

Figure 47 shows the values of elevation of non-treated and 30 s immersed membrane samples as a function of time.

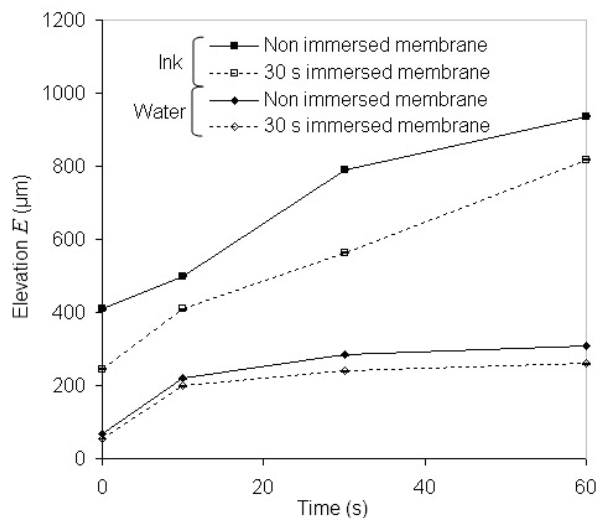


Figure 47 Elevation at 0, 10, 30 and 60 s after the deposition of drops of water or model ink on non immersed and 30 s immersed membranes

The deposition of ink drops induced a high elevation on both membranes. After the same time, ink drops caused higher membrane elevation than water drops. For the non immersed Nafion<sup>®</sup> membrane, the elevation value ranged between  $410 \pm 20 \mu\text{m}$  and  $940 \pm 20 \mu\text{m}$  between 0 and 60 s. The immersed membrane showed lower elevation, equal to  $240 \pm 20 \mu\text{m}$  at 0 s and  $820 \pm 20 \mu\text{m}$  at 60 s, showing the beneficial effect of the immersion on the membrane stability.

## 2.3 Membrane behaviour in contact with water and ink

### 2.3.1 Evolution of the apparent contact angle of water drops with the immersion duration and time

The contact angle of water drops with immersed membranes was smaller than with non immersed membranes. Similar wettability phenomena (measurement of sessile drop contact angle) had already been observed by Bass [2010] with other references of Nafion<sup>®</sup> that had been immersed for a 16 hours period. Goswami [2008] showed that the advancing

contact angle of water drops on several types of Nafion<sup>®</sup> membranes were higher than the receding contact angle. In the latter case, the measurement of the receding contact angle was performed after soaking the tested Nafion<sup>®</sup> membranes for 24 hours in deionised water.

In these two studies, such behaviour was related to a structural change in the Nafion<sup>®</sup> membranes. This phenomenon was particularly characterised in very narrow subsurface layers by Bass [2010] using X-ray scattering or at the membrane surface using atomic force microscopy [Affoune *et al.*, 2005; Ma *et al.*, 2006; Hiegsen *et al.*, 2009].

In dry gas conditions, the PTFE parts of the Nafion<sup>®</sup> polymer tended to cover the membrane surface. When the Nafion<sup>®</sup> membrane was in contact with water, its hydrophilic parts, *i.e.* the sulfonic acid groups, tended to migrate toward the Nafion<sup>®</sup>-water interface. As a consequence, the Nafion<sup>®</sup> surface was covered by three distinct elements:

- a hydrophobic PTFE skin,
- hydrophilic sulfonic groups
- that surrounded water clusters having a size of few nanometers [Kim *et al.*, 2003; Rubatat *et al.*, 2002; Karakashev *et al.*, 2005; Affoune *et al.*, 2005; Ma *et al.*, 2006; Hiegsen *et al.*, 2009].

This structural change was combined to roughening of the Nafion<sup>®</sup> membrane surface. Finally, the water immersion treatment or the deposition of water drops had a significant influence on Nafion<sup>®</sup> properties, which changed its surface behaviour from hydrophobic to hydrophilic.

Despite the short duration of the immersion in the present study, which were limited to 120 s, the wettability phenomena is consistent with the conclusions of the works previously cited. Consequently, the present results may be explained by similar modifications of the surface at the interface between Nafion<sup>®</sup> membranes and water.

At  $t = 0$  s, the apparent contact angle of water drops on immersed membranes reached a substantially high value, compared to those reached at  $t = 10$  s. They were in the same order of magnitude than those measured for the non immersed membranes as noticed in the section 2.1.1.

This particular behaviour might have been explained by the effect of the wiping stage that could remove a part of the water that formed the clusters at the membrane interface. It can also traduce the adaptation of the surface passing from a gaseous/solid to a liquid/solid interface.

For both non immersed and immersed membranes, the modifications of the apparent contact angle with respect to the drop deposition time were explained by a change in the water-Nafion<sup>®</sup> interface. These changes were modelled by an increase in the surface fraction of water clusters. This latter was estimated using the Cassie-Baxter model [De Gennes, 2002]. This model considers a chemically heterogeneous surface composed of two distinct elements. As an approximation, the Nafion<sup>®</sup> membrane surface was here considered to be only covered by a PTFE skin and water clusters. Therefore, this model neglected the fraction of the surface covered by the PVE chains and sulfonic acid groups. In such a case, the Cassie-Baxter model relates the apparent contact angle  $\theta$  of a liquid on the Nafion<sup>®</sup> surface as (Equ. 22).

$$\cos \theta = \phi \cos \theta_{\alpha} + (1 - \phi) \cos \theta_{\beta} . \quad \text{Equ. 22}$$

This equation related  $\theta$  with  $\theta_{\alpha}$  and  $\theta_{\beta}$  the contact angles of water on the water clusters  $\alpha$  and the PTFE  $\beta$ , respectively, and the surface fraction of water clusters  $\phi$ . The contact angle  $\theta_{\alpha}$  of water on itself is zero, and the contact of water onto PTFE was taken at  $113.4^{\circ}$  [Janczuk et al, 1997]. Using the data for  $\theta$  given in Figure 44, the calculated values of the surface fraction of water clusters  $\phi$  are shown in Figure 48.

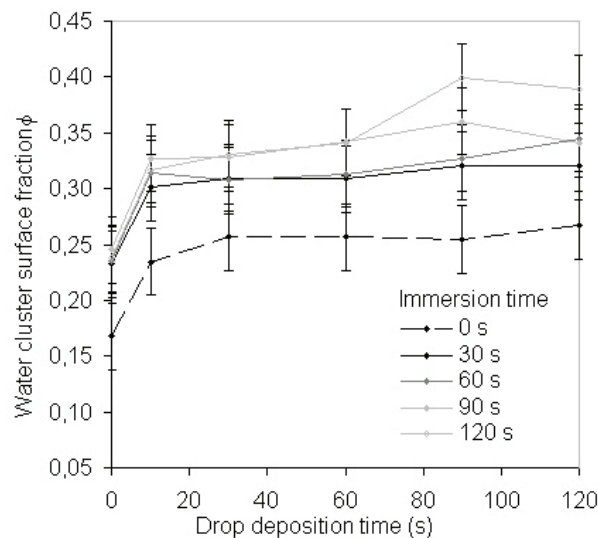


Figure 48 Surface fraction of water clusters onto Nafion<sup>®</sup> membranes immersed during 0, 30, 60, 90 and 120 s

The model predicted a surface fraction of water clusters ranging from 17 % and 27 % for the non-immersed membrane whereas this fraction ranged from 24 % and 40 % for the immersed membranes. For example, Affoune [2005] stored membrane samples more than two days in water. The obtained sample exhibited a surface covered at 50 % by water

clusters (surface fraction estimated using ImageJ). This model indicated that immersion treatment led to create more water clusters and/or make them more accessible to water.

### 2.3.2 Blistering phenomenon in the case of the deposition of water drops

The variation of the Nafion<sup>®</sup> membranes elevation in contact with water drops can be explained according to the hydromechanical model proposed by Goswami [2008]. These authors related the elevation phenomenon of membranes to hydroexpansion mechanisms. In their model the Nafion<sup>®</sup> membrane was considered as a laminate: the differential expansion that occurred between the parts of the membrane where water diffused and the parts free of water caused the membrane elevation. This behaviour was related to the diffusion of water within Nafion<sup>®</sup> membranes which was known to induce the swelling of this material, as shown for instance by Gebel [2000]. As diffusion phenomena progressed from the interface through the core of the Nafion<sup>®</sup> as exemplified by Majsztrik [2007], the measured elevation evolved during the drop deposition experiments. The moistening of the core of the Nafion<sup>®</sup> membrane was linked to large molecular rearrangements [Aspler *et al.*, 1993; Gebel, 2000; Majsztrik *et al.*, 2007; Termonia, 2007; Goswami *et al.*, 2008; Chaabane *et al.*, 2008; Collette *et al.*, 2009; Kusoglu *et al.*, 2009]. This influenced the diffusion kinetics [Majsztrik *et al.*, 2007], and was coupled with drastic changes of the mechanical performances of such membranes: they became more and more flexible when the moisture content increased as their in-plane Young's modulus decreased [Hofmann *et al.*, 2009].

There was a substantial difference between the elevation behaviour of non immersed and immersed membranes as well as between the immersed membranes depending on their immersion time. Several hypotheses may explain this particular behaviour:

- the immersion induced water sorption phenomena that might have decreased the hydroexpansion potential of the membrane: the longer the immersion, the weaker the hydroexpansion. Thus the phenomena of differential hydroexpansion were limited and the membrane elevation may have followed the same trend.
- the water uptake reduced the mechanical properties such as the in plane Young's modulus: immersed membranes had weaker mechanical properties compared to non immersed ones. The mechanical properties decreased again when water diffusion phenomena occurred once a water drop was deposited on their surface. Such phenomena hindered the elevation of the membrane. During tests of the present study, the collapse of the membrane under the

drop weight was observed during the tests for the longest immersion and deposition times. Such observation was made, for example, in the case of membranes immersed for 90 s and 120 s and after deposition times of 90 s and 60 s, respectively: *i.e.* which corresponds to a total time of contact between the membranes and water above 180 s.

Hence, the immersion stage gave a positive effect regarding the reduction of the membrane dimensional instability in contact with water although such treatment also drastically reduced the membrane mechanical properties.

#### **2.4 Interactions between Nafion<sup>®</sup> membrane and the water-based ink**

Water was the major component of the ink  $I_0$ , this explained why the measured apparent contact angles at a deposition time  $t = 0$  s were quite similar to those obtained with pure water. These angles also decreased when the drop deposition time increased. Besides, similar effect of the immersion treatment was observed on the wettability behaviour of the Nafion<sup>®</sup> membranes with ink as with water. Nonetheless, for each kind of membrane, the apparent contact angles measured using water were higher than when using ink at a given deposition time. This behaviour was due to alcoholic additives in the Nafion<sup>®</sup> dispersion that entered in the composition of the vehicle of the model ink [Goswami *et al.*, 2008; Chaabane *et al.*, 2008].

The presence of these additives also explained the deformation of the membranes that was more pronounced when they were in contact with the model ink compared to water. The immersion treatment had a beneficial effect on the dimensional stability of the Nafion<sup>®</sup> membranes.

#### **2.5 Ageing of the pre-treated membranes**

As it was performed on non-treated membrane samples in section 1.2.2.5, ageing cycling was applied onto immersed membrane samples. For comparison of the behaviour of the two types of membrane samples, the strain values at 20 and 80 RH% as a function of time are shown in Figure 49.

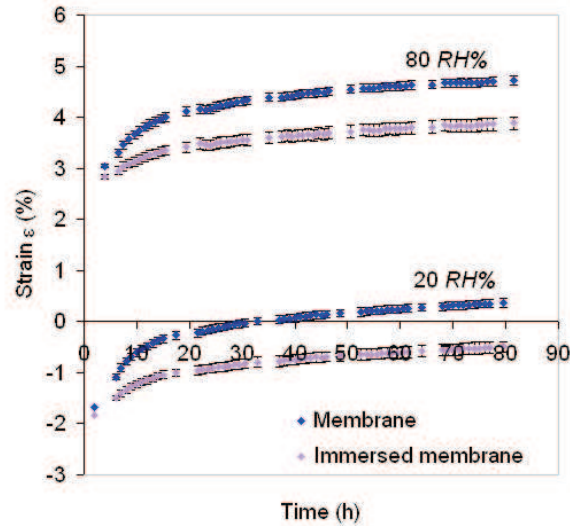


Figure 49 Ageing cycle of immersed and non immersed samples: strain as a function of time

The strain values were measured and are presented in Table 18.

Table 18 Comparison of the strain parameters of immersed and non immersed samples placed under ageing cycling

Strain parameters		Samples treatment	Characterisation cycles		Values difference between of C1 and C6
			C1	C6	
Strain $\varepsilon$ (%)	at 20 RH%	Non immersed	$-1.66 \pm 0.03$	$0.37 \pm 0.08$	<b><math>2.0 \pm 0.1</math></b>
		immersed	$-1.83 \pm 0.05$	$-0.5 \pm 0.1$	<b><math>1.3 \pm 0.1</math></b>
	at 80 RH%	Non immersed	$3.05 \pm 0.05$	$4.7 \pm 0.1$	<b><math>1.7 \pm 0.1</math></b>
		immersed	$2.84 \pm 0.08$	$3.9 \pm 0.1$	<b><math>1.1 \pm 0.1</math></b>
$\varepsilon_{ave}$ (%)		Non immersed	$0.7 \pm 0.1$	$2.5 \pm 0.3$	<b><math>1.8 \pm 0.4</math></b>
		immersed	$0.5 \pm 0.1$	$1.7 \pm 0.3$	<b><math>1.2 \pm 0.4</math></b>
$\Delta\varepsilon$ (%)		Non immersed	$4.71 \pm 0.09$	$4.4 \pm 0.2$	$-0.36 \pm 0.3$
		immersed	$4.66 \pm 0.09$	$4.4 \pm 0.2$	$-0.3 \pm 0.3$
$\varepsilon_{irr}$ (%)		Non immersed	$0.73 \pm 0.09$	$0.0 \pm 0.2$	$0.7 \pm 0.3$
		immersed	$0.6 \pm 0.1$	$0.0 \pm 0.2$	$0.6 \pm 0.3$

The pre-treatment by immersion had also a measurable influence on the behaviour of the membrane under different RH% values. At the first cycle applied onto the samples, both types of membrane have closed strain values at 20 and 80 RH%. However, after the second cycle, differences appeared depending on the membranes treatment. From C1 to C6, an irreversible strain occurred on the non immersed and immersed sample that was respectively equal to  $2.0 \pm 0.1$  % and  $1.3 \pm 0.1$  %. Moreover, the time for stabilising the behaviour of the immersed sample was evaluated at 15 h, twice lower than for the non-immersed samples.

Consequently, the membrane immersion 30 s into water also reduced the irreversible strain and the time for stabilising the material.

## 2.6 Membrane printing

Membrane samples were printed by flexography using a multilayer protocol that superimposed several ink layer wet and wet.

Two inks were tested; the model ink  $I_0$ , already used before in section 2.2, and the ink  $I_{33}$  which contains catalyst. Their physical properties are reported in Table 19.

Table 19 Ink properties

Ink	Viscosity	Surface tension
$I_{33}$	$80 \pm 20$ mPa s	$31 \pm 4$ mN m <sup>-1</sup>
$I_0$	$190 \pm 30$ mPa s	$44 \pm 5$ mN m <sup>-1</sup>

The ink  $I_0$  was used for evaluated the membrane printability (2.6.1), and the ink  $I_{33}$  for manufacturing catalyst layer suitable for fuel cell tests (2.6.2).

### 2.6.1 Evaluation of the membrane printability

The best wettability and dimensional stability were reached when using the immersed membranes. Consequently, non immersed and immersed Nafion<sup>®</sup> samples were printed by superimposing 1, 2, 3 and 5 wet ink layers with the Flexiproof device in order to obtain solid patterns with a sufficient ink quantity to fulfil the catalyst layer for PEM fuel cells' requirements. Figure 50 compares the scanned surface appearance of a printed non immersed membrane (I) and an immersed membrane (II) on which three ink layers were superimposed. On these printed membranes, the optical density values ( $OD$ ) of the printed areas were in a narrow range: the  $OD_{non\ immersed}$  was equal to  $2.37 \pm 0.02$  and  $OD_{30\ s\ immersed}$  was equal to  $2.40 \pm 0.01$ . Consequently, the ink was successfully transferred in a similar way on both membranes during the printing stage. However, non-printed zones were visible. The printed zones appear in black and the whiter zones, that form lines, indicate lacks of ink. For a non immersed membrane, like membrane I in Figure 50, the number of such defects was estimated to be larger than  $0.7$  defects cm<sup>-2</sup>, whereas the immersed membranes, like membrane II in Figure 50, had only about  $0.05$  defects per cm<sup>2</sup>, *i.e.* a nearly one order of below the value of membrane I.

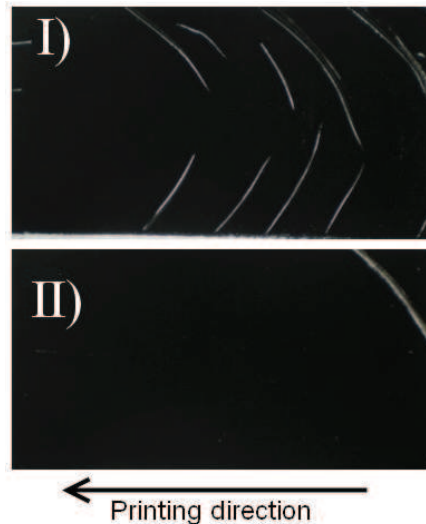


Figure 50 Printed zones of I) non immersed Nafion<sup>®</sup> and II) 30 s immersed Nafion<sup>®</sup>, printing speed: 25 m min<sup>-1</sup>

In Figure 51, the ink coverage ( $X\%$ ) of the solid pattern area was measured on treated and non treated samples printed by superimposing 1, 2, 3 and 5 layers of inks.

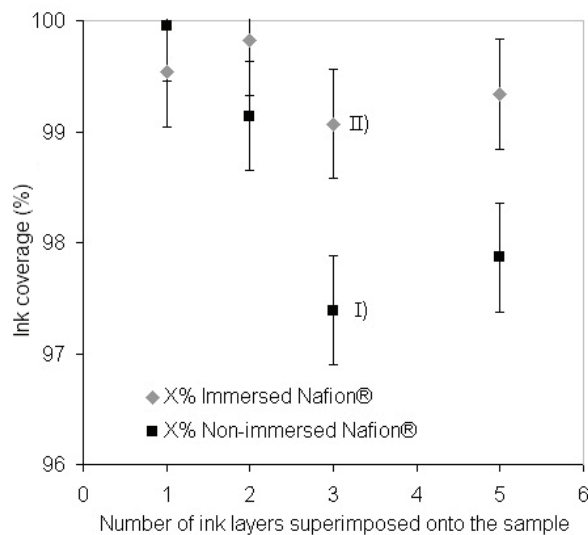


Figure 51 Surface fraction of ink  $X\%$  of printed immersed and non immersed membranes as a function of the number of ink layers transferred by flexography (the data measured for the previous I and II samples are reported in this figure)

The ink coverage on non immersed and immersed membranes with one or two ink layers were close and ranged between 98.6 % and 100 %. However, when more ink layers were superimposed, the coverage on non immersed membranes decreased to 96.8 %, whereas the on immersed membranes it stayed above 98.5 %. The immersed Nafion<sup>®</sup> membranes had an improved behaviour during successive ink depositions compared to non immersed samples.

For three superimposed ink layers, while the number of defects per unit of surface substantially varied depending of the treatment,  $X\%$  showed close deviation: 1.7 % and

2.8 % for respectively non immersed and immersed membranes printed samples. Therefore, the number of defects calculated before had a minor influence on the ink coverage.

The decrease of the ink coverage was the result of either partial ink removal or membrane creasing during the superimposition of ink layers. Printing could have induced fast Nafion<sup>®</sup> differential expansion phenomena between the solid pattern area and the non inked area of the Nafion<sup>®</sup> membrane. The blistered zone corresponding to the solid pattern area was observed to progressively crease when entering between the printing cylinders. Due to this particular deformation, the ink was not correctly transferred in the creased area.

The membranes that had fewer defects had the highest dimensional stability. Moreover, Figure 52 compares the cross views of catalyst layers printed on non treated and treated substrate (as respectively I and II). Consequently, the 30 s immersed improved the samples stability during printing.

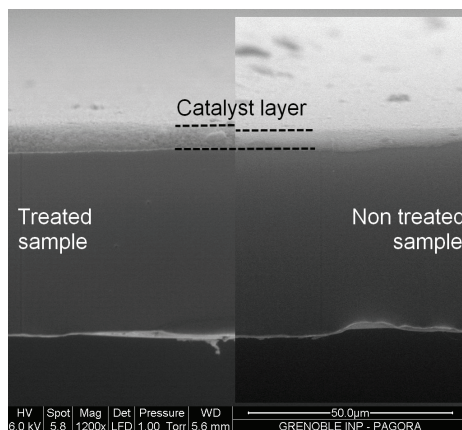


Figure 52 Cross view of catalyst layers printed by superimposing three layers of ink by flexography on treated and non treated membrane samples

This picture gives an estimation of the catalyst layers thicknesses:  $4 \pm 1 \mu\text{m}$  and  $6 \pm 1 \mu\text{m}$  for the deposits on respectively non-treated and treated samples. The treatment by immersion should also improve the ink transfer. Stabilising the membrane, the treatment gave a better printability, with thicker catalyst layers, with lower defect density and higher ink coverage.

### 2.6.2 Electrochemical characterisation of printed catalyst layers

Membrane samples were printed using the ink I<sub>33</sub> for catalyst layer manufacturing. The membrane samples were printed by superimposing two and three ink layers by flexography.

The method detailed in chapter 2 for measuring the ink and platinum loading of the catalyst layer was hardly applicable for CCM. Indeed, as previously demonstrated in this chapter, the membrane has a substantial sensitivity to the variations of humidity. Consequently, since the quantity of ink deposited onto the membrane samples was small, the ink and platinum loading values could not be measured accurately. Consequently, the platinum loading deposited onto the membranes samples were supposed similar to those obtained on CCB in chapter 4. Under such assumption, the superimposition of two and three ink I<sub>33</sub> layers onto a GDL led to catalyst layers with about 0.15 and 0.2 mg<sub>Pt</sub> cm<sup>-2</sup>. The CCMs were placed as cathode in a MEA, with a SGL 24 BC, and an anode loaded at 0.2 mg<sub>Pt</sub> cm<sup>-2</sup> made by coating a SGL 24 BC. The polarisation curves of these two MEAs are presented in Figure 53.

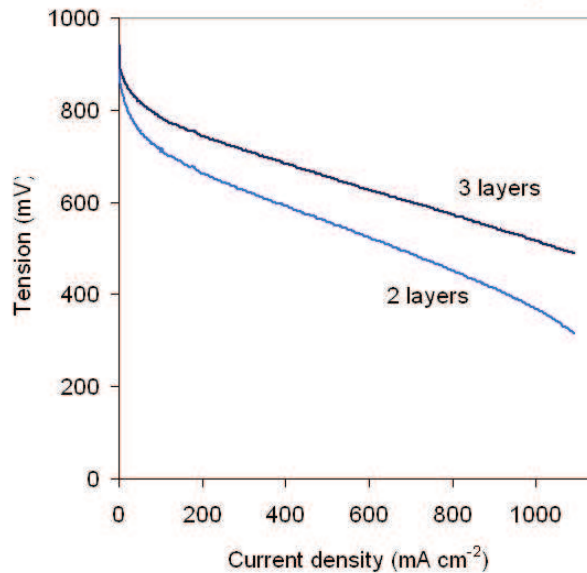


Figure 53 Polarisation curves of MEA, with a cathode manufactured by CCM using flexography (80°C, 50RH%, 1.5 air)

The two cathodes prepared by flexography were shown to be used in PEMFC. The higher were the platinum loadings, the higher were the electrochemical performances.

## 2.7 Conclusion

Nafion<sup>®</sup> membranes were treated by immersion in water (for different time durations 30, 60, 90 and 120 s). The wettability properties and the dimensional stability of such pre-treated membranes were compared with those of non-treated membranes by depositing ink and water drops onto the samples.

The apparent angle of water drops on the non immersed membranes remained over 90° whereas this parameter had a value below 90° in the case of the immersed membranes.

Under the drop vicinity, the non-treated samples showed higher elevation than the immersed samples.

The behaviour of the immersed and non immersed Nafion<sup>®</sup> membranes under ink drop deposition showed comparable evolution for both parameters, but lower apparent contact angles and more pronounced elevation phenomena. The alcoholic additives of the ink vehicle led to improve the wettability properties but were thought to increase the dimensional instability of the Nafion<sup>®</sup> membranes.

These improvements of the membrane printability thanks to the immersion pre-treatment were explained by surface structural modifications which formed water clusters at the Nafion<sup>®</sup> surface even immersion durations were short.

In this context, printability tests onto the two types of Nafion<sup>®</sup> membranes were performed using the model ink and the flexography printing process. Solid patterns were deposited by superimposing several ink layers. Due to a better membrane stability and wetting, the catalyst layers manufactured on immersed samples have:

- less printing defects,
- better ink coverage the printing surface,
- and higher thickness.

The pre-treatment made possible the manufacturing of catalyst layers by direct deposition of ink I<sub>33</sub> onto the membrane. They were successfully tested as cathodes in MEAs.

### Conclusion of chapter 3

The direct printing onto the membrane was a challenge. Indeed, the strong ability of the membrane to diffuse protons and water was also a drawback for direct CCM manufacturing: in contact with water in vapour or liquid state, the membrane swelled and curled and it limited the membrane printability.

When different RH% values were applied to the membrane, it deformed very rapidly. The influence of the RH% induced more deformation at higher RH% than at low RH%. Moreover, the first cycle of RH% applied onto the membrane sample impacted more the membrane dimension than the following cycles. Considering the cycles applied in this study, 30h of cycling were required for achieving a complete stabilisation of the membrane.

If the membrane samples had different behaviour depending on the RH% conditions and their RH% history, it could badly impact the runnability of the membrane in a printing press.

The direct printing membrane gave catalyst layers with many defects and problems. Consequently a pre-treatment was proposed: 30 s immersion into water (i) reduced the contact angle of ink deposited onto the membrane and (ii) limited the impact of the membrane dimensional instability during the printing step. Printing tests with the model ink I<sub>0</sub>, then with the ink I<sub>33</sub> for manufacturing catalyst layer provided efficient catalyst layers that were tested as cathode in an operating fuel cell.

# Chapter 4

## Catalyst Coated Backing



<b>INTRODUCTION .....</b>	<b>129</b>
<b>1 GAS DIFFUSION LAYERS PRINTABILITY .....</b>	<b>131</b>
1.1 EVALUATION OF THE GDL PRINTABILITY .....	131
1.1.1 <i>Substrate characterisation</i> .....	131
1.1.2 <i>Discussion on the GDL dimensional stability during printing</i> .....	132
1.1.2.1 Dimensional variations induced by physico-chemical interactions between GDL and the inks	132
1.1.2.2 Physical strains applied by the printing system.....	133
1.1.3 <i>GDL interaction with solvents</i> .....	133
1.1.4 <i>Surface energy estimation</i> .....	135
1.1.5 <i>GDL affinity with flexography ink</i> .....	137
1.1.6 <i>Conclusion on the evaluation of the GDL printability</i> .....	139
1.2 FABRICATION OF CCB BY DIFFERENT DEPOSITIONS TECHNIQUES.....	139
1.2.1 <i>Inks and dispersions</i> .....	140
1.2.2 <i>Deposition protocols</i> .....	141
1.3 COMPARISON OF THE CATALYST LAYERS SURFACE AS REGARDS TO THE DEPOSITION PROCESS.....	143
1.3.1 <i>Monolayer deposition: blade coating and screen printing</i> .....	143
1.3.2 <i>Processes with specific deposition: spray and ink jet</i> .....	144
1.3.3 <i>Process with multilayer deposition: flexography</i> .....	145
1.3.4 <i>Conclusion on the evaluation of the printing process relevance for catalyst layer manufacturing</i> .....	146
1.4 CONCLUSION.....	146
<b>2 GAS DIFFUSION ELECTRODES MADE BY FLEXOGRAPHY .....</b>	<b>148</b>
2.1 INFLUENCE OF THE FLEXOGRAPHY MULTILAYER PROTOCOL ON THE CATALYST LAYER PHYSICAL STRUCTURE .....	148
2.1.1 <i>Catalyst layers fabrication</i> .....	150
2.1.2 <i>Catalyst layer permeability</i> .....	151
2.1.3 <i>Catalyst layers surface observation</i> .....	154
2.2 INFLUENCE OF THE FLEXOGRAPHY PROCESS ON THE ELECTROCHEMICAL PROPERTIES OF CATALYST LAYERS .....	158
2.3 INFLUENCE OF THE MICROSTRUCTURE ON THE ELECTROCHEMICAL PROPERTIES OF THE CATALYST LAYERS .....	161
2.4 CONCLUSION.....	162
<b>CONCLUSION OF THE CHAPTER 4.....</b>	<b>164</b>



## Introduction

As detailed in the literature review, the fabrication of catalyst layer by different types of deposition techniques onto the GDL produces Catalyst Coated Backing (CCB), also named Gas Diffusion Electrodes (GDEs).

The gas diffusion layer (SIGRACET® GDL 24 BC) used in this study was manufactured by SGL Group. Two layers compose this substrate:

- a macroporous layer (Figure 54.b): carbon fibres network with 5 w/w% of polytetrafluoroethylene polymer,
- and SGL standard microporous layer composed of carbon nanoparticles and 10 w/w % of PTFE (Figure 54.a and Figure 55). In the present work, the surface characterisations and the printing tests are performed on this side of the GDL.

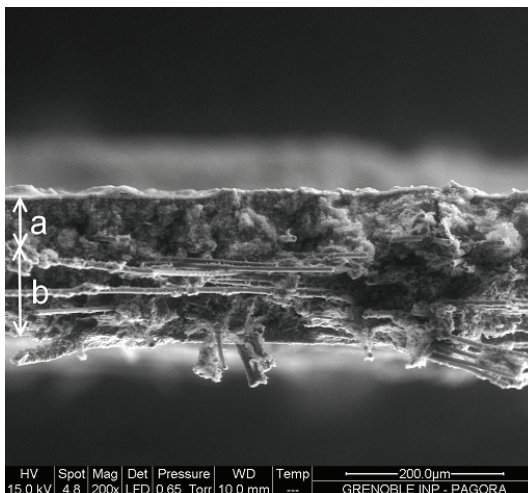


Figure 54 SEM cross view of SGL 24 BC: a) microporous layer and b) macroporous layer

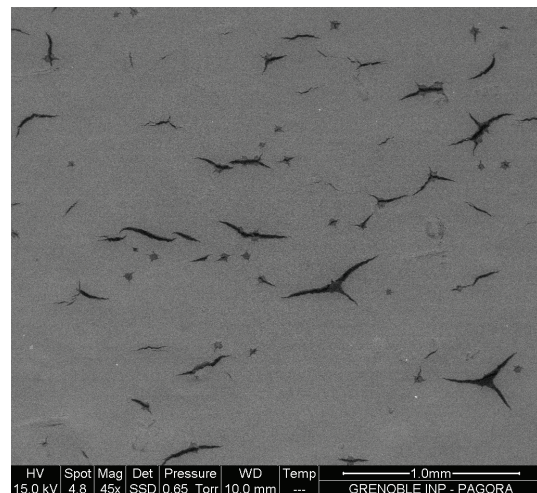


Figure 55 SEM surface view of SGL 24 BC (microporous layer surface)

Besides the specific properties required for the fuel cell applications, this material had to reach a sufficient printability. The substrate should have:

- a high stability, with low dimensional variations during printing,
- and an adequate affinity with the ink, which makes it possible to deposit the ink.

The experimental methods of CCB manufacturing is schematically summarised by the Figure 56.

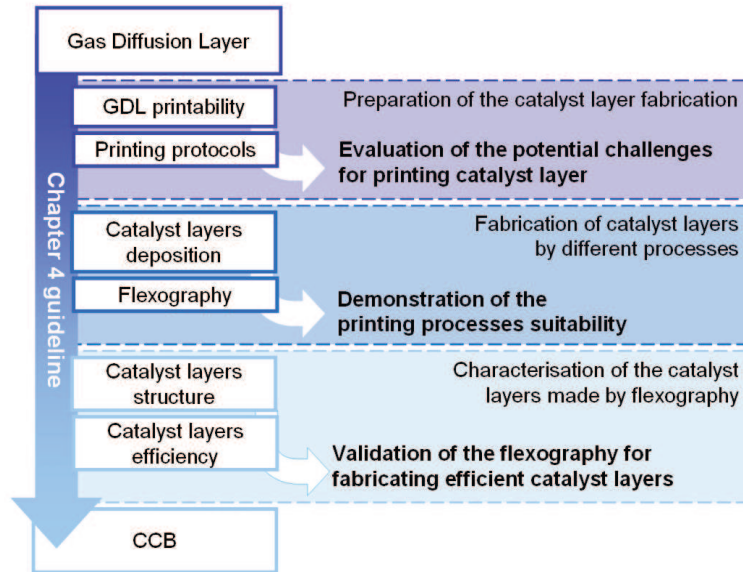


Figure 56 outline of the chapter 4

The first part of the chapter develops the evaluation of the GDL properties as a printing substrate. The main concern focused on the presence of PTFE on the substrate that suggested future affinity problems. After the evaluation of the GDL printability, different deposition techniques were tested for the manufacture of catalyst layers. This step required different inks and protocols depending on the process. Finally, the impacts of each process on the CCB manufacturing were assessed.

The second part deals with the fabrication of CCB made by the flexography printing process. The goal of this work was to enlighten which could be the advantages of the flexography for manufacturing catalyst layer compared to conventional processes.

## 1 Gas diffusion layers printability

The use of GDL as a printing substrate requires investigations on the specificities of this material. For fuel cell application, PTFE is a crucial component for electrochemical properties because it contributes to eject the water from the fuel cell core. However, this component is highly hydrophobic and consequently water-based liquids are repelled when they are deposited on such material. That is why, when using a water-based ink, its presence in a printing substrate is a sign of potential issues for achieving a sufficient printing quality.

Samples were characterised in order to evaluate the GDL printability (section 1.1). Then, they were used for manufacturing CCB (section 1.2):

- by printing processes: screen printing, ink jet and flexography,
- and by two conventional processes: spray and blade coating techniques.

For each process, the inks or dispersions (part 1.2.1) and protocols (part 1.2.2) were adapted to the process. The impact of each process on the catalyst surface structure was observed (1.3) and advantages and limitations were extracted in order to determine the relevance of the processes for manufacturing catalyst layers by CCB protocols (1.3.4).

The catalyst layers manufactured by screen printing, ink-jet, spray and blade coating were made in a partner laboratory (CEA laboratory, Grenoble France) by Anne-Gaëlle Mercier [Mercier *et al.*, 2010].

### 1.1 Evaluation of the GDL printability

The GDL was characterised in order to evaluate the properties that could be critical during printing. Besides the substrate characterisation, commonly performed for printing substrates (1.1.1), two relevant properties are focused:

- the dimensional variations of the material in contact with solvents (part 1.1.2), which could impact the stability of the substrate during the process.
- and the apparent contact angles between drops of solvents and the GDL surface (part 1.1.3), for evaluating the substrate affinity with the ink.

#### 1.1.1 Substrate characterisation

The GDL were characterised as a classic printing substrate such as paper or polymer. The GDL has a thickness of  $247 \pm 2 \mu\text{m}$ , a specific weight of  $102 \pm 2 \text{ g m}^{-2}$ , a bulk of  $2.42 \pm 0.07 \text{ (cm}^3 \text{ g}^{-1}\text{)}$  and a density of  $410 \pm 12 \text{ kg m}^3$ . The use of Bendtsen device showed an air flow permeability of  $22 \pm 1 \text{ cm}^3 \text{ s}^{-1}$ .

The GDL surface roughness was observed, as shown in Figure 57, and measured by extracting surface profile (Figure 58) using the Alicona device.

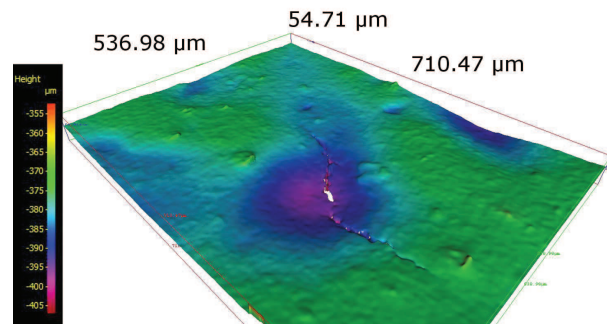


Figure 57 GDL surface observed by Alicona

The surface of the GDL in Figure 57 and Figure 58 appears as mainly smooth with some aggregates in relief and some deep cracks.

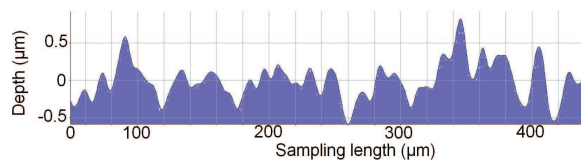


Figure 58 Profile of a GDL sample, LC = 80 μm, sampling length 450 μm

The  $R_a$  (the arithmetic average of the profile absolute values) and the  $R_{max}$  (maximum peak to valley height of roughness) parameters for roughness were equal to 0.2 μm and 1.2 μm respectively, when they were measured on the parts of the surface that is not covered by cracks or aggregates.

### 1.1.2 Discussion on the GDL dimensional stability during printing

Dimensional variations of a printing substrate can be caused by chemical interaction between the ink and the GDL or by physical strains caused by stress or pressure induced by the printing press.

#### 1.1.2.1 Dimensional variations induced by physico-chemical interactions between GDL and the inks

The deposition of an ink by printing onto a substrate is often followed by dimensional variations. In the GDL, the carbon fibres and carbon nanoparticles have a high chemical resistance [Chuang *et al.*, 2008], except for oxidation (or the corrosion occurring in the acid environment of the running fuel cell). Teflon<sup>®</sup>, composed by perfluorinated polymers, is known to be highly inert to almost all chemicals and solvents [Ren *et al.*, 2011].

Moreover, the hydrophobic character of the GDL limits the diffusion and sorption of hydrophilic liquids into the substrate. The inks used in the present study were water-

based. Consequently, during the printing steps, they had a low impact on the GDL components stability, and thus the GDL dimensional variations were neglected during the tests.

### 1.1.2.2 Physical strains applied by the printing system.

The influence of compressive stresses applied on the GDL and on the fuel cell core was already studied [Kumar *et al.*, 2011; Escribano *et al.*, 2006]. These authors showed that when the applied stresses increased from 0.5 to 10 MPa during hot pressing of the MEAs, the electrochemical performances decreased in operating fuel cell.

In the flexography press, compressive stresses are applied onto the substrate in the nip zone. In this work, a GDL sample is printed up to six times when six ink layers were superimposed. That is why, in order to evaluate the impact of the printing step onto the GDL thickness, GDL samples got six times onto the nip zones, similarly to a printing trial. The samples thickness values were measured before the trial, after three and six times through the nip as shown in Table 20.

Table 20 GDL initial thickness and after 3 and 6 times in through the nip

Passages in the nip	Initial	3	6
GDL average thickness	247.9 ± 1.3 μm	247.7 ± 1.2 μm	248.1 ± 1.5 μm

The GDL samples thickness did not vary significantly. Indeed, the pressure applied in the nip zone in flexography was evaluated lower than 0.5 MPa, which is a value widely under the pressure applied during the MEA hot pressing (about 3.5 MPa). Consequently, the substrate compression during printing was also neglected in this study.

In flexography web-press, a tension is applied to the web that may cause dimensional variations. However, in these studies, Flexiproof is a sheet fed device. At each trial, the samples were taped on the printing cylinders. The samples were just put in contact with the cylinder. Poor tensile stresses were applied and therefore, neither length nor width variations were measured as shown in Table 21.

Table 21 GDL initial width and length and after 3 and 6 times in through the nip

Passages in the nip	Initial	3	6
GDL average width	71 ± 2 mm	72 ± 3 mm	70 ± 3 mm
GDL average length	209 ± 4 mm	210 ± 3 mm	208 ± 4 mm

### 1.1.3 GDL interaction with solvents

The surface energy of the GDL was measured using seven solvents. The values of surface tension of these liquids are detailed in Table 22.

Table 22 Surface tension and corresponding polar and dispersive contributions of solvents

Solvents	$\gamma_L$ (mN m <sup>-1</sup> at 20°C)	$\gamma_L^d$ (mN m <sup>-1</sup> at 20°C)	$\gamma_L^p$ (mN m <sup>-1</sup> at 20°C)
Water	72,8	21,8	51
Glycerol	63	33	30
Ethylene glycol	48,3	29,3	19
Hexadecane	27,6	27,6	0
1-Bromonaphtalen	44,6	44,6	0
DMSO (Dimethyl sulfoxide)	44	36	8
Diiodomethane	50	47,4	2,6

The average values of at least ten apparent contact angles of all sorts of liquids onto the GDL are given in Figure 59.

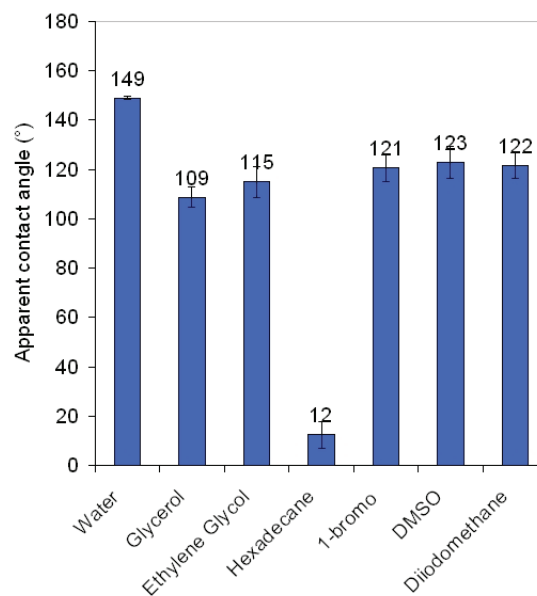


Figure 59 Average apparent contact angles of liquids on GDL samples

In Figure 59, except for hexadecane, all the solvents showed apparent contact angle values above 90°. These high values indicate a highly hydrophobic surface because of the presence of Teflon<sup>®</sup>. Therefore, the wetting of these liquids on the GDL surface was considered as poor.

On the contrary, the hexadecane droplets had low contact angles onto the GDLs. The liquid spread onto the surface of the samples and showed a high wetting.

The high hydrophobic character of the GDL indicates that the surface energy has a low polar contribution. The affinity with non polar solvent was expected to be good.

Two liquids were tested that are only dispersive solvents: hexadecane and 1-bromonaphtalene. They had contact angles reaching  $12 \pm 5^\circ$  and  $121 \pm 5^\circ$  respectively. As expected, the hexadecane spread onto the surface. However, the 1-bromonaphtale dewetted the microporous layer surface. Such behaviour can be explained considering the

Owens-Wendt equation detailed in chapter 2. Indeed, the lower is the contact angle, the closer are the surface energy contributions of the solid to the surface tension contributions of the liquid.

Consequently, the surface energy of the microporous layer had contributions that had closer values to those of the hexadecane than to those of the 1-bromonaphtalene.

#### 1.1.4 Surface energy estimation

The estimation of the surface energy  $\gamma_s$  used the Owens-Wendt model using Equ. 23 .

$$\frac{\gamma_L \cdot (1 + \cos(\theta))}{2 \cdot \sqrt{\gamma_L^d}} = \sqrt{\frac{\gamma_L^p}{\gamma_L^d}} \cdot \sqrt{\gamma_s^p} + \sqrt{\gamma_s^d} \quad \text{Equ. 23}$$

The parameters  $\gamma_L$ ,  $\gamma_L^p$  and  $\gamma_L^d$  (mN m<sup>-1</sup>) of the seven solvents were given in Table 22. The unknown parameters were  $\gamma_s^p$  and  $\gamma_s^d$  of the GDL surface. Both were evaluated by linear regression  $Y = a \cdot X + b$ , with Equ. 24:

$$Y = \frac{\gamma_L \cdot (1 + \cos(\theta))}{2 \cdot \sqrt{\gamma_L^d}} \quad \text{Equ. 24}$$

and Equ 25:

$$X = \sqrt{\frac{\gamma_L^p}{\gamma_L^d}} \quad \text{Equ. 25}$$

Y was plotted as a function of X in Figure 60 for each of the seven tested solvents, and a linear regression was calculated, which is drawn in dotted line.

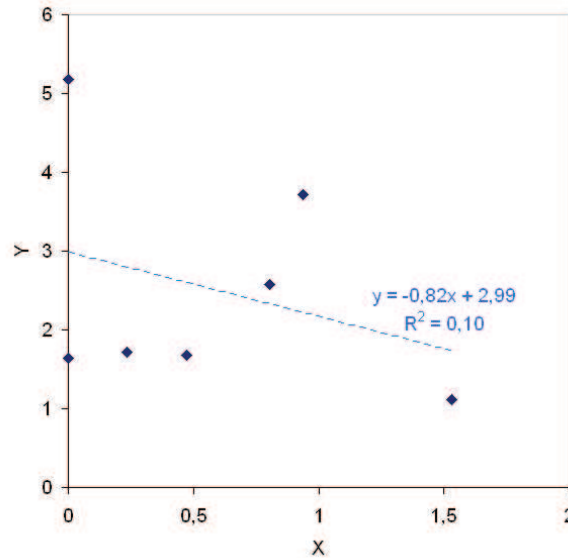


Figure 60 Linear regression used for calculation polar and dispersive contributions of the surface energy of GDL samples

The standard deviation values of a and b were obtained using the excel equation “droitereg”. The values are reported in Table 23. The standard deviations were used for

calculating the maximal and minimal values of a and b, noted  $a_{\max}$ ,  $a_{\min}$ ,  $b_{\max}$  and  $b_{\min}$ . Then, each coefficient  $a_{\max}$  and  $a_{\min}$  (respectively  $b_{\max}$  and  $b_{\min}$ ) were used for calculating maximal and minimal values of  $\gamma_s^p$  (respectively  $\gamma_s^d$ ) (Equ. 26). The results are given in Table 23.

$$\begin{aligned} a^2 &= \gamma_s^p \\ b^2 &= \gamma_s^d \end{aligned} \quad \text{Equ. 26}$$

Table 23 Calculations using a and b coefficients

Coefficients	Value	Extremum value		Squared extremum value	
a	$-0.8 \pm 1.1$	$a_{\min}$	-1.9	$(a_{\min})^2$	3.7
		$a_{\max}$	0.3	$(a_{\max})^2$	0.1
b	$3.0 \pm 0.8$	$b_{\min}$	2.1	$(b_{\min})^2$	4.6
		$b_{\max}$	3.8	$(b_{\max})^2$	15

Table 24 Estimation of the surface energy, and its polar and dispersive contributions

Surface energy value	Minimal value	Maximal value
$\gamma_s^p$ (mN m <sup>-1</sup> )	0.1	3.7
$\gamma_s^d$ (mN m <sup>-1</sup> )	4.6	15
$\gamma_s$ (mN m <sup>-1</sup> )	4.7	18

In Table 24, the polar contribution ranged from 0.1 to 3.7 mN m<sup>-1</sup>, the dispersive contribution from 4.6 to 15 mN m<sup>-1</sup> and the surface energy of the microporous layer of the GDL varies from 4.7 to 18 mN m<sup>-1</sup>. The surface energy and its contributions ranged about one order of magnitude.

Such a low precision was expected considering the poor linear regression of Figure 60. Moreover, the use of Owens-Wendt model requires the value of the Young's contact angle, which is obtained on a chemically homogeneous, smooth and non-permeable surface. However, this was not the case when depositing drops on the macroporous layer, because the GDL surface was composed of carbon powder and Teflon<sup>®</sup> polymer and consequently, was chemically heterogeneous. Moreover, the surface has a permeable and rough structure with chemical heterogeneities as it was described in part 1.1.1., which are properties that influence the apparent contact angle. This apparent contact angle is a great advantage for rapid evaluation of the affinity between a liquid and such a surface. However, it is hardly applicable in the Owens-Wendt theory for determining the surface energy of the substrate.

Whatever the relevance of the technique, by apparent contact angles of Figure 59 in part 1.1.3 or by Owens-Wendt in this section, the polar contribution of the surface energy was estimated to be really low, and the surface of the macroporous layer had a substantial hydrophobic character.

### 1.1.5 GDL affinity with flexography ink

Complementary to the evaluation of the affinity of GDL surface with solvents and the estimation of its surface energy evaluation, the affinity between flexography inks ( $I_{33}$ ) and the GDL surface was quantified. For that purpose, apparent contact angle measurements were performed by depositing droplets of the flexography ink on GDL samples. Moreover, in order to deeply understand the impact of ink components on the affinity with the GDL surface, the ink vehicle and the major ink components were also deposited onto GDL samples. The fraction values of these components are given in weight by weight percentage (w/w %) as respect to the all ink vehicle in Table 25.

Table 25 Formulation of the ink vehicle

Ink vehicle components	(w/w %)
Nafion <sup>®</sup> dispersion	40.9
Water	13.6 ± 0.8
Polymer content	8.5 ± 0.5
1-propanol	17.6 ± 0.8
Water	59.1

Droplets of five liquids were deposited onto the GDL 24BC:

- pure Nafion<sup>®</sup>,
- the ink vehicle composed of 40.9 w/w % of Nafion<sup>®</sup> dispersion and 59.1 w/w % of water,
- pure 1-propanol,
- pure water,
- and the ink.

The contact angles of these five liquids deposited on the GDL 24 BC are presented in Figure 3, which shows the influence of each component of the catalyst layer ink on the affinity between the ink and the GDL.

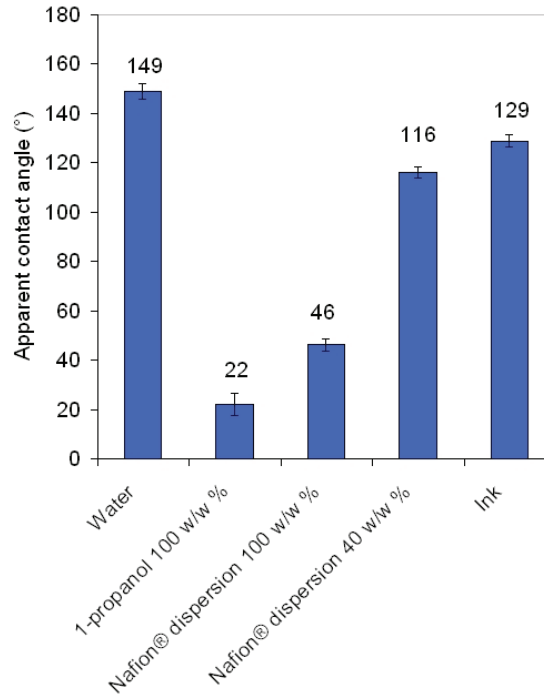


Figure 61 Contact angles between each component of the catalyst layer ink and the GDL 24BC

The pure water highlighted the strong hydrophobic behaviour of the 5 w/w % PTFE microporous layer of the GDL (contact angle closed to  $150^\circ$  as measured before in section 1.1.3).

The other tested liquids had different behaviours on the GDL surface:

- pure 1-propanol:

Similarly to the hexadecane behaviour noticed in section 1.1.3, the 1-propanol completely wetted the surface, since the contact angle was equal to  $22^\circ$ .

- pure Nafion® dispersion:

The Nafion® dispersion was composed of Nafion®, of 19.6 w/w % 1-propanol and 18.2 w/w % of water. The apparent contact angle of Nafion® dispersion was equal to  $46^\circ$ . Its affinity with the GDL surface was lower than the one of the 1-propanol but remained under  $90^\circ$  and showed a good wetting behaviour on the GDL.

- Nafion® dispersion at 40 w/w%:

The addition of water in the Nafion dispersion, such as in the ink formulation (40.9 w/w % of Nafion dispersion in water), tended to drastically increase the apparent contact angle of the dispersion from  $46$  to  $116^\circ$ . This dispersion had a contact angle higher than  $90^\circ$ . This indicates a poor affinity that limits the wetting of the GDL surface.

- ink:

When incorporating the carbon supported platinum into the ink the contact angle reached  $129^\circ$ . Consequently, the carbon catalyst reduced the affinity of the ink on the GDL. Water, the major component, decreased the wetting of the ink and the substrate.

Consequence of the low wettability of the ink, the printability of the GDL by this ink is expected to be poor.

### 1.1.6 Conclusion on the evaluation of the GDL printability

The substrate characteristics that influence the GDL printability are highlighted in Table 26.

Table 26 influence of the GDL characteristics on its printability

Surface and bulk properties		Potentially improves the GDL printability	Potentially limits the GDL printability
Microporous surface properties	Roughness	$R_a = 0.2 \mu\text{m}$ $R_{\text{max}} = 1.2 \mu\text{m}$	smooth surface with cracks and aggregates
	Wettability	Good affinity with non-polar solvent $\theta_{\text{Hexadecane}} = 10 \text{ to } 20^\circ$	Poor affinity with polar solvents $\theta_{\text{Water}} = 149 \pm 1^\circ$ $\theta_{\text{Glycerol}} = 110 \pm 4^\circ$ $\theta_{\text{Ethylene glycol}} = 115 \pm 6^\circ$ $\theta_{\text{1-Bromo}} = 120 \pm 5^\circ$ $\theta_{\text{DMSO}} = 123 \pm 5^\circ$ $\theta_{\text{Diiodomethane}} = 122 \pm 2^\circ$ Poor affinity with water-based ink such as $I_{33}$ mainly due to the water vehicle $\theta_{\text{Water}} = 129 \pm 2^\circ$
Bulk properties	Components	high chemical and dimensional stability of the carbon fibres network	hydrophobic behaviour of the PTFE polymer
	Permeability	$21.7 \pm 1.0 \text{ cm}^3 \text{ s}^{-1}$	

As regards to this table, the main issue in CCB manufacturing by printing processes dealt with the hydrophobicity of the surface of the printing substrate.

## 1.2 Fabrication of CCB By different depositions techniques

Manufacturing catalyst layer required:

- the formulation of inks, providing functional characteristics (part 1.2.1),
- the adaptation of the printing protocol, in order to reach the physical characteristics (catalyst layer geometry, ink film thickness...) (part 1.2.2).

### 1.2.1 Inks and dispersions

As detailed in the chapter 2, the water was chosen as the major component for the ink vehicle of flexography inks. The same reasons led to formulate water-based inks and dispersion for the other deposition processes. The selected components insuring functional properties of the inks were Nafion<sup>®</sup> polymer dispersion (22 w/w % Nafion) in aliphatic alcohols and deionised water (DuPont TM, Wilmington, USA), and carbon-supported platinum catalysts (Tanaka Kikinzo, Tokyo, Japan) with 45.4 w/w % platinum as regards to the carbon-supported platinum. Because the cost of the functional components (platinum catalyst and Nafion<sup>®</sup> ionomer) is significant on the total catalyst layer production cost, the inks and dispersions were described by their solid content which are reported in Table 27.

Table 27 General inks formulation

Ink components	Ink vehicle formulation	Solid content (w/w %)
Carbon supported catalyst (w/w ink %)	About 70 w/w <sup>0</sup> % of the solid content	99
Carbon (w/w of catalyst %)	54.6	
Platinum (w/w of catalyst %)	45.4	
Nafion <sup>®</sup> dispersion (w/w of ink vehicle %)	About 30 w/w <sup>0</sup> % of the solid content	21 ± 1
Water (w/w of dispersion %)	34 ± 2	
Polymer content (w/w of dispersion %)	21 ± 1	
1-propanol (w/w of dispersion %)	46 ± 2	
Water (w/w of ink vehicle %)	Depending on the process	0

As shown in the chapter 1, the average ionomer content in the dried catalyst layer was about 30 w/w %.

The solid content of each ink was calculated considering the mass and the solid content of each component that composed the ink (as shown in Table 27). For example, for each gram of Nafion<sup>®</sup> dispersion incorporated into the ink, 0.21 ± 0.01 g of Nafion<sup>®</sup> polymers were included into the ink solid content. The same way, each gram of catalyst led to incorporate 0.449 g of platinum nanoparticles in the ink solid content. The solid content in the inks was adjusted to obtained inks with suitable properties for each deposition process as described in Table 28.

Table 28 Solid content of the ink as regards to the process of deposition

Types of process	Solid content of the ink (w/w ink %)
Conventional processes	
Blade coating	18.5
Spray	5.2
Printing processes	
Screen printing	20
Ink jet	1
Flexography	26 correspond to ink $I_{33}$

### 1.2.2 Deposition protocols

The sequence of deposition highly depends on the process characteristics, as explained in Table 29.

Table 29 Comparison of the deposition process regarding their deposition type and their pattern reproduction

Deposition and reproduction types	Process with a mask for reproducing the pattern	Maks-less process for reproducing the pattern
Monolayer deposition	Blade coating	Screen printing
Specific deposition	Spray	Ink-jet

The sequence of deposition of blade coating and screen printing was a monolayer deposition. It consisted in depositing only one ink layer with the required amount of ink. As detailed in the literature review, spray and blade coating techniques require a mask in order to delimit the catalyst layers edges, while printing processes are able to precisely depositing the ink where required.

The spray technique had a specific deposition technique. The GDL (Figure 62.1) was covered by a mask (Figure 62.2), the cone of dispersion scanned the substrate in one direction (Figure 62.3), then in the perpendicular direction (Figure 62.4), with overlapping the previous passage in order to cover the sample with the required and homogeneous quantity of ink. Finally, the mask was removed (Figure 62.5) and the CCB was dried (Figure 62.6).

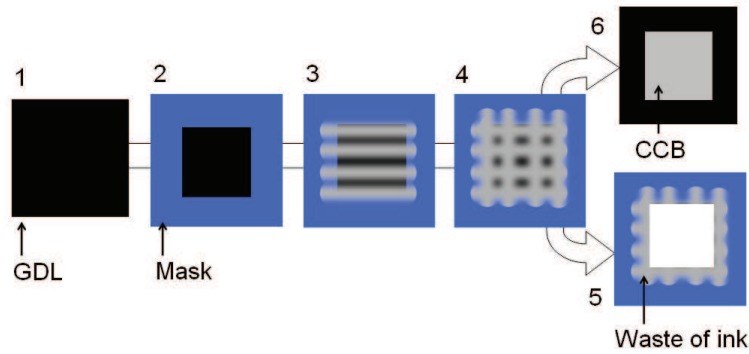


Figure 62 Fabrication of a CCB by spray deposition, 1. GDL, 2. deposition of a mask for demarcating the catalyst layer, 3. one direction spraying, 4. perpendicular direction spraying, 5. removing of the mask covered with wasted ink and 6. CCB

The ink-jet technique required the deposition of drops following a grid-pattern on all the surface of the catalyst layer. The pattern was repeated in order to fill the non-printed area until the whole surface is covered with ink [Mercier *et al.*, 2010].

Besides, these different deposition sequences induced specific catalyst layer characteristics. They are summarised in Table 30.

Table 30 Characteristics of the deposition techniques that have an influence on the manufacturing catalyst layer

Deposition techniques		Advantages	Limiting points for manufacturing catalyst layers
Conventional processes	Blade coating	One passage deposits 0.2 or 0.4 $\text{mg}_{\text{Pt}}\cdot\text{cm}^{-2}$	Unable to deposit low ink loadings Require a mask
	Spray	Enable to deposit small ink quantity	Required several spraying for completely covering the deposition zone demarcated by the mask
Printing processes	Screen printing	One passage deposits 0.2 or 0.4 $\text{mg}_{\text{Pt}}\cdot\text{cm}^{-2}$ Mask-less process	Unable to deposit small ink loadings
	Ink jet	Accuracy of deposition Mask-less process	The ink film is composed of several drops for covering the printing zone

As a comparison, flexography used a multilayer protocol, which allows superimposition of ink layers with a small quantity of ink up to the required ink loading.

The catalyst layers were produced by CCB with the five processes. The platinum loading and figure number of the surface views of the catalyst layers are detailed in Table 31.

Table 31 Samples reference and characteristics

Types of process		Sample	Platinum loading ( $\text{mg}_{\text{Pt}} \text{cm}^{-2}$ )	Figure
Conventional	Blade coating	BC 1	0.22	Figure 63
		BC 2	0.46	Figure 64
Printing processes	Spray	S 1	0.02	Figure 67
		S 2	0.20	Figure 68
	Screen printing	SP 1	0.09	Figure 65
		SP 2	0.11	Figure 66
	Ink jet	IJ 1	0.10	Figure 69
		IJ 2	0.20	Figure 70
Flexography	F 1	0.07	Figure 71	
	F 2	0.26	Figure 72	

### 1.3 Comparison of the catalyst layers surface as regards to the deposition process

#### 1.3.1 Monolayer deposition: blade coating and screen printing

From Figure 63 to Figure 66, the catalyst layer made by blade coating and screen printing show surfaces that were uniformly covered by the ink. Therefore, no printability problems neither platinum heterogeneity are visible on the pictures.

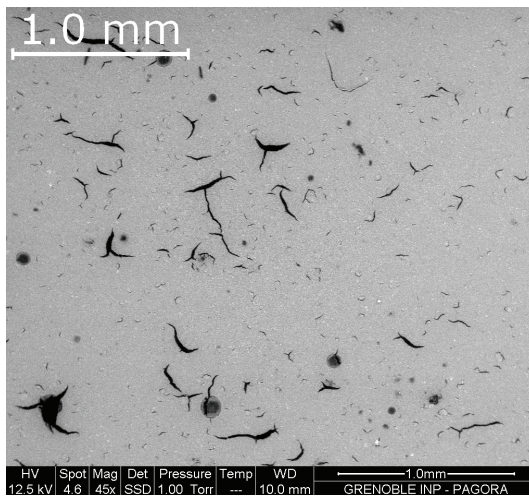


Figure 63 Blade coated catalyst layer 0.22  $\text{mg}_{\text{Pt}} \text{cm}^{-2}$  (sample BC 1)

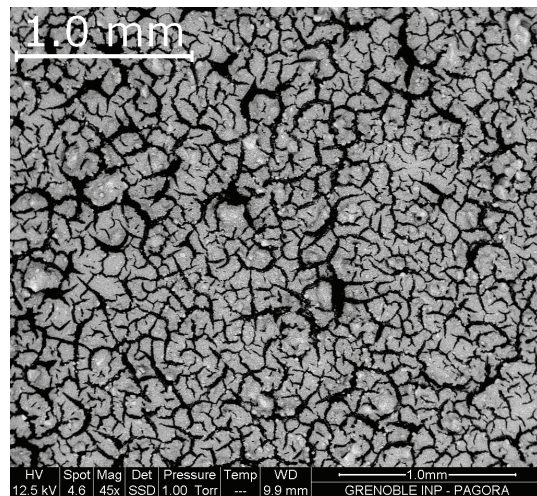


Figure 64 Blade coated catalyst layer 0.46  $\text{mg}_{\text{Pt}} \text{cm}^{-2}$  (sample BC 2) (BSE)

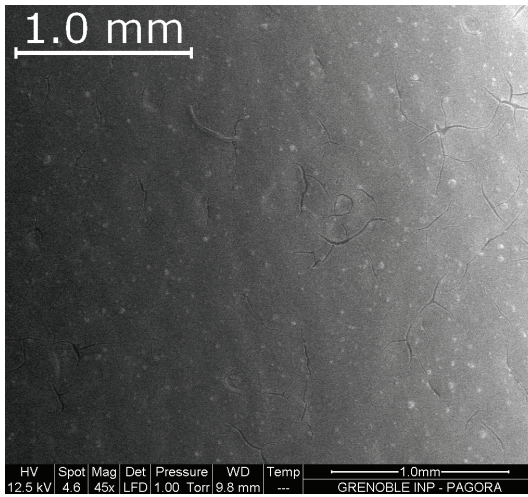


Figure 65 Screen printed catalyst layer 0.09  $\text{mg}_{\text{Pt}} \text{cm}^{-2}$  (sample SP 1)

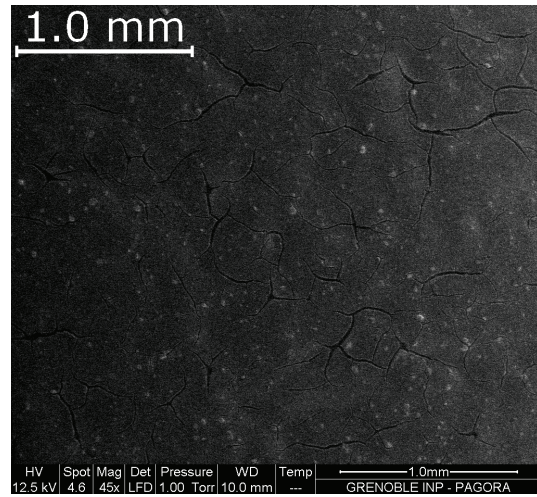


Figure 66 Screen printed catalyst layer 0.11  $\text{mg}_{\text{Pt}} \text{cm}^{-2}$  (sample SP 2) BSE

However, cracks covered the surface of the catalyst layers, especially on the catalyst layer loaded at  $0.46 \text{ mg}_{\text{Pt}} \text{cm}^{-2}$ .

### 1.3.2 Processes with specific deposition: spray and ink jet

Figure 67 and Figure 68 show surface of catalyst layers made by spray technique.

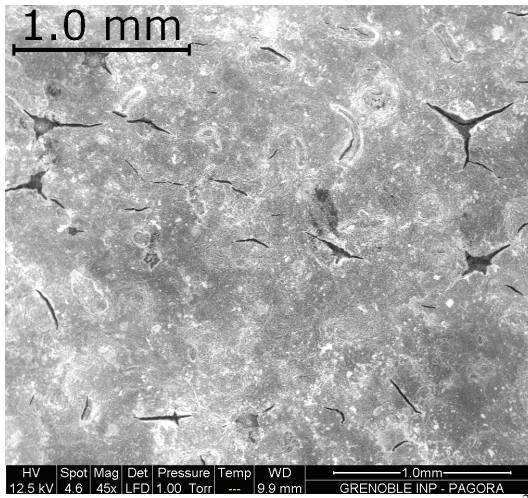


Figure 67 Sprayed catalyst layer  $0.020 \text{ mg}_{\text{Pt}} \text{cm}^{-2}$  (sample S 1) BSE

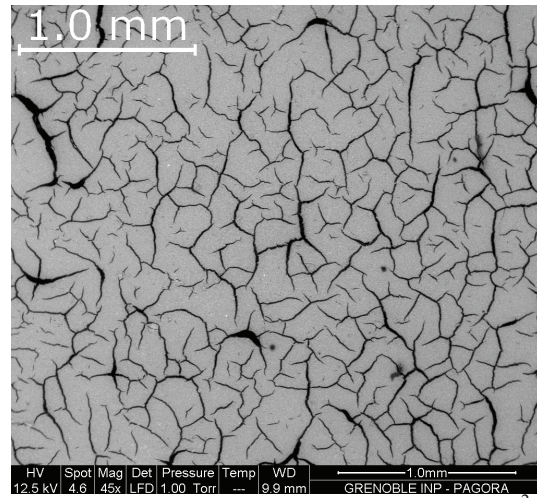


Figure 68 Sprayed catalyst layer  $0.20 \text{ mg}_{\text{Pt}} \text{cm}^{-2}$  (sample S 2) BSE

At very low platinum loading ( $0.02 \text{ mg}_{\text{Pt}} \text{cm}^{-2}$ ), the platinum element was not homogeneously covering the surface of the substrate. This heterogeneity could be caused by an ink poorly dispersed or by an ink film that was so thin that the ink layer was not able to cover the entire surface. At  $0.20 \text{ mg}_{\text{Pt}} \text{cm}^{-2}$ , the surface was homogeneously covered by platinum, but also by cracks.

As presented in Figure 69 and Figure 70, the surface of the catalyst layers manufactured by ink jet process had some lack of ink.

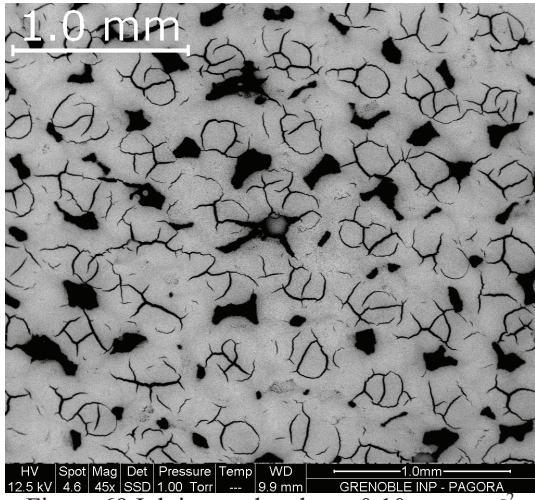


Figure 69 Ink jet catalyst layer  $0.10 \text{ mg}_{\text{Pt}} \text{ cm}^{-2}$   
(sample IJ 1)

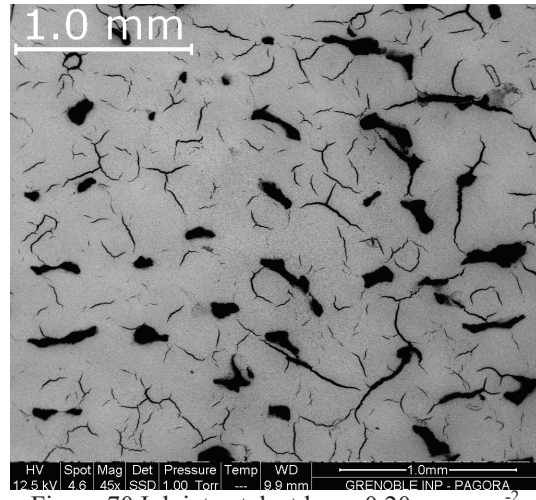


Figure 70 Ink jet catalyst layer  $0.20 \text{ mg}_{\text{Pt}} \text{ cm}^{-2}$   
(sample IJ 2)

Moreover, excess of ink seems to be frequently localised where the ink drops were ejected onto the GDL. The drops had not a sufficient affinity with the substrate to spread and then could not form a continuous ink film.

Cracks are also observed on the surface of this catalyst layer. They are located at the top of the non-coalesced drops.

### 1.3.3 Process with multilayer deposition: flexography

The surface of the catalyst layer produced by flexography presents a printing defect called marbling. This defect typically occurs when the affinity between the ink and the substrate is poor as confirmed by the contact angle measurements (see section 1.1.5). Moreover, at higher platinum content ( $0.26 \text{ mg}_{\text{Pt}} \text{ cm}^{-2}$ ), cracks appeared on the printed surface. Further studies were made on this flexography defect. They are presented in next part 2.

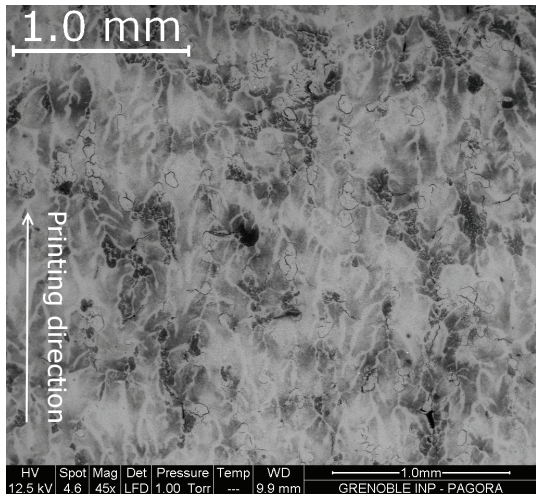


Figure 71 Flexography made catalyst layer 0.07  $\text{mg}_{\text{Pt}} \text{cm}^{-2}$  (sample F 1)

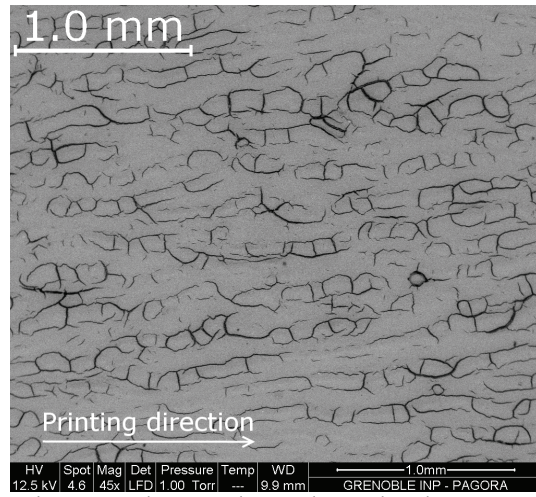


Figure 72 Flexography made catalyst layer 0.26  $\text{mg}_{\text{Pt}} \text{cm}^{-2}$  (sample F 2)

### 1.3.4 Conclusion on the evaluation of the printing process relevance for catalyst layer manufacturing

The defects on the catalyst layers surface were observed when low platinum loading was deposited onto the substrate:

- Affinity problems were found on catalyst layers made by flexography and ink jet, loaded at 0.07 (Figure 69) and 0.10 (Figure 71)  $\text{mg}_{\text{Pt}} \text{cm}^{-2}$ . The poor affinity induced a bad wetting of the inks onto the GDL surface, which led to either marbling defect or drops non-coalescence.
- Catalyst bad dispersion was observed on Figure 67 loaded at 0.02  $\text{mg}_{\text{Pt}} \text{cm}^{-2}$

These defects appeared on catalyst layers made by processes with specific or multilayer deposition protocol. Indeed, in the case of processes with a monolayer protocol, the surfaces appeared more homogeneous, even at loading equal to 0.09 in Figure 65. The type of deposition protocol induced specific defects, which were highlighted at low platinum loading. The surface defects tended to be concealed when the platinum loading was increasing. However, on catalyst layer with platinum loading higher than 0.2  $\text{mg}_{\text{Pt}} \text{cm}^{-2}$ , and whatever the deposition protocol, blade coating (Figure 64), flexography (Figure 72) and spray (Figure 68) cracks appeared on catalyst layers.

## 1.4 Conclusion

The GDL ability to be printed was evaluated by measuring physical and physico-chemical properties of the surface and of the bulk of the GDL. The impact of each of these GDL characteristics on its printability is detailed in Table 26. The main parameter that potentially limits the GDL printability was the surface hydrophobicity. The affinity

between an ink for flexography and the substrate was evaluated by apparent contact angle measurement (equal to  $129^\circ$ ) and thus shows a poor wetting.

In conventional printing, for such a case, the ink formulation should be chosen to suit to the surface properties. However, considering the applications, the incorporation of solvents into the ink could pollute the catalyst layer and decrease its electrochemical properties. Consequently, the inks were formulated using water as the major solvent, with different solid contents depending on the process.

In order to manufacture catalyst layers, the inks were deposited by the five techniques tested (blade coating, spray, screen printing, ink jet and flexography). Each process had different deposition protocol for reaching a given platinum loading (and so an ink loading): monolayer, multilayer and specific deposition were tested. The observations of the surface of the manufactured catalyst layers demonstrated the impact of the poor wettability of the ink. It induced defects that are typical from the process, which were enhanced at low platinum loading. At higher platinum loading, cracks covered the catalyst layer, whatever the deposition process used for their manufacturing.

Compared to the four processes already used in the fuel cell field, the flexography gave promising results. In order to develop the advantages of this process, the following part focuses on this continuous deposition process.

## 2 Gas diffusion electrodes made by flexography

In part 1 of this chapter, an ink was formulated and was deposited by a multilayer protocol using flexography process. Some defects were observed on the catalyst layer.

In order to investigate the flexography relevance for manufacturing catalyst layer, this section is dedicated to the evaluation of the parameters that impacted both the microstructure and the electrochemical performances of the catalyst layer, especially the ink affinity with the GDL and the multilayer protocol (2.1).

Besides, the relation between microstructure and electrochemical properties of catalyst layers made either by flexography or by blade coating was compared (2.2) and correlated (2.3).

### 2.1 Influence of the flexography multilayer protocol on the catalyst layer physical structure

In order to validate the transferability of the water-based ink onto the highly hydrophobic GDL, the ink was deposited on GDL by the superimposition of 1 to 5 ink layers using the Flexiproof device. SEM observations were performed on these catalyst layers. They are presented in Figure 73.

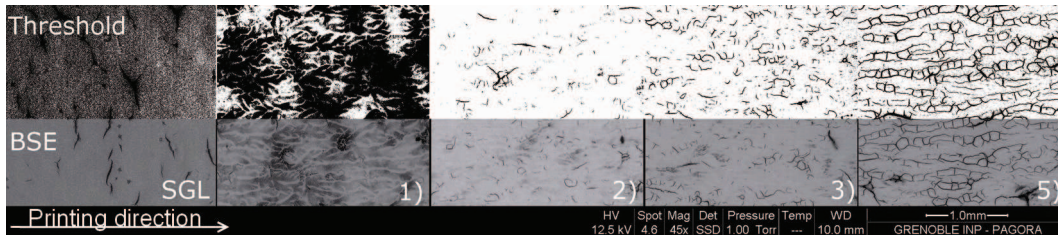


Figure 73 BSE SEM and threshold observations of catalyst layer surface during manufacturing by flexography process: influence of the superimposition of ink layer on the surface state 1) one layer of ink, 2) two superimposed layers, 3) three layers and 5) five layers

When one ink layer was transferred onto the GDL, a patterning occurred with a marbling appearance. This defect is a typical printing problem, well known as indicating a lack of affinity between the ink and the surface. Thus, the ink film splitting in the nip was not favourable to ink transfer. The ink was only partially transferred. This led to an inhomogeneous ink layer thickness. This patterning had a main direction, parallel to the printing direction with sidelines. This observation confirms the poor affinity between the ink and the substrate that was previously described. Catalyst layers made by the superimposition of 2 or 3 ink layers do not show marbling defect anymore. It means that there was a sufficient amount of platinum on the entire SGL surface to be detected by the BSE device. However, thickness heterogeneities may have remained.

In Figure 73.5, a second major defect is observable: the layer cracked. Crack structure and modelling were the topic of numerous studies since material desiccation is a common issue [Cohen *et al.*, 2009]. Mud cracks [Gaul *et al.*, 2011], polymers [Weh and Venthur, 2004], and calcium carbonate paste [Kitsunezaki, 2006] drying had been investigated. The more ink layers were superimposed, the more the cracks are visible. Due to gradients of solvent evaporation or temperature, the layer structure was submitted to tensile stresses. The energy was released by structure brakes. Heterogeneities were described as brake precursors in the case of shrinkage-cracks [Goehring *et al.*, 2009]. Indeed, a strong thickness heterogeneity existed, created by the marbling patterning. One hypothesis was that the marbling defects, which induced thickness variations in the first layers of the catalyst layer, could also act as shrinkage-cracks precursors.

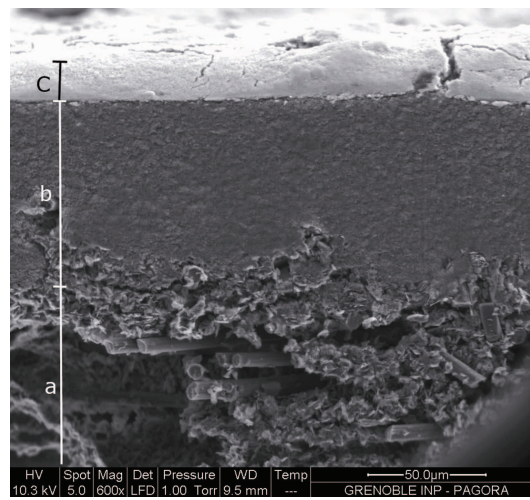


Figure 74 BSE CCB cross view, (a) macroporous, (b) microporous and (c) printed catalyst layers cross section

Figure 74 is a cross sectional view of the CCB presented in Figure 73.5. It was made by the superimposition of 5 ink layers. Despite the printing defects observed in Figure 73.5 the catalyst layer continuously covered the highly hydrophobic gas diffusion layer. The catalyst layer thickness, evaluated by difference of the thickness value between the GDL and the CCB, was equal to  $14.5 \pm 0.4 \mu\text{m}$  and reached a platinum loading value of  $0.26 \text{ mg}_{\text{Pt}} \text{ cm}^{-2}$ .

The printing results show that the high hydrophobic behaviour of the GDL was not a limiting parameter of GDL printability by contact process such as flexography. The ink follows three steps in the nip of printing process with contact: (i) contact, (ii) wetting and (iii) anchorage. Whereas the contact and wetting were poor, the pressure applied during the ink transfer forced the ink into the pores of the substrate. The air contained in the pores was drained due to the high air permeability of GDL.

The influence of the marbling and the cracking defects on the physical and electrochemical properties of the catalyst layer were measured and are discussed in the following parts.

### 2.1.1 Catalyst layers fabrication

Catalyst layers were manufactured by blade coating and flexography. As in the part 1 of this chapter, monolayer and multilayers protocols were respectively applied with the two processes.

Figure 76 shows the variation of the platinum loading of the catalyst layer with the number of superimposed ink layers that composed the catalyst layer.

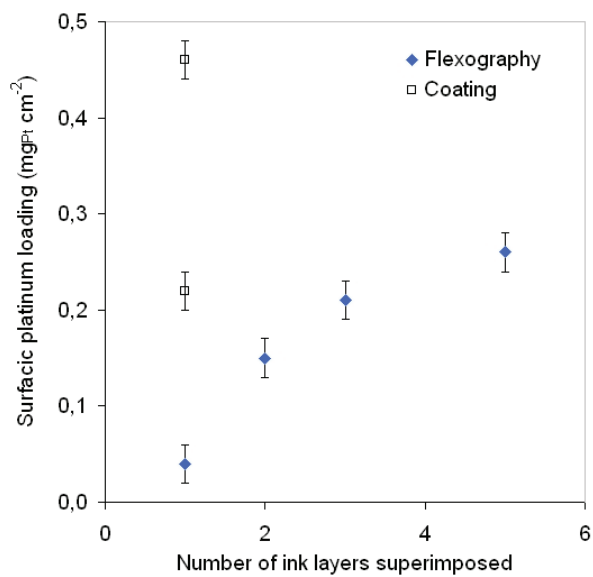


Figure 75 Platinum loading of CCBs obtained by flexography and blade coating as a function of the number of ink layers superimposed

In flexography, the superimposition of one to five ink layers realised catalyst layers with platinum loading that varied from  $0.04 \pm 0.02$  to  $0.26 \pm 0.02$  mg cm<sup>-2</sup>, with thickness values varying from  $0.50 \pm 0.01$  to  $14.2 \pm 0.3$  μm. By blade coating, the catalyst layers were obtained by monolayer deposition. After drying, the catalyst layer reached  $0.22 \pm 0.02$  and  $0.46 \pm 0.02$  mg cm<sup>-2</sup>. These values are standard platinum loading for respectively anode and cathode catalyst layers. The thickness values of these catalyst layers were equal to  $9.3 \pm 0.1$  and  $32.6 \pm 0.8$  μm.

The details of the platinum loading and thickness values of the catalyst layers are given in Table 32.

Table 32 Catalyst layers characteristics

Process	Flexography				Blade coating	
	1	2	3	5	1	1
Number of layers deposited						
Platinum loading ( $\text{mg}_{\text{Pt}} \text{cm}^{-2}$ )	$0.04 \pm 0.02$	$0.15 \pm 0.02$	$0.21 \pm 0.02$	$0.26 \pm 0.02$	$0.22 \pm 0.02$	$0.46 \pm 0.02$
Thickness ( $\mu\text{m}$ )	$0.5 \pm 0.01$	$3.3 \pm 0.1$	$9.3 \pm 0.2$	$14.2 \pm 0.3$	$9.3 \pm 0.1$	$32.6 \pm 0.8$
Platinum loading ( $\text{mg}_{\text{Pt}} \text{cm}^{-3}$ )	$800 \pm 200$	$460 \pm 60$	$240 \pm 40$	$180 \pm 20$	$240 \pm 50$	$140 \pm 20$

The volumetric platinum loading is also detailed in this table; it evaluated the platinum density of the catalyst layer. This parameter is plotted as regards to the surfacic platinum loading in Figure 76.

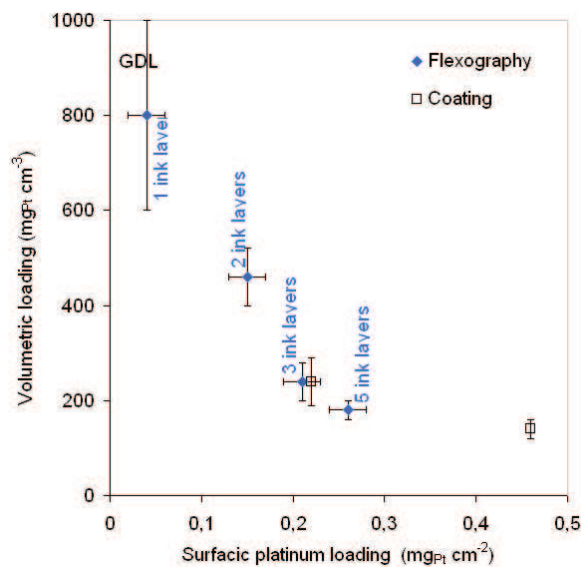


Figure 76 Volumetric loading as a function of the surfacic platinum loading of catalyst layers obtained by flexography and blade coating

The platinum density of the catalyst layers made by flexography and blade coating decreased and followed similar trends when the surfacic platinum loading increased. Such behaviour was not related to the process of deposition, but it could rather traduce a change in microstructural properties of the catalyst layer. In order to complete this observation, the permeability of the catalyst layers is measured in the following part.

### 2.1.2 Catalyst layer permeability

Figure 77 highlights the intrinsic permeability variations of the GDE ( $K_{GDE}$ ) as a function of surfacic platinum loading of catalyst layers.

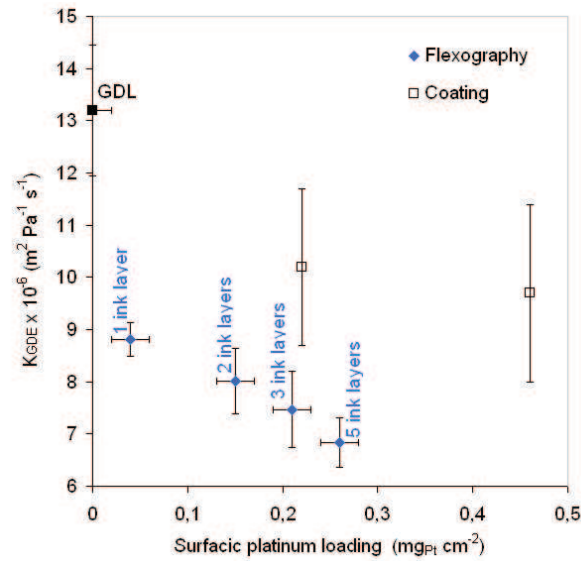


Figure 77 Permeability of GDL and GDEs made by flexography and by blade coating calculated from Bendtsen measurements as a function of their platinum loading

$K_{GDE}$  parameter represents the value of the average permeability for a unit of volume of GDE (the GDL with a catalyst layer). The values are given in Table 33.

Table 33 Intrinsic permeability values of the GDEs and catalyst layers

Process	GDL	Flexography				Blade coating	
Number of layers deposited		1	2	3	5 (a)	1 (c)	1 (b)
Platinum loading ( $\text{mg}_{\text{Pt}} \text{cm}^{-2}$ )		$0.04 \pm 0.02$	$0.15 \pm 0.02$	$0.21 \pm 0.02$	$0.26 \pm 0.02$	$0.22 \pm 0.02$	$0.46 \pm 0.02$
$K_{GDE}$ ( $\text{m}^2 \text{s}^{-1} \text{Pa}^{-1}$ ) $10^{-6}$	$13.2 \pm 1.2$	$8.8 \pm 0.3$	$8.0 \pm 0.6$	$7.5 \pm 0.7$	$6.8 \pm 0.5$	$10.2 \pm 1.5$	$9.7 \pm 1.7$
$K_{CL}$ ( $\text{m}^2 \text{s}^{-1} \text{Pa}^{-1}$ ) $10^{-7}$		$0.5 \pm 1.1$	$2.7 \pm 1.2$	$6.0 \pm 1.6$	$7.3 \pm 1.3$	$12 \pm 6.1$	$38 \pm 15$

As expected, the deposition of catalyst layer using the two techniques at the surface of the GDL led to decrease the GDE intrinsic permeability. The blade coating made GDEs that were more permeable than those made by flexography. The GDE made by flexography were less and less permeable when more ink layers were superimposed at the GDL surface.

The intrinsic permeability values of the catalyst layers,  $K_{CL}$ , were calculated and are reported in Figure 78 and Table 33.

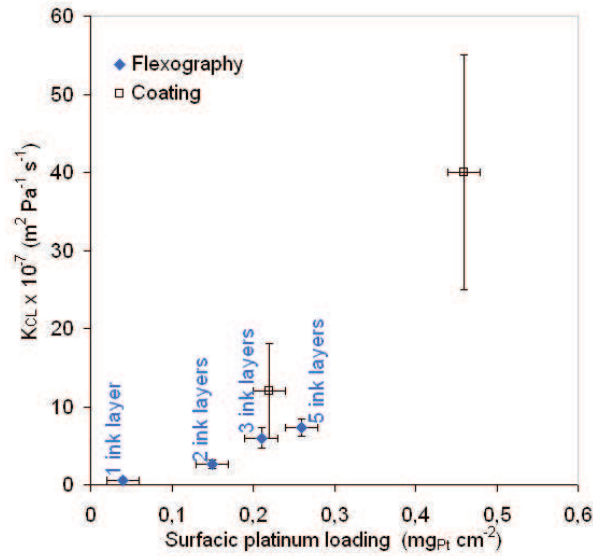


Figure 78 Permeability of catalyst layers made by flexography and by blade coating calculated from Bendtsen measurements as a function of their platinum loading

The intrinsic permeability  $K_{CL}$  was lower than the intrinsic permeability of the GDE. It also seemed that the catalyst layer intrinsic permeability  $K_{CL}$  increased when ink was added to the catalyst layer. Consequently, and according to the evolution of the platinum density, the catalyst layers became more permeable and less dense when they were thicker and heavier. Thus, a change in the catalyst layer structure such as a porosity increasing could be presumed.

At similar platinum loading, around  $0.2 \text{ mg}_{\text{Pt}} \text{ cm}^{-2}$ , the catalyst layers made by blade coating ( $0.22 \pm 0.02 \text{ mg}_{\text{Pt}} \text{ cm}^{-2}$ ) and flexography ( $0.21 \pm 0.02 \text{ mg}_{\text{Pt}} \text{ cm}^{-2}$ ) had similar platinum density ( $240 \pm 40$  and  $240 \pm 50$  respectively), but the coated layer is about twice more permeable ( $6.0 \pm 1.6 \times 10^{-7}$  and  $12 \pm 6.1 \times 10^{-7} \text{ m}^2 \text{ s}^{-1} \text{ Pa}^{-1}$ ).

Increasing the amount of ink deposit on the GDL to manufacture catalyst layer led to increase the thickness and its platinum loading of the catalyst layers. Moreover, it influenced the physical properties of the catalyst layer as well. Indeed, the more the platinum loading of a catalyst layer was high, the less dense the catalyst layer appeared. The decrease in the density of platinum nanoparticles indicated a more porous morphology. This observation was confirmed by the calculation of the intrinsic permeability of the catalyst layers. They became more permeable when increasing the platinum loading. At similar platinum loading, the catalyst layers made by blade coating were more permeable than those made by flexography.

The two processes had different deposition sequences: the blade coating performed monolayer deposition and the flexography manufactured catalyst layers by multilayer deposition. Despite of that, both processes allowed the fabrication of catalyst layers with

similar platinum loading and thickness values ( $0.2 \text{ mg cm}^{-2}$  and  $9.3 \text{ }\mu\text{m}$ ). Nonetheless, but the catalyst layers showed different structural properties that impacted the permeability values of the GDEs and of the catalyst layers.

Moreover, thanks to its multilayer deposition sequence, the flexography process manufactured catalyst layers with lower platinum loading than those made by monolayer deposition using blade coating.

### 2.1.3 Catalyst layers surface observation

In order to compare the flexography and blade coating impact on the catalyst layers surface four samples are studied. Their manufacturing conditions and samples are shown in Table 34.

Table 34 Manufacturing conditions and thicknesses of 4 catalyst layers made by flexography and coating in view of micro structural characterisations

Sample	Manufacturing process	Platinum loading	Thickness	Drying temperature
a	Flexography	$0.26 \text{ mg}_{\text{Pt}} \text{ cm}^{-2}$	$14.5 \pm 0.3 \text{ }\mu\text{m}$	Room temperature
b	Coating	$0.46 \text{ mg}_{\text{Pt}} \text{ cm}^{-2}$	$32.6 \pm 0.8 \text{ }\mu\text{m}$	$80^\circ\text{C}$ for 2h
c	Coating	$0.22 \text{ mg}_{\text{Pt}} \text{ cm}^{-2}$	$9.0 \pm 0.1 \text{ }\mu\text{m}$	$80^\circ\text{C}$ for 2h
d	Coating	$0.20 \text{ mg}_{\text{Pt}} \text{ cm}^{-2}$	$9.6 \pm 0.1 \text{ }\mu\text{m}$	Room temperature

Samples a), b) and c) have been characterised in the previous section. Sample d) was used for the evaluation the impact of the drying condition on the surface state of the catalyst layers.

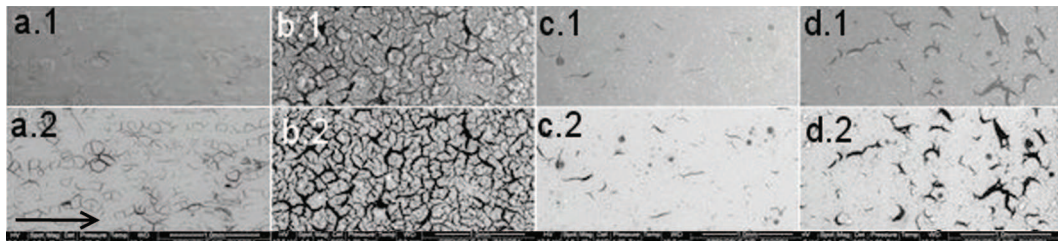


Figure 79 1) SE and 2) BSE pictures of catalyst layers for the four samples described in Table 4 :

- a) flexography,  $0.26 \text{ mg}_{\text{Pt}} \text{ cm}^{-2}$ , drying at room temperature, with a arrow showing the printing direction, b) coating,  $0.46 \text{ mg}_{\text{Pt}} \text{ cm}^{-2}$ , drying  $80^\circ\text{C}$  2H, c) coating,  $0.22 \text{ mg}_{\text{Pt}} \text{ cm}^{-2}$ , drying  $80^\circ\text{C}$  2H, d) coating  $0.20 \text{ mg}_{\text{Pt}} \text{ cm}^{-2}$  drying at room temperature

The SE pictures, in Figure 79.1, illustrate some surface defects, mainly cracks that appeared on the four different samples:

- on sample a) made by flexography, the cracks observed were parallel to the printing direction. Cracks could follow the marble form as previously suggested.
- the coated sample b) was covered by numerous cracks.
- circular defects appeared on coated samples c) and d). They were dried at  $80^\circ\text{C}$  for 2 h and in room conditions for 24h respectively. There was slightly less

defects on sample c) than on sample d). They might have indicated either solvent bubble formations during drying or aggregates that did not contain any platinum elements.

BSE observations, in part 2 of Figure 79, enhanced the platinum distribution at the catalyst layer surface. The homogeneous bright grey on the pictures means that the thickness of the catalyst layer was sufficiently high for being detected as a homogeneous distribution of platinum nanoparticles. The surface area of defects was calculated using a threshold. It represents 4 %, 17 %, 1% and 5 % of the samples a) to d) respectively. Considering the representativeness of the pictures used, it was supposed that samples a), c), and d) had similar surface area of defects compared to sample b), which was highly covered by cracks. Consequently, compared to process of deposition and drying condition, the thickness was the main parameter that governed cracks formation. The thicker the layer was, the more it was covered by cracks. The increase thickness induced an increase of the stiffness, which led to amplify drying stresses applied on the layer. Stresses energy were dissipated by the formation of cracks [Cohen et al., 2009 and Kitsunezaki, 2006].

The crack morphology characterisation was fulfilled by three dimensional topography measurements. The samples a, b and c are presented in the following 3D topography pictures respectively Figure 80, Figure 81 and Figure 82.

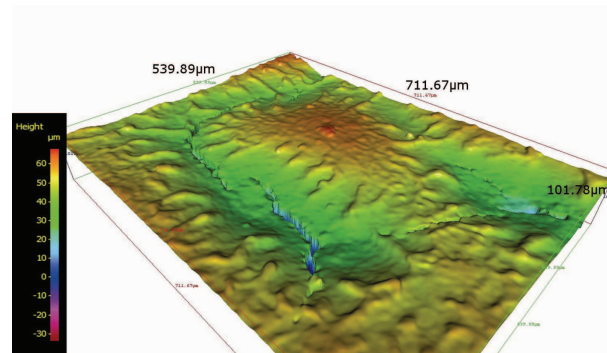


Figure 80 Sample a 3D topography (flexography  $0.26 \text{ mgPt cm}^{-2}$ )

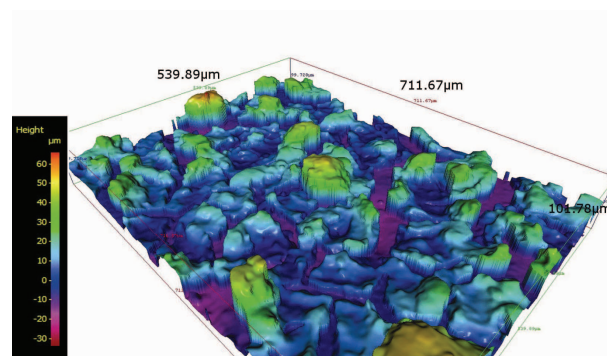


Figure 81 Sample b 3D topography (coating  $0.46 \text{ mgPt cm}^{-2}$ )

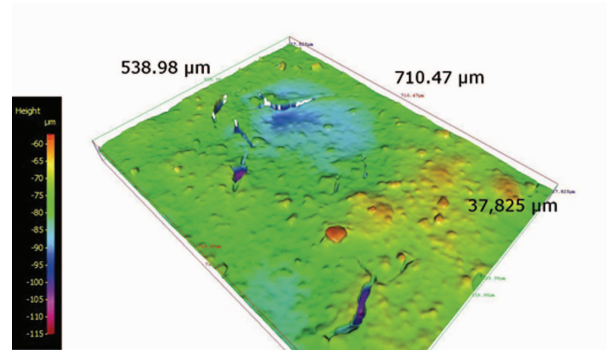


Figure 82 Sample c 3D topography (coating  $0.22 \text{ mg}_{\text{Pt}} \text{ cm}^{-2}$ )

The measures were focused on the cracks. The topography of the coated catalyst layer with  $0.46 \text{ mg}_{\text{Pt}} \text{ cm}^{-2}$  platinum loading (Figure 81) confirms that the catalyst layer was cut into pieces like a puzzle. The pieces of catalyst layer were not in contact with each other, since the cracks go all the way to the substrate. The catalyst layer made by flexography ( $0.26 \text{ mg}_{\text{Pt}} \text{ cm}^{-2}$ , Figure 80) and the coated catalyst layer with a platinum loading of  $0.22 \text{ mg}_{\text{Pt}} \text{ cm}^{-2}$  (Figure 82) had few cracks. The crack formations preferentially happened where the ink film had the lowest thickness and thus where the layer was the most fragile. In flexography, such lack of ink was caused by the marbling printing defect. This confirms the influence of the marbling on the distribution of cracks. Furthermore, a patterning occurs on the highest ink relief. These wave-like shapes indicate a problem of ink film splitting during the ink transfer onto the printing surface.

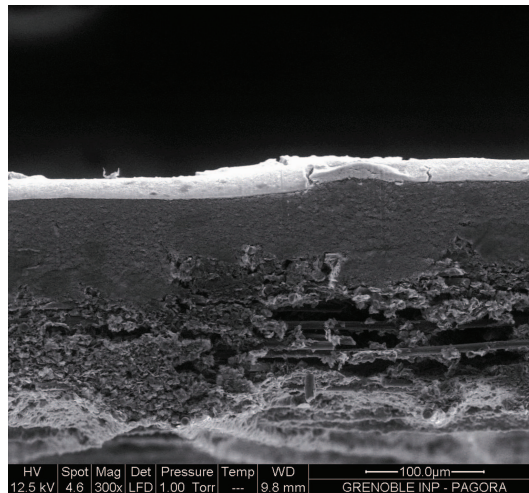


Figure 83 SEM Cross view of the sample a made by flexography  $0.26 \text{ mg}_{\text{Pt}} \text{ cm}^{-2}$

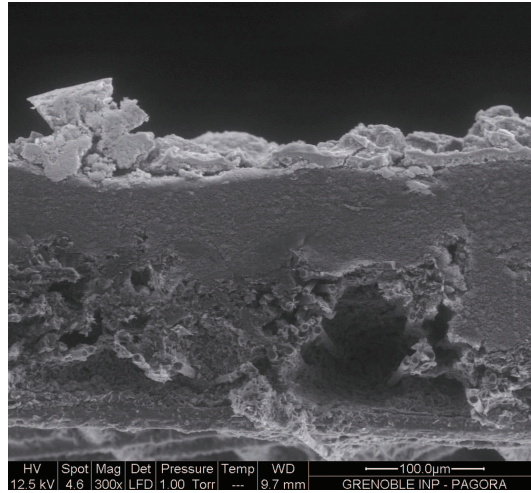


Figure 84 SEM Cross view of the sample b made by blade coating  $0.46 \text{ mg}_{\text{Pt}} \text{ cm}^{-2}$

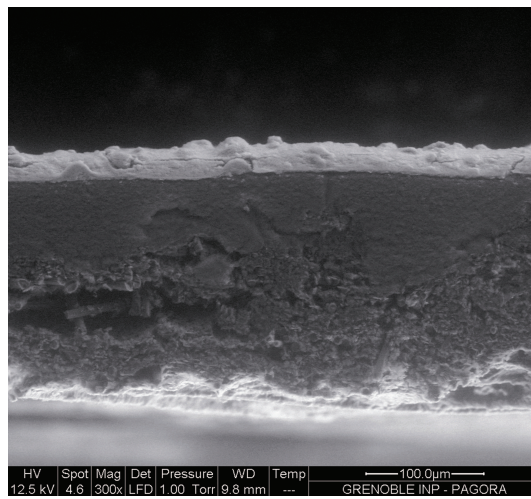


Figure 85 SEM Cross view of the sample c made by blade coating  $0.22 \text{ mg}_{\text{Pt}} \text{ cm}^{-2}$

The catalyst layer prepared by printing (Figure 83) and coating with  $0.22 \text{ mg}_{\text{Pt}} \text{ cm}^{-2}$  (Figure 85) show continuous layer even if the coated catalyst layer with  $0.22 \text{ mg}_{\text{Pt}} \text{ cm}^{-2}$  (sample c) shows some irregularities at its surface. The coated layer b ( $0.46 \text{ mg}_{\text{Pt}} \text{ cm}^{-2}$ ) in Figure 84 as appears to be split into aggregates and the layer was peeled off from its substrate. The average diameter of the aggregates on Figure 79.b.3 is evaluated at  $0.12 \pm 0.04 \text{ mm}$ . Similarly, the bigger aggregates observed on Figure 84 has a diameter about  $0.1 \text{ mm}$ . The presence of the aggregates seemed to induce a poor adhesion between the catalyst layer and the substrate.

Consequently, the process had an influence on crack formation by generating some specific type of ink heterogeneity:

- the thickness was the major parameter that influences the crack formation,
- the increase in cracks led to increase the permeability of the catalyst layer,
- and the cracks seemed to limit the catalyst layer adhesion to the GDL.

## 2.2 Influence of the flexography process on the electrochemical properties of catalyst layers

Printing manufacturing efficiency in catalyst coated backing production was validated by electrochemical tests. GDE made by flexography (sample a) was assembled in a MEA that was called MEA A.

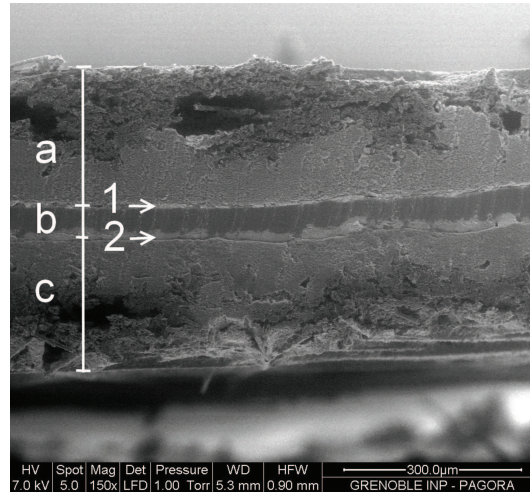


Figure 86 Membrane Electrode Assembly, a) cathode, b) membrane c) anode, with catalyst layers obtained by 1) flexography, and 2) coating

It was placed as a cathode (Figure 83.a), the membrane was a Nafion NRE 212 (Figure 83.b), and a coated GDE was used as the anode (Figure 83.c). Such a protocol was performed on the samples b and c to make the MEA B and C

Cyclic voltammetry characterisations were performed on the three cathodes (Figure 87) and the Electrochemical Surface Areas (ESA) are detailed in Table 35.

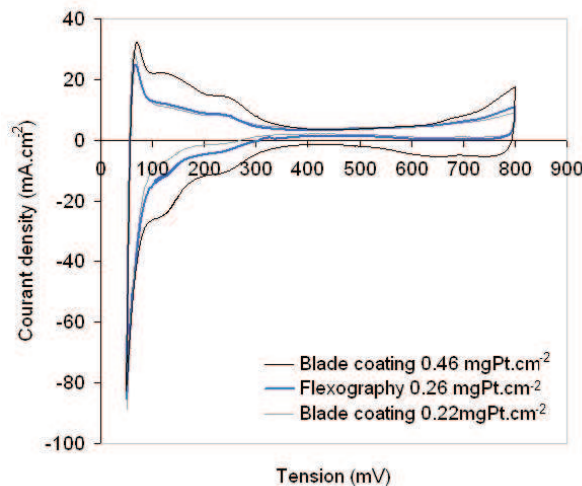


Figure 87 Voltammograms of MEAs a (cathode flexography  $0.26 \text{ mg}_{\text{Pt}} \text{ cm}^{-2}$ ), b (cathode blade coating  $0.46 \text{ mg}_{\text{Pt}} \text{ cm}^{-2}$ ) and c (cathode blade coating  $0.22 \text{ mg}_{\text{Pt}} \text{ cm}^{-2}$ )

Table 35 Electrochemical properties of catalyst layers manufactured by flexography and coating

MEA	Process	Platinum loading (mg cm <sup>-2</sup> )	ESA (cm <sup>2</sup> cm <sup>-2</sup> )	ESA.mg <sup>-1</sup> Pt (cm <sup>2</sup> mg <sup>-1</sup> )
A	Flexography	0.26	171	658
B	Coating	0.46	303	659
C	Coating	0.22	143	650

The three cathodes offered different platinum active surface (or ESA in cm<sup>2</sup> cm<sup>-2</sup>). It evolved similarly to their platinum loadings. Consequently, the platinum accessibility values to hydrogen were close: between 650 and 659 cm<sup>2</sup> mg<sup>-1</sup>.

In Figure 88, the fuel cell performances of the MEAs A, B and C were measured with similar testing conditions and device.

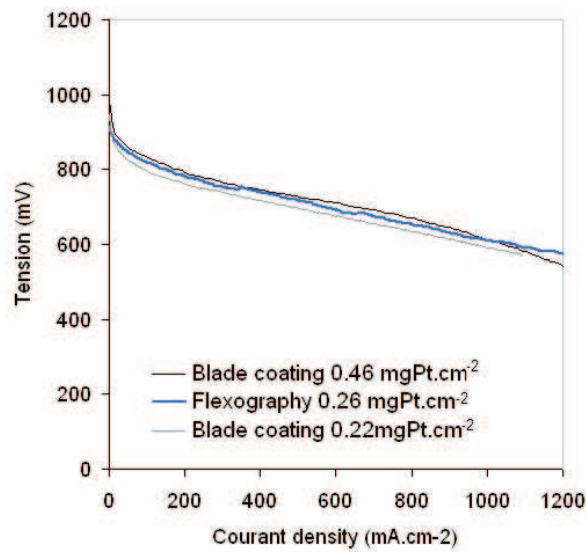


Figure 88 Polarisation curves of MEA with cathodes a) flexography made 0.26 mg<sub>Pt</sub> cm<sup>-2</sup>, b) blade coated made 0.46 mg<sub>Pt</sub> cm<sup>-2</sup> and c) blade coated made 0.22 mg<sub>Pt</sub> cm<sup>-2</sup>

From 0 to 900 mA cm<sup>-2</sup>, the polarisation curves have the same variations and voltage values as a function of the current density. Consequently, at lower current densities (< 200 mA.cm<sup>-2</sup>), the voltage losses of the MEAs were comparable in this potential region. Then at middle current densities (200 to 1,000 mA cm<sup>-2</sup>), the ionic resistance of the membranes and the ohmic resistance of the interfaces appears similar. However, at high current densities (> 1,000 mA cm<sup>-2</sup>), the MEA B shows lower tension values than those of the MEAs A and C. It indicates an insufficient gas diffusion to feed the catalyst.

For further investigations, impedance diagrams of the three cathodes were also performed (Figure 89).

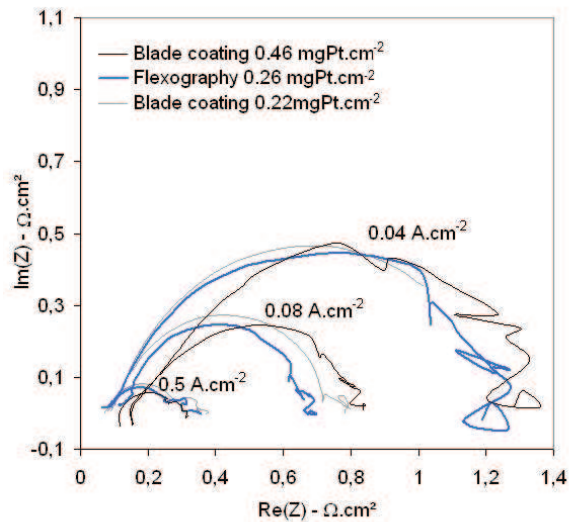


Figure 89 Impedance diagrams at 0.04, 0.08 and 0.5 A cm<sup>-2</sup> of catalyst layer manufactured by flexography and blade coating

The impedances diagrams of the MEA B show significant differences compared to the MEAs A and C. The impedance values at high frequencies are presented in the following Table 36.

Table 36 Impedance values at high frequencies as regards to the MEA

Diagram at 0.08 A cm <sup>-2</sup>	MEA A Flexography 0.26 mg <sub>Pt</sub> cm <sup>-2</sup>	MEA B Blade coating 0.46 mg <sub>Pt</sub> cm <sup>-2</sup>	MEA C Blade coating 0.22 mg <sub>Pt</sub> cm <sup>-2</sup>
Re(Z) (Ω cm <sup>-2</sup> )	0.11	0.15	0.11
Im(Z) (Ω cm <sup>-2</sup> )	0.02	-0.04	0.02

Similarly, the impedance values measured on the MEAs A, B and C at low frequencies are described in Table 37.

Table 37 Impedance values at low frequencies as regards to the MEA

Diagram at 0.08 A.cm <sup>-2</sup>	MEA A Flexography 0.26 mg <sub>Pt</sub> cm <sup>-2</sup>	MEA B Blade coating 0.46 mg <sub>Pt</sub> cm <sup>-2</sup>	MEA C Blade coating 0.22 mg <sub>Pt</sub> cm <sup>-2</sup>
Re(Z) (Ω cm <sup>-2</sup> )	0.67 to 0.70	0.80 to 0.85	0.70 to 0.80
Im(Z) (Ω cm <sup>-2</sup> )	0.00	0.02	0.00

Moreover, this Figure shows that the EIS of two MEAs with low-loaded catalyst layers (a and c) have a more semi circular shape than the one made by blade coating with a high loaded catalyst layer. The MEAs with the 0.46 mg<sub>Pt</sub> cm<sup>-2</sup> coated cathode shows a linear shape at high frequencies and a quarter circular shape at lower frequencies. The linear parts have a slope that ranges between 38 and 47° as regard to the abscissa axis.

Springer et al. [1996] details that high frequencies loops are determined by interfacial change, transfer resistance and catalyst layer properties, while low frequencies arcs are

determined by gas phase transport limitation. Moreover, the slope at high frequencies detailed the proton diffusion; a slope close to  $45^\circ$  is typical of a high proton diffusion limitation.

Consequently:

- the ohmic resistances of the MEA A and C are lower than those of the MEA B,
- the gas phase transport limitations of the MEA A is lower than those of the MEAs B and C,
- and the proton diffusion is more limited in the MEA B than in the MEAs A and C.

### 2.3 Influence of the microstructure on the electrochemical properties of the catalyst layers

The three tested cathodes showed similar platinum accessibility to the hydrogen. The catalyst layers, before their incorporation in the cell, offered a similar platinum accessibility that was not significantly influenced by the manufacturing process. Moreover, the catalyst layers had close density of platinum nanoparticles.

The ohmic resistances of the MEA B evaluated thanks to the polarisation curve (Figure 88) and the EIS diagrams (Figure 89) appeared higher than those of the MEAs A and C.

Two structural parameters may have an impact:

- the catalyst layer thickness (a:  $14.5 \pm 0.3 \mu\text{m}$ , b:  $32.6 \pm 0.8\mu\text{m}$  and c:  $9.3 \pm 0.1\mu\text{m}$ ). Hence, in the GDE b, the electrons have to cover a higher distance.
- as compared to the GDEs a and c, exhibited continuous catalyst layer, the sample GDE b was discontinuous with the presence of aggregates. Consequently, the aggregates limited the carbon percolation and then the electron transportation.

The proton diffusion of the MEA B was lower than those of the MEAs A and C.

- the high catalyst layer aggregation and the low percolation, once again, may have limited the ionomer continuity in the catalyst layer and the proton diffusion,
- the catalyst layer intrinsic permeability (a:  $7.3 \pm 1.3$ , b:  $38 \pm 15$  and c:  $12 \pm 6.1 \text{ m}^2 \text{ s}^{-1} \text{ Pa}^{-1} \times 10^{-7}$ ) made possible a higher gas diffusion into the catalyst layer. It can also have induced membrane drying, and consequently, lower proton diffusion.

The gas transport to the catalyst was higher in the MEA A than in the MEAs B and C.

- the permeability values of the GDEs b and c were higher than the permeability measured in the MEA a (a:  $6.8 \times 10^{-6} \pm 1.5 \times 10^{-6}$ , b:  $9.7 \times 10^{-6} \pm 1.7 \times 10^{-6}$ , c:  $10.2 \times 10^{-6} \pm 1.5 \times 10^{-6} \text{ m}^2 \text{ s}^{-1} \text{ Pa}^{-1}$ ). The aggregation phenomenon led to open the structure and induced an increase in the average intrinsic permeability values of the catalyst layers B and C. However, the gas had to diffuse into the aggregates toward the catalyst elements to be efficient.
- moreover, such a structure can limit the water ejection. Water can block the gas access to catalysts. Therefore, the MEA B structure was not efficient to achieve a good water management in the catalyst layer.

The structure of the cathode b leads to obtain performances that were similar to those of cathodes a and c which respectively have 1.77 and 2.01 times lower platinum loading. Consequently, the catalyst layer structure was a major parameter on the fuel cell performances. Cathode cracks have already been investigated [Karst *et al.*, 2010]. Cell drying and flooding were decreased in a cathode catalytic layer with 8 % of its surface covered by cracks compared to a non-cracked continuous cathode. Actually, the water tended to be preferentially located close to cracks. Furthermore, it was shown that oxygen diffusion was enhanced, because the diffusion barrier was reduced on the side of the cracks. Thus, catalyst layer cracking and structuring improved fuel cell performance. However, the peeling phenomenon observed on the coated layer b is a limit to cracking benefits.

The comparison of the catalyst layers a and c highlighted small differences of behaviour in operating fuel cells. It is clear that each process had an impact on catalyst layer structure, however further studies have to be performed before concluding on the impacts of the electrochemical properties.

## 2.4 Conclusion

Catalyst layer manufacturing had been successfully performed with the flexography printing. Gas diffusion layers were printable and the platinum loading was well controlled by multilayer manufacturing. The density of platinum nanoparticles in catalyst layers made by flexography had been found to be similar to those made by coating.

The characterisation of the intrinsic permeability highlighted the influence of a multilayer protocol on the catalyst layer structure. The greater the increasing in the amount of ink, the more the catalyst layer was permeable to air. It was explained by the formation of shrinkage cracks that appear on the catalyst layer. Their number increased with increasing layer thickness and thus, the porosity of the catalyst layer was amplified. The crack

formation tended to preferentially happen following marbling printing defects that were induced by the poor affinity between the ink and the hydrophobic substrate.

The flexography catalyst layers were less permeable to air than the coated sample.

Gas diffusion electrodes made by flexography reached close performances acquired with coated catalyst coated backing with 0.22 and 0.46  $\text{mg}_{\text{Pt}} \text{cm}^{-2}$ . Consequently, at similar platinum loading, flexography and blade coating offered catalyst layers with comparable performances.

The coated catalyst layer with a platinum loading equal to 0.46  $\text{Pt} \text{cm}^{-2}$  was compared to the two other catalyst layers. Observations by SEM and optical topography highlighted the micro-structural properties of the layers. The coated layer with a platinum loading of 0.46  $\text{Pt} \text{cm}^{-2}$  appeared as cut into a puzzle of aggregates that were pulled from the GDL surface. The visibly poor percolation and adhesion with the substrate surface may explain the higher charge and gas diffusion resistances.

The benefits of the cracks on the performances have been investigated by another study [Karst *et al.*, 2010]. The limit between benefits and drawbacks can be developed by controlling cracks formation.

Finally, this study showed the interest in manufacturing fuel cell by a flexography printing process. The multilayer protocol used with flexography permits to control the platinum deposition. It printed catalyst layers in a large range of platinum content and with similar accuracy to coated layers. In addition, this printing process was able to manufacture catalyst layers with very low platinum loading (with one ink layer deposition for example) and a selective transfer of the ink onto the GDL by using a patterned printing plate.

### **Conclusion of the chapter 4**

This chapter 4 contributed to investigate the ability to manufacture the catalyst layers by CCB protocol with different deposition techniques.

The main issue, the poor printability of the GDL, was over passed. Moreover, the relevance of printing processes for manufacturing fuel cell components was proven by comparing the influence of each deposition techniques on the structural properties of catalyst layers made either by printing processes or by conventional deposition techniques. The printing techniques have demonstrated their ability to offer relevant solutions for manufacturing technically efficient catalyst layer. Moreover, each of them has specific advantages that should allow them to be part of the catalyst layer development.

Among the printing processes, flexography is a good candidate to large surface production, which follows the trend of the growing fuel cell market.

# Chapter 5

## Multilayer







## Introduction

In the previous chapter, the ability to manufacture efficient catalyst layers by flexography for PEM fuel cell was demonstrated.

This chapter describes the application of specificities of the printing field dedicated for fuel cells. The experimental approach is shown in Figure 90.

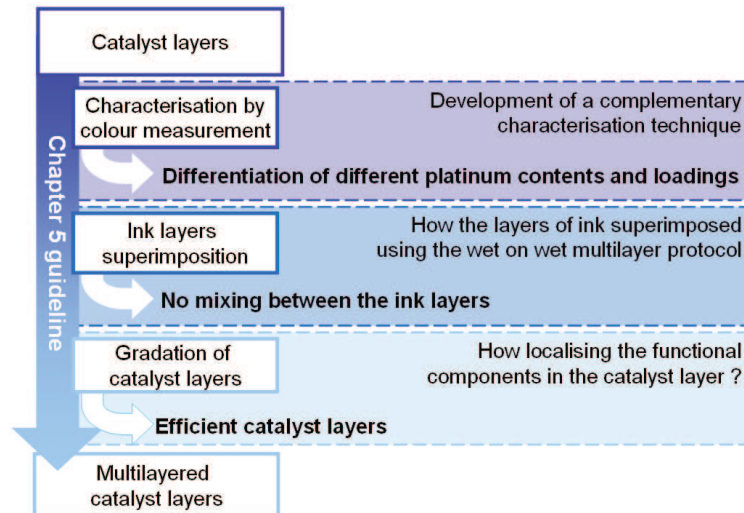


Figure 90 Outline of the chapter 5

One of the characterisation techniques largely used in the printing industry is colour measurement. This is a fast, non-destructive technique that can be implemented on-line. Its potential for fuel cell applications is evaluated in the first part of this chapter.

In conventional printing, during one run, a press is able to accurately deposit various types of ink onto a same substrate at a high speed. For example, in four-colours printing, the press is composed of several printing units, each of them is dedicated to transfer one type of ink onto the substrate. This ability can be used for catalyst layer manufacturing.

Unlike four-colours process that deposited inks with different colours, in this study, the Flexiproof transferred inks with different amount of functional elements (Nafion<sup>®</sup> and catalyst). The objective was to achieve multilayered catalyst layers with different amounts of functional elements in their thickness.

The targeted application is to locate with accuracy functional components specifically where they are required in order to improve the Nafion<sup>®</sup> and catalyst efficiency and diminishing their global use. The two studies of this chapter provide a new contribution of the printing field to the main challenge of the fuel cell domain: diminishing the cost of the power produced by PEM fuel cells.

## 1 Multilayer characterisation

In Chapter 4, the manufacturing of catalyst layer by CCB was demonstrated. Electrochemical characterisations validated the catalyst layers prepared by flexography. These characterisations required specific equipment and several hours [Bultel Y. et al., 2002; Pozio A. et al., 2002; Franco A. *et al.*, 2007; Yuan et al., 2011]. It is therefore crucial to characterise the print quality of the catalyst layers at each step of the flexography manufacturing. As the print quality is commonly quantified by colour measurements, the relevance of two techniques was investigated: optical density (section 1.2.1) and visible spectrophotometry (section 1.2.2) measurements. The relevance of these two techniques was evaluated with samples of catalyst layers containing:

- various ink loading values (section 1.2.2.1). The ink loading ( $\text{mg cm}^{-2}$ ) is the parameter describing the mass of dried ink transferred onto one square centimetre of substrate. For that purpose, catalyst layers were made using the ink I<sub>33</sub>, with one to six superimposed layers. Two different anilox cylinders with 4 and 13  $\text{cm}^3 \text{m}^{-2}$  were used.
- various platinum amounts (section 1.2.2.2), where the platinum amount (w/w%) is the mass percentage of platinum nanoparticles in the dry content of the ink. Two inks were printed:
  - the standard ink I<sub>33</sub>, with a platinum amount of 33w/w%,
  - the model ink free of platinum designated I<sub>0</sub>.

Moreover, optical density and visible spectrophotometry have the major advantages to be fast, in-line and non destructive.

### 1.1 Catalyst layers manufacturing for sampling

The multilayer protocol is able to deposit water-based inks onto the hydrophobic surface of the GDL. As the matter of fact, as the affinity between the ink and the substrate is poor, the first ink layer acts as an adhesion promoter: it insures the good transferability of the upper ink layers. The multilayer protocol produces continuous catalyst layers (Figure 91), which reached electrochemical properties similar to those of catalyst layers made by conventional processes.

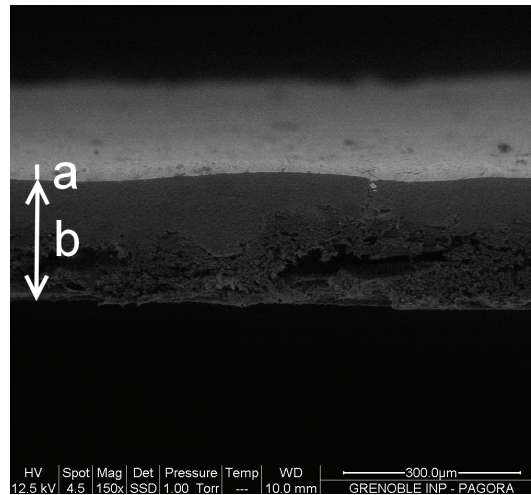


Figure 91 SEM (BSE) cross view of a catalyst layer (a) printed on a GDL (b) by the superimposition of five layers of ink I33 with the anilox of  $4 \text{ cm}^3 \text{ m}^{-2}$

Catalyst layer manufacturing by flexography aims at transferring a precise quantity of functional ink onto a specific substrate. The ink quantity is a significant parameter since the catalyst layers are defined by their quantity of platinum by surface unit ( $\text{mg cm}^{-2}$ ) referred to as loading. For each anilox cylinder, the number of ink layers superimposed can be varied.

The ink loading of each sample was measured as shown in Figure 92.

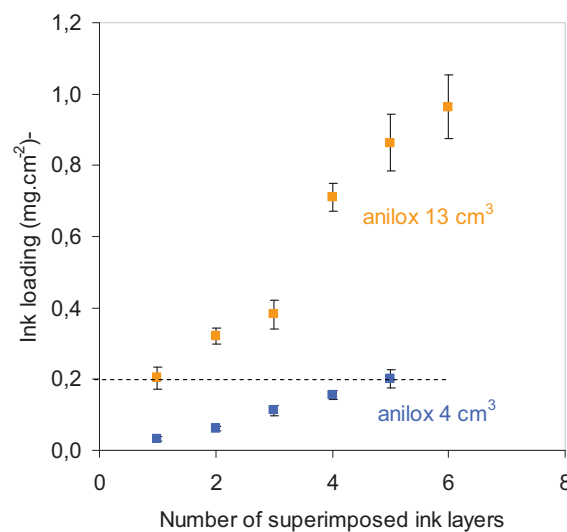


Figure 92 Ink loading as a function of the number of superimposed ink layers onto GDL

For each anilox cylinder, the ink loadings increase, with the number of ink layers transferred. The average amount of ink deposited at each transfer is  $0.04 \pm 0.01$  and  $0.17 \pm 0.03 \text{ mg cm}^{-2}$  for anilox cylinders of 4 and  $13 \text{ cm}^3 \text{ m}^{-2}$  respectively. At each transfer, the  $13 \text{ cm}^3$  anilox leads to the deposition of four times more ink loading onto the substrate than the  $4 \text{ cm}^3 \text{ m}^{-2}$  anilox. This value was close to the ratio of the two anilox volumes.

The manufactured catalyst layers have ink loadings that range from  $0.03 \pm 0.01$  to  $0.20 \pm 0.01 \text{ mg cm}^{-2}$  by superimposing one to five layers of ink with the anilox cylinders of  $4 \text{ cm}^3 \text{ m}^{-2}$ . The catalyst layers made with the anilox of  $13 \text{ cm}^3 \text{ m}^{-2}$  have an ink loading that varies from  $0.20 \pm 0.01$  to  $0.96 \pm 0.05 \text{ mg cm}^{-2}$  by superimposing from one to six ink layers.

Figure 92 also highlights that catalyst layers made by the superimposition of five ink layers with the  $4 \text{ cm}^3 \text{ m}^{-2}$  anilox reaches a similar ink loading ( $0.2 \text{ mg cm}^{-2}$ ) as a catalyst layer made by the deposition of one ink layer with the anilox cylinder of  $13 \text{ cm}^3 \text{ m}^{-2}$ .

The catalyst layer thickness values are presented in Figure 93. The protocol of thickness measurement is unable to give reliable thickness values for the catalyst layers prepared with the anilox of  $4 \text{ cm}^3 \text{ m}^{-2}$ . Indeed, the thickness of these catalyst layers were too low to be discriminated from the substrate thickness variations (the standard deviation of the GDL thickness has been estimated at  $1.3 \text{ }\mu\text{m}$  in part 2.3). Figure 93 only presents the thickness values measured on catalyst layers made with the  $13 \text{ cm}^3 \text{ m}^{-2}$  anilox.

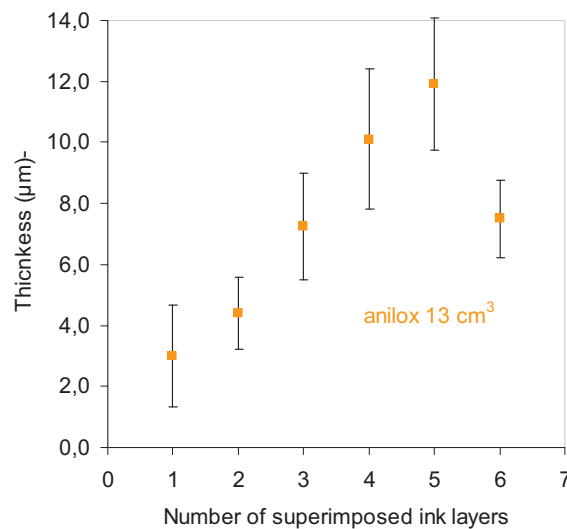


Figure 93 Thickness as a function of the number of superimposed ink layers onto GDL

The thickness values increase from  $3.0 \pm 1.7 \text{ }\mu\text{m}$  to  $11.9 \pm 2.2 \text{ }\mu\text{m}$  when the number of ink layers superimposed on the substrate increases from one to five. When six layers of ink are superimposed, even if the ink loading remains consistent with the expected trend described in Figure 4, the thickness decreases to  $7.5 \pm 1.3 \text{ }\mu\text{m}$ . Such phenomenon might highlight a possible ink strike through the substrate. SEM observations might highlight this phenomenon. However, it would be difficult to distinguish if the ink has entered into the substrate because of the deposition technique or because of the preparation of SEM samples.

## 1.2 Spectrophotometry measurement relevance for characterising fuel cell components

### 1.2.1 Relevance of optical density measurements for catalyst layer

Optical density was tested as a characterisation technique on samples of catalyst layer previously described. The investigations focused on:

- the influence of the platinum amount in the ink on the optical density,
- and the influence of the number of ink layers superimposed.

The variations of optical density as a function of ink loading are shown in Figure 94.

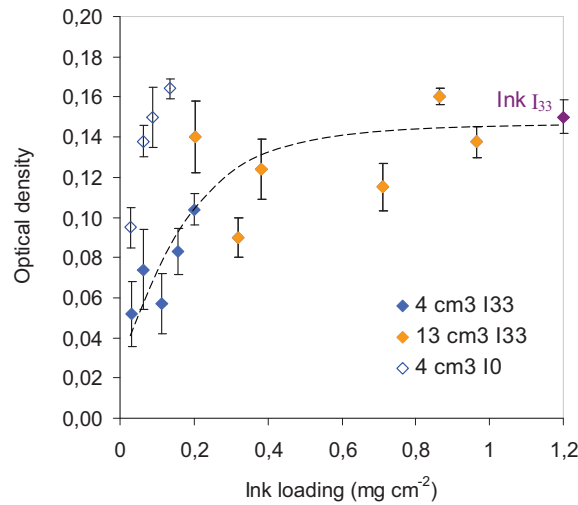


Figure 94 Optical densities of samples of GDLs made by multilayer protocol and of the ink  $I_{33}$  (the ink is arbitrarily placed at an ink loading equal to  $1.2 \text{ mg cm}^{-2}$ , the dotted line have been drawn for understanding)

Considering the samples manufactured with the anilox cylinder with a volume equal to  $4 \text{ cm}^3 \text{ m}^{-2}$ , and for each number of superimposed layers, the optical densities discriminates the inks  $I_0$  and  $I_{33}$ .

The optical densities of the layers made with the ink  $I_{33}$  present noticeable differences as a function of the anilox volume. Considering the ink  $I_{33}$ , the optical densities of the samples made with the anilox with a volume equal to  $13 \text{ cm}^3 \text{ m}^{-2}$  are higher than the one obtained with the  $4 \text{ cm}^3 \text{ m}^{-2}$ . With this ink, the optical densities increased with the ink loading then tend to reach an asymptote. The value of this asymptote could be equal to the intrinsic optical density ( $OD_{\infty}$ ) of the Ink  $I_{33}$ . Consequently, at higher platinum loading, the optical densities of samples made with the ink  $I_{33}$  show poor variations.

The optical density makes it possible to discriminate of:

- the tested ink: with or without platinum, at the same ink loading,

- and the variations of ink loadings, such as the difference of loadings, induce by the use of 13 or 4 cm<sup>3</sup> m<sup>-2</sup> anilox, with the same ink type.

However, it appears difficult to measure the ink loading influence from the optical density at ink loading higher than 0.3 mg cm<sup>-2</sup>. Moreover, parameters, such as the presence of platinum in the ink, the anilox volume use, or the number of ink layer cannot be determined with such a technique.

### 1.2.2 Relevance of characterisation of catalyst layers by spectrophotometry

The optical density tests, the characterisation of catalyst layer by spectrophotometry was performed on:

- samples with the same platinum amount in the ink, but different ink loading values (1.2.2.1),
- samples with similar ink loading values, but different platinum amounts in their dry contents (1.2.2.2).

#### 1.2.2.1 Influence of the ink loading on the reflectance value

In this section, all catalyst layers were manufactured using the ink I<sub>33</sub> that contains platinum nanoparticles.

The reflectance measured on catalyst layers prepared with the anilox cylinders at 4 and 13 cm<sup>3</sup> m<sup>-2</sup> are shown in Figure 95 and Figure 96 respectively. The reflectance spectra of the substrate and the intrinsic reflectance of the ink are also shown on these figures.

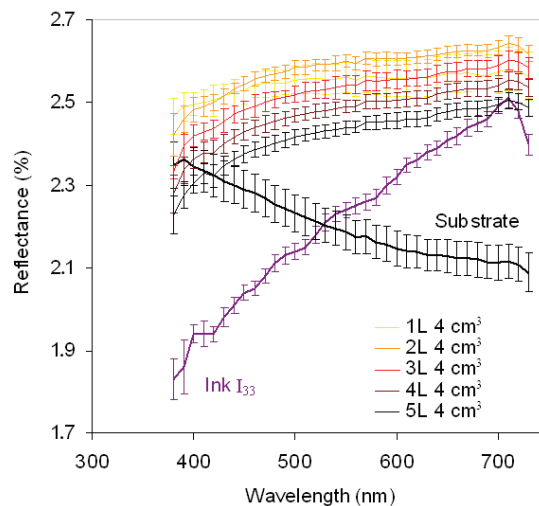


Figure 95 Reflectance spectra of samples made with the ink I<sub>33</sub> deposited with an anilox of 4 cm<sup>3</sup> m<sup>-2</sup>

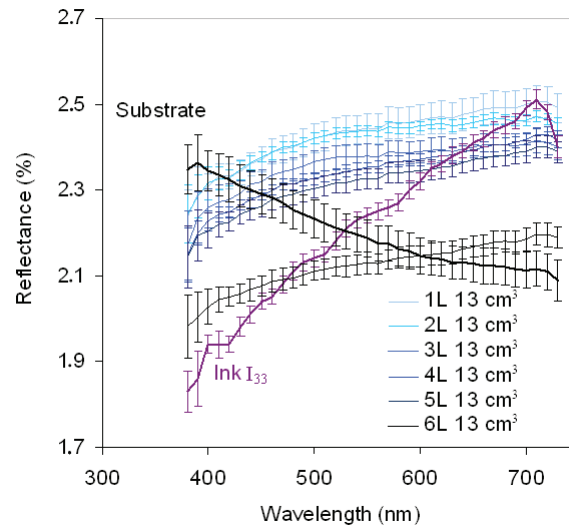


Figure 96 Reflectance spectra of samples made with the ink I33 deposited with an anilox of  $13 \text{ cm}^3 \text{ m}^{-2}$

Whatever the wavelength value, the major trend is that the increase in the catalyst layer ink loading reduces the reflectance values. The reflectance values show that the substrate influence diminishes with increasing the number of superimposed ink layers. The reflectance values tend toward the intrinsic values of the ink as expected by the Kubelka-Munk model [Mc Donald *et al.*, 1987]. Thereby, the catalyst layers made with the  $4 \text{ cm}^3 \text{ m}^{-2}$  anilox have higher reflectance values than those obtained on the catalyst layers made with the  $13 \text{ cm}^3 \text{ m}^{-2}$  anilox cylinder.

However, the samples made by the deposition of one layer with the 4 and  $13 \text{ cm}^3 \text{ m}^{-2}$  anilox cylinders have lower reflectance values than their counterpart made by the superimposition of two layers. In the previous part, similar printing defects appeared when the first layer of ink is transferred onto the SGL 24 BC. Figure 97 is a surface view of one layer of I<sub>33</sub> ink with anilox cylinders of 4 and  $13 \text{ cm}^3$  volumes.

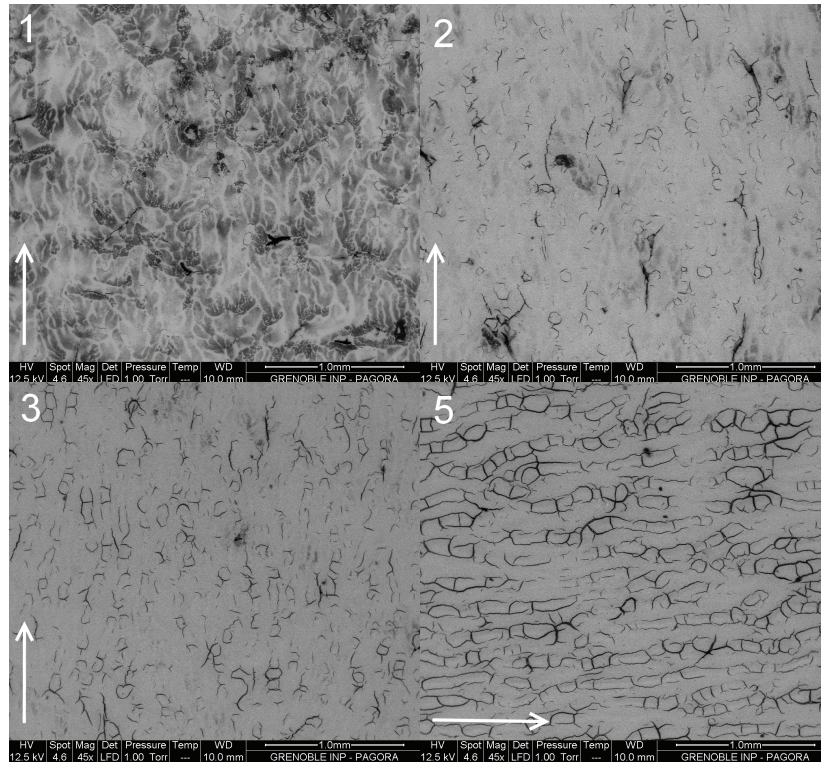


Figure 97 SEM (BSE) observations of the surface of catalyst layers made by the superimposition of one, two, three and five ink layer(s). The printing direction is indicated by the white arrows

A patterning occurs with a marbling appearance. This defect is a typical printing problem. It indicates a lack of affinity between the ink and the surface. It was expected during the deposition of a water-based ink onto a substrate with such a high hydrophobic behaviour. Thus, the ink film splitting in the nip is not favourable to ink transfer and the ink is only partially transferred. This leads to an inhomogeneous ink layer. Consequently, the reflectance spectra of samples made by one layer are impacted by the substrate surface. This hypothesis is supported by (i) the surface fractions of substrate that is not covered by the ink when one ink layer is transferred onto the substrate; the values are estimated to reach  $60 \pm 10\%$  and  $30 \pm 5\%$  with the anilox cylinders 4 and  $13 \text{ cm}^3 \text{ m}^{-2}$  respectively. (ii), the reflectance spectrum of the substrate. The reflectance values range from  $2.35 \pm 0.06\%$  at 380 nm to  $2.09 \pm 0.05\%$  at 730 nm when the intrinsic reflectance spectrum of the ink  $I_{33}$  varies from  $1.85 \pm 0.07\%$  at 380 nm to  $2.44 \pm 0.05\%$  at 730 nm. If 60 to 30 % of the substrate are not covered by the ink, the substrate influence on the reflectance of the catalyst layer may be significant, as it is when considering half tone reproduction [Yang, 2003]. In this study, it will tend to increase the reflectance value of the catalyst layer at low wavelength and reduce the reflectance values of the samples at higher wavelength values compared to the intrinsic reflectance of the ink.

Manufacturing catalyst layer by superimposing several ink layers improves print quality. Consequently, when more ink layers are superimposed, the fraction of substrate not covered by the ink decreases. The reflectance values of the catalyst layer decrease, it becomes darker and darker as expected. At the higher ink loading tested in this study ( $0.96 \pm 0.5 \text{ mg cm}^{-2}$ ) the reflectance values do not reach the values of the intrinsic reflectance of the ink, probably due to the substrate on the reflectance measure.

The values of reflectance for wavelength equals to 390, 550 and 650 nm were extracted from the reflectance spectra and are given as a function of the ink loading in Figure 98.

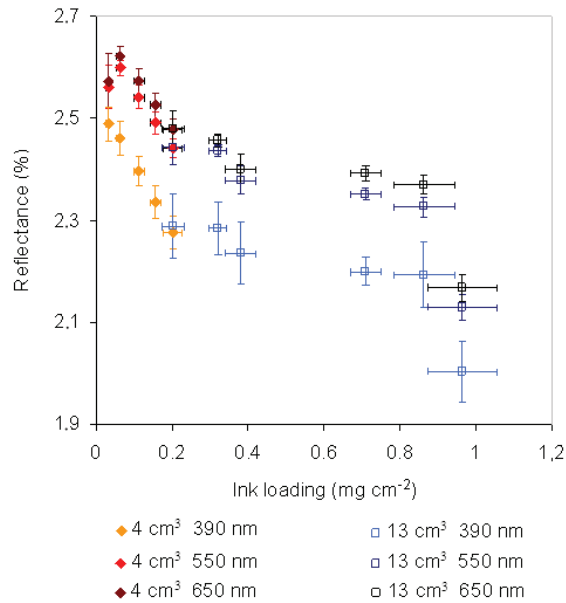


Figure 98 Reflectance value as a function of the samples ink loadings

As already noticed, when the ink loading increased the reflectance value at a given wavelength decreased. However when only one ink layer is deposited with the anilox of  $4 \text{ cm}^3 \text{ m}^{-2}$  an unexpected result appeared: the reflectance value is lower than the reflectance value when two layers of inks were deposited with the same printing parameters. Such a result was already noticed in section 1.2.2.1 by substrate influence on the reflectance measure at low ink loading.

In addition, this catalyst layer had an ink loading equal to  $0.20 \pm 0.01 \text{ mg cm}^{-2}$ , which is a similar value to the catalyst layer sample made by the superimposition of five layers with a  $4 \text{ cm}^3 \text{ m}^{-2}$  anilox ( $0.20 \pm 0.01 \text{ mg cm}^{-2}$ ). Whatever the wavelength, both samples showed very close reflectance values. For example at 650 nm, they respectively reached  $2.48 \pm 0.04 \%$  and  $2.47 \pm 0.03 \%$ .

Hence, it confirms the correlation between ink loading and reflectance value.

### 1.2.2.2 Influence of the platinum amount on the reflectance values

The influence of the platinum amount on the reflectance values of catalyst layers was evaluated using two inks  $I_{33}$  (with 33 w/w% platinum in the ink dry content) and  $I_0$  (free of platinum). In order to obtain samples with similar platinum loadings, catalyst layers are manufactured with these two inks by superimposing one, two and three ink layers with the anilox of  $4 \text{ cm}^3 \text{ m}^{-2}$ .

The reflectance values are measured on the catalyst layers and compared with the reflectance spectrum of the substrate in Figure 99.

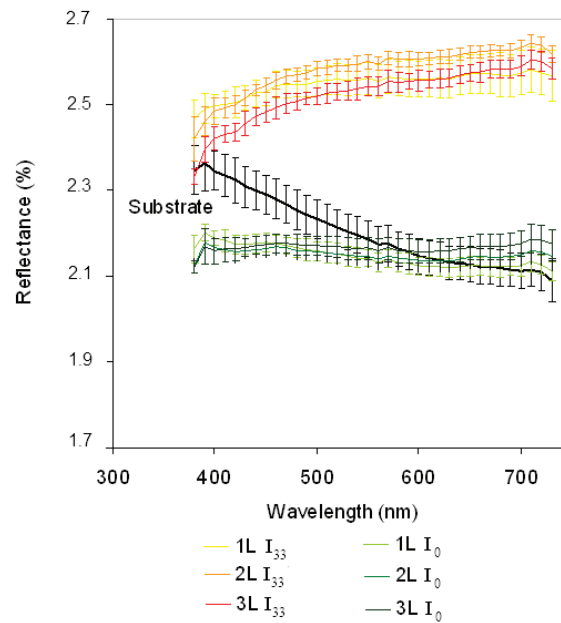


Figure 99 Reflectance spectra of samples made with the ink  $I_{33}$  and  $I_0$  deposited with an anilox of  $4 \text{ cm}^3 \text{ m}^{-2}$

The reflectance values of the samples made with the ink  $I_0$  have values that range from  $2.1 \pm 0.02$  to  $2.2 \pm 0.02$  %. These values are significantly lower than the reflectance values of catalyst layers made with the ink  $I_{33}$  that varies from  $2.64 \pm 0.05$  % to  $2.33 \pm 0.02$  %. Therefore, the catalyst layer that did not contain platinum nanoparticles appears darker than the one containing platinum. Moreover, the curves shapes differ depending of the platinum presence. It also may use to indicate the type of ink transferred onto the SGL substrate. It is an additional information that can be taken from reflectance spectrum measurement.

### 1.3 Use of spectrophotometry to characterise the superimposition of layers with different platinum amounts

Spectrophotometry accurately discriminated the two inks studied in this article. Subsequently, this technique was applied to visualise the consequences of the multilayer protocol on the structure of the catalyst layer manufactured by flexography. Tests were performed to observe where the components of an ink layer were located, after the superimposition wet on wet of several ink layers.

Three layers of ink  $I_{33}$  were transferred onto SGL 24 BS samples. Then, without any drying, layers of ink  $I_0$  were superimposed.

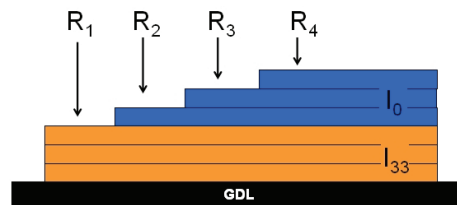


Figure 100 Scheme of the spectrophotometry measurements performed on the multilayer made by the superimposition of the three layers of both inks  $I_{33}$  and  $I_0$

SEM observations of such samples aim to follow the location of the platinum nanoparticles in the bulk of the catalyst layer (Figure 101).

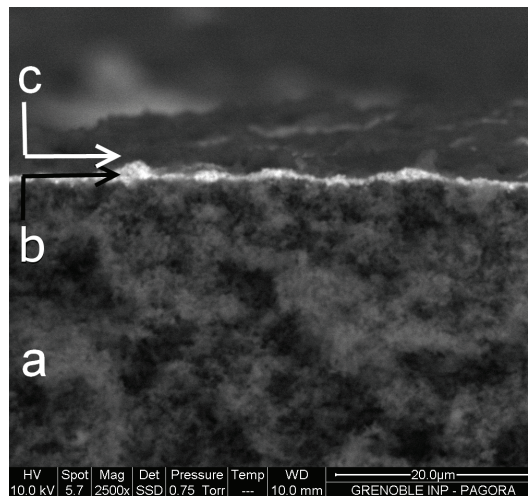


Figure 101 Cross view of GDL (a) printed with three layers of ink with platinum nanoparticles (b) covered by three layers platinum free ink (c)

This cross view is similar to those of the conventional catalyst layer of Figure 91. Indeed, it shows the microporous layer (Figure 101. a) of the GDL on which a printed catalyst layer was transferred. As compared to Figure 91, here, the catalyst layer shows a double layer: close to the GDL, the three ink layers with platinum nanoparticles appear brighter (Figure 101. b), and above them, the three layers of ink  $I_0$  (Figure 101. c) are as dark as the microporous layer, as it was expected.

The recovering of catalyst layers with platinum by layers without platinum nanoparticles is estimated in Figure 102, which shows SEM surface view taken with the BSE device on different samples:

- (1) the sample printed by three layers of ink  $I_{33}$ , this is used as the reference of brightness of surface view of layers containing platinum,
- (2-4) the previous sample (1) of ink  $I_{33}$  is then covered by one, two and three layer(s) of ink  $I_0$ ,
- (5) finally, another reference is made by printing three layers of ink  $I_0$ , this sample is a reference of brightness of surface view of layers without platinum.

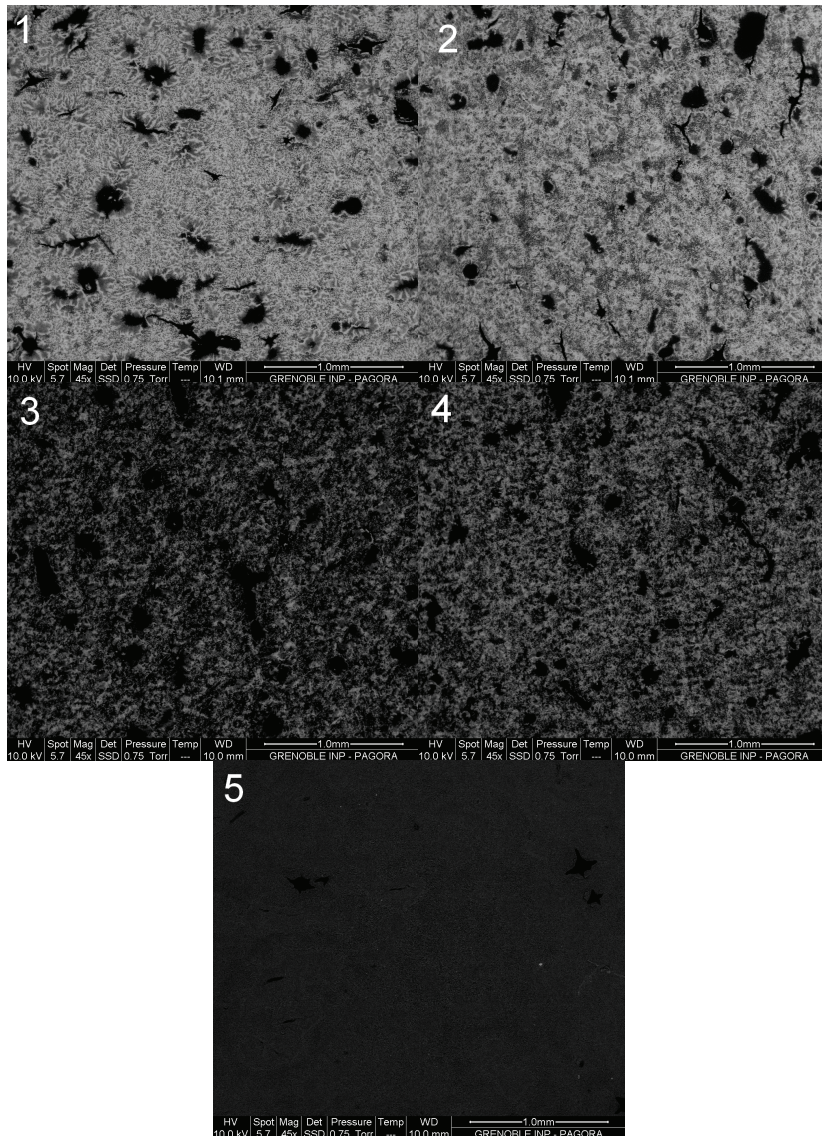


Figure 102 SEM (BSE) observations of the surface of samples printed by (1) three layers of ink with platinum  $I_{33}$ , on which are transferred (2) one (3) two and (4) three layers of ink  $I_0$ , and (5) three layers of ink  $I_0$

These observations are completed with the reflectance values of these samples at 390 nm (Figure 103). The reflectance values at 390 nm of the samples previously described are compared with the reflectance values of samples made by one, two and three ink layers of the inks  $I_{33}$  or  $I_0$  that were discussed in the previous sections.

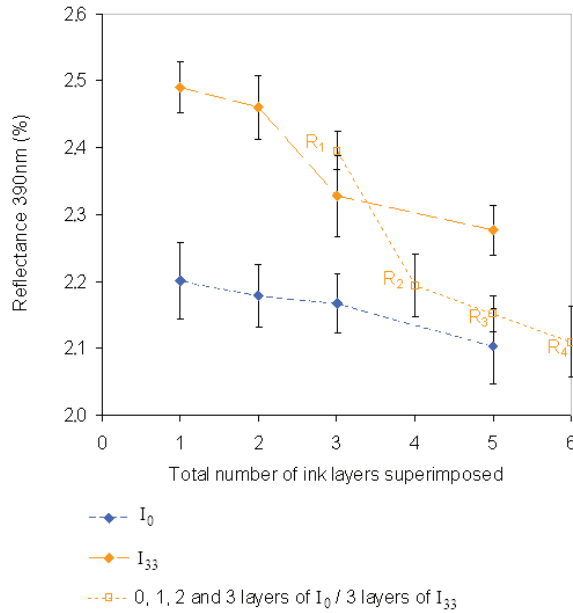


Figure 103 Reflectance of catalyst layer samples at 390 nm deposited on GDL as a function of the number of total ink layers transferred onto the substrate

The reflectance values at 390 nm and the surface views of the samples present the same trends:

- the reflectance value  $R_1$  of the sample composed by three layers of ink  $I_{33}$  (Figure 102. 1) is similar to the expected reflectance value,
- the more layers of ink  $I_0$  are superimposed onto the three layers of ink  $I_{33}$  (Figure 102 samples 2, 3 and 4), the more the brightness of the SEM pictures diminishes, and the more the reflectance values at 390 nm tend from the reflectance values of layers only made by the ink  $I_{33}$  toward the reflectance of those only made by layer of ink  $I_0$ .

However, the multilayer (Figure 102. 4) appears more heterogeneous than the reference made by three layers of ink  $I_0$  (Figure 102. 5), which confirms that the continuity of the ink layers is still improvable at low anilox volume.

The superimposition of ink layers with different composition is possible without mixing between the layers with different compositions. Moreover, using the 4  $\text{cm}^3$  anilox, the transfer of ink layer had a measurable impact on the reflectance value. Finally, with these

parameters, three ink layers free of platinum brought a sufficient ink quantity for recovering and masking the platinum nanoparticles of the underneath layers.

#### 1.4 Conclusion

In order to evaluate the ink loading deposited onto a GDL for manufacturing fuel cell components by a multilayer protocol, two characterisation techniques have been tested on catalyst layers:

- optical density in black offers a possible discrimination between catalyst layers with strong difference of ink loadings and catalyst layers with different amount of platinum nanoparticles. However, neither the ink loading variations nor the ink amount can be quantified using this technique.
- reflectance spectra were measured by visible spectrophotometry. This characterisation technique discriminates catalyst layers with the same ink loading and different platinum amounts as well as catalyst layer with different ink loadings for the two types of anilox used.

The spectrophotometry is then applied to evaluate the potential migration of platinum nanoparticles when several ink layers are superimposed. Ink layers with platinum nanoparticles are printed on a GDL, and then they are recovered by layers free of platinum element. The reflectance values of this multilayer are completed by SEM cross and surfaces view and tend to confirm that no mixing is measurable or visible between the different ink layers.

The measure of the reflectance is technically suitable for catalyst layer characterisation. Moreover, it is a fast, continuous and on-line technique and then economically pertinent compared to the conventional characterisation techniques. As a complementary characterisation, this technique will be a great opportunity that will help to develop the use of continuous printing processes for fuel cell manufacturing.

Further studies will look into the possibility of reflectance spectrum measurements to discriminate platinum quantity, not only by the superimposition of ink layers made with the same amount of platinum, but also to define the amount of platinum in layers made by inks formulated with different amounts of platinum.

## 2 Designing catalyst layers

The printing processes have specific properties compared to the conventional processes that gave them potential for contributing in the cost reduction of the power supplied by a fuel cell.

In Part 1, the flexography was able to discriminate ink layers with no measurable mixing between the components of two layers. Which could be the advantages of such ability? Does the location of functional components into the thickness of the catalyst layer have an influence on the electrochemical properties? How localising the functional components in the thickness of the catalyst layer?

In the literature, such questions were already studied. Models of platinum nanoparticles and Nafion<sup>®</sup> distributions in the thickness of the catalyst layer for improving the catalyst layer electrochemical properties were proposed.

A first work took into consideration that the main parameter influencing the catalyst layer efficiency was its porosity. If the catalyst layer had a non-porous structure, the platinum loading should have decreased from the GDL to the membranes interfaces. In the contrary, a porous GDL should have been designed with an increased platinum loading from the GDL to the membrane interface. Such a structure, combining high porosity and increasing platinum loading led to the better catalyst layer efficiency [Antoine *et al.*, 2000].

In a second work, a two parameter model indicated that the platinum loading and the Nafion<sup>®</sup> ionomer content should respectively increase in a convex function and linearly from the GDL interface to the membrane interface [Song *et al.*, 2005].

Designing catalyst layer in the thickness impacts positively on the fuel cell performances. Consequently, this study aims to demonstrate that flexography is able to manufacture designed catalyst layers and that the created designs improve the functional properties.

For that purpose:

- various types of ink were formulated, and their printability were evaluated by manufacturing homogeneous catalyst layers (2.1),
- designing catalyst layer using these inks were experimented (2.2),
- and finally, the catalyst layer designs that was manufactured by flexography were electrochemically characterised (2.3).

The goal was to manufacture catalyst layers composed by ink layers that had different functional components amounts. This is a single parameter study, for example, if the

platinum amount changed in a thickness of a catalyst layer, the ionomer content remained as much as possible constant and vice-versa.

## 2.1 Validation of inks for manufacturing multilayered catalyst layer

### 2.1.1 Ink formulation

Five types of ink were used in this study. They are named  $I_{X-Y}$  with I for Ink, X the amount of platinum nanoparticles and Y the Nafion<sup>®</sup> amount in w/w % in the solid content.

The inks with different amounts of platinum were formulated by mixing inks  $I_0$  and  $I_{33-26}$  at various ratios. These two inks were already used in the previous studies.

On the contrary, the inks with different ionomer contents were specifically formulated for this purpose. The ionomer dispersion was switched by a dispersion of water and aliphatic alcohol similar to the Nafion<sup>®</sup> dispersion vehicle. The viscosity of the ink with the lower Nafion<sup>®</sup> amount ( $I_{33-9}$ ) was about  $70 \pm 20$  mPa s, and its surface tension was equal to  $30 \pm 6$  mN m<sup>-1</sup>.

The compositions of the solid content of the five inks are detailed in the Table 38.

Table 38 Inks formulation

Ink denomination	Ink solid content (w/w% total ink)	Platinum (w/w% ink dry content)	Platinum (w/w % on carbon and platinum)	Nafion <sup>®</sup> (w/w% ink dry content)
$I_{33-26}$ (standard)	28.0	<b>33.5</b>	<b>45.4</b>	<b>26.1</b>
$I_{24-29}$	25.5	<b>24.5</b>	<b>34.7</b>	29.3
$I_{13-33}$	22.9	<b>13.6</b>	<b>20.4</b>	33.1
$I_{33-17}$	25.0	33.6	45.4	<b>17.3</b>
$I_{33-9}$	23.3	33.8	45.4	<b>9.5</b>

The amount of ionomer as a function of the platinum loading is also visible in Figure 104.

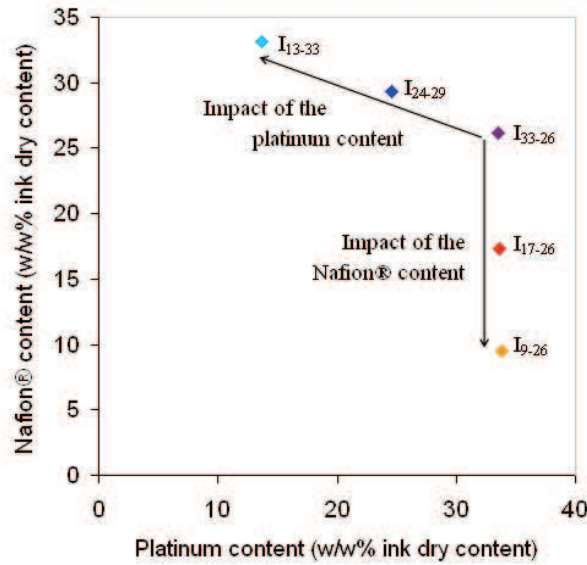


Figure 104 Nafion® content as a function of the platinum content in the ink solid content

### 2.1.2 Inks deposition: Uniform catalyst layer manufacturing

The standard ink I<sub>33-26</sub> was used as a reference. The five types of ink were printed on GDL samples by superimposing one to six layers of ink as described in Table 39.

Table 39 Printing protocol characteristics for each kind of catalyst layer

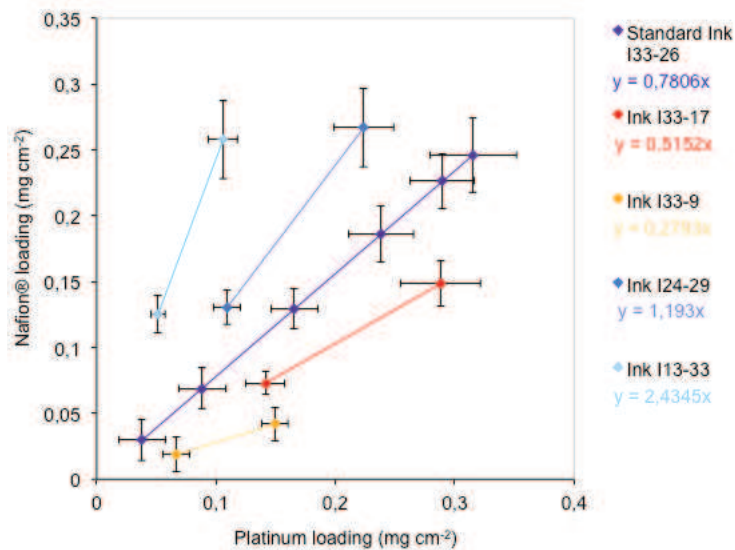
Ink used	Number of ink layers transferred	Denomination of the catalyst layers
I <sub>33-26</sub> (standard)	1	I <sub>33-26</sub> 1L
	2	I <sub>33-26</sub> 2L
	3	I <sub>33-26</sub> 3L
	4	I <sub>33-26</sub> 4L
	5	I <sub>33-26</sub> 5L
	6	I <sub>33-26</sub> 6L
I <sub>24-29</sub>	3	I <sub>24-29</sub> 3L
	6	I <sub>24-29</sub> 6L
I <sub>13-33</sub>	3	I <sub>13-33</sub> 3L
	6	I <sub>13-33</sub> 6L
I <sub>33-17</sub>	3	I <sub>33-17</sub> 3L
	6	I <sub>33-17</sub> 6L
I <sub>33-9</sub>	3	I <sub>33-9</sub> 3L
	6	I <sub>33-9</sub> 6L

### 2.1.3 Characterisation of the catalyst layers

The catalyst layers characterisation began by measuring their ink loadings (Table 40), which were used to calculate their platinum and ionomer loadings (Figure 105). The characterisation was completed by SEM observations of the catalyst layers surface.

Table 40 Ink loading ( $\text{mg cm}^{-2}$ ) of each catalyst layers detailed in Table 39

Denomination of the catalyst layer	Ink loading ( $\text{mg cm}^{-2}$ )	Figure
I <sub>33-26</sub> 1L	$0.11 \pm 0.01$	
I <sub>33-26</sub> 2L	$0.26 \pm 0.03$	
I <sub>33-26</sub> 3L	$0.50 \pm 0.06$	Figure 106
I <sub>33-26</sub> 4L	$0.71 \pm 0.08$	
I <sub>33-26</sub> 5L	$0.86 \pm 0.08$	
I <sub>33-26</sub> 6L	$0.94 \pm 0.11$	
I <sub>24-29</sub> 3L	$0.44 \pm 0.04$	Figure 107
I <sub>24-29</sub> 6L	$0.91 \pm 0.10$	
I <sub>13-33</sub> 3L	$0.38 \pm 0.04$	Figure 108
I <sub>13-33</sub> 6L	$0.78 \pm 0.09$	
I <sub>33-17</sub> 3L	$0.42 \pm 0.02$	Figure 109
I <sub>33-17</sub> 6L	$0.86 \pm 0.10$	
I <sub>33-9</sub> 3L	$0.20 \pm 0.05$	Figure 110
I <sub>33-9</sub> 6L	$0.44 \pm 0.05$	

Figure 105 Nafion<sup>®</sup> loading as a function of the platinum loading of the catalyst layers detailed in Table 39

The visible influences of the ink formulations (catalyst and ionomer amount) on the ink loadings and on the surface structure of the catalyst layers are outlined in the next sections 2.1.3.1 and 2.1.3.2 respectively.

### 2.1.3.1 Influence of the catalyst amount in the ink on the catalyst layer structure and loadings

The catalyst layers made with the inks I<sub>33-26</sub>, I<sub>24-29</sub> and I<sub>13-33</sub> by the superimposition of six ink layers had ink loadings equal to  $0.94 \pm 0.11$ ,  $0.91 \pm 0.10$  and  $0.78 \pm 0.09$  mg cm<sup>-2</sup> respectively. Those made by the superimposition of three ink layers had ink loadings equal to  $0.50 \pm 0.06$ ,  $0.44 \pm 0.04$  and  $0.38 \pm 0.04$  mg cm<sup>-2</sup> respectively. When the amount of platinum nanoparticles decreased in the ink, the ink loading of the catalyst layer decreased as well.

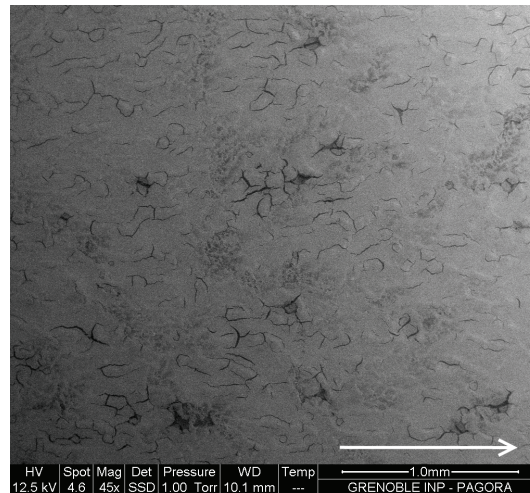


Figure 106 SEM BSE surface view of catalyst layer I<sub>33-26</sub> 3L (the arrow points at the printing direction)

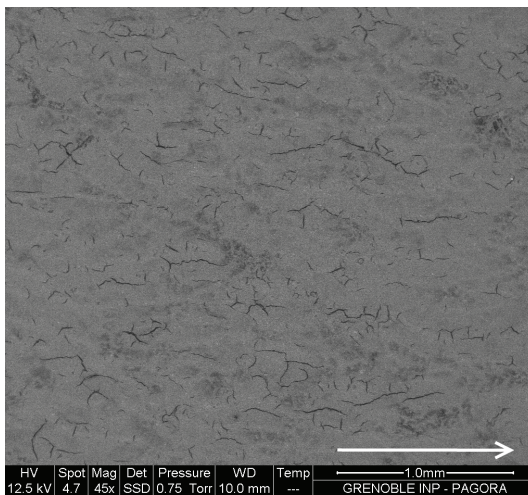


Figure 107 SEM BSE surface view of catalyst layer I<sub>24-29</sub> 3L (the arrow points at the printing direction)

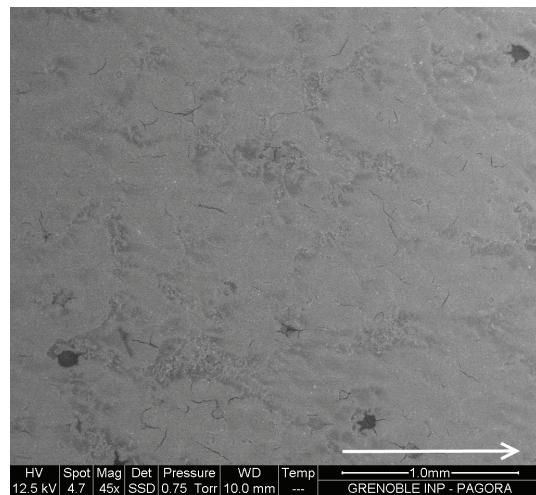


Figure 108 SEM BSE surface view of catalyst layer I<sub>13-33</sub> 3L (the arrow points at the printing direction)

Figure 106, Figure 107 and Figure 108 show surfaces of catalyst layers with similar defects and surface states. There was no major difference of printability between the three

tested inks. The amount of platinum nanoparticles does not induce any substantial printability change on the catalyst layer but gives different ink loading values.

Such behaviour can be explained by the evolution of the density of the solid content of the ink. Because the platinum density ( $21.45 \text{ g cm}^{-3}$  [Grigoriev *et al.*, 1997]) is higher than the carbon density (whatever its physical configuration from  $1.8$  to  $3.5 \text{ g cm}^{-3}$ ). The more the ink has an important amount of platinum nanoparticles, the more its density will increase. Accordingly, at each transfer, a similar volume of ink was transferred by the printing group. Subsequently, a catalyst layer made by an ink with a higher amount of platinum had a higher ink loading compared to the catalyst layer made by the ink with a lower platinum amount.

Figure 105 shows that the catalyst layers had close Nafion<sup>®</sup> loadings ( $0.25$ ,  $0.27$  and  $0.26 \pm 0.03 \text{ mg cm}^{-2}$  for 6 layers of inks  $I_{33-26}$ ,  $I_{24-29}$  and  $I_{13-33}$  superimposed) and different platinum nanoparticles loadings ( $0.31 \pm 0.03$ ,  $0.22 \pm 0.02$  and  $0.10 \pm 0.01 \text{ mg cm}^{-2}$ ), as expected.

### 2.1.3.2 Influence of the ionomer amount in the ink on the catalyst layer structure and loadings

The catalyst layers made by the superimposition of six layers of the inks  $I_{33-26}$ ,  $I_{33-17}$  and  $I_{33-9}$ , had ink loadings equal to  $0.94 \pm 0.11$ ,  $0.86 \pm 0.10$ ,  $0.44 \pm 0.05 \text{ g cm}^{-3}$  respectively. The superimposition of three layers of these inks gave catalyst layers with an ink loading of  $0.50 \pm 0.06$ ,  $0.42 \pm 0.02$  and  $0.20 \pm 0.05 \text{ g cm}^{-3}$  respectively.

The smaller the Nafion<sup>®</sup> amount in the ink is, the smaller the ink loading is. Two phenomena may explain this behaviour:

- the solid content of the ink decreased from 28 to 23 w/w %, from the ink  $I_{33-26}$  to  $I_{33-9}$ . Consequently, for a same volume of inks  $I_{33-26}$  and  $I_{33-9}$  deposited onto the GDL, the dried ink loading of the catalyst layer made using the ink  $I_{33-9}$  was smaller.
- besides its influence on the ink density, the ionomer amount has also an influence on the ink printability on the GDL. It was commonly illustrated in the literature, that the ionomer content ranges between 25 to 35 w/w % in the dry catalyst layers for optimising the electrochemical properties [Xie *et al.*, 2010; Antolini *et al.*, 1999; Paganin *et al.*, 1996; Uchida *et al.*, 1995]. If the ionomer is required for protons diffusion, it is well known to be a good binder for the carbon supported catalyst nanoparticles in the dispersion [Cheng *et al.*, 2006; Modestov *et al.*, 2009] and in the dry catalyst layer.

This last phenomenon should also explain such a low transfer of the ink, which is visible when comparing the Figure 106 and Figure 109 with the Figure 110.

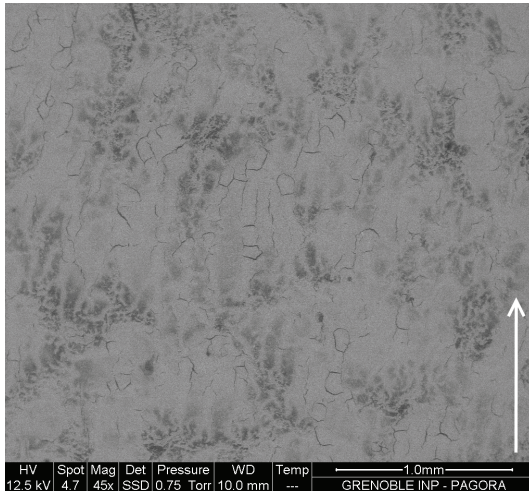


Figure 109 SEM BSE surface view of catalyst layer I<sub>33-17</sub> 3L (the arrow points at the printing direction)

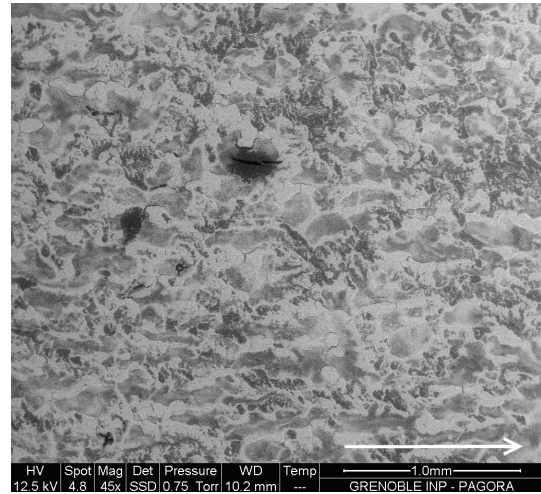


Figure 110 SEM BSE surface view of catalyst layer I<sub>33.9</sub> 3L (the arrow points at the printing direction)

In these SEM observations, the ink I<sub>33.9</sub> gave catalyst layers with a heterogeneous surface covered by printing defects.

#### 2.1.4 Conclusion on the printability of the inks

The inks with various amounts of platinum nanoparticles (I<sub>24-29</sub> and I<sub>13-33</sub>) were formulated from two inks (I<sub>33-26</sub> and I<sub>0</sub>) whose the printability was already demonstrates. As expected, the inks I<sub>24-29</sub> and I<sub>13-33</sub> reach a sufficient transferability.

However, changing the ionomer amount into the inks impacted on their printability. Indeed, the the ionomer has a double effect of proton conductor and ink binder. It leads to diminish the inks printability, especially for the ink I<sub>33.9</sub>, with 9 w/w % of ionomer content in the solid content.

Consequently, the inks I<sub>33-26</sub>, I<sub>24-29</sub> and I<sub>13-33</sub> were good candidates to design catalyst layers with different platinum distribution in their thickness. Nevertheless, several improvements are still required to formulate inks that could be used to design catalyst layers with different ionomer contents distribution in their thickness.

#### 2.2 Ability of the flexography to manufacture multilayer catalyst layers

The ability to manufacture homogeneous catalyst layers using inks with three different amounts of platinum (I<sub>33-26</sub>, I<sub>24-29</sub> and I<sub>13-33</sub>) by flexography was previously demonstrated. Consequently, the challenge in the following parts was to demonstrate that the

flexography multilayer protocol established in part 1.3 was also able to fabricate catalyst layers with complex designs.

### 2.2.1 Deposition protocol

The multilayer protocol developed in chapter 3 for homogeneous CCBs was adapted to design these specific structures. All of the designs gave catalyst layers with close ink and platinum loadings. The targeted values of ink and platinum loadings were those of a six-layered homogeneous catalyst layer made with the ink  $I_{24-29}$ , ( $0.9 \pm 0.1$  and  $0.22 \pm 0.02$   $\text{mg cm}^{-2}$  respectively)

Three designs were proposed to be manufactured by flexography:

- bi-layer designs (Figure 111):

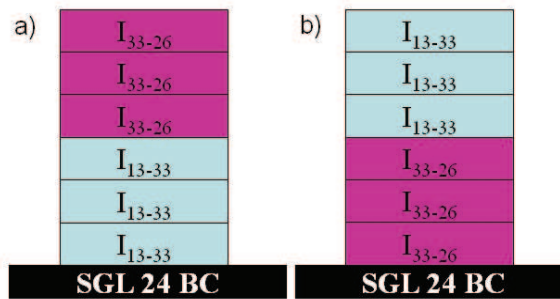


Figure 111 Bilayer designs, a) increasing and b) decreasing designs

- tri-layer designs (Figure 112):

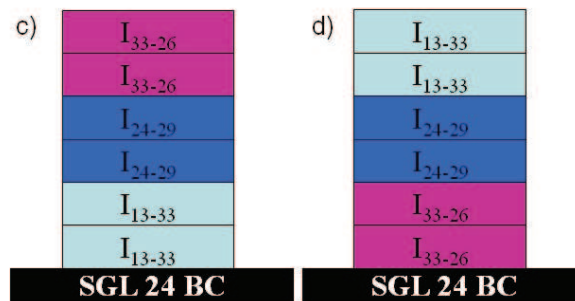


Figure 112 Tri-layer designs, c) increasing and d) decreasing designs

- and, symmetrical designs (Figure 113):

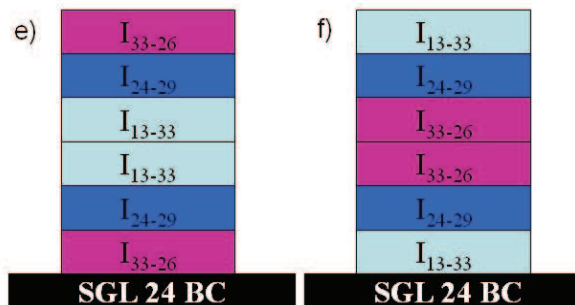


Figure 113 Symmetrical designs, e) outer-directed and f) inner-directed designs

As it was crucial to measure the ink loading brought by the deposition of each type of ink, the dry ink loading was measured after the deposition of each type of inks. For example, for characterising an increasing bi-layered catalyst layer (a):

- the GDL mass was measured,
- then three layers of ink  $I_{13-33}$  were printed,
- they were dried in room condition for 24h,
- then the GDL with the three layers of ink  $I_{13-33}$  was weighted,
- three layers of ink  $I_{33-26}$  were transferred onto the three dried layers of ink  $I_{13-33}$ ,
- the multilayer was dried for 24h,
- and finally, the mass of the GDL and of the six layers was measured.

Such a change in the protocol should have induced an influence on the catalyst layer itself. Moreover, the addition of mass measurements led to increase measurement error.

### 2.2.2 Characterisation of the designed catalyst layers

The values of ink and platinum loading are described in Figure 114, Figure 115 and Figure 116. These figures show the contribution of each type of ink on the ink and platinum loading for the bi layered, tri layered and symmetrical designed catalyst layers respectively. As each of the given value was obtained by two mass measures, the measurement error of these values was inferior or equal to  $0.02 \text{ mg cm}^{-2}$ .

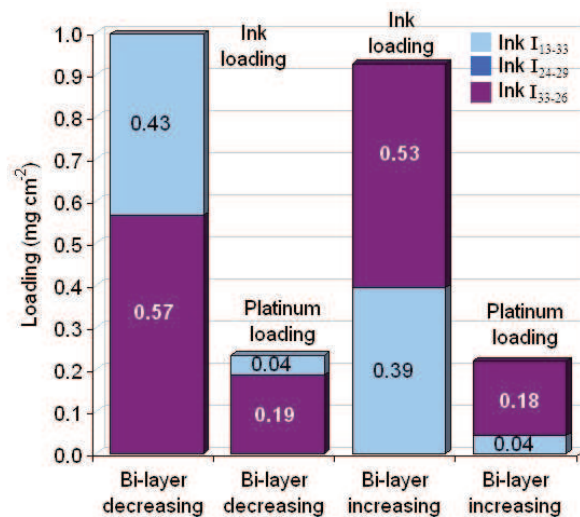


Figure 114 Ink and platinum loadings of each of the layers that composed the bi-layered catalyst layers

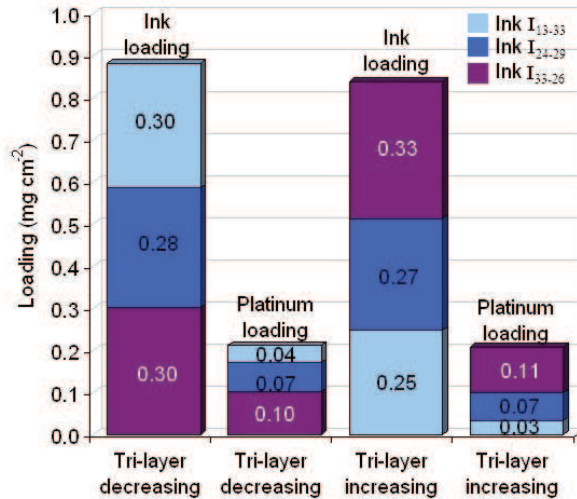


Figure 115 Ink and platinum loadings of each of the layers that composed the tri-layered catalyst layers

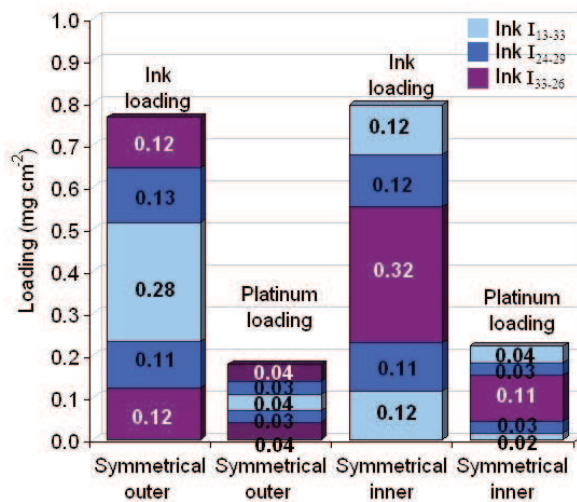


Figure 116 Ink and platinum loadings of each of the layers that composed symmetrical catalyst layers

Small differences of ink loading appeared as regards to the type of ink used, as it was previously observed in section 2.1.3.1.

It seems that the more there were steps required for manufacturing a catalyst layer (two for a bi-layered, three for a tri-layered and five for a symmetrical) the less the ink loading was high (0.99, 0.88 and 0.79 mg cm<sup>-2</sup> respectively). Unfortunately, the importance of the measurement errors (0.1, 0.2 and 0.2 mg cm<sup>-2</sup>) limits the relevance of this trend that should indicate an influence of the number of manufacturing steps on the catalyst layers characteristics.

Observations of cross view of the designed catalyst layers were performed, and are depicted in Figure 117, Figure 118 and Figure 119.

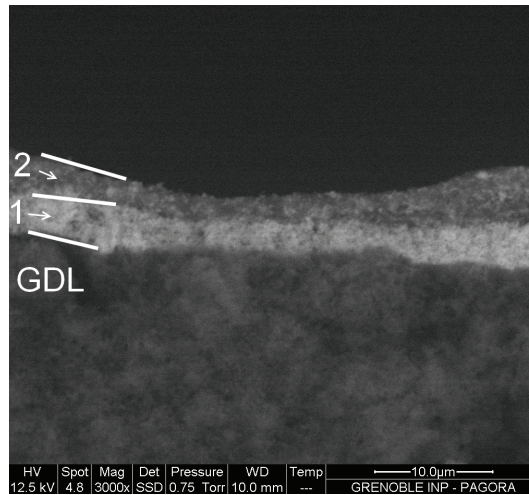


Figure 117 SEM BSE cross view of a decreasing bi-layered catalyst layers composed of 1) three layers of ink I<sub>33-26</sub> and 2) three layers of ink I<sub>13-33</sub>

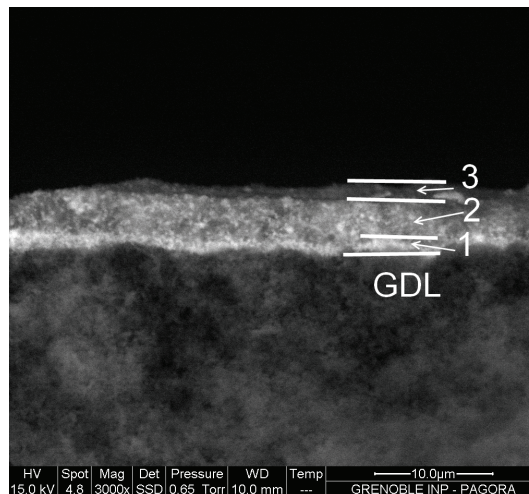


Figure 118 SEM BSE cross view of a decreasing tri-layered catalyst layers composed of 1) two layers of ink I<sub>33-26</sub>, 2) two layers of ink I<sub>24-29</sub> and 3) two layers of ink I<sub>13-33</sub>

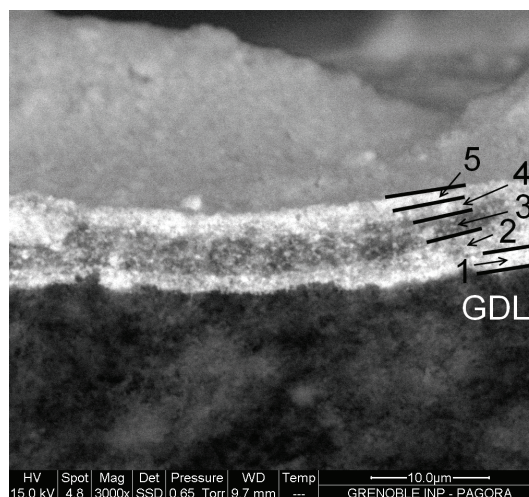


Figure 119 SEM BSE cross view of a symmetrical (outer) catalyst layers composed of 1) one layers of ink I<sub>33-26</sub>, 2) one layers of ink I<sub>24-29</sub>, 3) two layers of ink I<sub>13-33</sub>, 4) one layers of ink I<sub>24-29</sub> and 5) one layers of ink I<sub>33-26</sub>

The catalyst layers that had their first layers in contact with the GDL made with the ink I<sub>33-26</sub> had a higher contrast when using the BSE device. It led to a better differentiation of each kind of layers composing the catalyst layers. That is why; these figures show decreasing bi-and tri- layered and outer symmetrical catalyst layers.

The catalyst layers thicknesses were evaluated directly on the picture and they varied from 5 to 8  $\mu\text{m}$ . This value is comparable to the one obtained for a homogeneous catalyst layer made by the superimposition of six layers that reached  $7.5 \pm 1.3$  (in the first part of this chapter).

The BSE device clearly distinguished the ink I<sub>33-26</sub> from I<sub>13-33</sub> (Figure 117), a good distinction between the three types of ink (Figure 118). However, due to the close amount of platinum in the inks and the fact that only one layer of each ink was deposited, it was more difficult to identify the layer of ink I<sub>33-26</sub> and I<sub>24-29</sub> in Figure 119.

These observations confirmed that the flexography multilayer protocol was able to superimpose ink layers with different amount of functional components.

### 2.3 Performances of the multilayer catalyst layers in a fuel cell

MEAs were fabricated using catalyst layers with specific designs in order to performed electrochemical characterisations in running cell conditions.

#### 2.3.1 Multilayered catalyst layer manufacturing

In the literature, the proposed design for porous catalyst layer was a linear and increasing amount of catalyst from the GDL to the membrane. Accordingly, catalyst layers were designed by flexography in such a way as described in Figure 120.

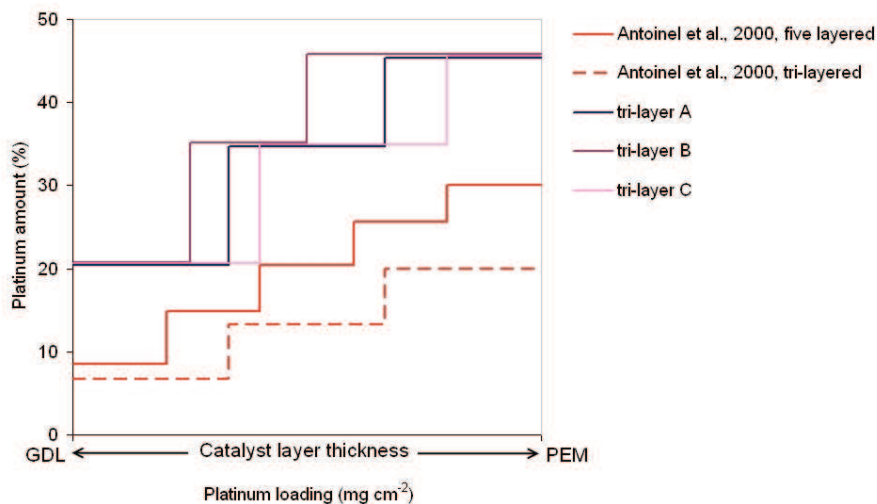


Figure 120 Amount of platinum of the catalyst layer from the GDL interface to the PEM interface (the catalyst layer thickness is normalized by the maximal thickness)

The two designs tested by Antoine [2000] had an average gradient of platinum (in w/w % of the total catalyst) of 14 and 24 for the tri- and five- layered respectively, with a minimal value close to the GDL equal to 6 and 8 respectively.

The three types of designs A, B and C made by flexography had gradients of platinum amounts that increased at a rate of 27, 26 and 26 w/w % with minimal amount equal to 20, 19 and 23 w/w % close to the GDL.

Two variations of the design A were manufactured. The A<sub>1</sub> and A<sub>2</sub> samples were obtained by superimposing respectively one and two layers of each type of ink. The details of the deposition protocol of these catalyst layers A<sub>1</sub> and A<sub>2</sub>, and also the catalyst layer B and C are given in Table 41.

Table 41 Deposition protocol of catalyst layers A, B and C

Design designation	Underneath sub layer	Middle sub layer Ink	Top sub layer Ink	Total number of superimposed ink layers
	Ink I <sub>33-26</sub>	Ink I <sub>24-29</sub>	Ink I <sub>13-29</sub>	
A <sub>1</sub>	1	1	1	3
A <sub>2</sub>	2	2	2	6
B	1	1	2	4
C	2	2	1	5

Each deposition protocol gave different catalyst layer, either made by three, four, five or six superimposed ink layers. The ink loading of these catalyst layers was equal to  $0.35 \pm 0.7$ ,  $0.8 \pm 0.1$ ,  $0.5 \pm 0.1$  and  $0.6 \pm 0.1$  mg cm<sup>-2</sup>. The calculated platinum loadings reached  $0.09 \pm 0.02$ ,  $0.19 \pm 0.04$ ,  $0.13 \pm 0.03$  and  $0.13 \pm 0.02$  mg cm<sup>-2</sup>.

The contributions in the ink and platinum loading of each of the three layers, underneath, middle and top layers described in Table 41, is depicted in Figure 121.

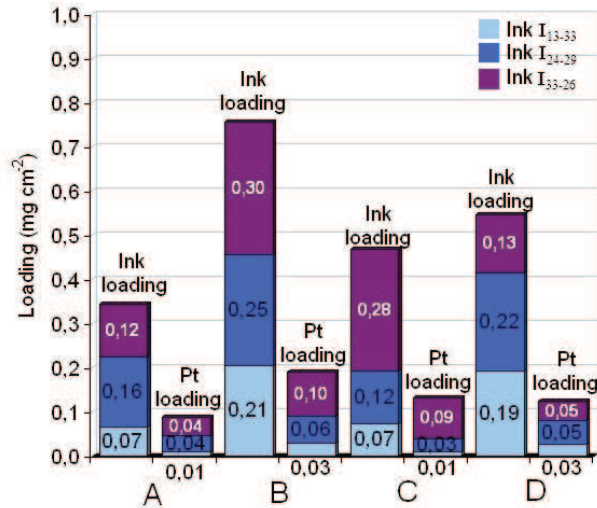


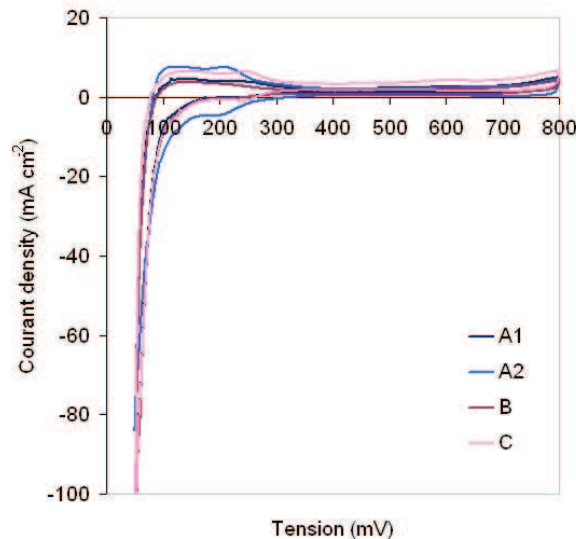
Figure 121 Ink and platinum loadings of catalyst layers A, B, C and D

The measurement error of the value given in was under  $0.01 \text{ mg cm}^{-2}$ .

### 2.3.2 Electrochemical characterisation of the designed catalyst layers

The catalyst layers were tested as cathodes, with  $0.05 \text{ mg cm}^{-2}$  anodes, and a Nafion<sup>®</sup> 211 membrane. This membrane was  $25 \mu\text{m}$  thick and had a similar equivalent weight to the Nafion<sup>®</sup> 212 membrane. The MEAs made using catalyst layer A<sub>1</sub> as cathode was named MAE A<sub>1</sub>, and so on.

Cyclic voltammograms of the four catalyst layers are given in the Figure 122.

Figure 122 Voltammograms of MEAs A<sub>1</sub>, A<sub>2</sub>, B and C

Electrochemical Surface Areas ( $\text{ESA cm}^2 \text{ cm}^{-2}$ ) of the four cathodes A<sub>1</sub>, A<sub>2</sub>, B and C were calculated thanks to the voltammograms. They were equal to 38, 87, 29 and  $50 \text{ cm}^2 \text{ cm}^{-2}$

respectively. These values are presented in Figure 123, as regards to the platinum loading of the cathodes.

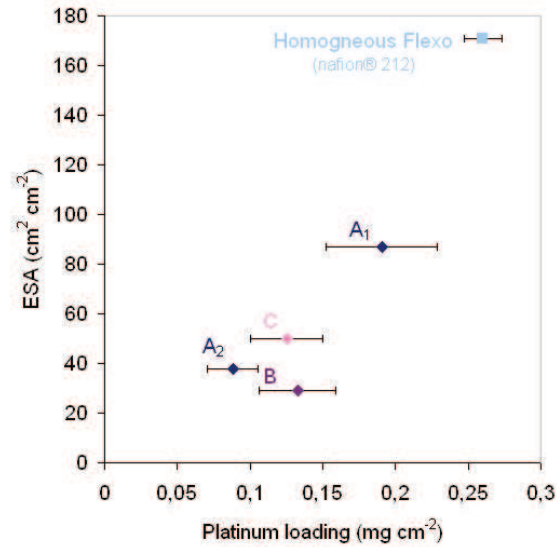


Figure 123 Platinum loading as a function of the ESA for designed catalyst layers and compared to a homogeneous catalyst layer (tested with Nafion<sup>®</sup> 212)

This Figure outlines the potential use of the platinum contained in the cathode. In the cathodes A<sub>1</sub>, A<sub>2</sub> and C the platinum potential use was estimated to reach  $440 \pm 90 \text{ cm}^2 \text{ mg}^{-1}$ . The cathode B reached  $220 \pm 40 \text{ cm}^2 \text{ mg}^{-1}$ , and the standard cathode (see chapter 3) reached  $660 \pm 30 \text{ cm}^2 \text{ mg}^{-1}$ . Therefore, the cathodes A<sub>1</sub>, A<sub>2</sub> and C had better potential platinum use than the cathode B. However, the standard homogeneous cathode still reached a higher potential use of the platinum catalyst.

The polarisation curves of the four cathode types are presented in Figure 124.

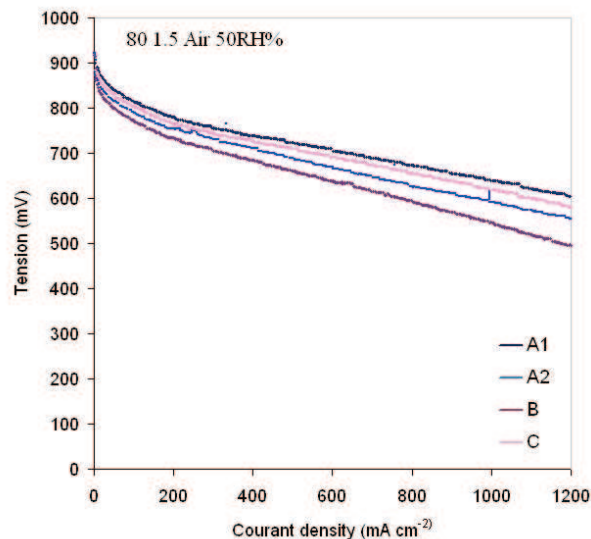


Figure 124 Polarisation curves of MEAs A<sub>1</sub>, A<sub>2</sub>, B and C

The low use potential use of catalyst of cathode B was confirmed by the lower polarisation curves among the four presented in this figure. The MEA A<sub>1</sub> A<sub>2</sub> and C had performances that followed the trend of their platinum loading.

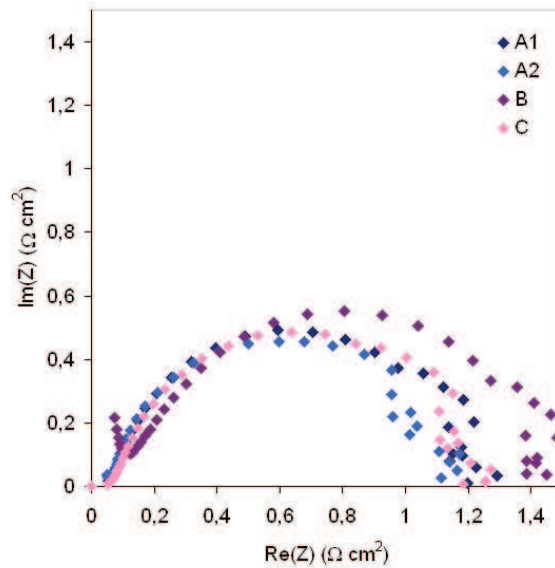


Figure 125 Impedance diagrams (for facilitating the lecture of the figure, only EIS at  $0.04 \text{ A cm}^{-2}$  are shown)

At high frequencies, MEAs A<sub>1</sub> A<sub>2</sub> and C had similar behaviours ( $\text{Im}(Z)$  around  $0 \text{ } \Omega \text{ cm}^2$ , and  $\text{Re}(Z)$  varies from  $0.05$  to  $0.1 \text{ } \Omega \text{ cm}^2$ ), and MEA B reached higher real and imaginary parts ( $\text{Im}(Z)$  around  $0.1 \text{ } \Omega \text{ cm}^2$  and  $\text{Re}(Z)$  varies from  $0.1$  to  $0.15 \text{ } \Omega \text{ cm}^2$ ). Moreover, the shape of the diagram of the MEA B was more linear in high frequencies than for three other MEAs.

At low frequencies, MEA A<sub>2</sub> had the lower real part (from  $1.1$  to  $1.2 \text{ } \Omega \text{ cm}^2$ ), followed by MEAs A<sub>1</sub> and C (which vary from  $1.2$  to  $1.3 \text{ } \Omega \text{ cm}^2$ ), and finally by MEA C, which ranged from  $1.4$  to  $1.5 \text{ } \Omega \text{ cm}^2$ ).

According to the literature, it is possible to conclude that:

- the ohmic resistances of the MEAs A<sub>1</sub> A<sub>2</sub> and C were lower than those of the MEA B,
- the gas phase transport limitations of the MEA A<sub>2</sub> were lower than those of the MEAs A<sub>1</sub> and C, which are lower than in MEA B.
- the proton diffusion was more limited in the MEA B than in the MEAs A<sub>1</sub> A<sub>2</sub> and C.

## 2.4 Conclusion and perspectives

The multilayer protocol firstly developed for manufacturing homogeneous catalyst layer by flexography was adapted to manufacture catalyst layers with different amounts of functional components in the thickness. Indeed, instead of depositing six layers of the same ink, each ink layer could be made using an ink with different amounts in functional particles.

The printability of five inks were tested: a standard ink, the same as in chapter 2 and 3, and two with lower platinum nanoparticles amounts and two with lower Nafion<sup>®</sup> amounts in their solid content. Homogeneous catalyst layers were manufactured by superimposing three or six layers of each type of ink. The inks with various amounts of platinum nanoparticles showed a sufficient printability, while the inks with a lower ionomer amount had a low printability which required more development before being used.

Consequently, catalyst layers were manufactured by superimposing ink layers with different platinum nanoparticles amounts. Six types of designs were proposed for validating, with success, the ability to superimpose of the three inks. Finally, three designs of catalyst layer, with an increasing amount in platinum, were electrochemically characterised. Some differences appeared between the different tested designs, but the tested MEAs showed good performances and ESA, reaching  $440 \pm 90 \text{ cm}^2 \text{ mg}^{-1}$ , compared to the standard cathode (described in chapter 4) that reached  $660 \pm 30 \text{ cm}^2 \text{ mg}^{-1}$ .

The flexography is able to accurately manufacturing catalyst layers with various designs and most of all; it leads to obtained efficient catalyst layers. Improvements are required for defining the most suitable design in order to reducing the platinum content in catalyst layer.

### **Conclusion of chapter 5**

In this chapter, the potential of application in the fuel cell domain of two characteristics of the printing industry were investigated.

Firstly, the use of reflectance spectrum measurement technique discriminates of the platinum amount and of the platinum loading. It showed that no platinum nanoparticles migrated from an ink layer to another when using the multilayer protocol.

The reflectance measurement technique is technically relevant. Moreover, it is also a good candidate for a complementary characterisation to conventional electrochemical characterisations, with numerous advantages: it is a fast, continuous and in-line technique.

The ability to deposit ink layers by the multilayer protocol with no observable migration of solid elements between the ink layers was used to design catalyst layers. Inks with various amounts of platinum nanoparticles were superimposed onto a GDL with different sequences. It led to obtain catalyst layers with different designs. They are electrochemically characterised as cathode and show good electrochemical properties.

# General conclusions



In a context of reduction of the pollutant emission and of the use of fossil fuel, the objective of the CATIMINHY project is to fabricate fuel cell components with innovative and economically relevant processes. Within the project, the goal of the thesis was the demonstration of the pertinence of printing processes applied for fuel cell components manufacturing.

The experimental approach focused on the manufacturing of direct CCM and CCB taking into account the specificities of the printing field for fuel cell applications.

The chapter 3 focused on the proton exchange membrane. First observations, corroborated by literature studies, demonstrated that the direct CCM is a complex method for manufacturing catalyst layers. The membrane affinity with water induces swelling and curling of the membrane.

In the present work, the proton exchange membrane was considered as a printing substrate for manufacturing direct CCM by flexography. The experimental approach evaluated the impact of the water, in vapour and liquid state on the membrane behaviour.

In a first part, variations of  $RH\%$  were performed onto membrane samples. Water uptake was measured and hygroexpansion tests showed that the membrane was very sensitive to these variations which induced fast and substantial dimensional variations. Such behaviour could be a problem for storing and processing the membrane during printing. Consequently, the  $RH\%$  conditions had to be controlled before and during printing.

In a second part, the membrane behaviour in contact with liquid water and ink was investigated. As strong dimensional variations occurred, a pre-treatment, based on a membrane immersion in water, was proposed in order to improve its dimensional stability and thus its printability. After this pre-treatment, the catalyst layers printed by flexography were successfully tested in operating fuel cells.

In chapter 4, conventional and printing techniques of CCB manufacturing were compared. Among them the flexography, which had never been tested before, appeared as a relevant technique. As a matter of fact, this technique was able to overpass the roughness and the poor printability of the GDL.

Moreover, the use of several printing groups in-line allows a multilayer deposition. This protocol led to catalyst layers with equivalent electrochemical performances than standard cathodes but with lower platinum loading.

In chapter 5, the ability to deposit ink layers by this multilayer protocol was used in order to design catalyst layers. Inks with various amounts of platinum nanoparticles were superimposed onto a GDL. As no migrations were observed between the different ink

layers, it was possible to propose different designs of catalyst layers. The few tested designed catalyst layers gave similar performances than standard cathodes. The multilayer protocol can be a promising way for improving the catalyst layers properties. In addition to the potential of the printing processes, usual non destructive characterisation techniques of print quality were implemented. For instance, the platinum loading could be evaluated by visible spectrophotometry. This technique is complementary to conventional electrochemical characterisations; besides it is fast and can be used in line after deposition step.

Future works should be dedicated to:

- characterisations of membranes as printing substrates.  
Hygroexpansion and water uptake at different temperatures, but also membrane ageing should be tested on other types of membranes.
- deposition selectivity of functional elements.  
Three dimensional designing of the catalyst layer should be performed (i) in thickness by multilayer protocol and (ii) in plane by printing pattern.

# Appendices



<b>APPENDIX 1: FUEL CELLS PRINCIPLES.....</b>	<b>209</b>
<b>1 SOLID OXIDE FUEL CELL (SOFC): THE FUEL CELL FED BY VARIOUS FUELS AND TOLERANT TO <math>CO_2</math>.....</b>	<b>211</b>
<b>2 MOLTEN CARBONATE FUEL CELL (MCFC): THE <math>CO_2</math> USER .....</b>	<b>212</b>
<b>3 ALKALINE FUEL CELL (AFC): THE CHEAPER CATALYSTS .....</b>	<b>212</b>
<b>4 PHOSPHORIC ACID FUEL CELL (PAFC): THE FIRST COMMERCIALISED ...</b>	<b>213</b>
<b>APPENDIX 2: STACK CHARACTERISATION .....</b>	<b>214</b>
<b>1 ELECTROCHEMICAL SURFACE AREA: THE ACTIVE SURFACE OF PLATINUM.....</b>	<b>214</b>
<b>2 <math>H_2</math> PERMEATION.....</b>	<b>215</b>
<b>3 RESISTANCES OF THE ELECTROCHEMICAL SYSTEM .....</b>	<b>216</b>
<b>4 ACTIVE ZONE EFFICIENCY .....</b>	<b>216</b>
<b>5 PEMFC COMPONENTS DURABILITY.....</b>	<b>218</b>
<b>APPENDIX 3: LIQUID/SUBSTRATE AFFINITY .....</b>	<b>219</b>
<b>APPENDIX 4: INTRINSIC PERMEABILITY UNCERTAINTIES .....</b>	<b>221</b>
<b>APPENDIX 5: VARIDIM MEASUREMENT LIMITATIONS .....</b>	<b>222</b>



**Appendix 1: Fuel cells principles**

Different types of fuel cell exist. Their electrochemical reactions, components, operating and economical characteristics are presented in the Table 42, Table 43, Table 44, Table 45 and Table 46.

Table 42 Electrochemical reaction at anode and cathode [Farooque *et al.*, 2001]:

Fuel cell	Anode reaction	Ion transport in electrolyte	Cathode reaction
SOFC	$H_2 + O^{2-} \rightarrow 2e^- + H_2O$	$\xleftarrow{O^{2-}}$	$2e^- + \frac{1}{2}O_2 \rightarrow O^{2-}$
MCFC	$H_2 + CO_3^{2-} \rightarrow 2e^- + H_2O + CO_2$	$\xleftarrow{CO_3^{2-}}$	$2e^- + \frac{1}{2}O_2 + CO_2 \rightarrow CO_3^{2-}$
PAFC	$H_2 \rightarrow 2e^- + 2H^+$	$\xrightarrow{2H^+}$	$2e^- + \frac{1}{2}O_2 + 2H^+ \rightarrow H_2O$
AFC	$H_2 + 2OH^- \rightarrow 2e^- + 2H_2O$	$\xleftarrow{2OH^-}$	$2e^- + \frac{1}{2}O_2 + H_2O \rightarrow 2OH^-$
PEMFC	$H_2 \rightarrow 2e^- + 2H^+$	$\xrightarrow{2H^+}$	$2e^- + \frac{1}{2}O_2 + 2H^+ \rightarrow H_2O$

Table 43 Components characteristics

Fuel cell	Electrolyte [Song, 2002]	Catalyst [Song, 2002]	Charge carrier [Farooque <i>et al.</i> , 2001; Song, 2002]	Cell hardware [Song, 2002]
SOFC	Ytria stabilised zirconia	<i>Ni</i>	$O^{2-}$	Ceramic
MCFC	Solution of <i>Li, Na, K</i> carbonates soaked in a matrix	<i>Ni</i>	$CO_3^{2-}$	Stainless steel
PAFC	Phosphoric acid soaked in a matrix	<i>Pt</i> or non-precious metals	$H^+$	Graphite based
AFC	Solution of <i>K</i> hydroxides soaked in a matrix	<i>Pt</i>	$OH$	Porous matrix
PEMFC	Perfluoro sulfonic acid	<i>Pt</i>	$H^+$	Carbon or metal based

Table 44 Operating characteristics 1

Fuel cell	Operating temperature (°C) [Song, 2002, Farooque <i>et al.</i> , 2001; Kamaruzzaman <i>et al.</i> , 2006; Peighambaroust <i>et al.</i> , 2010]	Fuels [Farooque <i>et al.</i> , 2001; Song, 2002]	Reforming [Farooque <i>et al.</i> , 2001; Song, 2002]	Gas pollutants [Farooque <i>et al.</i> , 2001; Song, 2002]
SOFC	700 – 7,000	$H_2$ , $CO$ , $CH_4$	Internal	$S$ ( $H_2S$ , $COS$ )
MCFC	600 – 700	$H_2$ , $CO$ , $CH_4$ , $NH_4$	Internal	$S$ ( $H_2S$ , $COS$ )
PAFC	150 – 200	$H_2$	External	$CO$ , $S$ ( $H_2S$ , $COS$ )
AFC	90 – 100	$H_2$	External	$CO_2$ , $S$ ( $H_2S$ , $COS$ )
PEMFC	50 – 100	$H_2$	External	$S$ ( $H_2S$ , $COS$ ), $NH_3$

Table 45 Operating characteristics 2

Fuel cell	Power (kW) [Farooque <i>et al.</i> , 2001; Song, 2002]	Power density ( $mW/cm^2$ ) [Peighambaroust <i>et al.</i> , 2010]	Life-time (h) [Peighambaroust <i>et al.</i> , 2010]	Star-up time [U.S. DOE]	Efficiency [Peighambaroust <i>et al.</i> , 2010]
SOFC	1 – 3,000	240	> 40,000	Long	55-65
MCFC	300 – 3,000	100	> 40,000	Long	60-65
PAFC	100 – 1,000	200	> 40,000	Long	55
AFC	10 - 100	100 – 200	> 10,000		40-60
PEMFC	0.1 - 100	350	> 40,000	Short	45-60

Table 46 Economical characteristics

Fuel cell	Capital cost (\$/kW) [Peighambaroust <i>et al.</i> , 2010]	Co-generation [Farooque <i>et al.</i> , 2001; Song, 2002]	Applications [Kamaruzzaman <i>et al.</i> , 2006; Peighambaroust <i>et al.</i> , 2010]
SOFC	1,500	High and low pressure steam and hot water Organic Rankine cycle Steam or gas turbine	Stationary: Auxiliary power Electric utility Distributed generation
MCFC	1,000	High and low pressure steam and hot water Organic Rankine cycle Steam or gas turbine	Stationary: Electric utility Distributed generation
PAFC	3,000	Low pressure steam, hot water and air conditioning	Stationary: Distributed generation
AFC	>200		Military Space
PEMFC	>200	Hot water	Transport and portative

Two main groups appear: the high and low operating temperature fuel cells. High temperature fuel cells are more dedicated for stationary power unit application (SOFC and MCFC), while low temperature fuel cells are more easily used in transportation (PAFC, AFC and PEMFC).

**1 Solid Oxide Fuel Cell (SOFC): the fuel cell fed by various fuels and tolerant to CO<sub>2</sub>**

SOFC emerges among the fuel cell technologies by proposing large, high power for stationary applications [Boudghene *et al.*, 2002]. This technology was developed in 1930s by Emil Baur and H. Preis. The first operating system was achieved in 1937. The versatility of fuels and the tolerance toward carbon monoxide made this fuel cell the core of several research studies in the 1950s: for example by the Central Technical Institute of The Hague, by the Consolidation Coal Company in Pennsylvania and by General Electric in New York. The other advantages and drawbacks of this technology are given in the Table 47.

Table 47 SOFC advantages and drawbacks

Advantages	Drawbacks
High efficiency	Cost (1 500 \$/kW)
Fuel flexibility thanks to internal reforming	Stress failure due to high operating temperature
Co-generation due to high operating temperature	Corrosion
Variety of catalyst (no noble and rare material)	Sulfur poisoning
Long life expectancy	Long start-up
	CO <sub>2</sub> production

The high operating temperature of the SOFC imposes specific properties such as resistance to thermal dilatation and stability for its components. For this reason, ceramics are mainly employed and the system fabrication cost is really high (1,500 \$/kW). In such a context, the reduction of the operating temperature to “intermediate temperatures” (700 – 900 °C) should increase the number of options for enhancing this technology [Tsipis *et al.*, 2011]. SOFC are manufactured either in tubular, planar or in monolithic shape. Tubular SOFCs are dedicated to stationary applications of more than several hundreds kilo-Watt [Farooque *et al.*, 2001] and planar shaped SOFC to smaller power unit. As this technology can be fuelled with either hydrocarbon-based gases or hydrogen [Paradis *et al.*, 2011], its flexibility appears adapted for a good transition solution to hydrocarbon to hydrogen economy. The U.S. DOE program for distributed generation fuel cell [Williams *et al.*, 2004] is developing high temperature fuel cells such as tubular SOFC.

Since late 1970's, the Siemens Westinghouse Power Corporation's Tubular SOFC Program developed tubular SOFCs and proposed 100, 200, 250 and 330 kW systems with some co-generating or turbine hybrids.

The Solid State Energy Conversion Alliance (SECA) SOFC program is one of the main DOE grant. It focuses on develop this technology at lower cost in order to make SOFC relevant for widespread market with a cost of 400 \$ kW<sup>-1</sup>. Small SOFC power unit (5 to 10 kW) are developing by Cummins and SOFCo, Siemens westinghouse or General Electric. Planar SOFC have been developed like the Delphi/Battelle 5 kW auxiliary power unit.

**2 Molten Carbonate Fuel Cell (MCFC): the CO<sub>2</sub> user**

In 1958, the first MCFC was built by Broers [1958 and 1960]. Molten Carbonate Fuel Cells are the only fuel cell technology that uses carbon dioxide as fuel [Tomczyk, 2006]. This high temperature technology has an operating temperature range from 600 to 700 °C. This range was described in the previous section as limiting the technical problems caused by a too high temperature. As high temperature fuel cells, MCFCs do not require pure hydrogen infrastructure and can be fuelled with natural gas, syngas or biogas. Moreover, the produced heat can be easily used [McPhail *et al.*, 2011]. The other MCFCs particularities are described in Table 48.

Table 48 MCFC advantages and drawbacks

Advantages	Drawbacks
High efficiency Co-generation Cheaper than SOFC	Electrolyte instability, Corrosion Sulfur poisoning Long start-up CO <sub>2</sub> production

The main key points for MCFC are: the high operating temperature, the corrosion of the molten alkaline carbonate and the nickel catalyst for internal reforming [Antolini, 2011]. They induce steam reforming limitation by catalyst dissolution, by coke formation and catalyst sintering. However, MCFC are considered as relevant by the DOE who is funding development of that technology. Direct Fuel Cell Energy, Inc. designed and commercialised power plants of 250, 1,000 and 2,000 kW [Williams *et al.*, 2004].

**3 Alkaline Fuel Cell (AFC): the cheaper catalysts**

Developed in 1939, this low temperature technology of fuel cell is known for its high efficiency and its catalysts that are cheaper and non-noble compared to PEMFC and PAFC [Varcoe *et al.*, 2005].

Table 49 AFC Advantages and drawbacks

Advantages	Drawbacks
High efficiency Non noble catalyst	Intolerant to $CO_2$ Corrosion High capital cost

Main issue of this technology is the pollution of the electrolyte by  $CO_2$  that reacts with the transfer ions  $OH$  to form carbonate and bicarbonate, which degrades the electrodes and the electrolyte. AFC are described as a mature technology use in the 1960s for the NASA Apollo missions [Lin *et al.*, 2006]. They are composed of a solid electrolyte that limits the risk of leaking of the liquid alkaline electrolyte in the case of transportation applications. Its popularity diminished when the other low temperature fuel cells appear.

#### 4 Phosphoric Acid Fuel Cell (PAFC): the first commercialised

In 1961 G.V. Elmore and H.A. Tanner firstly published their work on PAFC. This technology was found to be poorly damaged by  $CO$  in low amount [Appleby, 1996]. Moreover, it is possible to use the heat provided by its relatively high temperature (Table 50).

Table 50 PAFC Advantages and drawbacks

Advantages	Drawbacks
Tolerant to impure $H_2$ Co-generation	Low power density Corrosion Sulfur poisoning Pt catalyst Long start-up

This technology is largely represented for stationary electricity generation with more than 500 plants in 2005 predominantly made by UTC Fuel Cell, Toshiba and Fuji Electric. The good reliability of these installations confers interest for electricity production during electricity production interruptions of conventional plants [Sammes *et al.*, 2004]. However, the PAFC demand slows with the commercialization of PEMFC for small power supply and MCFC or SOFC for high power supply.

## Appendix 2: Stack characterisation

### 1 Electrochemical Surface Area: the active surface of platinum

The cyclic voltammetry allows the measure of the active surface of catalyst also called the Electrochemical Surface Area (ESA). The  $H_2$  adsorption and desorption at the surface of the catalyst are measured. To obtain this value, the experiment consists in measuring the current, when imposing a potential variation to an active electrochemical system. The imposed parameters are the solicitation speed  $\nu$  (mV/s) and the range of the applied potential.

One electrode is tested. The operating electrode is fed with hydrated or dry argon gas, while the counter electrode is fed with hydrated hydrogen in order to maintain the conductivity of the electrolyte. An external reference electrode made of mercury and sulphate mercury is required to measure the applied potential.

A typical graph, as shown in Figure , gives the value of the current  $I$  (mA) or current density (mA/cm<sup>2</sup>) as a function of the applied potential  $E$  (mV). Three distinct areas appear this Figure 126:

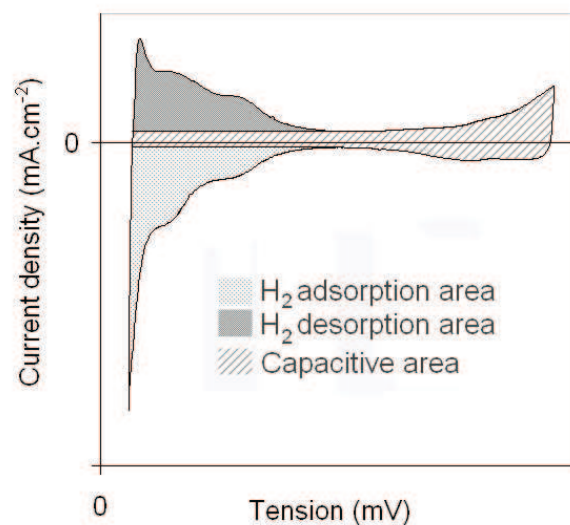


Figure 126 Typical shape of a curve representing cyclic voltammetry

- for  $I < 0$ , the protons from the electrolyte are reduced and hydrogen is produced and adsorbed onto the catalysts following the reaction in Equ. 27.



- for  $I > 0$ , the counter reaction occurs (Equ. 28), and  $H_2$  desorbs and is oxidised:



- the third zone is called the capacitive zone since the cell reacts as a capacitor that loads and de-loads.

The ESA is the ratio of the experimental electricity quantity  $Q$  (C/cm<sup>2</sup>) corresponding to the adsorption and desorption of H<sub>2</sub> and to the platinum specific load  $Q_{Pt}$  (equal to 210 μC cm<sup>-2</sup>) (Equ. 29).

$$ESA = \frac{Q}{Q_{Pt}} \quad \text{Equ. 29}$$

The experimental electricity quantity  $Q$  is the ratio between the cyclic voltammetry area  $CV$  area and the solicitation speed  $v$  (mV/s) given by the equation Equ. 31.

$$Q = \int I \cdot dt = \int \frac{I \cdot dU \cdot dt}{dU} = \int \frac{I \cdot dU}{\frac{dU}{dt}} = \frac{CV_{area}}{v} \quad \text{Equ. 30}$$

Finally the ESA is the ratio between the cyclic voltammetry area  $CV$  area (cm<sup>2</sup>) and the product of the solicitation speed  $v$  (mV/s) by the platinum specific load  $Q_{Pt}$  in Equ. 31.

$$ESA = \frac{CV_{area}}{v \cdot Q_{Pt}} \quad \text{Equ. 31}$$

## 2 H<sub>2</sub> permeation

The voltammetry also allows the hydrogen permeation measurement. The operating electrode is fed by nitrogen gas, and the counter electrode is fed by hydrogen. The applied potential speed  $v$  is slower in order to let the system stabilises. The curve of the current  $I$  (mA) as a function of the applied potential  $E$  (mV) shows three steps. In the first step, the current is negative due to the reduction of the proton in the membrane into hydrogen. Then, from about 100 mV to 300 mV, the current becomes positive, and the hydrogen coming from reduction of the protons of the membrane is oxidised. It corresponds to the maximum of the curve. Finally, the curve stabilised from about 300 mV when the hydrogen that go through the membrane is oxidised.

The H<sub>2</sub> flow (mol/s/cm<sup>2</sup>) is calculated in Equ. 32 using the current intensity  $I$  (A) measured in the stabilised part of the curve.

$$F_{H_2} = \frac{n_{H_2}}{S \cdot dt} = \frac{n_{e^-}}{2 \cdot F \cdot S \cdot dt} = \frac{I}{2 \cdot F \cdot S} \quad \text{Equ. 32}$$

Where  $F$  (C mol<sup>-1</sup>) the faraday number equal to 96 500 C mol<sup>-1</sup>

$S$  (cm<sup>2</sup>) the electrode surface

### 3 Resistances of the electrochemical system

Electrochemical Impedance Spectroscopy (EIS) allows the characterisation of different phenomena taking place on the running cathode catalyst layer (Bultel *et al.*, 2002; Pozio *et al.*, 2002; Franco *et al.*, 2007). Impedance is measured and diagrams are plotted. Redox reactions are commonly modelled by resistor / capacitor in parallel equivalent circuits. The impedance diagram of such a circuit without mass-transfer limitation is a Nyquist diagram representing the opposite of the imaginary part of the impedance as a function of the impedance modulus. It forms a semicircular curve (Figure 127.a) with a diameter equal to the equivalent resistance of the system. At higher frequencies (Figure 127.1), the interfacial charge-transfer resistance and the catalyst layer properties are highlighted. At lower frequencies (Figure 127 .2)), the gas transport limitations in the gas diffusion layer are determined.

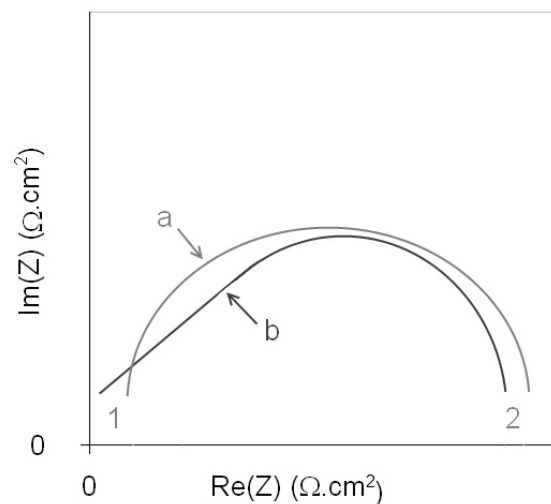


Figure 127 schematic representation of a EIS diagrams

The slope at high frequencies detailed the proton diffusion; a slope close to  $45^\circ$  is typical of a high proton diffusion limitation (Figure 127.b)). The extreme high frequencies value gives the ionic and electric resistance of the system. Moreover, an increase of the diameter of the semi circular curve shows a higher charge transfer resistance.

### 4 Active zone efficiency

In the catalyst layer, the electrochemical reactions are located in catalyst site where the reactants meet the catalyst. The reactants and products transports require protons and electrons conductors. Consequently, the catalyst is surrounded by carbon powder for the

electrons conduction and electrolyte ionomers for the protons conduction and they form a triple-point site.

The phenomena that happen in this site can be limited and then the system efficiency is reduced. At the gas/catalyst interfaces, the reaction can be limited by the catalyst efficiency and by the catalyst accessibility for the gas. At the ionomer/catalyst interfaces, ionic resistances can occur. At the carbon/catalyst interfaces, ohmic resistances may happen.

These resistances are characterised by polarisation curves of tension/current, which are divided in three main parts in the typical curve of the Figure 128.

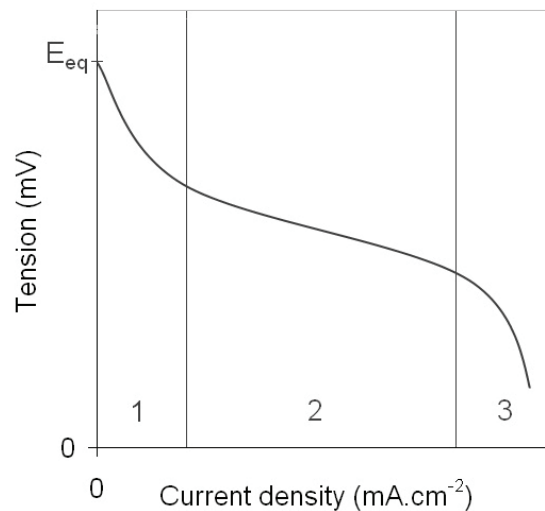


Figure 128 Polarisation curve, 1) catalyst activation, 2) ionic and electronic resistances, 3) gas diffusion.

- at small current density values, the prior limitation depends on the catalyst activation, especially due to the cathodic reaction (Figure 128. 1)).
- then, the ionic resistance of the membrane and the ohmic resistances of all the interfaces of the cell system decrease the cell tension (Figure 128. 2)).
- and, for high current values, the gas diffusion is insufficient to correctly feed the catalyst. Then it lower the electricity production (Figure 128. 3)).

The performances are highly influenced by the temperature and pressure. An increase of these parameters allows:

- increasing the kinetic of the electrochemical reactions inducing lower activation polarisation,
- diminishing the ohmic of the PEM by increasing its protonic conductivity,

- enhancing the gas diffusion in the electrodes, diminishing the ohmic resistance of due to mass transport.

However, pressure and temperature increase is limited the impact it induce on the complexity and cost of the balance of stack.

## **5 PEMFC components durability**

The previous techniques can be applied on cells that have been aged under temperature, relative humidity and potentials variations. These parameters are cycled, with conditions that depend on the chosen standard. The effects of aging are measured on the fuel cell structure, GDL hydrophobic character, the membrane thinning, and on the catalyst and carbon corrosion.

The cells degradation occurring under operating is one of the major issues for their implementation. DOE 2015 targets 5,000 h life-time, equivalent to 7 months in operating vehicle conditions, and more than 40,000 h, equivalent to 4.5 years of continuous operating for stationary applications. The current life-time for these applications is respectively 1,700 and 10,000 h.

### Appendix 3: Liquid/substrate affinity

The measure of the interactions between a liquid and a surface could be performed by the deposition of a liquid droplet onto the surface. The deposition of a drop falling vertically on a horizontal surface has been studied in order to investigate the wetting properties of the liquids and the different contact angle values obtained depending on the couple of tested liquid and surface.

The deposition of a liquid  $L$  droplet onto a flat surface chemically homogeneous  $S$  forms a typical system described in Figure 129. The system is composed of two interfaces  $L/S$  and  $L/V$ , the edge of the drop on the surface are a line of triple phases  $L/S/V$ . At this triple point, the angle  $\theta$  between the interfaces  $S/L$  and  $L/S$  is measured.

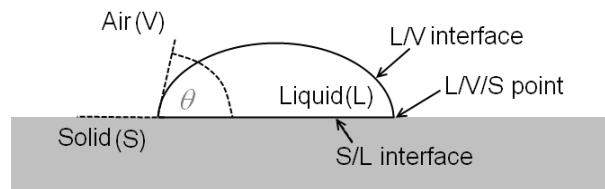


Figure 129 Cross view of a liquid drop on a surface: interfaces between liquid, air and solid

The relation between the liquid, the air and the solid characteristics is given by the Young relation in Equ. 33 thanks to the Young's contact angle  $\theta$ :

$$\cos \theta = \frac{\gamma_{S/V} - \gamma_{S/L}}{\gamma_{L/V}} \quad \text{Equ. 33}$$

In this equation,  $\gamma$  is the interfacial tension between two different phases (S, L or V). The interfacial tension ( $\text{N m}^{-1}$  or  $\text{J m}^{-2}$ ) quantifies the energy required to create an interface between two phases of one square meter.

In the general case, at low temperature, the interfacial tension is decomposed into polar  $\gamma^p$  and dispersive  $\gamma^d$  contributions in Equ. 34 that described the van der Waals interactions.

$$\gamma = \gamma^p + \gamma^d \quad \text{Equ. 34}$$

In this equation,  $\gamma^p$  includes the hydrogen bonding, acid-base, the Keesom and Debye interactions and  $\gamma^d$  the London interaction.

Different theories link the contact angle and the dispersive and polar contributions of the interfacial tension. The Owens-Wendt two-parameters equation (Equ. 35, also presented in chapter 4) allows the calculation of the contributions  $\gamma_S^p$  and  $\gamma_S^d$  of the interfacial tension of a solid by measuring on its surface the Young's contact angles  $\theta$  of drops of different liquids with known interfacial tensions contributions  $\gamma_L^p$  and  $\gamma_L^d$ .

$$\gamma_L (\cos \theta - 1) = 2 \left( \sqrt{\gamma_L^p \cdot \gamma_S^p} + \sqrt{\gamma_L^d \cdot \gamma_S^d} \right) \quad \text{Equ. 35}$$

However, the solid surfaces are generally rough and covered by chemical heterogeneities. For example, Johnson and Dettre have shown the influence of the roughness on the contact angle of water drops on wax surface. Consequently, there is the Young's contact angle  $\theta$  that is intrinsic to the surface chemistry. However, material surface are often rough or heterogeneous. Consequently, the measure of a contact angle of a liquid on such a surface does not give the Young's contact angle but the apparent contact angle  $\theta^*$  that takes into account the other surface characteristics.

In 1936, Wenzel has calculated a roughness parameter  $r$  Equ. 36 that is the ratio of the real area  $A_{real}$  of the surface one the projected area  $A_{projected}$ .

$$r = \frac{A_{real}}{A_{projected}} \quad \text{Equ. 36}$$

He used  $r$  to link the Young's contact angle  $\theta$  with the apparent contact angle  $\theta^*$  of a rough surface (Equ. 37).

$$r \cdot \cos \theta = \cos \theta^* \quad \text{Equ. 37}$$

The Wenzel model supposes that the liquid follows the surface of the roughness.

In the case of a surface covered by two types of chemical material (called 1 and 2), the relation between the Young's contact angles  $\theta_1$  and  $\theta_2$  of the two different material 1 and 2 and the apparent contact angle  $\theta^*$  measured on the heterogeneous surface is given by the Cassie-Baxter's model in Equ. 38.

$$\cos \theta^* = \varphi_1 \cos \theta_1 + \varphi_2 \cos \theta_2 \quad \text{Equ. 38}$$

The Cassie-Baxter equation is also used for rough surface. As the contrary to Wenzel's model, it supposes that the liquid drop is in contact only with the roughness crests. Such a liquid behaviour is also called "fakir" state.

#### Appendix 4: Intrinsic permeability uncertainties

Uncertainties of the Equ. 39 firstly detailed in chapter 2 section 2.3.3 are calculated by considering that the main error on  $K_{CL}$  result from air flows  $Q_{GDL}$  and  $Q_{GDE}$  and thicknesses  $T_{GDE}$  and  $T_{GDL}$  (Equ. 40 and Equ. 41).

$$K_{CL} = \left( \frac{Q_{GDE} \cdot Q_{GDL}}{Q_{GDE} - Q_{GDL}} \right) \cdot \frac{T_{CL}}{\Delta P \cdot S} \quad \text{Equ. 39}$$

$$dK_{CL} = \frac{\delta K_{CL}}{\delta Q_{GDE}} \cdot dQ_{GDE} + \frac{\delta K_{CL}}{\delta Q_{GDL}} \cdot dQ_{GDL} + \frac{\delta K_{CL}}{\delta T_{CL}} \cdot dT_{CL} \quad \text{Equ. 40}$$

and

$$dK_{CL} = \frac{T_{CL}}{\Delta P \cdot S} \cdot \left( \frac{Q_{GDL}}{Q_{GDE} - Q_{GDL}} \right)^2 \cdot dQ_{GDE} - \frac{T_{CL}}{\Delta P \cdot S} \cdot \left( \frac{Q_{GDE}}{Q_{GDE} - Q_{GDL}} \right)^2 \cdot dQ_{GDL} + \frac{1}{\Delta P \cdot S} \cdot \left( \frac{Q_{GDL} \cdot Q_{GDE}}{Q_{GDE} - Q_{GDL}} \right) \cdot dT_{CL}$$

Equ. 41

Consequently, the uncertainty of the intrinsic permeability KCL is given by Equ. 42

$$\frac{\Delta K_{CL}}{K_{CL}} = \left| \frac{Q_{GDL}}{Q_{GDE} - Q_{GDL}} \right| \cdot \frac{\Delta Q_{GDE}}{Q_{GDE}} + \left| \frac{Q_{GDE}}{Q_{GDE} - Q_{GDL}} \right| \cdot \frac{\Delta Q_{GDL}}{Q_{GDL}} + \frac{\Delta T_{CL}}{T_{CL}} \quad \text{Equ. 42}$$

The fabrication of catalyst layers creates an interface between the surface of a substrate and a solidified deposit. The surface of the substrate, the process and the dispersion directly impacts the quality of this interface. In this study, the application set the GDL and PEM as printing substrates. Consequently, the measurement of their physical and chemical surface properties was essential data for evaluating the match between surface/dispersion/process's characteristics that insured the creation of an interface.

**Appendix 5: Varidim measurement limitations**

Precisions on the impact of the *RH%* setting changes on the membrane expansion are detailed in Figure 130 and Figure 131.

The Figure 130 shows the rate of expansion of the membrane samples ( $\mu\text{m s}^{-1}$ ) and the rate of *HR%* variations ( $\% \text{s}^{-1}$ ) as a function of time (h).

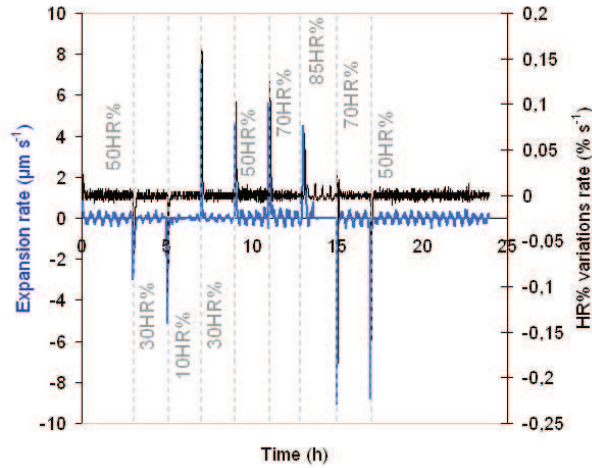


Figure 130 Expansion rate ( $\mu\text{m s}^{-1}$ ) and *HR%* variations rate ( $\% \text{s}^{-1}$ ) as a function of time (h)

The Figure 130 shows two curves that regularly varied with Diracs impulses occurring each two hours. The basic variations described effect of the device *RH%* setting control on the *RH%* values in the chamber and on the membrane dimension. The Diracs impulses were the effects of the setting changes. Consequently, changing the setting induced high *RH%* variations and samples dimensional variations. Some of these Diracs impulses reached higher values: when *RH%* varied from 10 to 30 %, from 85 to 70 and to 50 %, and some other shows lower values: when *RH%* varied from 50 to 30 %, and from 70 to 85 %. For a better understanding, the rates of expansion and the rate of *RH%* variations are reported in Table 51.

Table 51 Impacts of the setting change on the membrane behaviour, the bold numbers highlight particular values

n°	Initial setting ( <i>RH%</i> )	Final setting ( <i>RH%</i> )	Duration of Expansion and <i>RH%</i> changes (s)	Maximal expansion rate ( $\mu\text{m s}^{-1}$ )	Maximal <i>RH%</i> variations rate ( $\% \text{s}^{-1}$ )	Times of maximal rates (s)
1	50	30	440 ± 40	<b>-2.99</b>	<b>-0.067</b>	<b>60 ± 20</b>
2	30	10	380 ± 40	-5.09	-0.11	100 ± 20
3	10	30	<b>320 ± 40</b>	7.36	0.16	100 ± 20
4	30	50	370 ± 40	4.15	0.10	80 ± 20
5	50	70	400 ± 40	5.63	0.12	140 ± 20
6	70	85	<b>680 ± 40</b>	4.47	0.068	<b>260 ± 20</b>
7	85	70	370 ± 40	<b>-8.84</b>	<b>-0.18</b>	220 ± 20
8	70	50	500 ± 40	-8.56	-0.16	140 ± 20

The Table 51 gives the maximum reached by the  $RH\%$  variations rates for each setting modifications. Each setting change is numbered from 1 to 8 for simplification. The average absolute maximal variation is equal to  $0.12 \pm 0.04 \text{ \% s}^{-1}$ . The lowest absolute values,  $-0.067$  and  $0.068 \text{ \% s}^{-1}$ , were reached at setting changes 1 and 6, which respectively corresponds to  $RH\%$  varying from 50 to 30 % and from 70 to 85 %. The highest absolute values,  $-0.18$  and  $-0.16 \text{ \% s}^{-1}$ , were reached at setting change 7 and 8, when  $RH\%$  decreased from 85 to 50  $RH\%$ .

In this table, the average absolute value of the expansion rate was about  $6 \pm 2 \text{ }\mu\text{m s}^{-1}$ , which varied from 3 to 9  $\mu\text{m s}^{-1}$ . Four values seem particular:

- the absolute minimum of this parameter,  $-2.99 \text{ }\mu\text{m s}^{-1}$ , was reached at the first setting change (n°1), when  $RH\%$  varied from 50 to 30 %.
- the maximal absolute values, equal to 8.84 and 8.56  $\mu\text{m s}^{-1}$ , were reached at the changes n° 7 and 8, when  $RH\%$  varied from 85 to 50 %.
- And finally, at setting change n° 3, from 10 to 30  $RH\%$ , the expansion rate reached 7.36  $\mu\text{m s}^{-1}$ .

Besides, this table gives the duration of the expansion and  $RH\%$  changes (s) that represents the times required by the device and by the sample to stabilise after a setting change. At first sight, the duration of the stabilisation of the membrane was similar to the time of stabilisation of the  $RH\%$ . A second specific time is given in this table: the time of maximal rates, which corresponding to the times when the maximal expansion rates and  $RH\%$  variations rates were measured. Once again, the maximal rates values of the  $RH\%$  and of the sample were measured at the same time. This indicated, the sample dimensional variations kinetic is limited by the device setting control.

Five setting changes appear different:

- n° 1, from 50 to 30  $RH\%$ , where the sample and the device had a low rate,
- n° 3, from 10 to 30  $RH\%$  where the sample and the device reached a high rate,
- n° 6, from 70 to 85  $RH\%$ , where the sample and the device had a low rate,
- n° 7 and 8, from 85 to 50  $RH\%$ , the sample and the device had a high rate.

The device and the sample variations were slower when moving away from the 50  $RH\%$  setting, and faster when moving closer to 50  $RH\%$ .

Such phenomenon can be explained by:

- either the influence of the room conditions. Indeed, the device was placed in a room at 50  $RH\%$  and 23 °C during the trial. Some air diffusion from the room to the closed chamber may influence the  $RH\%$  value in the closed

chamber and acted as a factor inertia that tended to maintain the  $RH\%$  close to 50 %.

- or/and the influence of the sample, which captured and released water during the trial and may also acted as a factor of inertia as well.

In order to put aside the impact of the device control on the sample expansion rate, the ratio of the expansion rate on the  $RH\%$  variations rate was calculated, and presented in Figure 131 as a function of the time of trial.

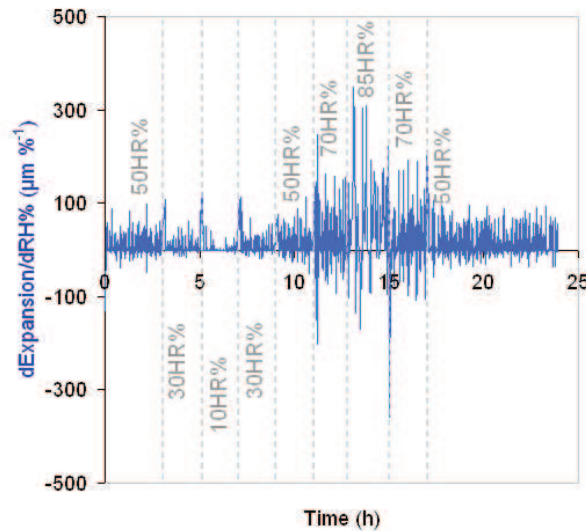


Figure 131 Expansion with respect to the  $RH\%$  variations as a function of the time (h)

This graphic shows that the impact of the  $RH\%$  variations on the sample dimensional variations depends of the  $RH\%$  values. At  $RH\%$  values varying from 10 to 50 %, the sample variations ranged between -100 and 100  $\mu\text{m } \%^{-1}$ . However, from 50 to 85  $RH\%$ , the value of sample expansion varied from -360 to 350  $\mu\text{m } \%^{-1}$ . The maximal values (349 and -357  $\mu\text{m } \%^{-1}$ ) were reached when the setting changed from 70 to 85 and from 85 to 70  $RH\%$ . 10  $RH\%$  is also a noticeable value since the sample variations reached their minimal values, lower than 50  $\mu\text{m } \%^{-1}$ .

The setting changes n° 6 and 7 (from 70 to 85 and to 70  $RH\%$ ) impacted more the membrane dimensions compared to the other setting changes. On the contrary, at low  $RH\%$  (10%), the membrane sample dimensions were less impacted by the  $RH\%$  variations.

The membrane deformed more at high  $RH\%$ , and less at low  $RH\%$ .

## Scientific publications



**Scientific journals**

Bois Chloé, Blayo Anne, Chaussy Didier, Vincent Rémi, Mercier Anne-Gaëlle, Nayoze Christine

2012 “Catalyst Layers for PEMFC Manufactured by Flexography Printing Process: Performances and Structure”  
Fuel Cells 12 2

Bois Chloé, Blayo Anne, Chaussy Didier, Vincent Rémi, Lionel Chagas, Nayoze Christine

2012 “Characterisation of catalyst layers for fuel cell printed by Flexography”  
Journal of Printing Media Technology Research, submitted in May 3<sup>rd</sup>

Bois Chloé, Dumont Pierre J. J., Blayo Anne, Vincent Rémi, Nayoze Christine, Chaussy Didier

2012 “Printing Process Ability to Manufacture Catalyst Coated Membrane for Fuel Cell”  
Journal of Fuel cell Science and Technology, submitted in December 15<sup>th</sup>

**Oral presentation in scientific meeting**

Bois Chloé, Blayo Anne, Chaussy Didier, Vincent Rémi, Mercier Anne-Gaëlle, Nayoze Christine

2011 “Printing process for up scaling Proton Exchange Membrane Fuel Cell manufacturing”  
Fundamentals and Developments of Fuel Cells, 19-21 January Grenoble France

Bois Chloé, Blayo Anne, Vincent Rémi, Nayoze Christine, Chaussy Didier

2011 “Characterisation of catalyst layers for fuel cell printed by Flexography”  
The International Association of Research Organizations for the Information, Media and Graphic Arts Industries, 11-14 September, Budapest, Hungary  
Published in Advances in printing and Media Technology 38 237-245

Bois Chloé, Blayo Anne, Vincent Rémi, Mercier Anne-Gaëlle, Nayoze Christine, Chaussy Didier

2012 “The Relevance of Printing Processes in Proton Exchange Membrane Fuel Cell Manufacturing”  
Technical Association of the Graphic Arts, 18-21 March, Jacksonville Florida USA



# References



- 1 Affoune A. M., Yamada A., Umeda M.  
2005 “Conductivity and surface morphology of Nafion membrane in water and alcohol environments”  
*Journal of Power Sources* 148 9–17
- 2 Andujar J.M. and Segura F.  
2009 “Fuel cells: History and updating. A walk along two centuries”  
*Renewable and Sustainable Energy Reviews* 13 2309–2322
- 3 Antoine O., Bultel Y., Ozil P. and Durand R.  
2000 “Catalyst gradient for cathode active layer of proton exchange membrane fuel cell”  
*Electrochimica Acta* 45 4493–4500
- 4 Antolini E., Giorgi L., Pozio A. and Passalacqua E.  
1999 “Influence of Nafion loading in the catalyst layer of gas-diffusion electrodes for PEFC”  
*Journal of Power Sources* 77 136–142
- 5 Appleby A.J.  
1996 “Issues in fuel cell commercialization”  
*Journal of Power Sources* 69 153-176
- 6 Arico A.S., Stassi A., Modica E., Ornelas R., Gatto I. and Passalacqua E.  
2008 “Performance and degradation of high temperature polymer electrolyte fuel cell catalysts”  
*Journal of Power Sources* 525 - 536.
- 7 Aspler J.S., De Grace J.H., Beland M.-C., Maine C. and Piquard L.  
1993 “Transfer and Setting of Water-Based Ink.Part 11: pH, Water Absorbency and Uncoated Paper Structure”  
*Journal of Pulp and Paper Science* 19 J203-J208
- 8 Atanasoski R. T. - 3M Company  
2011 “Durable Catalysts for Fuel Cell Protection During Transient Conditions”  
DOE Hydrogen and Fuel Cells Program, FY 2011 Annual Progress Report  
[In line]  
[http://www.hydrogen.energy.gov/pdfs/progress11/v\\_d\\_3\\_atanasoski\\_2011.pdf](http://www.hydrogen.energy.gov/pdfs/progress11/v_d_3_atanasoski_2011.pdf)
- 9 Barclay Satterfield M. and Benziger Jay B.  
2009 “Viscoelastic Properties of Nafion at Elevated temperature and Humidity”  
*Journal of Polymer Science: Part B: Polymer Physics* 47 11–24
- 10 Bass M., Berman A., Singh A., Konovalov O. and Freger V.  
2010 “Surface Structure of Nafion in Vapor and Liquid”  
*Journal of Physical Chemistry B* 114 3784–3790
- 11 Bello S. M., Parfitt S. A. and Stringer C.  
2009 “Quantitative micromorphological analyses of cut marks produced by ancient and modern handaxes”  
*Journal of Archaeological Science* 36 1869
- 12 Bender G., Zawodzinski T. A. and Saab A. P.  
2003 “Fabrication of high precision PEFC membrane electrode assemblies”  
*Journal of Power Sources* 124 114–117
- 13 Bi W. and Fuller T. F.  
2008 “Modeling of PEM fuel cell Pt/C catalyst degradation”  
*Journal of Power Sources* 188 - 196

- 14 Blayo A. and Pineaux B.  
2005 “Printing Processes and their Potential for RFID Printing”  
Joint sOc-EUSAI conference, Grenoble, France
- 15 Blumenthal G., Cappadonia M. and Lehmann M  
1996 “Investigation of the Proton Transport in Nafion<sup>®</sup> Membranes as a Function of Direction, Temperature and Relative Humidity”  
Ionics 2 2 102-106
- 16 Bockris John O’M. 2002  
“The origin of ideas on a Hydrogen Economy and its solution to the decay of the environment”  
International Journal of Hydrogen Energy 27 731 – 740
- 17 Bockris John O’M. 2008  
“Hydrogen no longer a high cost solution to global warming: New ideas”  
International Journal of Hydrogen Energy 33 2129 – 2131
- 18 Bonifácio R. N., Armani Paschoal J. O., Linardi M. and Cuenca R.  
2011 “Catalyst layer optimization by surface tension control during ink formulation of membrane electrode assemblies in proton exchange membrane fuel cell”  
Journal of Power Sources 196 4680–4685
- 19 Bossel U.  
2006 “Does a Hydrogen Economy Make Sense?”  
Proceedings of the IEEE 94 10
- 20 Boudghene Stambouli A. and Traversa E.  
2002 “Solid oxide fuel cells (SOFCs): a review of an environmentally clean and efficient source of energy”  
Renewable and Sustainable Energy Reviews 6 433–455
- 21 Broers G. H. J.  
1958 “High Temperature Galvanic Fuel Cells”  
Thesis. University of Amsterdam, The Netherlands
- 22 Broers G.H. J. and Ketelaar J. A. A.  
1960 “High-temperature fuel cells”  
Industrial and Engineering Chemistry 32 303
- 23 Bultel Y., Genies L., Antoine O., Ozil P. and Durand R.  
2002 “Modeling impedance diagrams of active layers in gas diffusion electrodes: diffusion, ohmic drop effects and multistep reactions”  
Journal of Electroanalytical Chemistry 527 143
- 24 Caillard A., Charles C., Ramdutt D., Boswell R. and Brault P.  
2009 “Effect of Nafion and platinum content in a catalyst layer processed in a radio frequency helicon plasma system”  
Journal Physics D: Applied Physics 045207
- 25 Chaabane L., Bulvestre G., Larchet C., Nikonenko V., Deslouis C. and Takenouti H.  
2008 “The influence of absorbed methanol on the swelling and conductivity properties of cation-exchange membranes Evaluation of nanostructure parameters”  
Journal of Membrane Science 323 167-175
- 26 Chaparro A.M., Gallardo B., Folgado M.A., Martín A.J. and Daza L.  
2009 “PEMFC electrode preparation by electrospray: Optimization of catalyst load and ionomer content”  
Catalysis Today 237–241
- 27

- Chatzidouros E.V., Papazoglou V.J., Tsiourva T.E. and Pantelis D.I.  
2011 “Hydrogen effect on fracture toughness of pipeline steel welds, with in situ hydrogen charging”  
International Journal of Hydrogen Energy 36 12626-12643
- 28 Cheng S., Liu H. and Logan B. E.  
2006 “Power Densities Using Different Cathode Catalysts (Pt and CoTMPP) and Polymer Binders (Nafion and PTFE) in Single Chamber Microbial Fuel Cell”  
Environmental Science and Technology 40 364-369
- 29 Chiarot P. R. and Jones T. B.  
2009 “Dielectrophoretic deflection of ink jets”  
Journal of Micromechanics and Microengineering 19 125018
- 30 Chuang C.-M., Sharma S. P., Ting J.-M., Lin H.-P., Teng H.H. and Huang C.-W.  
2008 “Preparation of sea urchin-like carbons by growing one-dimensional nanocarbon on mesoporous carbons”  
Diamond & Related Materials 17 606–610
- 31 Cindrella L., Kannana A.M., Lin J.F., Saminathan K., Hoc Y., Lind C.W. and Wertz J.  
2009 “Gas diffusion layer for proton exchange membrane fuel cells—A review”  
Journal of Power Sources 194 146–160
- 32 Cohen Y., Mathiesen J. and Procaccia I.  
2009 “Drying Patterns: Sensitivity to Residual Stresses”  
Physical Review 79 046109
- 33 Collette F. M., Lorentz C., Gebel G. and ThomINETTE F.  
2009 “Hygrothermal aging of Nafion<sup>®</sup>”  
Journal of Membrane Science 330 21–29
- 34 CRC Handbook of Chemistry and Physics, 92<sup>nd</sup> Edition, 2011-2012
- 35 De Castro E. S. - BASF Fuel Cell, Inc.  
2011 “High Speed, Low Cost Fabrication of Gas Diffusion Electrodes for Membrane Electrode Assemblies”  
DOE Hydrogen and Fuel Cells Program, FY 2011 Annual Progress Report  
[in line] [http://www.hydrogen.energy.gov/pdfs/progress11/vi\\_7\\_decastro\\_2011.pdf](http://www.hydrogen.energy.gov/pdfs/progress11/vi_7_decastro_2011.pdf)
- 36 de Gennes P.G.  
2002 Gouttes, Bulles, Perles et Ondes  
Belin Editeur, 2002
- 37 Debe M. K. - 3M Company,  
2011 “Advanced Cathode Catalysts and Supports for PEM Fuel Cells”  
DOE Hydrogen and Fuel Cells Program, FY 2011 Annual Progress Report  
[in line] [http://www.hydrogen.energy.gov/pdfs/progress11/v\\_d\\_1\\_debe\\_2011.pdf](http://www.hydrogen.energy.gov/pdfs/progress11/v_d_1_debe_2011.pdf)
- 38 Denneulin A.  
2010 “Inkjet printing of Conductive Inks for RFID Technology: Influence of the Substrate, Ink and Process”  
Thesis, Grenoble 26 october 2010
- 39 DuPont<sup>™</sup> Nafion<sup>®</sup> PFSA Membranes description  
[in line] [http://www2.dupont.com/FuelCells/en\\_US/assets/downloads/dfc201.pdf](http://www2.dupont.com/FuelCells/en_US/assets/downloads/dfc201.pdf)
- 40 Ender D., Omer Necati C. and Muammer K.  
2011 “Experimental investigations on the corrosion resistance characteristics of coated metallic bipolar plates for PEMFC”  
International Journal of Hydrogen Energy 36 7162-7173
- 41

- Engle R.  
2012 “Maximizing the Use of Platinum Catalyst by Ultrasonic Spray Application”  
Journal of Fuel Cell Science and Technology 9 014501-1
- 42 Escribano S., Blachot J.-F., Ethève J., Morin A. and Mosdale R.  
2006 “Characterization of PEMFCs gas diffusion layers properties”  
Journal of Power Sources 156 8–13
- 43 Escudero M.J., Hontanon E., Schwartz S., Boutonnet M. and Daz L.  
2002 “Development and performance characterisation of new electrocatalysts for PEMFC”  
Journal of Power Sources 106 206–214
- 44 Faraday M., Schönbeing C. F.  
1899 “The letters of Faraday and Schönbein”  
[In line] Universidad de California  
<http://www.archive.org/stream/lettersoffaraday00fararich>
- 45 Farooque M. and Maru H.C.  
2001 “Fuel Cells—The Clean and Efficient Power Generators”  
Proceeding of the IEEE 89 12
- 46 Fernandes A. C., Ticianelli E. A.  
2009 “A performance and degradation study of Nafion 212 membrane for proton exchange membrane fuel cells”  
Journal of Power Sources 547 - 54.
- 47 FFTA  
1999 “Flexography: Principles and Practices”
- 48 Franco A., Schott P., Jallut C., and Maschke B.  
2007 “A multi-scale dynamic mechanistic model for the transient analysis of PEFCs”  
Fuel Cells 7 99
- 49 Garzon F. H.– Los Alamos National Laboratory  
2011 “The Science and Engineering of Durable Ultralow PGM Catalysts”  
DOE Hydrogen and Fuel Cells Program, FY 2011 Annual Progress Report  
[in line] [http://www.hydrogen.energy.gov/pdfs/progress11/v\\_d\\_7\\_garzon\\_2011.pdf](http://www.hydrogen.energy.gov/pdfs/progress11/v_d_7_garzon_2011.pdf)
- 50 Gaul H., Weber G. and Rethmeier M.  
2011 “Evaluation of fatigue crack propagation in spot welded joints by stiffness measurements”  
International Journal of Fatigue 33 4 740
- 51 Gebel G.  
2000 “Structural evolution of water swollen perfluorosulfonated ionomers from dry membrane to solution”  
Polymer 41 5829–5838
- 52 Geletii Y.i V., Gueletii A. and Weinstock I. A.  
2007 “Electron capture and transport by heteropolyanions: Multi-functional electrolytes for biomass-based fuel cells”  
Journal of Molecular Catalysis A: Chemical 262 59–66
- 53 Glipa X., Roy F., Antoni L. and Poirot-Crouvezier J.-P.  
2012 « Pile à combustible GENEPAC »  
Techniques de l'Ingenieur
- 54 Goehring L., Morris S. W. and Lin Z.  
2009 “Criticality and pattern formation in fracture by residual stresses”  
Physical Review 79 046109

- 55 Gojkovic S.Lj., Babic B.M., Radmilovic V.R. and Krstajic N.V.  
2010 “Nb-doped TiO<sub>2</sub> as a support of Pt and Pt–Ru anode catalyst for PEMFCs”  
*Journal of Electroanalytical Chemistry* 639 161–166
- 56 Goltsova Victor A. and Veziroglu T. Nejat  
2001 “From hydrogen economy to hydrogen civilization”  
*International Journal of Hydrogen Energy* 26 909–915
- 57 Goswami S., Klaus S. and Benziger J.  
2008 “Wetting and Absorption of Water Drops on Nafion Films”  
*Langmuir* 24 8627–8633
- 58 Grigoriev Igor S. and Meilikhov Evgenii Z.  
1997 *Handbook of Physical Quantities*  
Boca Raton: CRC Press 116
- 59 Grimes Patrick G.  
2000 “Historical Pathways for Fuel Cells”  
*The New Electric Century, IEEE AES Systems Magazine*
- 60 Grot S.- Ion Power Incorporated  
2011 “Corrugated Membrane Fuel Cell Structures”  
DOE Hydrogen and Fuel Cells Program, FY 2011 Annual Progress Report  
[in line] [http://www.hydrogen.energy.gov/pdfs/progress11/v\\_c\\_8\\_grot\\_2011.pdf](http://www.hydrogen.energy.gov/pdfs/progress11/v_c_8_grot_2011.pdf)
- 61 Grove W. R.  
1839 a “On voltaic series and the combination of gases by platinum”  
*Philosophical Magazine* 14 86
- 62 Grove W. R.  
1839 b “On a small voltaic battery of great energy; some observations on voltaic combinations and forms of arrangement; and on the inactivity of a copper positive electrode in nitro-sulphuric acid”  
*Philosophical Magazine* 15 96 287–293
- 63 Gudgila R. and Leclerc C. A.  
2011 “Support Effects on the Oxidative Dehydrogenation of Ethane to Ethylene over Platinum Catalysts”  
*Industrial Engineering Chemistry Research* 50 8438–8443
- 64 Hamrock S. – 3M  
2011 “Membranes and MEAs for Dry, Hot Operating Conditions”  
DOE Hydrogen and Fuel Cells Program, FY 2011 Annual Progress Report  
[in line] [http://www.hydrogen.energy.gov/pdfs/progress11/v\\_c\\_1\\_hamrock\\_2011.pdf](http://www.hydrogen.energy.gov/pdfs/progress11/v_c_1_hamrock_2011.pdf)
- 65 Hansch R., Chowdhury M. R. R., Menzler N.H.  
2009 “Screen printing of sol–gel-derived electrolytes for solid oxide fuel cell (SOFC) application”  
*Ceramics International* 35 803–811
- 66 Hébert M. and Hersch R. D.  
2006 “Reflectance and transmittance model for recto–verso halftone prints”  
*Journal of the Optical Society of America A* 23 10
- 67 Herring A. M. - Colorado School of Mines  
2011 “Novel Approaches to Immobilized Heteropoly Acid (HPA) Systems for High Temperature, Low Relative Humidity Polymer-Type Membranes”  
DOE Hydrogen and Fuel Cells Program, FY 2011 Annual Progress Report;  
[http://www.hydrogen.energy.gov/pdfs/progress11/v\\_c\\_6\\_herring\\_2011.pdf](http://www.hydrogen.energy.gov/pdfs/progress11/v_c_6_herring_2011.pdf)

- 68 Hiesgen R., Aleksandrov E., Meichsner G., Wehl I., Roduner E., Friedrich K.A.  
2009 “High-resolution imaging of ion conductivity of Nafion<sup>®</sup> membranes with electrochemical atomic force microscopy”  
*Electrochimica Acta* 55 423–429
- 69 Hirano S., Kim J. and Srinivasan S  
1997 “High performance proton exchange membrane fuel cells with sputter-deposited Pt layer electrodes”  
*Electrochimica Acta* 42 10 1587-1593
- 70 Hofmann D.W. M., Kuleshova L., D’Aguanno B., Di Noto V., Negro E. and Conti F.  
2009 “Investigation of Water Structure in Nafion<sup>®</sup> Membranes by Infrared Spectroscopy and Molecular Dynamics Simulation”  
*Journal of Physical Chemistry B* 113 632-639
- 71 Hsu W.Y. and Gierke T.D.  
1983 “Morphological Effects on the Physical Properties of Polymer Composites”  
*Macromolecules* 16 1945-1947
- 72 Hu J., Zhang H., Zhai Y., Liu G. and Yi B.  
2006 “500 h Continuous aging life test on PBI/H3PO4 high-temperature PEMFC”  
*International Journal of Hydrogen Energy* 31 1855
- 73 Huang C.-W.  
2008 “Preparation of sea urchin-like carbons by growing one-dimensional nanocarbon on mesoporous carbons”  
*Diamond & Related Materials* 17 606–610
- 74 Hwang D. S., Park C. H., Yi S. C. and Lee Y. M.  
2011 “Optimal catalyst layer structure of polymer electrolyte membrane fuel cell”  
*International journal of hydrogen energy* 36 9876-9885
- 75 Janczuk B., Zdziennicka A. and Wojcik W.  
1997 “Relationship between Wetting of Teflon by Etyltrimethylammonium Bromide Solution and Absorption”  
*European Polymer Journal* 33 7 1093-1098
- 76 Jeon S., Lee J., Rios G. M., Kim H.-J., Lee S.-Y., Cho E.A., Lim T.-H. and Jang J. H.  
2010 “Effect of ionomer content and relative humidity on polymer electrolyte membrane fuel cell (PEMFC) performance of membrane-electrode assemblies (MEAs) prepared by decal transfer method”  
*International Journal of Hydrogen Energy* 35 9678-9686
- 77 Jewell E.H., Claypole T.C., Bohan M.F.J. and Von Grol M.  
2000 “Modelling the flow in a flexographic ink chamber”  
*TAGA Proceedings* 487-502
- 78 Ji M. and Wei Z.  
2009 “A Review of Water Management in Polymer Electrolyte Membrane Fuel Cells”  
*Energies* 2 1057-1106
- 79 Jiao K. and Li X.  
2011 “Water transport in polymer electrolyte membrane fuel cells”  
*Progress in Energy and Combustion Science* 37 221-291
- 80 Kamaruzzaman Sopian and Wan Ramli Wan Daud  
2006 “Challenges and future developments in proton exchange”  
*Renewable Energy* 31 719–727

- 81 Karakashev S. I., Phan C.M. and Nguyen A.V.  
2005 “Effect of sodium dodecylbenzene sulfonate on the motion of three-phase contact lines on the Wilhelmy plate surface”  
*Journal of Colloid and Interface Science* 291 2 489-496
- 82 Karst N., Faucheux V., Martinent A., Bouillon P. and Simonato J.-P.  
2010 “Improvement of water management in polymer electrolyte membrane”  
*Journal of Power Sources* 195 5228
- 83 Kettler P. B.  
2003 “Platinum Group Metals in Catalysis: Fabrication of Catalysts and Catalyst Precursors”  
*Organic Process Research & Development* 7 342-354
- 84 Khalate A. A., Bombois X., Babuska R., Wijshoff H. and Waarsing R.  
2011 “Performance improvement of a drop-on-demand inkjet printhead using an optimization-based feedforward control method”  
*Control Engineering Practice* 19 (2011) 771–781
- 85 Kim D., Jeong S., Park B. K. and Moon J.  
2006 “Direct writing of silver conductive patterns: Improvement of film morphology and conductance by controlling solvent compositions”  
*Applied Physics Letters* 264101
- 86 Kim H. S., Kang J. S., Park J. S., Hahn H. T., Jung H. C. and Joung J. W.  
2009 “Inkjet printed electronics for multifunctional composite structure”  
*Composites Science and Technology* 69 1256–1264
- 87 Kim K.-H., Lee K.-Y., Kim H.-J., Cho E.A., Lee S.-Y., Lim T.-H., Yoon S. P., Hwang I. C. and Jang J. H.  
2010 “The effects of Nafion<sup>®</sup> ionomer content in PEMFC MEAs prepared by a catalyst-coated membrane (CCM) spraying method”  
*International Journal of Hydrogen Energy* 2119–2126
- 88 Kim Y. S., Wang F., Hickner M., McCartney S., Taik Hong Y., Harrison W., Zawodzinski T. A. and McGrath J. E.  
2003 “Effect of Acidification Treatment and Morphological Stability of Sulfonated Poly(arylene ether sulfone), Copolymer Proton-Exchange Membranes for Fuel-Cell Use above 100 °C”  
*Journal of Polymer Science: Part B: Polymer Physics* 41 (2003) 2816–2828
- 89 Kipphan H.  
2011 “Handbook of Print Media”  
Heidelberg Springer
- 90 Kitsunezaki S.  
2006 “Crack Propagation Speed in the Drying Process of Paste”  
*Journal of the Physical Society of Japan* 6 064801
- 91 Kopola P., Aernouts T., Sliz R., Guillerez S., Ylikunnari M., Cheyns D., Välimäki M., Tuomikoski M., Hast J., Jabbour G., Myllylä R. and Maaninen A.  
2011 “Gravure printed flexible organic photovoltaic modules”  
*Solar Energy Materials and Solar Cells* 95 1344–1347
- 92 Krishnan N.N., Prabhuram J. , Hong Y.T., Kim H.-J., Yoon K., Ha H.-Y., Lim T.-H. and Kim S. K.  
2010 “Fabrication of MEA with hydrocarbon based membranes using low temperature decal method for DMFC”  
*International Journal of Hydrogen Energy* 35 (2010) 5647-5655

93

- Krucinska I., Skrzetuska E. and Urbaniak-Domagala W.  
2011 “The Use of Carbon Nanotubes in Textile Printing”  
Journal of Applied Polymer Science 121 483-490
- 94 Krupk J. and Pater J.  
2007 “Catalytic and mechanistic aspects of the hydrogenation of N-substituted aliphatic aldimines over solid catalysts”  
Applied Catalysis A: General 330 96–107
- 95 Kumar R. J. F., Radhakrishnan V. and Haridoss P.  
2011 “Effect of electrochemical aging on the interaction between gas diffusion layers and the flow field in a proton exchange membrane fuel cell”  
International Journal of Hydrogen Energy 36 7207-7211
- 96 Kusoglu A., Tang Y., Santare M. H., Karlsson A. M., Cleghorn Simon and Johnson William B.  
2009 “Stress-Strain Behavior of Perfluorosulfonic Acid Membranes at Various Temperatures and Humidities: Experiments and Phenomenological Modeling”  
Journal of Fuel Cell Science and Technology 6
- 97 Kwok D. Y., Gietzelt T., Grundke K., Jacobasch H.-J. and Neumann A. W.  
1997 “Contact Angle Measurements and Contact Angle Interpretation. 1. Contact Angle Measurements by Axisymmetric Drop Shape Analysis and a Goniometer Sessile Drop Technique”  
Langmuir 13, 2880-2894
- 98 Lattina W.C. and Utgikar V.P.  
2007 “Transition to hydrogen economy in the United States: A 2006 status report”  
International Journal of Hydrogen Energy 32 3230 – 3237
- 99 Lee H.-K. , Park J.-H., Kim D.-Y. and Lee T.-H.  
2004 “A study on the characteristics of the diffusion layer thickness and porosity of the PEMFC”  
Journal of Power Sources 131 (2004) 200–206
- 100 Li X.  
2006 “Principles of fuel cells”  
New York: Taylor & Francis
- 101 Lin Betty Y.S., Kirk Donald W. and Thorpe Steven J.  
2006 “Performance of alkaline fuel cells: A possible future energy system?”  
Journal of Power Sources 161 474–483
- 102 Lin Jing-Chie, Lai Chien-Ming, Ting Fu-Ping, Chyou San-Der and Hsueh Kan-Lin  
2009 “Influence of hot-pressing temperature on the performance of PEMFC and catalytic activity”  
Journal of Applied Electrochemistry 39 1067–1073
- 103 M. A. Herring - Colorado School of Mines  
2011 “Novel Approaches to Immobilized Heteropoly Acid (HPA) Systems for High Temperature, Low Relative Humidity Polymer-Type Membranes”  
DOE Hydrogen and Fuel Cells Program, FY 2011 Annual Progress Report  
[in line] [http://www.hydrogen.energy.gov/pdfs/progress11/v\\_c\\_6\\_herring\\_2011.pdf](http://www.hydrogen.energy.gov/pdfs/progress11/v_c_6_herring_2011.pdf)
- 104 Ma S., Siroma Z. and Tanaka H.  
2006 “Anisotropic Conductivity Over In-Plane and Thickness Directions in Nafion<sup>®</sup>117”  
Journal of the Electrochemical Society 153 12 2274-2281

- 105 Macknight W. J., Taggart W. P. and Stein R. S.  
1974 “A model for the structure of ionomers”  
Journal of Polymer Science: Polymer Symposia 45 113-128
- 106 Majsztrik P. W., Barclay Satterfield M., Bocarsly A. B. and Benziger J. B.  
2007 “Water sorption, desorption and transport in Nafion membranes”  
Journal of Membrane Science 301 93–106
- 107 Marcinkoski J., Kopasz J. P. , Benjamin T. G.  
2008 “Progress in the US DOE fuel cell subprogram efforts in polymer electrolyte fuel cells”  
International Journal of Hydrogen Energy 33 3894 – 3902
- 108 Markovic N. M. – Argonne National Laboratory  
2011 “Nanosegregated Cathode Alloy Catalysts with Ultra-Low Platinum Loading”  
DOE Hydrogen and Fuel Cells Program, FY 2011 Annual Progress Report  
[in line]  
[http://www.hydrogen.energy.gov/pdfs/progress11/v\\_d\\_5\\_markovic\\_2011.pdf](http://www.hydrogen.energy.gov/pdfs/progress11/v_d_5_markovic_2011.pdf)
- 109 Mc Donald R., Best R. P., Bridgeman, Hill A. R., Mc Laren K., Patterson D. and Rigg B.  
1987 “Colour physics for industry”  
Mc Donald R.
- 110 Mazur P. , Soukup J., Paidar M. and Bouzek K.  
2011 “Gas diffusion electrodes for high temperature PEM-type fuel cells: role of a polymer binder and method of the catalyst layer deposition”  
Journal of Applied Electrochemistry 41 1013–1019
- 111 McPhail Stephen J., Aarva Anja, Devianto Hary, Bove Roberto and Moreno Angelo  
2011 “SOFC and MCFC: Commonalities and opportunities for integrated research”  
International Journal of Hydrogen Energy 36 10337-10345
- 112 Mercier A.-G., Vincent R., Nayoze C., Blayo A. and Soucemariandin A.  
2010 “Inkjet printing of catalyst layers used in fuel cells membrane electrode assemblies”  
Advances in Printing and Media Technology 4 03
- 113 Mevlut Fatih P., Ömer Necati C. and Muammer K.  
2011 “Investigations on the variation of corrosion and contact resistance characteristics of metallic bipolar plates manufactured under long-run conditions”  
International Journal of Hydrogen Energy 36 15427-15436
- 114 Meyer G., Gebel G., Gonon L., Capron P., Marscaq D., Marestin C.  
2006 “Degradation of sulfonated polyimide membranes in fuel cell conditions”  
Journal of Power Sources 293-301
- 115 Millington B., Whipple V., Pollet B. G.  
2011 “A novel method for preparing proton exchange membrane fuel cell electrodes by the ultrasonic-spray technique”  
Journal of Power Sources 196 (2011) 8500– 8508
- 116 Mittelsteadt C.- Giner Electrochemical Systems (GES)  
2011 “LLC, Dimensionally Stable Membranes (DSMs)”  
DOE Hydrogen and Fuel Cells Program, FY 2011 Annual Progress Report  
[in line]  
[http://www.hydrogen.energy.gov/pdfs/progress11/v\\_c\\_2\\_mittelsteadt\\_2011.pdf](http://www.hydrogen.energy.gov/pdfs/progress11/v_c_2_mittelsteadt_2011.pdf)
- 117 Modestov A. D., Tarasevich M. R., Filimonov V. Ya. and Leykin A. Yu.  
2009 “Influence of Catalyst Layer Binder on Catalyst Utilization and Performance of Fuel Cell with Polybenzimidazole- H<sub>3</sub>PO<sub>4</sub> Membrane”  
Journal of the Electrochemical Society 156 5 650-656

- 118 Mond Ludwig and Langer Carl  
1889 “A New Form of Gas Battery”  
Proceedings of the Royal Society of London 46 296-304
- 119 Mond Ludwig, Langer Carl and Quincke Friedrich  
1890 “Action of carbon monoxide on nickel”  
Journal of the Chemical Society, Transactions, 57 749-753
- 120 Mukerjee S. – Northeastern University  
2011 “Development of Novel Non-PGM Electrocatalysts for Proton Exchange Membrane Fuel Cell Applications”  
DOE Hydrogen and Fuel Cells Program, FY 2011 Annual Progress Report  
[in line]  
[http://www.hydrogen.energy.gov/pdfs/progress11/v\\_d\\_11\\_mukerjee\\_2011.pdf](http://www.hydrogen.energy.gov/pdfs/progress11/v_d_11_mukerjee_2011.pdf)
- 121 Muradova N.Z. and T.N. Veziroglu  
2005 “From hydrocarbon to hydrogen–carbon to hydrogen economy”  
International Journal of Hydrogen Energy 30 225–237
- 122 Murthi V. S. - UTC Power Corporation (UTCP)  
2011 “Highly Dispersed Alloy Catalyst for Durability”  
DOE Hydrogen and Fuel Cells Program, FY 2011 Annual Progress Report  
[in line] [http://www.hydrogen.energy.gov/pdfs/progress11/v\\_d\\_2\\_murthi\\_2011.pdf](http://www.hydrogen.energy.gov/pdfs/progress11/v_d_2_murthi_2011.pdf)
- 123 Ortiz-Rivera Eduardo I., Reyes-Hernandez Angel L., and Febo Rey A.  
2007 “Understanding the History of Fuel Cells”  
2007 IEEE Conference on the History of electric
- 124 Paganin V. A., Ticianelli E. A. and Gonzalez E. R.  
1996 “Development and electrochemical studies of gas diffusion electrodes for polymer electrolyte fuel cells”  
Journal of Applied Electrochemistry 26 297-304
- 125 Paradis Hedvig, Andersson Martin, Yuan Jinliang and Sundén Bengt  
2011 “Simulation of alternative fuels for potential utilization in solid oxide fuel cells”  
International Journal of Energy Research 35 1107–1117
- 126 Park I.-S., Li W. and Manthiram A.  
2010 “Fabrication of catalyst-coated membrane-electrode assemblies by doctor blade method and their performance in fuel cells”  
Journal of Power Sources 195 7078-7082
- 127 Park S., Lee J.-W. and Popov B. N.  
2008 “Effect of PTFE content in microporous layer on water management in PEM fuel cells”  
Journal of Power Sources 177 2 457-463
- 128 Peighambardoust S.J., Rowshanzamir S. and Amjadi M.  
2010 “Review of the proton exchange membranes for fuel cell applications”  
International Journal of Hydrogen Energy 35 9349-9384
- 129 Piao J., Sun K., Zhang N. and Xu S.  
2008 “A study of process parameters of LSM and LSM–YSZ composite cathode films prepared by screen-printing”  
Journal of Power Sources 175 288–295

- 130 Pintauro P. N. - Vanderbilt University  
2011 “NanoCapillary Network Proton Conducting Membranes for High Temperature Hydrogen/Air Fuel Cells”  
DOE Hydrogen and Fuel Cells Program, FY 2011 Annual Progress [in line] Report;  
[http://www.hydrogen.energy.gov/pdfs/progress11/v\\_c\\_5\\_pintauro\\_2011.pdf](http://www.hydrogen.energy.gov/pdfs/progress11/v_c_5_pintauro_2011.pdf)
- 131 Pischinger S., Schönfelder C., Ogrzewalla J.  
2006 “Analysis of dynamic requirements for fuel cell systems for vehicle applications”  
Journal of Power Sources 154 420–427
- 132 Pivovar B. - National Renewable Energy Laboratory  
2011 “Extended, Continuous Pt Nanostructures in Thick, Dispersed Electrodes”  
DOE Hydrogen and Fuel Cells Program, FY 2011 Annual Progress Report  
[http://www.hydrogen.energy.gov/pdfs/progress11/v\\_d\\_4\\_pivovar\\_2011.pdf](http://www.hydrogen.energy.gov/pdfs/progress11/v_d_4_pivovar_2011.pdf)
- 133 Pozio A., De Francesco M., Cemmi A., Cardellini F. and Giorgi L.  
2002 “Comparison of high surface Pt/C catalysts by cyclic voltammetry”  
Journal of Power Sources 105 13
- 134 Prasanna M., Ha H.Y., Cho E.A., Hong S.-A. and Oh I.-H.  
2004 “Investigation of oxygen gain in polymer electrolyte membrane fuel cells”  
Journal of Power Sources 137 1–8
- 135 Prasanna M., Ha H.Y., Cho E.A., Hong S.-A. and Oh I.-H.  
2004 “Investigation of oxygen gain in polymer electrolyte membrane fuel cells”  
Journal of Power Sources 137 1–8
- 136 Rajalakshmi N. and Dhathathreyan K.S.  
2007 “Catalyst layer in PEMFC electrodes—Fabrication, characterisation and analysis”  
Chemical Engineering Journal 129 31–40
- 137 Ren K., Dai W., Zhou J., Su J. and Wu H.  
2011 “Whole-Teflon microfluidic chips”  
Proceedings of the national Academy of Sciences of the United States of America, May 17, 108, 20 8162–8166
- 138 Reshetenko T.V., Kim H.T., Lee H., Jang M., Kweon H.J.  
2006 “Performance of a direct methanol fuel cell (DMFC) at low temperature: Cathode optimization”  
Journal of Power Sources 160 2 925-932
- 139 Rikukawa M. and Sanui K.  
2000 “Proton-conducting polymer electrolyte membranes based on hydrocarbon polymers”  
Progress in Polymer Science 25 1463-1502
- 140 Rosle M. F., Abdullah S., Hamid M. A. A. and Daud A. R.  
2010 “Surface Topographical Characterization of Gold Aluminide Compound for Thermosonic Ball Bonding”  
Journal of Electronic Packaging 132 041014
- 141 Rubatat L., Rollet A.-L., Gebel G. and Diat O.  
2002 “Evidence of Elongated Polymeric Aggregates in Nafion”  
Macromolecules 35 4050-4055
- 142 Sahu A. K., Pitchumani S., Sridhar P. and Shulkla A. K.  
2009 “Nafion<sup>®</sup> and modified-Nafion<sup>®</sup> membranes for polymer electrolyte fuel cells: An overview”  
Bulletin of Material Science 32 3 285–294

- 143 Sammes Nigel, Bove Roberto and Stahl Knut  
2004 "Phosphoric acid fuel cells: Fundamentals and applications"  
Current Opinion in Solid State and Materials Science 8 372–378
- 144
- Sasikumar G., Ihm J.W. and Ryu H.  
2004 "Dependence of optimum Nafion content in catalyst layer on platinum loading"  
Journal of Power Sources 132 11–17
- 145 Satyapal S., Petrovic J., Read C., Thomas G. and Ordaz G.  
2007 "The U.S. Department of Energy's National Hydrogen Storage Project: Progress towards meeting hydrogen-powered vehicle requirements"  
Catalysis Today 120 246–256
- 146 Schönbeing C.F.  
1843 "On the theory of the gaseous voltaic battery"  
Philosophical Magazine 22 144
- 147 Serov A. and Kwak C.  
2009 "Review of non-platinum anode catalysts for DMFC and PEMFC application"  
Applied Catalysis B: Environmental 90 313–320
- 148 Sharma S., Gupta M., Anand S. and Kumar N.  
2011 "Design and Development of a Sheet Metal Plastic Backed Proton Exchange Membrane Fuel Cell"  
Journal of Fuel Cell Science and Technology 8 054501-1
- 149 Siegel F., Kohl A., Enns E., Deger W., Dziallas H., Willert A., Bauman R. R.  
2011 "Gravure Printing of Thick Film Electrodes for PEM fuel Cell Production"  
Advanced in Printing Media Technology 247-252
- 150 Soboleva T., Xie Z., Shi Z.Q., Tsang E., Navessin T.C. and Holdcroft S.  
2008 "Investigation of the through-plane impedance technique for evaluation of anisotropy of proton conducting polymer membranes"  
Journal of Electroanalytical Chemistry 622 2 145-152
- 151 Song C.  
2002 "Fuel processing for low-temperature and high-temperature fuel cells challenges, and opportunities for sustainable development in the 21st century"  
Catalysis Today 77 17–49
- 152 Song D., Wang Q., Liu Z., Eikerling M., Xie Z., Navessin T. and Holdcroft S.  
2005 "A method for optimizing distributions of Nafion and Pt in cathode catalyst layers of PEM fuel cells"  
Electrochimica Acta 50 3347–3358
- 153 Song W., Yu H., Hao L., Miao Z., Yi B. and Shao Z.  
2010 "A new hydrophobic thin film catalyst layer for PEMFC"  
Solid State Ionics 181 (2010) 453–458
- 154 Spendelow J. S. and Papageorgopoulos D. C.,  
2011 "Progress in PEMFC MEA Component R&D at the DOE Fuel Cell Technologies Program"  
Fuel Cells 11 6 775–786
- 155 Springer T.E., Zawodzinski T.A., Wilson M.S. and Gottesfeld S.  
1996 "Characterization of Polymer Electrolyte Fuel Cells Using AC Impedance Spectroscopy"  
Journal of the Electrochemical Society, 143, 587-599

- 156 Stone Charles and Morrison Anne E.  
2002 “From curiosity to “power to change the world””  
*Solid State Ionics* 152–153 1–13
- 157 Sukeshini M. A. and Cummins R.  
2009 “Ink-Jet Printing: A Versatile Method for Multilayer Solid Oxide Fuel Cells Fabrication”  
*Journal of the American Ceramic Society*, 92 [12] 2913–2919
- 158 Sun L, Ran R, Shao Z.  
2010 “Fabrication and evolution of catalyst-coated membranes by direct spray deposition of catalyst ink onto Nafion membrane at high temperature”  
*International Journal of Hydrogen Energy* 35 2921–5
- 159 Sun L., Ran R. and Shao Z.  
2010 “Fabrication and evolution of catalyst-coated membranes by direct spray deposition of catalyst ink onto Nafion membrane at high temperature”  
*International Journal of Hydrogen Energy* 35 2921–2925
- 160 Sun Y., Delucchi M. and Ogden J.  
2011 “The impact of widespread deployment of fuel cell vehicles on platinum demand and price”  
*International Journal of Hydrogen Energy* 36 11116–11127
- 161 Suzuki A., Sen U., Hattori T., Miura R., Nagumo R., Tsuboi H., Hatakeyama N., Endou A., Takaba H., Williams M. C. and Miyamoto A.  
2011 “Ionomer content in the catalyst layer of polymer electrolyte membrane fuel cell (PEMFC): Effects on diffusion and performance”  
*International Journal of Hydrogen Energy* 2221–2229
- 162 Taherian R., Nozad G. A. and Hadianfard M. J.  
2011 “The effect of mold pressing pressure and composition on properties of nanocomposite bipolar plate for proton exchange membrane fuel cell”  
*Materials and Design* 32 3883–3892
- 163 Tang H., Wang S., Jiang S. P. and Pan M.  
2007a “A comparative study of CCM and hot-pressed MEAs for PEM fuel cells”  
*Journal of Power Sources* 170 140–144
- 164 Taylor A. D., Kim E. Y., Humes V. P., Kizuka J. and Thompson L. T.  
2007b “Inkjet printing of carbon supported platinum 3-D catalyst layers for use in fuel cells”  
*Journal of Power Sources* 171 101–106
- 165 Termonia Y.  
“2007 Nanoscale modeling of the structure of perfluorosulfonated”  
*Polymer* 48 1435–1440
- 166 Thanasilp S. and Hunsom M.  
2010 “Effect of MEA fabrication techniques on the cell performance of Pt–Pd/C electrocatalyst for oxygen reduction in PEM fuel cell”  
*Fuel* 89 3847–3852
- 167 The Department of Energy Hydrogen and Fuel Cells Program Plan  
[in line] [http://www.hydrogen.energy.gov/pdfs/program\\_plan2011.pdf](http://www.hydrogen.energy.gov/pdfs/program_plan2011.pdf)
- 168 Therdthianwong A., Saenwiset P. and Therdthianwong S.  
2012 “Cathode catalyst layer design for proton exchange membrane fuel cells”  
*Fuel* 91 192–199

- 169 Tomczyk Piotr  
2006 “MCFC versus other fuel cells—Characteristics, technologies and prospects”  
Journal of Power Sources 160 858–862
- 170 Troegel D. and Stohrer J.  
2011 “Recent advances and actual challenges in late transition metal catalyzed hydrosilylation of olefins from an industrial point of view”  
Coordination Chemistry Reviews 255 1440–1459
- 171 Tsai Ming-Jui , Chun-Lin Chu, Shyong Lee,  
2010 “La<sub>0.6</sub>Sr<sub>0.4</sub>Co<sub>0.2</sub>Fe<sub>0.8</sub>O<sub>3</sub> protective coatings for solid oxide fuel cell interconnect deposited by screen printing”  
Journal of Alloys and Compounds 489 576–581
- 172 Tsipis Ekaterina V. and Kharton Vladislav V.  
2011 “Electrode materials and reaction mechanisms in solid oxide fuel cells: a brief review. III. Recent trends and selected methodological aspects”  
Journal of Solid State Electrochemistry 15 1007–1040
- 173 Uchida M., Aoyama Y., Eda N., Ohta A.  
1995 “Investigation of the Microstructure in the Catalyst Layer and Effects of Both Perfluorosulfonate Ionomer and PTFE-Loaded Carbon on the Catalyst Layer of Polymer Electrolyte Fuel Cells”  
Journal of the Electrochemical Society 142 4143–4149
- 174 US DOE  
[in line] <http://www1.eere.energy.gov/hydrogenandfuelcells/fuelcells/>
- 175 van der Heijden P. C., Rubatat L., and Diat O.  
2004 “Orientation of Drawn Nafion at Molecular and Mesoscopic Scales”  
Macromolecules 37 5327–5336
- 176 van der Zwaan B.C.C., Schoots K., Rivera-Tinoco R. and Verbong G.P.J.  
2011 “The cost of pipelining climate change mitigation: An overview of the economics of CH<sub>4</sub>, CO<sub>2</sub> and H<sub>2</sub> transportation”  
Applied Energy 88 3821–3831
- 177 Varcoe J.R. and Slade R.C.T.  
2005 “Prospects for alkaline anion-exchange membranes in low temperature fuel cells”  
Fuel Cells 5, 2
- 178 Vernhes P., Bloch J.-F., Blayo A. and Pineaux B.  
2009 “Effect of calendaring on paper surface micro-structure: A multi-scale analysis”  
Journal of Materials Processing Technology 209 5204–5210
- 179 Veziroglu T. N.  
2000 “Quarter century of hydrogen movement 1974-2000”  
International Journal of Hydrogen Energy 25 1143-1150
- 180 Wang T., He J. , Sun D., Guo Y., Ma Y., Hu Y., Li G., Xue H., Tang J. and Sun X.  
2011 “Synthesis of mesoporous carbon-silica-polyaniline and nitrogen-containing carbon-silica films and their corrosion behavior in simulated proton exchange membrane fuel cells environment”  
Journal of Power Sources 196 9552– 9560
- 181 Weh L., and Venthur A.  
2004 “Crack Patterns in Thin Polymer Layers”  
Macromolecular Materials and Engineering 3 227-237

- 182 Wei Z.D., Feng Y.C., Li L., Liao M. J., Fu Y., Suna C.X., Shao Z.G. and Shen P.K.  
2088 “Electrochemically synthesized Cu/Pt core-shell catalysts on a porous carbon electrode for polymer electrolyte membrane fuel cells”  
*Journal of Power Sources* 180 (2008) 84–91
- 183 Wilde P. M.; Maendle M.; Murata M. and Berg N.,  
2004 “Structural and Physical Properties of GDL and GDL/BPP Combinations and their Influence on PEMFC Performance”  
*Fuel Cell* 2004 4 3
- 184 Williams M.C., Strakey J.P. and Singhal Subhash C.  
2004 “U.S. distributed generation fuel cell program”  
*Journal of Power Sources* 131 79–85
- 185 Xie J., Xu F., Wood D. L., More K. L., Zawodzinski T. A. and Smith W. H.  
2010 “Influence of ionomer content on the structure and performance of PEFC membrane electrode assemblies”  
*Electrochimica Acta* 7404–7412
- 186 Yang C. and Ogden J.  
2007 “Determining the lowest-cost hydrogen delivery mode”  
*International Journal of Hydrogen Energy* 32 268 – 286
- 187 Yang L.  
2003 “Characterization of inks and ink application for ink-jet printing: model and simulation”  
*Optical Society of America* 20 7
- 188 Yoon Y. J., Kim T.-H., Kim S. U., Yu D. M. and Hong Y. T.  
2011 “Low temperature decal transfer method for hydrocarbon membrane based membrane electrode assemblies in polymer electrolyte membrane fuel cells”  
*Journal of Power Sources* 196 9800– 9809
- 189 Young D., Sukeshini A. M., Cummins R., Xiao H., Rottmayer M. and Reitz T.  
2008 “Ink-jet printing of electrolyte and anode functional layer for solid oxide fuel cells”  
*Journal of Power Sources* 184 191–196
- 190 Yu H. N., Lim J. W., Suh J. D. and Lee D. G.  
2011 “A graphite-coated carbon fiber epoxy composite bipolar plate for polymer electrolyte membrane fuel cell”  
*Journal of Power Sources* 196 9868– 9875
- 191 Yu Xiao, Yuan Jinliang and Sundén Bengt  
2011 “Review on the Properties of Nano-/Microstructures in the Catalyst Layer of PEMFC”  
*Journal of Fuel Cell Science and Technology* 8, 034001
- 192 Zhang J., Wang X., Wu C., Wang H., Yi B. and Zhang H.  
2004 “Preparation and Characterisation of Pt/C Catalysts for PEMFC cathode: Effect of Different Reduction Methods”  
*Reaction Kinetics and catalysis letters* 83 2 229-236
- 193 Zhang Y., Lü Z., Huang X., An M., Wei B. and Su W.  
2011 “Fabrication and performance test of solid oxide fuel cells with screen-printed yttria-stabilized zirconia electrolyte membranes”  
*Journal of Solid State Electrochemistry* 15 2661–2665
- 194 Zhao J., He X., Tian J., Wan C. and Jiang C.  
2007 “Reclaim/recycle of Pt/C catalysts for PEMFC”  
*Energy Conversion and Management* 48 450–453

**Standards**

- 195 ISO 25178:2012  
Geometric Product Specifications (GPS) – Surface texture: areal
- 196 ISO 5-3:2009  
Photography and graphic technology - Density measurements - Part 3: Spectral conditions
- 197 ISO 534:2005  
Paper and board - Determination of thickness, density and specific volume
- 198 ISO 5-4:2009  
Photography and graphic technology - Density measurements - Part 4: Geometric conditions for reflection density
- 199 ISO 5636-3:1992  
Paper and board - Determination of air permeance (medium range) - Part 3: Bendtsen method

# Résumé



<b>1</b>	<b>INTRODUCTION.....</b>	<b>251</b>
1.1	CONTEXTE SCIENTIFIQUE DE LA THESE .....	251
1.1.1	<i>Proton Exchange Membrane Fuel Cell (PEMFC)</i> .....	251
1.1.2	<i>Travaux de recherche dédiés à la fabrication de couches actives</i> .....	252
1.2	LE PROJET CATIMINHY .....	254
1.3	LE LGP2 .....	255
1.4	ORIENTATION DES TRAVAUX DE RECHERCHE MENES PENDANT LA THESE .....	256
<b>2</b>	<b>IMPRESSION DE LA MEMBRANE .....</b>	<b>258</b>
2.1	ETUDE DE LA STABILITE DIMENSIONNELLE DE LA MEMBRANE .....	258
2.2	AMELIORATION DE L'IMPRIMABILITE DE LA MEMBRANE.....	259
2.3	IMPRESSION DE COUCHES ACTIVES SUR LA MEMBRANE PAR FLEXOGRAPHIE.....	261
<b>3</b>	<b>IMPRESSION DE LA COUCHE DE DIFFUSION.....</b>	<b>263</b>
3.1	ETUDE DE L'IMPRIMABILITE DE LA COUCHE DE DIFFUSION .....	263
3.2	IMPRESSION DE COUCHES ACTIVES SUR LA COUCHE DE DIFFUSION PAR DIFFERENTS PROCEDES.....	265
<b>4</b>	<b>CARACTERISATION DES COUCHES ACTIVES PAR SPECTROPHOTOMETRIE 268</b>	
<b>5</b>	<b>STRUCTURATION DES COUCHES ACTIVES.....</b>	<b>270</b>
	<b>CONCLUSION ET PERSPECTIVES .....</b>	<b>274</b>



## 1 Introduction

### 1.1 Contexte scientifique de la thèse

La pénurie annoncée en combustibles fossiles ainsi que la nécessité de réduire la production de polluants incitent à se tourner vers de nouvelles sources d'énergie renouvelables et propres.

Une des solutions proposées est l'économie de l'hydrogène. Elle est basée sur l'équation 1 qui relie l'oxygène, l'hydrogène, l'eau et l'énergie.



Le dispositif qui permet la conversion de l'énergie chimique de l'oxygène et de l'hydrogène en énergie électrique est la pile à combustible, celle-ci ne rejetant que de l'eau.

L'intérêt récent pour cette technologie vieille de plus de 150 ans se porte vers des applications portables, résidentielles ou de transport. Cependant, de nombreux défis doivent encore être relevés. En particulier, le coût de l'énergie produite par cette méthode demeure beaucoup trop élevé et les procédés de fabrication actuels ne sont pas adaptés à la production de masse. Ainsi, le Department of Energy (US DOE) s'est fixé pour principal objectif de rendre compétitif les véhicules électriques avec les véhicules à moteur thermique. Pour cela, un véhicule électrique doit être capable de fournir une puissance dont le coût doit être compris entre 25 et 35 \$ kW<sup>-1</sup> (équipé d'un moteur de 80 kW<sub>net</sub> produit à 500 000 exemplaires par an).

#### 1.1.1 Proton Exchange Membrane Fuel Cell (PEMFC)

Ce travail se concentre sur un type de pile à combustible, les piles à combustible à membrane échangeuse de protons (ou PEMFC : Proton Exchange Membrane Fuel Cell). Ces piles ont une faible température de fonctionnement (80°C), ce qui les dédie à l'application de transport. Les piles sont composées de plusieurs centaines de cœurs de pile appelés Assemblages Membranes Electrodes (AMEs) alimentés en gaz réactifs et dans lesquels la réaction 1 se produit (dans le sens direct). Les AMEs sont scindées en deux électrodes :

- l'anode, alimentée en hydrogène. Ce gaz est alors réduit en protons et électrons selon l'Equ. 1,



- et la cathode, alimentée en oxygène, lequel est oxydé en présence de protons et d'électrons pour former de l'eau, selon l'Equ. 2.



Comme décrit dans la Figure 1, chaque électrode est composée d'une couche de diffusion, appelée GDL (Gaz Diffusion Layer) et d'une couche active ou couche catalytique.

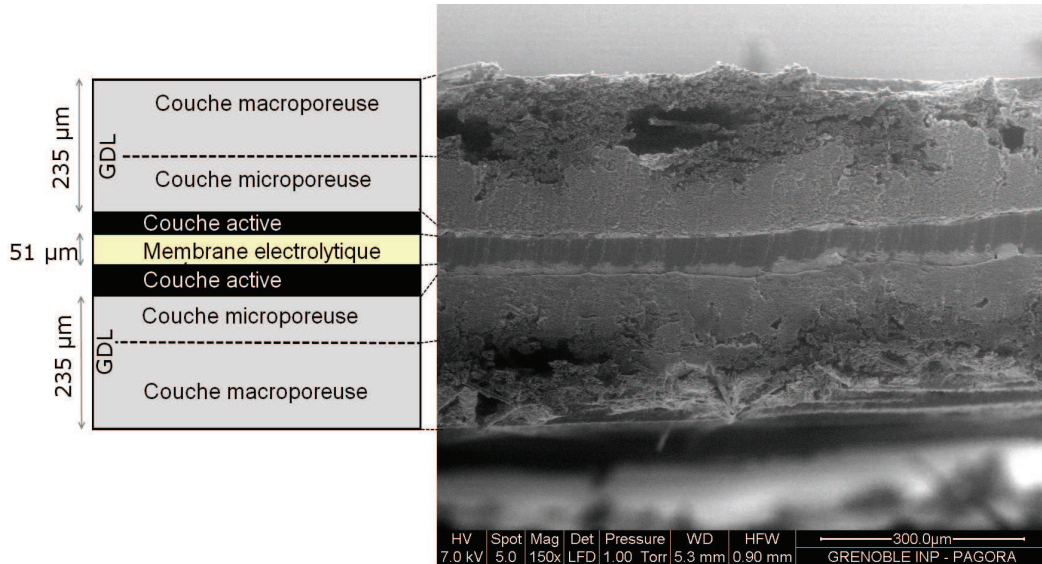


Figure 1 Schéma (gauche) et coupe MEB (droite) d'une AME

Une membrane échangeuse de protons sépare les deux électrodes. Elle empêche la diffusion directe des électrons de l'anode vers la cathode. Ces derniers sont alors contraints d'emprunter le circuit électrique placé aux deux bornes de la pile, créant ainsi un courant électrique. La membrane utilisée dans cette étude est composée d'ionomères perfluorosulfoniques sous forme acide (Figure 2), commercialisés sous le nom de Nafion® (DuPont, Wilmington, USA).

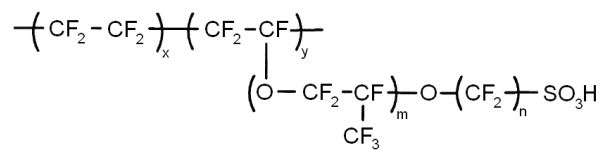


Figure 2 Monomère de membrane perfluorosulfonique acide, avec  $m = 1$ ,  $n = 2$ ,  $x = 5 - 13.5$ ,  $y = 1$  pour le Nafion®

Au sein des couches actives, les réactions d'oxydoréduction décrites dans les Equ. 1 et Equ. 2 nécessitent la présence de catalyseurs. Généralement composés de platine, ils sont rares et extrêmement onéreux. La couche active représente par conséquent 34% du coût de fabrication d'une AME (selon le DOE, pour une application automobile).

La couche active est donc un des éléments sur lesquels travailler pour réduire le coût de l'énergie produite par une pile à combustible de type PEMFC.

### 1.1.2 Travaux de recherche dédiés à la fabrication de couches actives

Les couches actives sont fabriquées :

- soit par dépôt direct sur la membrane ou sur la GDL,
- soit par dépôt indirect ou transfert, où la couche active est d'abord déposée sur une toile en téflon ou sur une feuille d'aluminium avant d'être pressée à chaud contre la membrane, tel un décalcomanie.

Les procédés de dépose de la couche active utilisent des dispersions composées de nanoparticules de carbone, de nanoparticules de platine et de ionomères de Nafion® formulées avec divers additifs. Les dispersions sont conventionnellement transférées sur un support par :

- brosseage, où comme pour une peinture, la dispersion est déposée à l'aide d'un pinceau sur le support. Cette technique, peu reproductible, est limitée aux fabrications en laboratoire.
- enduction, où la dispersion est raclée sur le support. La distance entre la racle et le support conditionne la quantité déposée. Cette technique permet des productions de grandes échelles.
- sérigraphie, avec ce procédé d'impression, l'encre est raclée contre un écran maillé qui contrôle la quantité d'encre déposée. Cette technique, tout comme en impression conventionnelle, permet des grandes productions.
- enfin, le spray, qui pulvérise l'encre sur le support, et qui est plutôt utilisé pour de faibles productions.

Les procédés de fabrication de couches actives pour PEMFC utilisés de façon conventionnelle sont le spray et l'enduction.

La fabrication de couches actives par brosseage, l'enduction et le spray requièrent l'utilisation de masques qui délimitent les zones de dépôt de la dispersion. Par conséquent, une partie des éléments fonctionnels est perdue car déposée le masque et non sur le support (Figure 3).

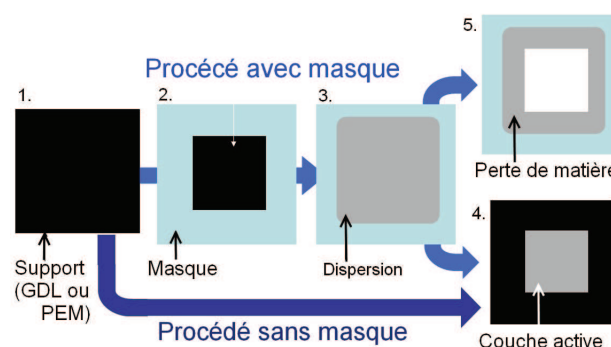


Figure 3 Description schématique et comparaison des étapes nécessaires lors de la fabrication de couches actives avec des procédés avec et sans masque

Les procédés d'impression, tels que la sérigraphie, sont des techniques de transfert sans masque. C'est pourquoi elles sont capables de limiter la perte de matériaux onéreux durant la fabrication des couches actives.

Cet avantage est mis en valeur dans plusieurs travaux de recherche sur l'utilisation des procédés d'impression appliqués aux piles à combustible :

- la sérigraphie fabrique communément des composants en céramique pour des piles à combustibles à hautes températures (Solid Oxyde Fuel Cells SOFCs).
- l'héliogravure, qui est un procédé de transfert direct avec contact souvent dédié aux longs tirages (par exemple l'impression de catalogues), a été testée pour fabriquer des couches actives. Ce procédé continu peut être appliqué aux très grandes productions.
- enfin le jet d'encre, plutôt dédié aux petites productions, a été testé avec succès dans la fabrication de couches actives par dépôt direct sur la GDL.

Ainsi, ces travaux ont prouvé la pertinence des procédés d'impression dans le domaine des piles à combustible et de l'énergie.

## 1.2 Le projet CATIMINHY

Les travaux de recherche présentés dans cette thèse ont été réalisés dans le cadre du projet CATIMINHY "Couches Actives développées par des Technologies d'IMpression Hybrides". Celui-ci a été financé par l'Agence Nationale de la Recherche (ANR) de janvier 2009 à juillet 2012 via le Plan National pour l'Hydrogen 2008 (PAN-H 2008).

Le projet a pour but d'évaluer les procédés d'impression comme techniques pour fabriquer des couches actives de piles à combustibles de types Proton Exchange Membrane Fuel Cells (PEMFCs).

En effet, ces techniques permettent de transférer directement de l'encre fonctionnelle sur un support, et d'imprimer un motif sans recourir à un masque, et ceci précisément et de façon répétable. Ces techniques permettent le contrôle précis de la quantité d'encre déposée. De plus, en fonction du procédé utilisé, les productions envisageables varient de l'échelle du laboratoire à la production de masse. Deux éléments des piles, la membrane échangeuse de proton et la couche de diffusion, peuvent être considérés comme des supports d'impression.

Le développement des procédés d'impression pour la fabrication de piles à combustible a été scindé en trois tâches qui sont décrites dans la Figure 4.

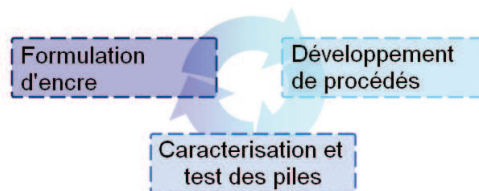


Figure 4 Division des tâches

Ces différentes tâches ont été divisées entre les partenaires du projet CATIMINHY, dont les laboratoires membres du projet étaient :

- le CEA, le Centre d'Énergie Atomique, lequel a modélisé, caractérisé, et testé les composants pour piles à combustible réalisés par les différents partenaires. Il a également développé les encres, le procédé de sérigraphie et réalisé une étude technico-économique;
- le LEGI, le Laboratoire des Écoulements Géophysiques et Industriels s'est intéressé aux procédés de transfert sans contact;
- le LGP2, le Laboratoire de Génie des Procédés Papetiers, par l'intermédiaire de cette thèse, a développé l'utilisation des procédés d'impression avec contact;

Les trois partenaires industriels du projet étaient:

- Siliflow, spécialisé dans la manipulation de liquides
- Paxitech, fabricant de piles à combustible
- et Rhodia, fournisseur de produits chimiques, en charge du développement d'additifs pour les encres.

### 1.3 Le LGP2

La thèse, intitulée «Réalisation de Piles à Combustible par Procédés d'Impression» s'est déroulée au LGP2. Ce laboratoire a, entre autres expertises, une connaissance et des compétences importantes sur les procédés d'impression.

Dans l'industrie, ces procédés sont employés de façon conventionnelle dans le domaine de l'édition et de l'emballage. Cependant, depuis quelques dizaines d'années, ces procédés sont utilisés avec succès à la fabrication de composants pour l'électronique. L'électronique imprimée a démontré la capacité des procédés d'impression à apporter de nouvelles fonctionnalités aux supports d'impression.

Parmi les divers procédés d'impression, la flexographie a été privilégiée par le LGP2 pour l'application aux piles à combustible. En effet, ce procédé est bien connu pour sa flexibilité, en particulier concernant le type de supports d'impression (papiers, carton ondulé, aluminium ou polymères). D'autre part, ce procédé est continu et les presses peuvent être alimentées en bobines, ce qui diminue les coûts de fabrication des grandes séries. Chaque presse est constituée de plusieurs unités d'impression, chacune capable de transférer un type d'encre différents. Une unité d'impression typique de flexographie est schématisée par la Figure 5.

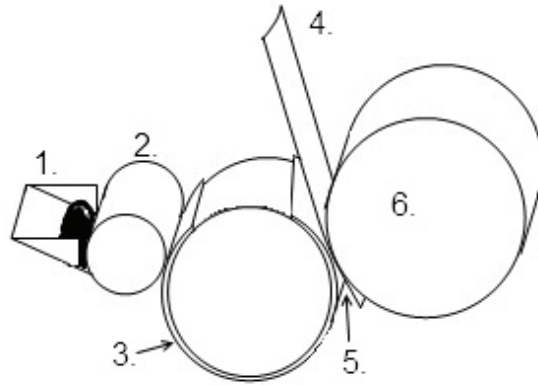


Figure 5 Unité d'impression flexographique

L'encre est contenue dans une chambre à racle (repère 1, figure 5) puis est transférée dans les alvéoles d'un cylindre gravé appelé anilox (repère 2, figure 5). La racle permet d'éliminer l'excédent d'encre à la surface des alvéoles afin de contrôler la quantité d'encre. L'encre est ensuite transférée sur une forme imprimante souple, le cliché (repère 3, figure 5), sur laquelle un motif en relief forme le motif d'impression. Dans le cas des couches actives, les motifs sont des aplats rectangulaires de plusieurs centimètres de côtés. Enfin, l'encre déposée sur les reliefs du cliché est pressée contre un support d'impression (repère 4, figure 5) dans la zone de pincement ou nip (repère 5, figure 5) formée entre le cylindre porte-cliché et le cylindre d'impression (repère 6, figure 5).

#### 1.4 Orientation des travaux de recherche menés pendant la thèse

La thèse a pour but de montrer la pertinence des procédés d'impression appliqués à la fabrication de composants pour piles à combustible. Le travail a été divisé en trois axes :

- la caractérisation des supports,
- l'évaluation de l'imprimabilité et son amélioration,
- et la fabrication de couches actives et leur perfectionnement.

Le premier axe de travail développe la fabrication de couches actives par impression directe sur la membrane échangeuse de proton (ou Catalyst Coated Membrane (CCM)). La caractérisation de ce matériau a montré que cette membrane a une très faible imprimabilité. En effet, d'une part sa surface est très hydrophobe, d'autre part elle se déforme en contact avec l'eau (liquide et vapeur) et avec des encres aqueuses.

Compte tenu de ces propriétés peu propices, l'utilisation de la membrane comme support d'impression était délicate. C'est pour cela qu'une solution a été proposée pour améliorer l'imprimabilité de la membrane et testée au cours d'impression en flexographie.

Le deuxième axe a étudié la capacité de la flexographie à transférer de l'encre aqueuse directement sur la couche de diffusion (ou Catalyst Coated Backing (CCB)). Tout comme la membrane, les couches de diffusion présentent un caractère très hydrophobe qui limite fortement leur imprimabilité.

Cependant, la flexographie a permis l'impression de couches actives, qui ont ensuite été comparées à des couches actives fabriquées par d'autres procédés.

Enfin, le dernier axe a développé les avantages des techniques d'impression dans le domaine des piles à combustible.

D'une part, la spectrophotométrie visible, utilisée dans les industries graphiques pour mesurer la qualité des imprimés colorés, a été introduite pour caractériser les couches actives. Cette technique permet le contrôle du procédé en ligne et pourrait limiter le nombre de tests hors-ligne effectué sur les composants.

Enfin, une seconde étude a détaillé la capacité de la flexographie à créer des couches actives structurées avec des compositions différentes en éléments fonctionnels dans l'épaisseur.

## 2 Impression de la membrane

Des études précédentes de fabrication de couches actives par dépôt direct sur la membrane ont mis en évidence deux problèmes majeurs :

- La membrane se déforme dès qu'elle est en contact avec de l'eau sous forme vapeur ou liquide, et donc aussi en contact avec des dispersions aqueuses :
  - les conditions de stockage peuvent influencer les propriétés de la membrane,
  - et d'autre part, il est difficile d'utiliser la membrane dans un procédé, telle qu'une technique d'impression.
- La surface de la membrane est très hydrophobe :
  - les dispersions forment donc difficilement un film continu sur la membrane, ce qui pourrait limiter le mouillage d'une encre sur ce support.
  - et l'adhésion avec la couche active sèche est donc limitée.

Afin d'évaluer la capacité de la membrane à être utilisée comme un support d'impression, une première étude a été menée sur la stabilité dimensionnelle de la membrane dans différentes conditions d'humidité relative (2.1), en préambule à l'étude de l'imprimabilité de la membrane(2.2).

### 2.1 Etude de la stabilité dimensionnelle de la membrane

Des échantillons de membranes ont été placés sous différentes valeurs d'humidité relative ( $RH\%$ ) variant de 10 à 85 %, à température constante de 23°C, et formant un cycle d'humidités relatives. La mesure de leur masse montre que ce matériau est capable d'absorber jusqu'à 10 % de son poids en eau.

Aucune variation d'épaisseur n'a pu être mise en évidence sous différentes conditions. Cependant, les échantillons se déforment dans le plan, de - 2,5 à 3,5 % comme observé sur la Figure 6.

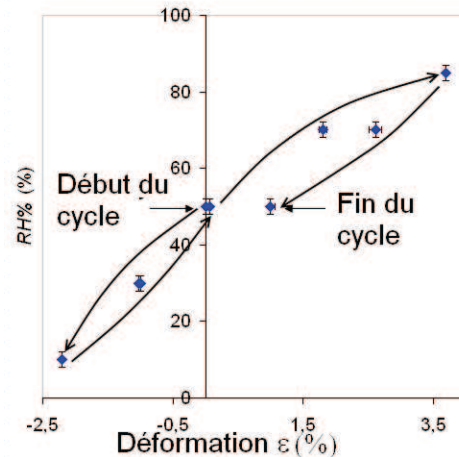


Figure 6 Déformation (%) en fonction des valeurs de RH% variant de 10 à 85 % (les lignes noires indiquent l'ordre dans lequel les valeurs de RHM ont été appliquées sur les échantillons)

Ces essais confirment l'influence des conditions de stockage, et de l'humidité de l'air sur les dimensions dans le plan du matériau, lesquels présentent un phénomène d'hystérésis. De plus, les échantillons ont subi plusieurs cycles d'humidité relative, qui ont permis de diminuer l'hystérésis du matériau et stabiliser sa réponse aux changements d'humidité relative.

Les conditions de stockage sont donc un paramètre crucial pour le contrôle des propriétés de stabilité dimensionnelle du Nafion®.

## 2.2 Amélioration de l'imprimabilité de la membrane

Le dépôt d'une goutte d'eau de 2  $\mu\text{L}$  pendant plusieurs minutes à la surface d'un échantillon de membrane met en évidence deux phénomènes, observables sur la Figure 7:

- la membrane se déforme sous la goutte,
- et la forme de la goutte semble changer avec le temps.

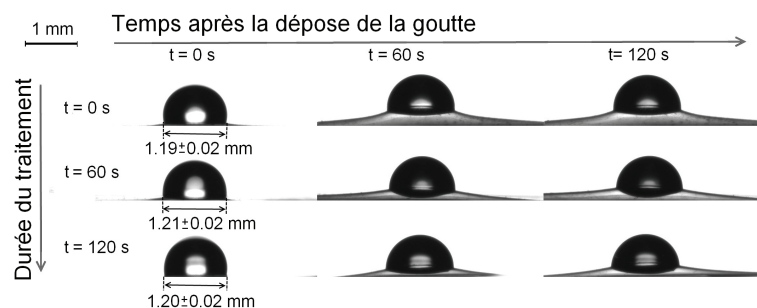


Figure 7 Vue de côté de gouttes d'eau 0, 60 et 120 s après leur dépôt sur des membranes de Nafion® traitées pendant 0, 60 et 120 s

Afin de limiter le phénomène d'hydro-expansion de la membrane, un pré-traitement par immersion dans l'eau a été appliqué afin de maximiser les déformations des échantillons avant une impression potentielle. Cela permet de limiter l'impact du dépôt d'encre sur les propriétés dimensionnelles des échantillons. Le traitement consistait à immerger des échantillons dans l'eau distillée. Plusieurs temps d'immersion ont été testés : 30, 60, 90 et

120 s (Figure 8.1). Les échantillons sont essuyés entre deux buvards afin d'éliminer les gouttes d'eau résiduelles (Figure 8.2) Puis ils peuvent être imprimés (Figure 8.3) pour fabriquer des couches actives (Figure 8.4).

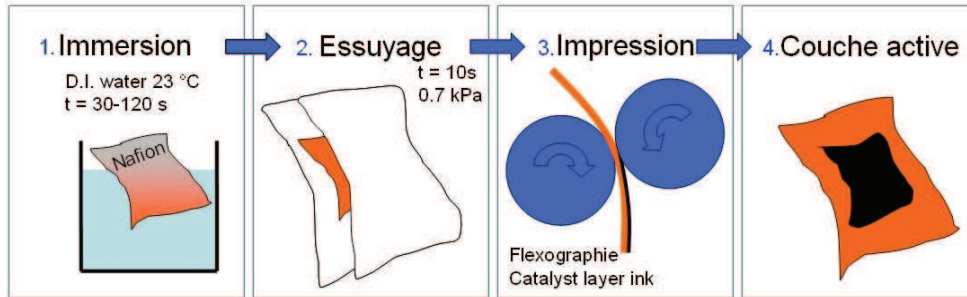


Figure 8 Etapes de fabrication des couches actives par CCM: 1. pré-traitement par immersion, 2. essuyage de la membrane, 3. impression en flexographie et 4. CCM utilisable en pile

L'efficacité du pré-traitement a été évaluée lors du dépôt de gouttes d'eau et d'encre pour couche active de 2  $\mu$ L grâce à la mesure de deux paramètres :

- l'angle de contact apparent, qui caractérise l'affinité entre un liquide et une surface. En dessous de 90°, l'affinité est considérée comme bonne, car le liquide mouille la surface sur laquelle il est posé. Au dessus de 90°, l'affinité est qualifiée de mauvaise car le liquide se rétracte à la surface et ne forme pas de film continu.
- l'élévation de la membrane sous la goutte, qui quantifie la déformation induite par le dépôt du liquide sur la membrane.

Un premier exemple de l'influence du pré-traitement sur ces deux paramètres est donné dans la Figure 7 : plus long est le traitement de la membrane, et moins la déformation sous la goutte est importante de même, l'angle de contact semble également diminuer. (les figures 10 et 11 précisent ces 2 comportements. ).

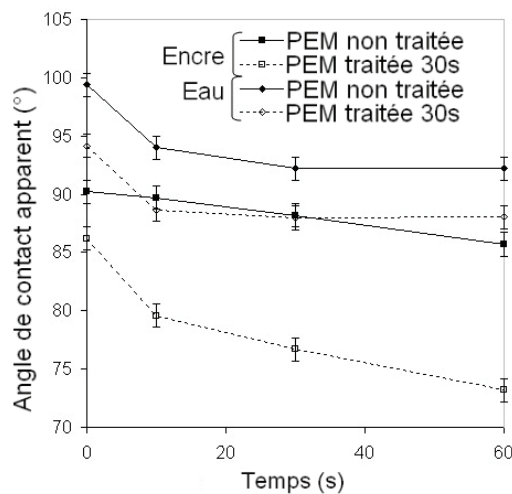


Figure 9 Angle de contact apparent de gouttes d'eau et d'encre déposée sur des membranes traitées 30 s ou non traités 0, 10, 30 et 60 s après la dépose des gouttes

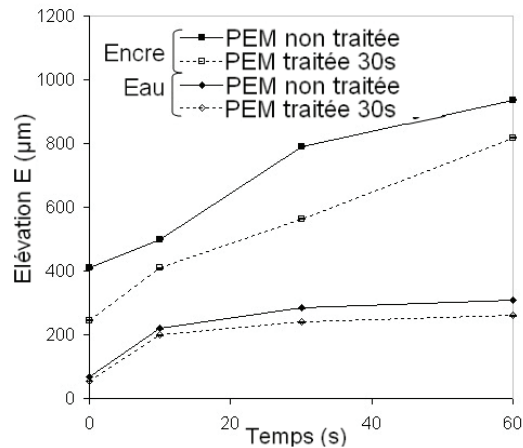


Figure 10 Hauteur de la membrane 0, 10, 30 et 60 s après la dépose de gouttes d'eau et d'encre sur des membranes traitées 30 s ou non traités

Quelle que soit la durée après le dépôt de la goutte, l'eau a une moins bonne affinité sur les membranes traitées et non traitées que l'encre. De plus, l'encre induit une plus grande déformation de la membrane. Quel que soit le liquide testé, le pré-traitement dans l'eau permet de diminuer l'angle de contact et l'élévation de la membrane sous la goutte.

Par conséquent, l'affinité et la stabilité au contact avec l'encre ont été toutes deux améliorées, ce qui laisse présager une amélioration de l'imprimabilité de la membrane.

### 2.3 Impression de couches actives sur la membrane par flexographie

Des tests d'impression ont été réalisés en flexographie sur des échantillons de membrane traités pendant 30 s dans l'eau et des échantillons de référence non traités. Les échantillons traités présentent moins de défauts d'impression que ceux de référence. D'autre part, l'épaisseur d'encre déposée est plus importante (Figure 11).

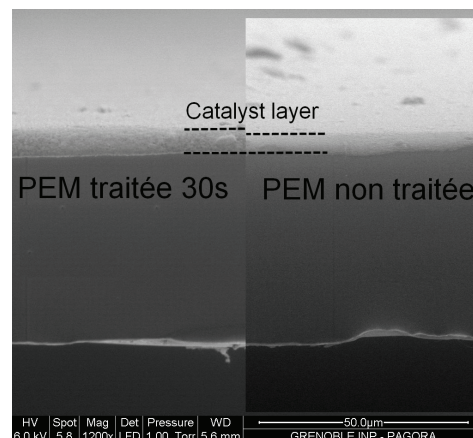


Figure 11 Vue en coupe de trois couches d'encre déposées par flexographie sur un échantillon traité (gauche) et non traité (droite)

La flexographie a permis de superposer plusieurs couches d'encre sur les membranes traitées afin d'augmenter la quantité d'encre déposée. Des échantillons composés de 2 et 3 couches d'encres ont été testés en piles avec succès dans des conditions relatives à l'application automobile (Figure 12).

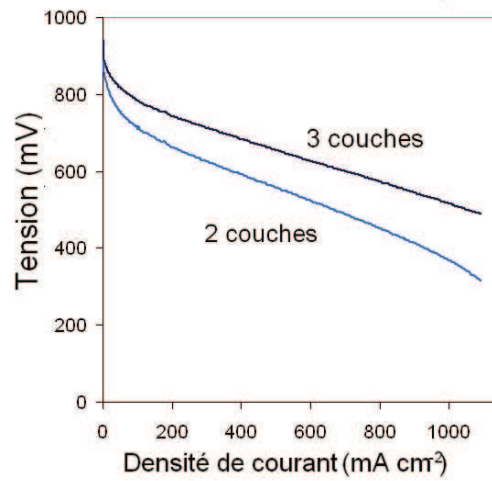


Figure 12 Courbes de polarisation d'une AME dont la cathode est réalisée en CCM par flexographie (conditions automobiles 80°C, 50RH%, 1.5 air)

Les performances des AMEs testées avec des couches actives réalisées par superposition de 3 couches d'encre en flexographie sont supérieures à celles composées de 2 couches d'encre.

### 3 Impression de la couche de diffusion

La fabrication de couches actives par dépôt direct sur les couches de diffusion est appelée Catalyst Coated Backing (CCB). Les couches de diffusions (également appelée GDLs pour Gas Diffusion Layers) sont composées de deux couches :

- une couche macroporeuse (Figure 13.b), constituée de fibres de carbone et de PTFE (Teflon®).
- une couche microporeuse (Figure 13.a et Figure 14), composée de nanoparticules de carbone et de PTFE.

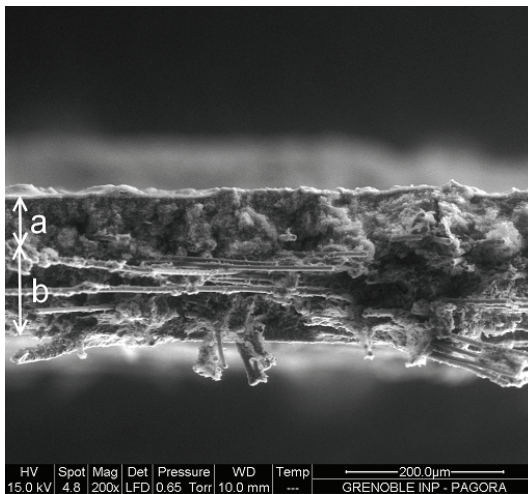


Figure 13 Vue en coupe d'une GDL: a) couche microporeuse et b) couche macroporeuse

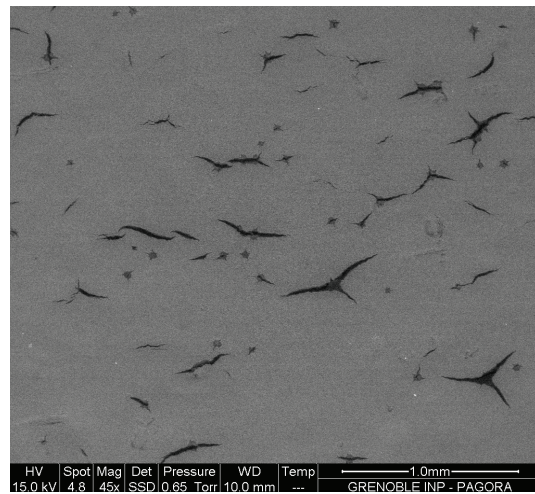


Figure 14 Vue en surface d'une couche microporeuse

Les dépôts s'effectuent à la surface de la couche microporeuse. Cette dernière étant composée de nanoparticules de carbone déposées sur un matelas de fibres de carbone, elle est donc stable. Cependant, la présence de PTFE peut lui conférer une forte hydrophobicité. Les défis à relever ici sont donc liés à des problématiques d'interface entre une surface hydrophobe et une encre hydrophile, dont le véhicule est majoritairement composé d'eau.

#### 3.1 Etude de l'imprimabilité de la couche de diffusion

L'imprimabilité de la GDL est limitée par l'affinité de la surface du microporeux avec l'encre. Afin de l'évaluer et de comprendre l'influence de chacun des constituants de l'encre, des gouttes de liquides ont été déposées à la surface de la GDL et leurs angles de contact apparents ont été mesurés (Figure 15).

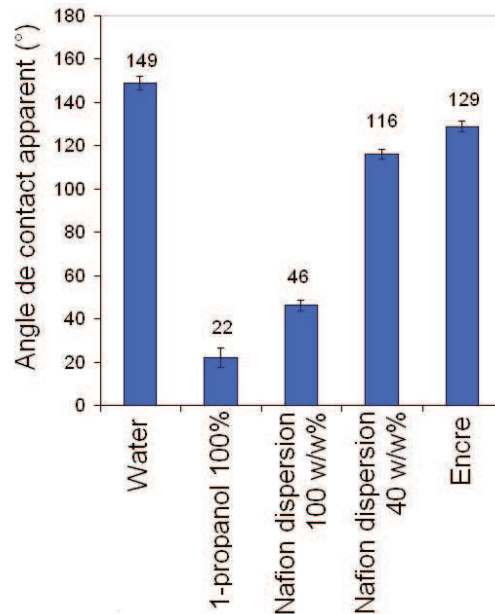


Figure 15 Angles de contact apparents de différentes dispersions mesurés sur une GDL

Les liquides testés sont :

- l'eau déionisée. L'angle de contact qu'elle forme avec la surface de la GDL est de  $149 \pm 5^\circ$ , car cette surface est très hydrophobe.
- l'isopropanol pur. Deuxième solvant du véhicule de l'encre, il provient de la dispersion de Nafion<sup>®</sup> utilisée. Son angle de contact très faible montre sa grande affinité avec la surface de la GDL.
- une dispersion de Nafion<sup>®</sup> pure. La dispersion, avec un angle de contact de  $46 \pm 5^\circ$ , a une bonne affinité avec la GDL.
- une dispersion de Nafion<sup>®</sup> à la concentration du véhicule de l'encre. L'ajout d'eau dans la dispersion a une influence importante sur l'affinité qui est limitée.
- l'encre. L'ajout du catalyseur (nanoparticules de carbone et platine) diminue encore l'imprimabilité de la GDL.

La faible affinité entre l'encre et la surface de la couche microporeuse est un facteur limitant pour son impression. Cependant, lors de l'étude et en partenariat Avec Anne-Gaëlle Mercier du CEA Grenoble, des couches actives ont été déposées sur des GDL à l'aide de différents procédés : enduction, spray, jet d'encre, sérigraphie, flexographie et héliogravure. Dans la plupart de ces procédés, la faible affinité a un impact visible sur la qualité du film d'encre déposé. Des défauts d'impression typiques de chacun des procédés utilisés sont apparus et ont mis en évidence l'impact d'une faible affinité encre/support. Le cas de la flexographie et de l'enduction est détaillé dans le paragraphe suivant.

### 3.2 Impression de couches actives sur la couche de diffusion par différents procédés

Afin de démontrer l'intérêt de la flexographie comme technique complémentaire aux procédés de fabrication conventionnels de couches actives, plusieurs électrodes (appelées aussi GDE, Gas Diffusion Electrodes) ont été fabriquées en flexographie et par enduction. La Figure 16 montre une coupe d'une électrode vue au microscope électronique à balayage.

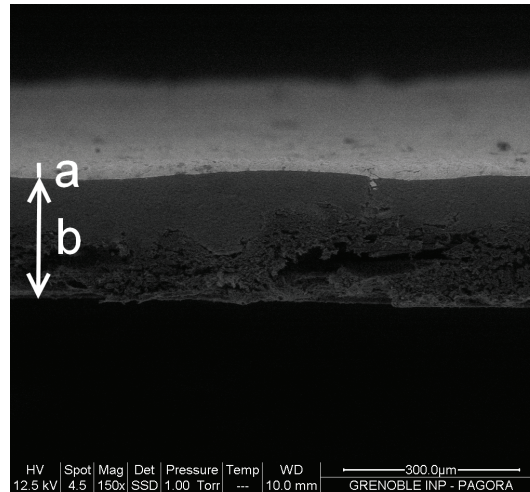


Figure 16 Vue en coupe d'une couche active (a) imprimée sur une GDL (b)

Le paramètre principal d'une couche active est son chargement en platine, donné en  $\text{mg}\cdot\text{cm}^{-2}$  ou  $\text{mg}_{\text{Pt}}\cdot\text{cm}^{-2}$  ; il permet de comparer rapidement les composants en fonction de leurs quantités de catalyseurs, comme sur la Figure 17.

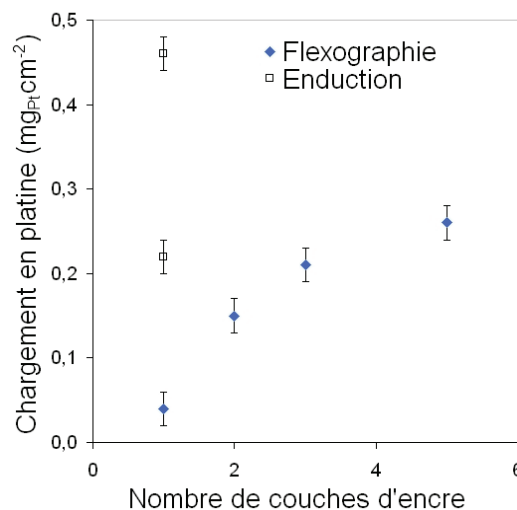


Figure 17 Chargement en platine de couches actives réalisées en flexographie et enduction en fonction du nombre de couches d'encre qui les composent

Ici, quatre couches actives ont été réalisées en flexographie. Leur valeur de chargement est donnée en fonction du nombre de couches d'encre superposées (de 1 à 5 couches). En effet, ce travail a permis le développement d'un protocole de fabrication de couches

actives en multicouche. Ainsi a-t-il été possible de contrôler la quantité de matière déposée sans modifier les paramètres d'impression en superposant des couches d'encre liquide sur liquide (c'est-à-dire sans étape de séchage entre chaque dépôt). Deux couches actives faites par enduction ont été utilisées comme référence de comparaison.

L'état de surface des couches réalisées par flexographie a été observé au microscope électronique à balayage à l'aide d'une technique permettant de différencier le platine du carbone (Back Scattering Electron ou BSE). Il a été possible de différencier les zones imprimées et non imprimées sur ces couches actives en fonction du nombre de couches d'encre qui les composent (Figure 18).

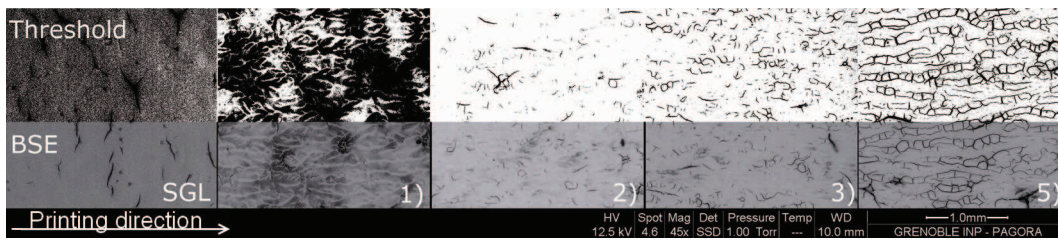


Figure 18 Vue de surface au MEB BSE de GDL et de couches actives réalisées en flexographie par superposition de une (1), deux (2), trois (3) et cinq (5) couches d'encre.

Ces couches actives réalisées par flexographie présentent des défauts spécifiques :

- Les couches actives composées d'une couche d'encre sont inhomogènes, formant un défaut appelé moirage qui est typique d'une mauvaise scission du film d'encre lorsque l'affinité entre l'encre et le support d'impression est mauvaise.
- Les couches actives composées de deux couches d'encre, montrent que l'ajout de matière limite l'observation du moirage.
- Lorsque les couches actives sont composées de trois et cinq couches superposées, des craquelures apparaissent. En particulier sur les couches actives réalisées par superposition de cinq couches d'encre, les craquelures sont parallèles au sens d'impression et aux défauts de moirage dont l'inhomogénéité d'épaisseur peut avoir influencé les zones de rupture du film.

Une autre observation de l'état de surface des couches actives a été réalisée par topographie optique. Cette technique a permis de comparer deux échantillons ayant les mêmes performances mais des chargements en platine différents: un échantillon fabriqué par flexographie ( $0,26 \text{ mg}_{\text{Pt}} \cdot \text{cm}^{-2}$ ) et un échantillon réalisé en enduction ( $0,46 \text{ mg}_{\text{Pt}} \cdot \text{cm}^{-2}$ ).

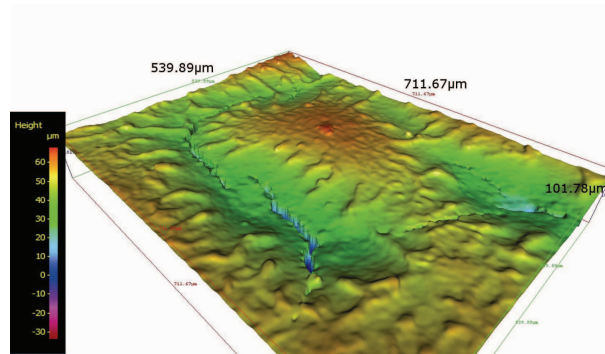


Figure 19 Topographie tridimensionnelle d'un échantillon fait par flexographie ( $0,26 \text{ mg}_{\text{Pt}} \cdot \text{cm}^{-2}$ )

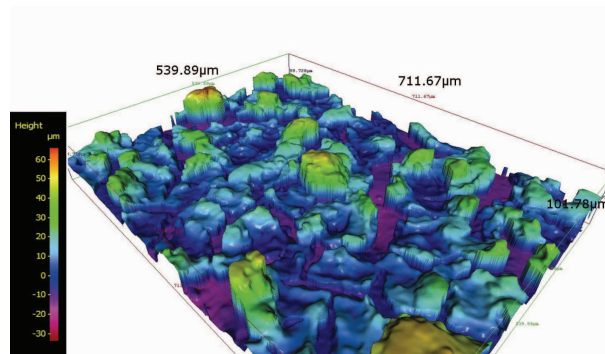


Figure 20 Topographie tridimensionnelle d'un échantillon fait par enduction ( $0,46 \text{ mg}_{\text{Pt}} \cdot \text{cm}^{-2}$ )

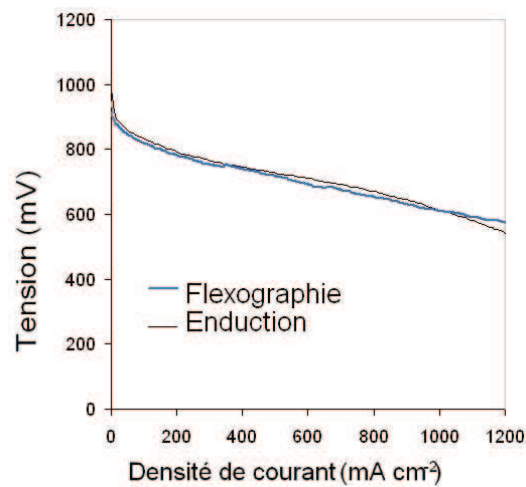


Figure 21 Courbes de polarisation de cathodes réalisées par a) flexographie  $0,26 \text{ mg}_{\text{Pt}} \cdot \text{cm}^{-2}$ , b) et enduction  $0,46 \text{ mg}_{\text{Pt}} \cdot \text{cm}^{-2}$  (conditions automobiles  $80^\circ\text{C}$ ,  $50\text{RH}\%$ , 1.5 air)

L'échantillon réalisé en flexographie (Figure 19) est peu craquelé. Les irrégularités présentes à la surface mettent en évidence l'effet du moirage sur l'épaisseur du film d'encre. En comparaison et à la même échelle d'observation (Figure 20), l'échantillon réalisé en enduction présente de nombreuses craquelures profondes. D'autres tests montrèrent que les deux types de couches actives avaient le même potentiel d'utilisation de leur catalyseur, des performances similaires (), mais l'échantillon fait par enduction présente de plus fortes résistances au transport des gaz et à la diffusion des protons. L'importance des craquelures observées sur cet échantillon semble diminuer la surface de contact entre la couche active et la GDL et ainsi potentiellement diminuer son efficacité.

#### 4 Caractérisation des couches actives par spectrophotométrie

Les techniques de caractérisation des couches actives sont généralement consommatrices en matière et en temps. C'est pourquoi la spectrophotométrie visible a été testée pour quantifier l'encre déposée sur une GDL. Cette technique est rapide, non destructrice et implantable en ligne, ce qui en fait un complément pertinent aux techniques de caractérisation actuelles.

Afin de démontrer son intérêt pour les piles à combustible, la spectrophotométrie visible a été testée sur des couches actives ayant différents chargements en encre et différentes concentrations en nanoparticules de platine.

Les mesures réalisées par spectrophotométrie visible donnent des courbes de reflectance en fonction de la longueur d'onde. La Figure 22 présente les valeurs de reflectance en fonction de la longueur d'onde des couches actives réalisées par superposition d'une à cinq couches d'encre.

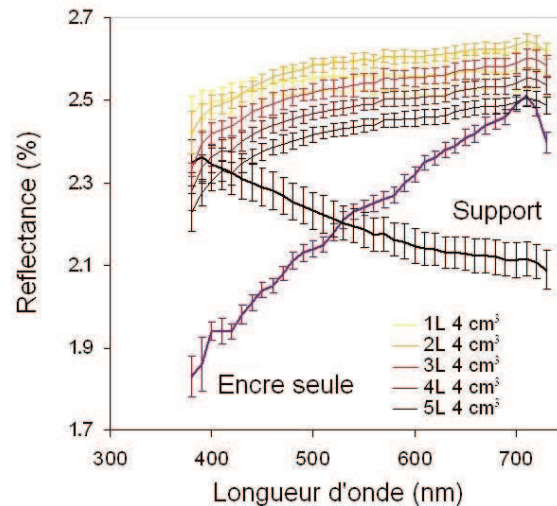


Figure 22 Courbes de reflectance en fonction de la longueur d'onde mesurées sur des couches actives réalisées par superposition de une à cinq couches d'encre avec platine

Quelle que soit la longueur d'onde, plus il y a de couches d'encre dans une couche active et plus ses valeurs de reflectance sont faibles. Une autre façon de présenter ces résultats est de donner les valeurs de reflectance pour une longueur d'onde en fonction du chargement en encre des couches actives (Figure 23).

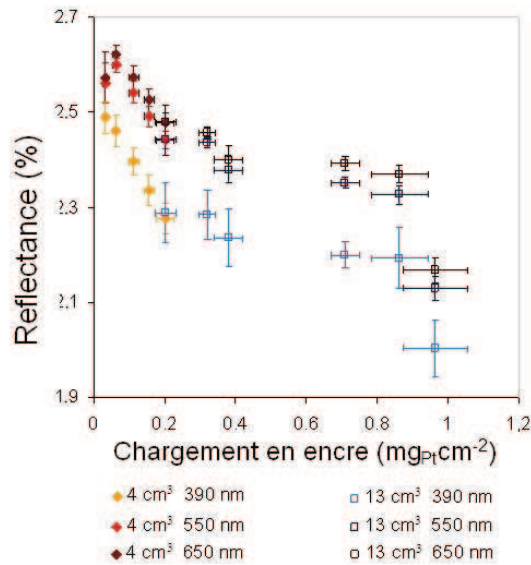


Figure 23 Valeurs de reflectance en fonction du chargement des couches actives

L'influence du nombre de couches d'encre sur les valeurs de reflectance à longueur d'onde donnée est visible. De plus, deux couches actives réalisées par des protocoles différents, mais ayant le même chargement en encre, présentent les mêmes valeurs de reflectance.

Cette technique est également capable de différencier des couches actives composées de 33% de platine d'autres couches actives fabriquées sans platine.

D'autres tests mettent en évidence la capacité de superposer les couches d'encre qui composent une couche active sans mélange. En effet, comme on le voit sur la coupe de couche active de la Figure 24, une couche d'encre ayant 33% w/wt de platine est recouverte par une couche d'encre sans platine. Sur cette figure, aucun mélange n'est visible, et les mesures de reflectance sur un tel empilement ne montrent pas la présence de nanoparticules de platine.

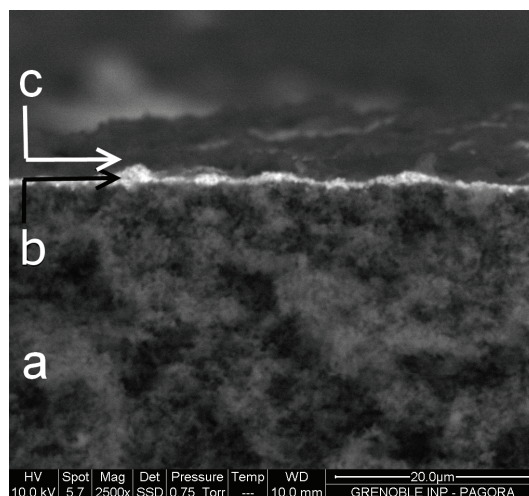


Figure 24 Vue de coupe d'une GDL (a) imprimée avec (b) trois couches d'encre avec platine sur lesquelles sont déposées (c) trois couches d'encre sans platine

La spectrophotométrie permet d'évaluer le chargement en encre d'une couche active et de discriminer des encres de concentrations en platine différentes. Cette technique permet également de démontrer que les couches d'encre qui constituent une couche active se superposent sans mélange.

## 5 Structuration des couches actives

Les résultats développés dans le chapitre précédent ont démontré la pertinence de la flexographie dans la fabrication de couches actives grâce à l'utilisation d'un protocole de dépôt en multicouche. Ce protocole ouvre une autre opportunité : la fabrication de couches actives structurées dans l'épaisseur par la superposition de couches d'encres de compositions différentes.

Deux éléments fonctionnels étaient intéressants à localiser de façon spécifique : le Nafion<sup>®</sup> et le platine. Pour réaliser cela, 5 encres ont été formulées. Ces encres ont permis d'obtenir des couches d'encre dont les extraits secs ont des concentrations en platine et Nafion<sup>®</sup> différentes (Figure 25).

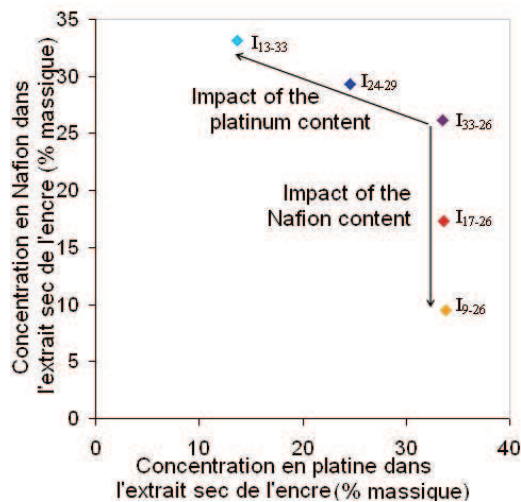


Figure 25 Concentration en Nafion<sup>®</sup> (w/wt%) dans l'extrait sec de l'encre en fonction de la concentration en platine (w/wt%) dans l'extrait sec de l'encre

L'imprimabilité de chacune de ces encres a été tout d'abord testée sur des GDL par dépôt de couches actives dites homogènes, c'est-à-dire réalisées par la superposition de couche d'un seul type d'encre.

Les chargements en platine et Nafion<sup>®</sup> de chacune de ces couches actives ont été mesurés (Figure 26).

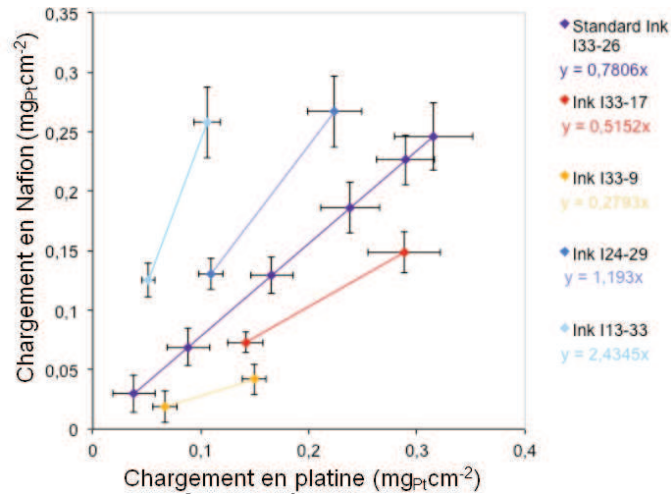


Figure 26 Chargement en Nafion® (mg cm<sup>-2</sup>) des couches actives en fonction du chargement en platine (mg cm<sup>-2</sup>) des couches actives

Les encres contenant différentes concentration en platine ont permis de réaliser des couches actives avec la même concentration en Nafion® et différentes concentrations en platine comme souhaité. Les images MEB des Figure 27, Figure 28 et Figure 29 présentent des états de surface similaires et acceptables.

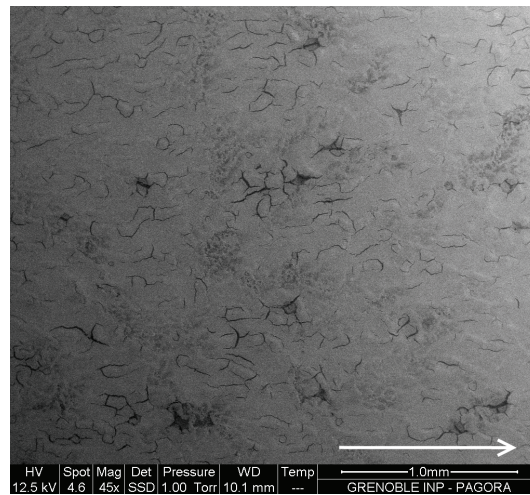


Figure 27 Surface de couche active au MEB BSE composée I<sub>33-26</sub> 3L (la flèche montre le sens d'impression)

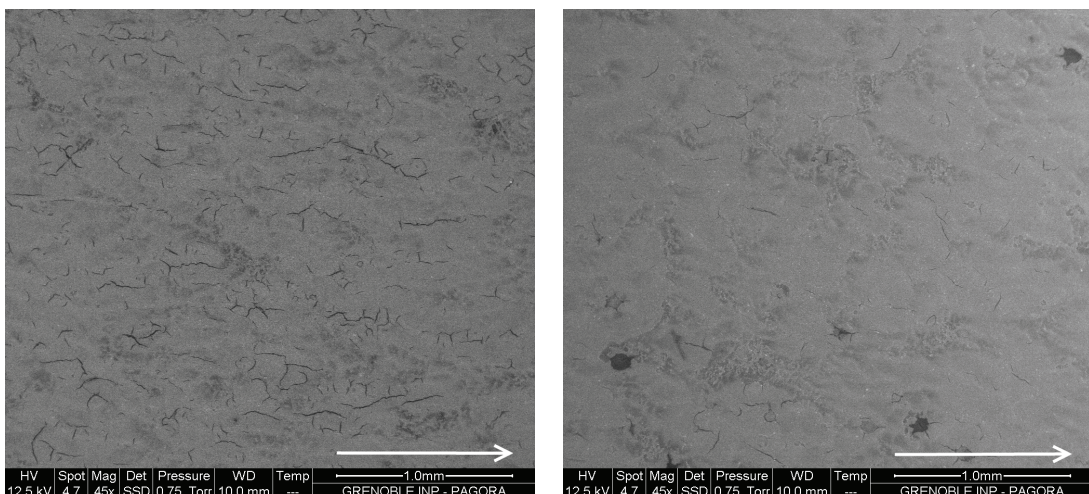


Figure 28 Surface de couche active au MEB BSE composée I<sub>24-29</sub> (la flèche montre le sens d'impression)

Figure 29 Surface de couche active au MEB BSE composée I<sub>13-33 29</sub> (la flèche montre le sens d'impression)

Cependant, les couches actives réalisées avec les encres à diverses concentrations en Nafion® présentent des chargements plus faibles en Nafion® et en platine, à cause de dépôts d'encre plus faibles, malgré des paramètres d'impression similaires. Les images de Figure 30 et Figure 31 montrent des états de surface dégradés, preuve d'une mauvaise imprimabilité de ces encres.

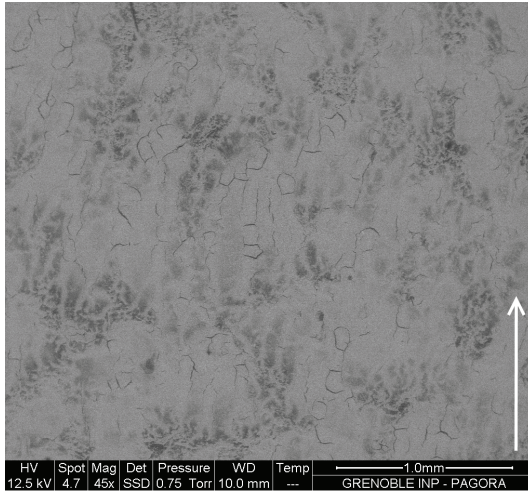


Figure 30 Surface de couche active au MEB BSE composée I<sub>33-17</sub> (la flèche montre le sens d'impression)

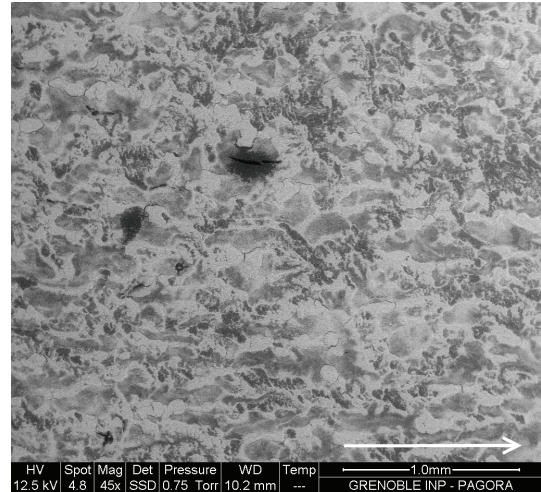


Figure 31 Surface de couche active au MEB BSE composée I<sub>33-9</sub> (la flèche montre le sens d'impression)

Pour cette raison, les couches actives ont été structurées à l'aide d'encres de concentrations variables en platine.

Les images au MEB de coupe de couches actives structurées dans l'épaisseur suivant diverses géométries des Figure 32, Figure 33 et Figure 34 démontrent la capacité de la flexographie de superposer des couches d'encres de types différents et de structurer des couches actives.

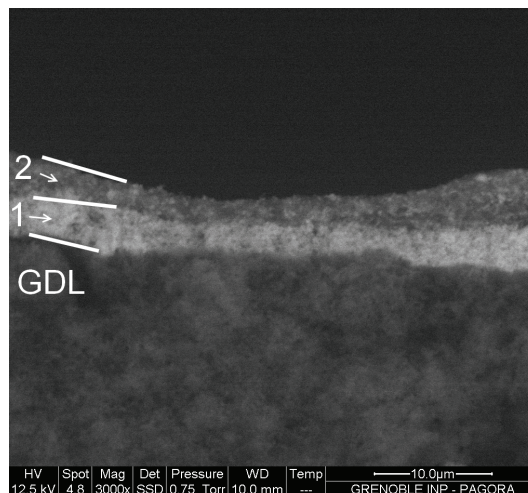


Figure 32 Coupe de couches actives au MEB BSE composées (de bas en haut) de 1) trois couches d'encre I<sub>33-26</sub> et 2) trois couches d'encre I<sub>13-33</sub>

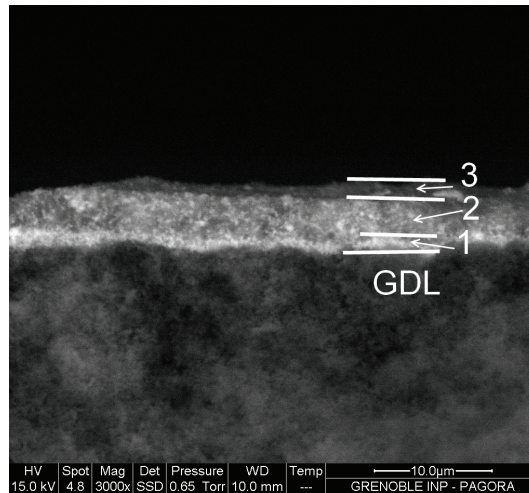


Figure 33 Coupe de couches actives au MEB BSE composées (de bas en haut) de 1) deux couches d'encre  $I_{33-26}$ , 2) deux couches d'encre  $I_{24-29}$  et 3) deux couches d'encre  $I_{13-33}$

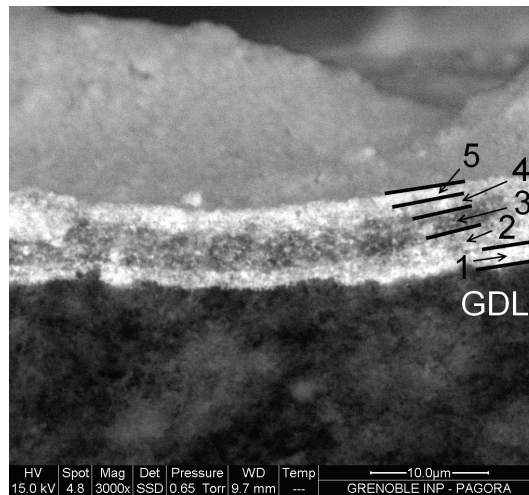


Figure 34 Coupe de couches actives au MEB BSE composées (de bas en haut) de 1) une couche d'encre  $I_{33-26}$ , 2) une couche d'encre  $I_{24-29}$ , 3) deux couches d'encre  $I_{13-33}$ , 4) une couche d'encre  $I_{24-29}$  et 5) une couche d'encre  $I_{33-26}$

Des couches actives structurées ont été testées en piles dans des conditions automobiles et ont montré de très bonnes performances (Figure 35).

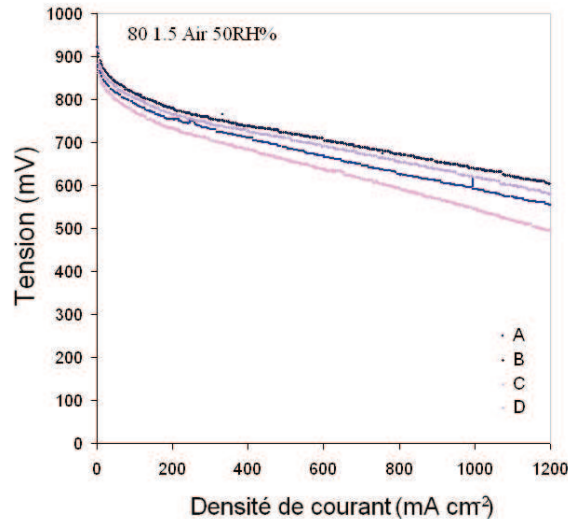


Figure 35 Courbes de polarisation de couches actives structurées (conditions automobiles 80°C, 50RH%, 1.5 air)

### Conclusion et perspectives

L'objectif de cette thèse était de démontrer que des AMEs pour PEMFC pouvaient être fabriquées par des procédés issus des industries graphiques. Il s'agissait de montrer que les couches actives peuvent être imprimées et que les couches de diffusion et la membrane échangeuse de protons (Nafion<sup>®</sup>) peuvent être considérées comme des supports d'impression. Plus précisément, ce travail s'est concentré sur le procédé flexographique utilisant des encres aqueuses (couches actives) et des supports d'impression (Nafion<sup>®</sup> et couches de diffusion). Une des principales difficultés rencontrée a été l'hydrophobicité des supports et leur instabilité dimensionnelle en présence d'humidité provenant de l'encre et/ou de l'environnement. Un pré-traitement a été mis au point pour stabiliser les supports avant impression. Enfin, un protocole en multicouche a été élaboré, ce qui limite l'influence de la mauvaise affinité encre/support et contrôle la quantité de particules fonctionnelles dans les couches actives, ceci avec une grande sélectivité de transfert. Ces couches actives présentent des propriétés électrochimiques comparables à celles fabriquées par des procédés conventionnels et démontrent la pertinence de la flexographie comme procédé de fabrication de couches actives pour PEMFC.

De futurs travaux porteront sur :

- la caractérisation des membranes comme support d'impression  
Influence de la température et du type de membrane sur l'hygroexpansion et la prise en eau.
- La déposition sélective des éléments fonctionnels  
La conception en trois dimensions des couches actives par structuration dans l'épaisseur et impression de motifs dans le plan.